First-principles Prediction of Catalytic Activity Tuned with Structure, Atomic Substitution and Vacancies: Applications to Energy and Environment

A Thesis
Submitted For the Degree of
DOCTOR OF PHILOSOPHY
in the Faculty of Science

by
Lakshay Dheer

CHEMISTRY AND PHYSICS OF MATERIALS UNIT
JAWAHARLAL NEHRU CENTRE FOR ADVANCED SCIENTIFIC RESEARCH
Bangalore - 560 064
SEPTEMBER 2021

To my Family

DECLARATION

I hereby declare that the matter embodied in the thesis entitled "***First-principles* Prediction of Catalytic Activity Tuned with Structure, Atomic Substitution and Vacancies: Applications to Energy and Environment**" is the result of investigations carried out by me at the Chemistry and Physics of Materials Unit, Jawaharlal Nehru Centre for Advanced Scientific Research, Bangalore, India under the supervision of Prof. Umesh V. Waghmare and that it has not been submitted elsewhere for the award of any degree or diploma.

In keeping with the general practice in reporting scientific observations, due acknowledgement has been made whenever the work described is based on the findings of other investigators.

Lakshay Dheer

CERTIFICATE

I hereby certify that the matter embodied in this thesis entitled "***First-principles* Prediction of Catalytic Activity Tuned with Structure, Atomic Substitution and Vacancies: Applications to Energy and Environment**" has been carried out by Mr. Lakshay Dheer at the Chemistry and Physics of Materials Unit, Jawaharlal Nehru Centre for Advanced Scientific Research, Bangalore, India under my supervision and that it has not been submitted elsewhere for the award of any degree or diploma.

Prof. Umesh V. Waghmare
(Research Supervisor)

Acknowledgements

First and foremost, I would like to express my deepest gratitude towards my advisor, Prof. Umesh V. Waghmare, for his constant motivation, guidance and endless support. I still remember the first interaction I had with him around 5 years ago, when he welcomed me in his group as a summer project student. I have been extremely fortunate to work under his umbrella and he has given me utmost freedom in selecting the problems which I found intriguing. His brilliance and devotion to science has inspired me countless times. I thank him for being patient with me, for encouraging me and believing in me. His valuable comments and suggestions while preparing for seminars and writing papers have been extremely helpful. Being under his mentorship has had a gigantic effect on my personal and professional growth. Thank you, Sir.

I thank my Collaborators, Prof. Daniel Strongin, Prof. Sebastian C. Peter, Prof. Ranjani Viswanatha, Prof. Ranjit Thapa, Dr. Meghna A. Manae, Dr. Akila Thenuwara, Dr. Nuwan Harsha, Dr. Soumyabrata Roy, Dr. Shreya Sarkar, Dr. Mahima Makkar, Dr. Rajamani and Arjun, for the interesting scientific discussions. A special thanks to Prof. Thapa and Dr. Manae for numerous scientific discussions and support.

I thank all the TSU, CPMU and NCU faculty, Prof. Umesh. V. Waghmare, Prof. S. Balasubramanian, Prof. T. K. Maji, Prof. M. Eswaramoorthy, Prof. C. Narayana, Prof. K. S. Narayan, Prof. S. Narasimhan, Prof. A. Sundaresan, Prof. Vidhyadhiraja N. S., Dr. M. K. Prakash, Dr. S. Rajaram, Dr. S. C. Peter, Dr. R. Ganapathy, for their excellent courses which were not only interesting but also enlightening.

It is my pleasure to thank the present and past members of Materials theory group, Koushik, Anjali, Suchitra, Meha, Pawan, Arpita, Sweta, Henu, Koyendrila, Narendra, Shashank, Raagya, Arijit, Bhuvaneswari, Surabhi, Unnimaya, Sarbajit, Prasad, Anuja,

Sampath, Shazia, Prashant, Arpita Sen, Durgesh and Meghna for many academic, non-academic and fun interactions.

I am thankful to Aruna and Kruti for making us feel like a family.

I also thank the Complab, Academic, Admin, Library, Dhanvantari, Utility store, Dining Hall and Hostel mess staff and TSU secretary for all their help.

A special thanks to my friends in JNCASR, Shashank, Meghna, Ashutosh, Rajendra and Neha for all the coffee sessions and not so scientific discussions.

Finally, I am grateful to Mumma, Papa, my brother Daksh, Maa, and Baba. A special thanks to my pillar throughout this journey, Ananya. Without your unwavering love and support, this trip would have been impossible. This thesis is dedicated to them.

Synopsis

Catalysts enhance the rate of a chemical reaction by providing an alternate, low energy barrier route connecting reactants to products, without undergoing any change themselves. At its core, the main purpose of a catalyst is to save energy. Production of clean fuels like H_2, conversion of waste and even harmful by-products (CO_2) to usable moieties (CH_3OH), and synthesis of industrially important chemicals (NH_3) are impacted greatly by catalysts. Determination of mechanisms of catalytic activity and its prediction are fundamentally challenging, because it involves physical and chemical interactions between different types of molecules and solids. Prediction and design of highly selective catalysts with efficient activity thus have huge academic and socioeconomic significance. Substantial advancement in computational modelling, algorithms and unprecedented growth of raw computing power have enabled the design and prediction of catalysts with calculations within first-principles density functional theory (DFT). These DFT-based simulations provide unbiased, non-empirical access to detailed atomistic and electronic structure and properties of materials, complementing experiments. In this thesis, we demonstrate how comprehensive analysis based on DFT calculations can be used to (a) understand and explain the activity of experimentally synthesized catalysts and (b) design and predict novel catalysts, for a number of reactions of relevance to tackling problems of energy and environment. We illustrate how the activity of a catalyst can be tuned with structure, defects (vacancies), and substitutional alloying, identifying relevant descriptors that would facilitate further work.

In Chapter 1 we give a brief introduction to some fundamental and important aspects of catalysis. This is followed by a brief description of methods and formalism used in our calculations in Chapter 2. Further, the thesis is divided into three parts, based on the types of catalytic reactions studied.

In the first part (Chapters 3-5) we focus on analysis of two half cell reactions associated with water splitting, hydrogen evolution reaction (HER) and oxygen evolution reaction (OER). The former is a reduction reaction used to generate H_2, a clean and renewable fuel, while the latter involves oxidation of H_2O to O_2. In Chapter 3, we present work on tuning catalytic activity by engineering atomic structure of catalysts: (a) introducing amorphicity in a Co-Mo-P catalyst (Chapter 3a) and (b) stabilizing the metastable 1T structure of MoS_2 by substitutional alloying (Chapter 3b). We evaluate the viability of these catalysts towards alkaline HER and provide mechanistic insights into experiments. In Chapter 4, we present analysis of enhancement of catalytic activity with substitutional alloying of a metal phosphide, Ni_2P, towards water splitting (Chapter 4a) and metal carbides, WC and MoC, towards HER (Chapter 4b). We show that the presence of surface oxygen leads to further increase in catalytic activity of Mn-substituted Ni_2P (Chapter 4a) while Ni-dopants in WC and MoC tune the electronic structure of metal carbides leading to superior HER activity (Chapter 4b). In Chapter 5, we predict a novel 2D catalyst for HER based on graphene:MoS_2 heterostructures, and show how the site-specific activity is tuned with substitutional N. Graphitic N-atoms exhibit high affinity to evolve H_2 with optimum ΔG^H_{ads} and work function (ϕ).

In the second part of thesis (Chapter 6 and 7), we present analysis of two intermetallic catalysts for (i) conversion of CO_2 into a useful fuel (CH_3OH) and (ii) use of such fuels (e.g. C_2H_5OH) in a fuel cell to generate electricity. In Chapter 6, we present detailed analysis of a Ni-In based intermetallic catalyst to convert the greenhouse CO_2 gas through hydrogenation to a value-added product, CH_3OH. We explore multiple pathways for CO_2 hydrogenation and show Ni_3In exhibits high selectivity towards CH_3OH as the product. Next, we study a catalytic reaction utilizing a related fuel (CH_3CH_2OH) to produce electricity. In Chapter 7, we explain the observed manyfold increase in activity of Pd_2Ge towards the electrooxidation reaction (EOR) of ethanol using substitutional Ni. Presence of Ni-substituents optimizes the adhesion strength of the main intermediates occurring

along the EOR pathway thus enhancing activity.

In the third part of thesis, we present our work on design and prediction of novel catalysts for synthesis of two commercially value-added products, H_2O_2 and NH_3. In Chapter 8, we present our work on design of a catalyst based on 1H-MoS_2 for the direct synthesis of hydrogen peroxide (DSHP). We show that a combination of substitutional Au and S-vacancies in MoS_2 monolayer act synergistically to catalyze the entire reaction without significant energy cost and renders high selectivity. Finally in Chapter 9, we report a metal-free catalyst based on borophene sheets for electrochemical reduction of nitrogen. C-decorated α polymorph of borophene is predicted to catalyze electrochemical nitrogen reduction reaction (eNRR) at a low limiting potential (U_L) and exhibit high selectivity. In addition, we identify two novel descriptors which can be employed in high throughput screening of catalysts for eNRR. We finally summarize the thesis and present an outlook.

List of Figures

List of Tables

Contents

Chapter 1

Introduction

The term "catalysis" was coined by Swedish chemist J. J. Berzelius in 1836 [5]. In those days, a report was published annually summarizing progress made in the entire subject of chemistry. For many years, this task was undertaken by Berzelius for the Stockholm Academy of Sciences [6]. In the 1836 report where he summarised his ideas of the "catalytic force", he wrote "It is, then, proved that several simple or compound bodies, soluble and insoluble, have the property of exercising on other bodies an action very different from chemical affinity. By means of this action they produce, in these bodies, decompositions of their elements and different recombinations of these same elements to which they remain indifferent." Berzelius concluded that a novel "catalytic force" operates and leads to decomposition of various chemicals *via* the process of "catalysis". Around that time, chemical affinity was recognised as the driving force, however there was no understanding of reaction rates at a molecular level.

Catalysis had in fact been exploited by humans for thousands of years in processes like fermentation of sugars to produce alcohol [7]. The first historical reference of catalysis as a chemical phenomenon appeared in 1597 [8] in Andreas Libavius's masterpiece "Alchemia", which is considered the first textbook of chemistry. However, unlike the description given

by Berzelius, Libavius interpreted the term 'catalysis' as the conversion of non-precious metals into gold and silver, the primary motivation behind alchemy. The earliest known report showcasing use of inorganic catalysts dates back to mid 16^{th} century when Varelius Cordus produced ether from alcohol using sulfuric acid as a catalyst [9, 10].

Catalysts increase the rate of reaction by lowering the energy barrier to transform reactants into products, without being consumed themselves. Based on their physical state, catalysts can be categorised into homogeneous and heterogeneous catalysts. As the name suggests, homogeneous catalysts exist in the same phase as reactants/products while heterogeneous catalysts are present in a different phase than that of the chemical species involved in the reaction. Catalysts are some of the most used materials and are at the heart of many industrial processes. It would not be a stretch to say that these materials, often employed in minute quantities, form the backbone of the modern world. Production of everyday items like beer, plastics, paper, petroleum, and industrially significant chemicals like ammonia (NH_3), sulfuric acid (H_2SO_4), hydrogen peroxide (H_2O_2), all involve catalysts. Perhaps one of the most vital role of catalysts is to carry out the chemical processes within the human body. These 'bio-catalysts', more commonly referred to as enzymes, are some of the most efficient catalysts in nature and are essential to life. Most industrially applied catalysts fall into the heterogeneous category while enzymes are examples of homogeneous catalysts.

Catalysts also find essential roles in technologies enabling sustainable production of energy, arguably the most important resource of all. In the 20^{th} century, fossil fuels provided the energy input for the industrial revolution. In the 21^{st} century we face one of the greatest challenges of replacing the non-renewable sources of energy with clean and sustainable one. Another dire predicament faced globally today is that of increased CO_2 emissions, which contribute significantly to global warming. While CO_2 occurs naturally in the earth's atmosphere originating from sources such as volcanoes, forest fires, hot springs

and geysers, its concentration has increased from pre-industrial levels of 280 ppm to 412 ppm in 2020 [11,12]. Such rise in CO_2 levels over the course of the industrial revolution is primarily anthropogenic and can be attributed largely to the increased use of fossil fuels. The energy demand will only continue to rise into the next century, and thus there is an urgent need for replacing fossil fuels with greener energy sources. One of the most viable options of these "green fuels" is molecule hydrogen (H_2). H_2 also plays a critical role as a reducing agent in hydrogenation of CO_2, converting it into fuels like methanol (MeOH) and ethanol (EtOH). H_2, by itself, is a zero-emission fuel with a high combustion energy, and can be used to power liquid-propellant rockets, automobiles, and fuel cells. H_2 is rarely found in its pure form in the atmosphere because of its molecular weight being significantly lower than air.

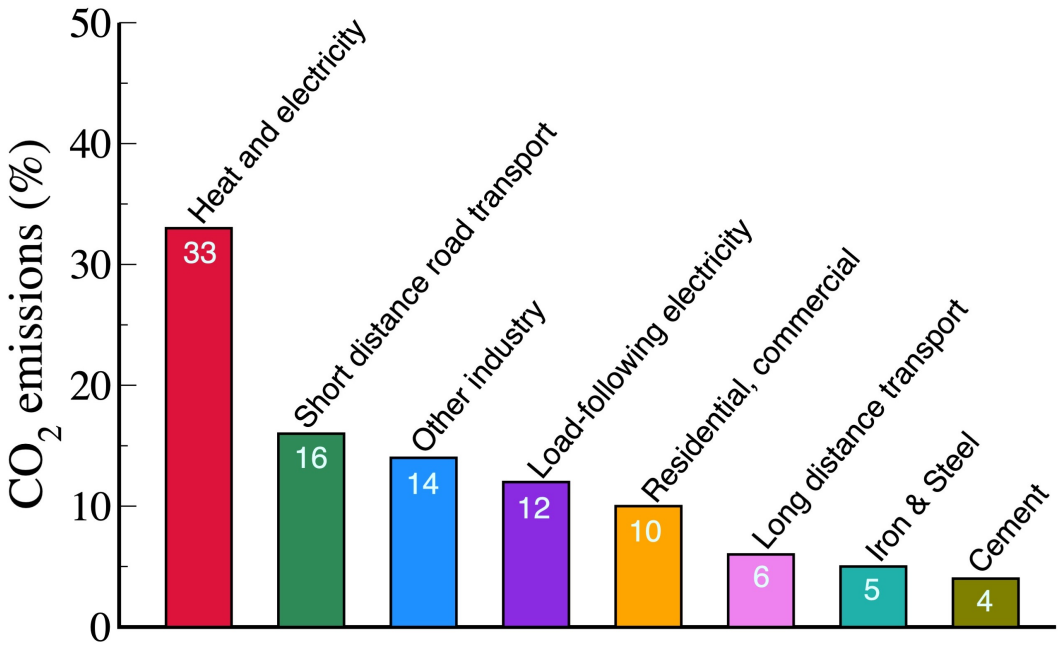

Figure 1.1: Share of CO2 emissions due to various human activities for the year 2014, with the percentages indicated inside the bars. The overall annual CO2 emissions amounts to 33.9 gigatons [1]. Reprinted with permission from [2]. Copyright (2021) by Springer Nature (Switzerland AG).

Developing efficient and inexpensive catalysts to produce fuels like H_2 and MeOH has

attracted immense research efforts in the past 50 yrs. Currently, MeOH is produced industrially by passing syngas (a mixture of H_2 and CO) over $Cu/ZnO/Al_2O_3$, at 50–100 bar and 473–573 K [13, 14]. Generating MeOH through CO_2 hydrogenation does not sufer from this disadvantage. As mentioned earlier, MeOH, generated from the addition of H_2 to CO_2, also amounts to chemical storage of H_2 and innovative portable use of H_2 as a fuel. CO_2 capture is the frst step towards converting it into a viable fuel. Of the various sources of CO_2 emissions [1] (Fig 1.1), not all qualify as emission streams which can be used readily as inputs in a CO_2 capture process. Sources which can be used as emission streams include the fuel gas from thermal power stations, emissions from oil refineries, blast furnace gas, and cement kiln of-gas [15]. In addition to being some of the strongest sources of CO_2 emissions, these sources also generate considerable amounts of waste heat. Therefore, a thermocatalytic approach to the generating MeOH from CO_2 is attractive because it would reduce CO_2 emissions while making use of the already generated waste heat. When the required intake of H_2 is generated using electrocatalytic and photoelectrocatalytic approaches, this further reduces the overall CO_2 emission in the process. Despite generating H_2 using clean energy sources, and carrying out CO_4 hydrogenation using waste heat, use of the produced MeOH as a fuel will add to CO_2 emissions. In principle, CO_2 generated from burning of MeOH as a fuel can be recycled back to generate more MeOH, making the process carbon neutral (Fig 1.2). Catalysts play a vital role at each step of the scheme. From capturing CO_2, converting it into MeOH via the 6 electron transfer reduction of CO_2, and also providing H_2 generated via the electrochemical splitting of water, each step highly dependent on various catalysts.

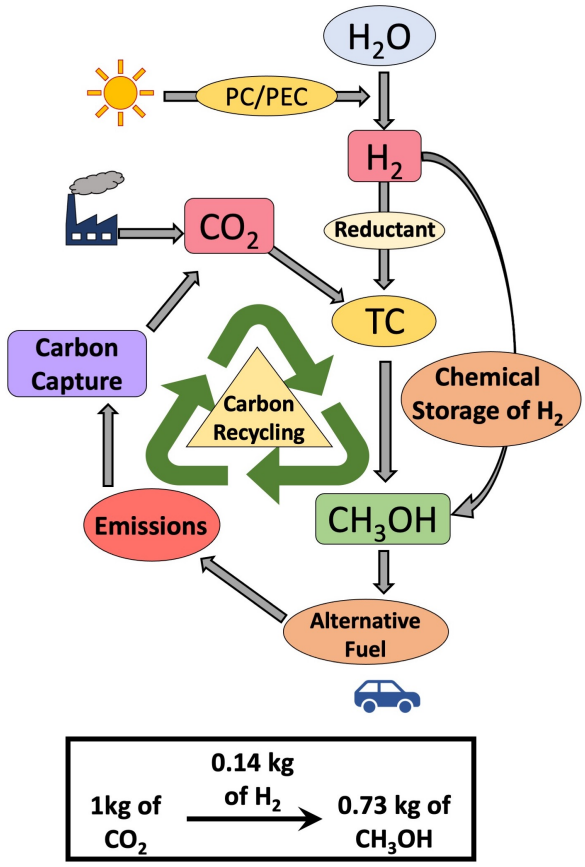

Figure 1.2: Schematic of a sustainable process where MeOH is generated. PC, PEC and TC denote photocatalytic, photoelectrocatalytic, and thermocatalytic, respectively. Reprinted with permission from [2]. Copyright (2021) by Springer Nature (Switzerland AG).

This thesis focuses on first-principles density functional theoretical analysis a number of reactions of relevance to tackling problems of energy and environment. In the studies presented here the reactants and products present in gas phase, reacting on the surface of a solid catalyst.

1.1 Energetics of catalytic reactions

Chemical reactions either require an energy input, or give out energy in the form of heat. The former is called an endothermic reaction while the latter is known as an exothermic

reaction. The energy change during a chemical reaction can be represented as a potential energy diagram (Fig. 1.3), where change in enthalpy (ΔH) is positive for endothermic reactions while negative for exothermic reactions. An exothermic reaction is spontaneous as the products are lower in energy while an endothermic reaction requires an external force to proceed. A chemical change occurs with rearrangement of the molecular or ionic structure of reactants, transforming them into products. This involves interaction between atoms/molecules accompanied with cleavage of chemical bonds and formation of new ones. Catalysts facilitate this by temporarily binding with the reactants, facilitating their conversion to intermediates and the final product. Consider an elementary chemical reaction R $\rightarrow$ P, proceeding *via* a short-lived local energy maximum $C^{\dagger}$, called the transition state. The energy required to cross this barrier is called activation energy (E_a) and is inversely related to the rate of the reaction. Catalysts essentially lower the E_a (Fig. 1.4) by providing an energetically favorable pathway connecting reactants (A+B) to the product (P). Thus, ΔH determines the direction of spontaneity of a chemical reaction while E_a controls the speed of the reaction.

1.1.1 Selectivity

Selectivity of a catalyst is its ability to produce specific products while suppressing alternative side reactions. A set of reactants may yield different products depending on the catalysts employed (Fig. 1.4). Syngas (CO + H_2), for example, converts to methane (CH_4) on a Ni [16, 17] catalyst, methanol (CH_3OH) on a Cu-Zn [18] catalyst and formaldehyde (HCHO) with Cu [19] as catalyst. In addition to being efficient, catalysts should also exhibit high selectivity towards a particular product in order to maximize their widespread application otherwise some of the reactants get converted to undesirable products, with additional separation and purification costs. Many chemical reactions have competing side reactions, and suppression of these undesired processes is vital. Production of H_2O_2 is an example where O_2 molecule often gets fully hydrogenated to H_2O [20] due to the

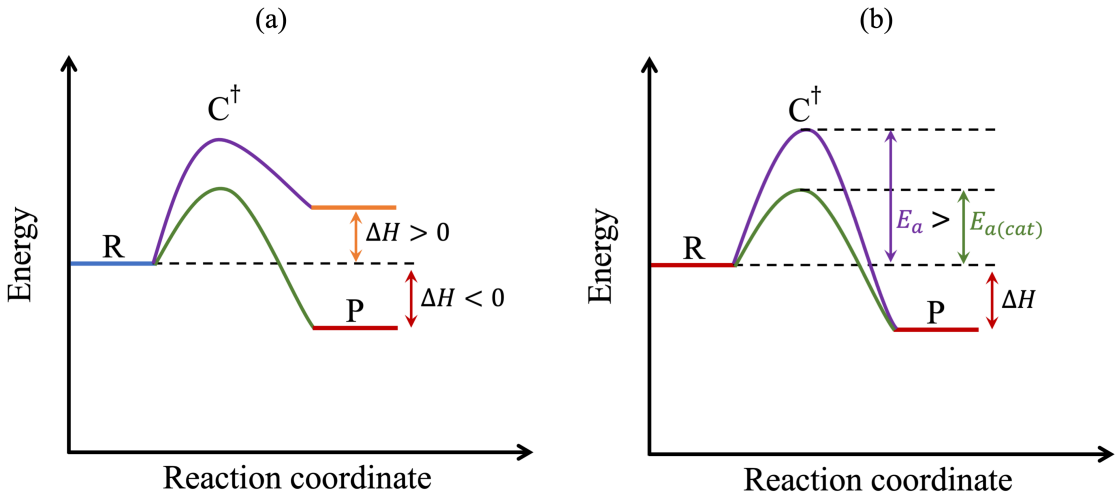

Figure 1.3: Potential energy landscape of a reaction demonstrating (a) ΔH for an exothermic (red) and endothermic (orange) reaction; and (b) reduction in activation barrier by a catalyst (green pathway).

unstable nature of product. Selectivity thus plays a crucial role in overall performance of a catalyst.

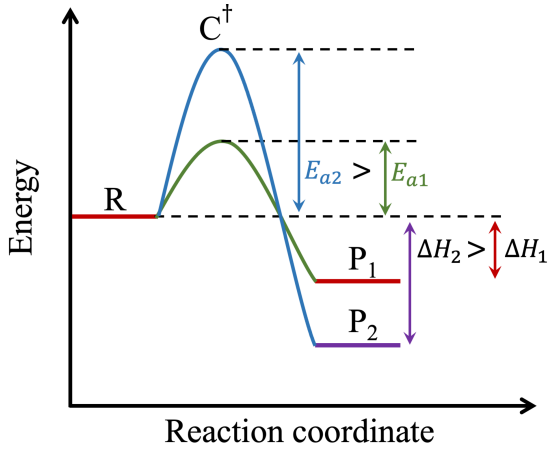

Figure 1.4: Potential energy diagram of a reaction with more than one possible products (P_1 and P_2) along green and and blue paths. Even though formation of P_2 is thermodynamically favoured, the activation barrier associated with P_1 (E_{a1}) is smaller: selective catalysis.

1.2 Designing catalysts using computer simulations within DFT

Remarkable progress has been achieved experimentally in engineering catalysts to perform optimally. However, experimental identification and isolation of reaction intermediates formed on the surface of a catalyst during a reaction can be challenging due to their short lifetimes. Computer simulations within DFT are powerful tools in complement to experiments in this task. Despite having short a lifetime, intermediates are typically local minima in the energy landscape of a reaction and are accessible to first-principles DFT calculations. Here, one determines the interatomic potential by simulating quantum motion of electrons that mediate to interactions between various reacting species, the catalyst surface and each other. Transition states have even shorter lifetimes and are typically first-order saddle points in the reaction energy landscape (Fig. 1.5). This topological difference between intermediates and transition states facilitates their identification and analysis.

First-principles calculations allow accurate estimation of energies of intermediates, reactants and products, using which thermodynamics of a reaction can be understood. The relative energy of intermediate products in comparison to reactants, the enthalpy, is the amount of heat generated or consumed in a given part of the reaction. Energies of the transition states, on the other hand, provide activation energies which control the rate of the reactions. They are a measure of energy to activate an intermediate through stretching or breaking of bonds. The structures and energies of reactants, products, all intervening intermediates and transition states constitute the complete pathway, or the mechanism, of a reaction. Structures of the catalyst-reacting species complexes are useful in identification of active sites on catalysts. This is especially important for multi-step reactions, where different active sites on a catalyst may catalyze different steps of the reaction. Identification of active sites also helps in rational design of more efficient, selective and

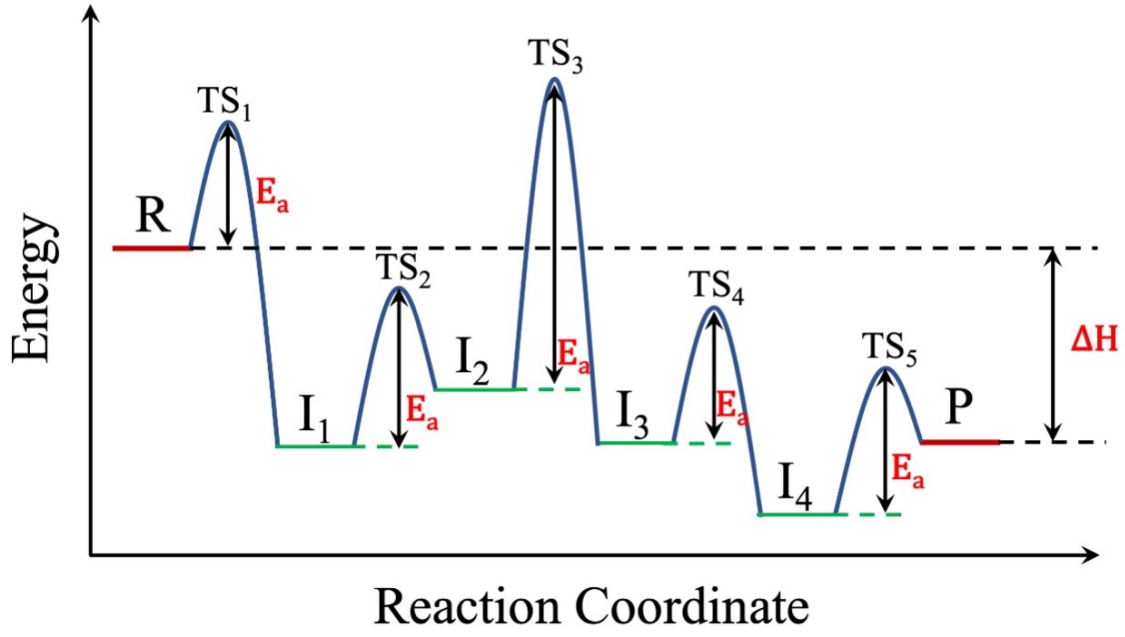

Figure 1.5: Schematic of a reaction mechanism, where, R, P, I, TS, represent the reactant, product, intermediates, transition states, respectively, and E_a, ΔH represent activation energies, and enthalpy of the reaction, respectively. Reprinted with permission from [2]. Copyright (2021) by Springer Nature (Switzerland AG).

cheaper catalysts.

In this thesis, we demonstrate how comprehensive DFT calculations can be used to (a) provide mechanistic insights into the activity of experimentally synthesized catalysts and (b) design and predict novel catalysts, for a number of reactions, important to tackle problems of energy and environment. The design parameters that tune the activity of a catalyst here are structure, defects (vacancies), and substitutional alloying, and we identify the relevant descriptors to facilitate further work.

1.3 Reactions for energy, environment and industry

In this thesis, we focus on theoretical analysis of catalytic materials and mechanisms of a few reactions that are central to renewable energy conversion, reduction of greenhouse gases and synthesis of industrial products like H_2O_2 and NH_3.

1.3.1 Water splitting

Fossil fuels have been crucial in powering the industrial revolution since early 18^{th} century. Being limited in quantity, these sources of energies need to be replaced with renewable ones. Moreover, these fuels have been the main source of chemical pollutants like carbon dioxide (CO_2), directly associated with global warming. As of April 2017, CO_2 concentration reached 410 parts per million (ppm) as compared to 280 ppm in 1958 [11, 21]. Hydrogen (H_2) is a viable and sustainable green fuel owing to its carbon (C)-free footprint and high gravimetric energy density [22]. The main challenge keeping H_2 dormant from practical application is the lack of sustainable production methods. As of now, almost all of the H_2 is generated by steam-reforming of fossil fuels [23] which releases CO_2 as a by-product making it non-viable. Clean and sustainable methods of H_2 synthesis are being explored extensively so as to establish a "Hydrogen Economy" [24]. A green and viable method to generate H_2 is by electrochemical splitting of water, first discovered in 1789. Water splitting consisting of two half-cell reactions [23]:

- Oxygen Evolution Reaction **(OER)**

$$2H_2O\ (l) \rightarrow O_2\ (g) + 4H^+ + 4e^- \tag{1.1}$$

- Hydrogen Evolution Reaction **(HER)**

$$4H^+ + 4e^- \rightarrow 2H_2\ (g) \tag{1.2}$$

- **Overall water splitting reaction**

$$2H_2O + 474.4\ \text{kJmol}^{-1} \rightarrow 2H_2 + O_2 \qquad 2005/06/28ver :$$

Oxygen evolution reaction

The oxidation half of water splitting, OER, is a four electron transfer process to generate molecular oxygen (O_2). Due to low turnover frequencies and large overpotentials, OER

is the kinetic bottleneck in overall water splitting and only a handful of precious metals and their oxides (Ir, IrO_2, Ru and RuO_2) [25–27] catalyze the reaction with reasonable efficiency. However, the dearth, high cost and low cyclability, limit their scalable use. Development of cheap, precious-metal-free materials which catalyze OER at low overpotentials is the key to advancing various sustainable processes of energy generation.

Three main intermediates, O*, HO* and HOO* occur along the reaction pathway of OER (* means adsorbed on catalytic surface). Evolution of O_2 molecule occurs either directly *via* two MO (M = metal) species or *via* decomposition of the hydroperoxyl (MOOH) intermediate (Fig. 1.6). The mechanism of OER is different depending on the pH of the reaction media [3]. Under alkaline conditions, readily available HO^- ions bind to the active sites of a catalyst forming MO/MOOH intermediate. In acidic media, the H_2O molecule splits to provide the HO^- ions.

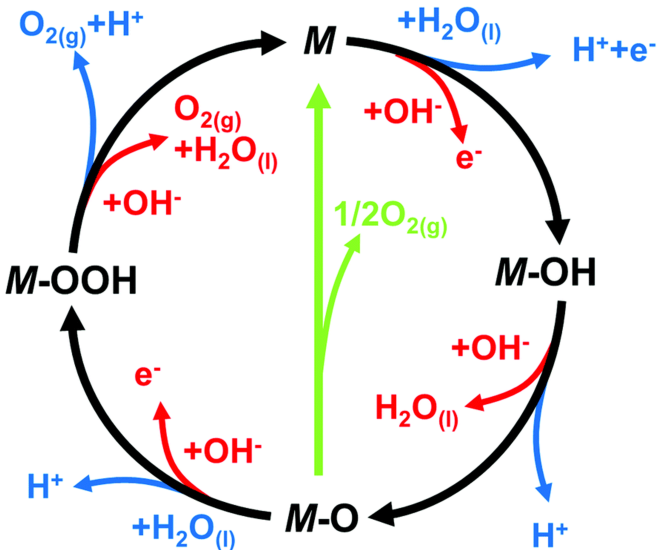

Figure 1.6: OER mechanism in acidic (blue line) and alkaline (red line) medium. The black line follows the hydroperoxyl (MOOH) intermediates for oxygen evolution while green line represents the direct route involving reaction of two adjacent oxo (MO) intermediate to produce O_2. Reprinted with permission from [3]. Copyright (2017) by Royal Society of Chemistry (Great Britain).

Hydrogen evolution reaction

HER is the cathodic half-cell reaction of water splitting and involves transfer of two electrons, reducing H^+ to evolve H_2. The reaction proceeds *via* two reaction pathways, Volmer-Tafel or Volmer-Heyrovsky, consisting of two elementary steps, each involving transfer of one electron from the cathode to H^+, evolving H_2. The first step (*Volmer*) is common and corresponds to adsorption of the first proton on an available active site of the catalyst. An electron transfers from catalyst to the proton yielding an adsorbed H^* intermediate. Following this, the formation and subsequent evolution of H_2 can occur *via* two dissimilar routes. *Heyrovsky* step, where, a proton from the solution reacts with the adsorbed H^* to form H_2 with transfer of another electron from the electrode evolving H_2. This step is also referred to as the *ion + atom reaction* [23]. The second pathway involves the *Tafel* step, where, another proton attaches to the electrode surface in the vicinity of H^* intermediate. The two adsorbed H^* coalesce to give H_2, and thus this is referred to as the *combination* reaction.

HER is generally carried out in acidic media where hydronium ions (H_3O^+) serve as the source of protons. Previously, it has been shown that some of the most effective materials for acidic HER are sulfides, carbides and phosphides [28–35].
Mechanism of HER in an acidic medium is:

$$H^+ + e^- \rightarrow H^* \qquad (Volmer\ Step) \tag{1.4}$$

$$H^* + H^* \rightarrow H_2 \qquad (Tafel\ Step) \tag{1.5}$$

$$H^* + H^+ + e^- \rightarrow H_2 \qquad (Heyrovsky\ Step) \tag{1.6}$$

However, for industrial scaling of HER, the oxidation half of the reaction, OER, should also be efficient in the same medium [28, 36–39] . Since many inexpensive OER catalysts fail in acidic medium, it is preferable to choose an alkaline medium to split water and

generate hydrogen [40]. Additionally, alkaline medium is known to reduce corrosion of non-noble metal catalysts keeping them functional for longer cycles. HER follows the same mechanisms in both acidic and alkaline media but there is an additional step involved in the latter. The catalyst also has to break the stronger covalent H–O–H bonds to produce H^+ for the reaction, instead of the dative covalent bond in H_3O^+ ion, which is weaker. Computer simulations of the H_2O adsorption and splitting give insights into the activity of a catalyst in alkaline medium based on the activation of the H–O–H bond [41–45] .
HER mechanism in alkaline medium:

$$H_2O + e^- \rightarrow H^* + HO^- \qquad (Volmer\ Step) \tag{1.7}$$

$$H^* + H^* \rightarrow H_2 \qquad (Tafel\ Step) \tag{1.8}$$

$$H^* + H_2O + e^- \rightarrow H_2 + HO^- \qquad (Heyrovsky\ Step) \tag{1.9}$$

1.3.2 CO_2 reduction reaction

There is an urgent need to control the increased CO_2 emissions as high levels of this greenhouse gas is a primary cause of global warming at an alarming rate. As mentioned earlier, CO_2 concentration increased by 50 % in *150* years from the pre-industrial levels [11, 21]. This rise is primarily anthropogenic and can be attributed largely to the increased use of fossil fuels. To combat CO_2 emissions, drastic scaling down of industrial activity is impractical. Rather, a more effective strategy for sustainability is to capture the emitted CO_2 and convert it into potentially useful, value-added chemicals. In this regard, the CO_2 reduction reaction (CO_2RR) is especially relevant, converting CO_2 to value-added compounds like formaldehyde, methane, methanol (MeOH) and dimethyl ether, and various two-carbon hydrocarbons.
CO_2 is a significantly stable molecule and hence the activation of the C=O bond is chemically challenging. Here, activation of a bond refers to cleavage or elongation of the bond.

Also, CO_2 is a Lewis acid, implying that a catalyst should have the ability to donate electrons to (the anti-bonding orbitals of) CO_2 for successful thermocatalytic conversion of CO_2. The overall reaction

$$CO_2 + 3H_2 \rightarrow CH_3OH + H_2O \tag{1.10}$$

is exothermic with an enthalpy of -49.3 kJ mol $^{-1}$ at 298.15 K [46]. However, selectivity of the catalyst employed is of paramount importance. Tuning the selectivity of the CO_2RR catalysts is an important aspect of its electrocatalysis, since the thermodynamic minimum potentials for most of the carbon-containing products are close to 0 V versus RHE, making the kinetically favourable H_2 production pathway (HER), a competing reaction.

CO_2RR is a multi electron transfer process and possibility of multiple products further complicates the design and screening of catalysts of interest. One of the products of CO_2RR MeOH, used as a precursor in industrial synthesis of several commodity chemicals, such as formaldehyde, acetic acid, methyl tertbutyl ether, among others. Methanol can also be readily used as an alternative fuel in internal combustion engines, in addition to its possible use as a cooking fuel [47, 48]. Use of MeOH in internal combustion engines, in lieu of fossil fuel derived petroleum, offers several advantages. It is significantly cheaper, and can also be derived from organic waste. Currently, MeOH is produced industrially by passing syngas (a mixture of H_2 and CO) over $Cu/ZnO/Al_2O_3$, at 50-100 bar and 473-573 K [13, 14]. Mechanism of a catalytic reaction naturally depends on the catalyst being used, and three established mechanisms of CO_2RR to MeOH on Cu as the catalyst are discussed below (since it is currently the most widely used catalyst) [49, 50]. These mechanisms are the standards with which reaction mechanisms on new catalytic materials can be compared, to assess their catalytic performance. The three mechanisms are formate (orange and purple pathways in Fig. 1.7), RWGS (CO hydrogenation) (red pathway in Fig. 1.7), and carboxylic acid (green and blue pathways in Fig. 1.7) mecha-

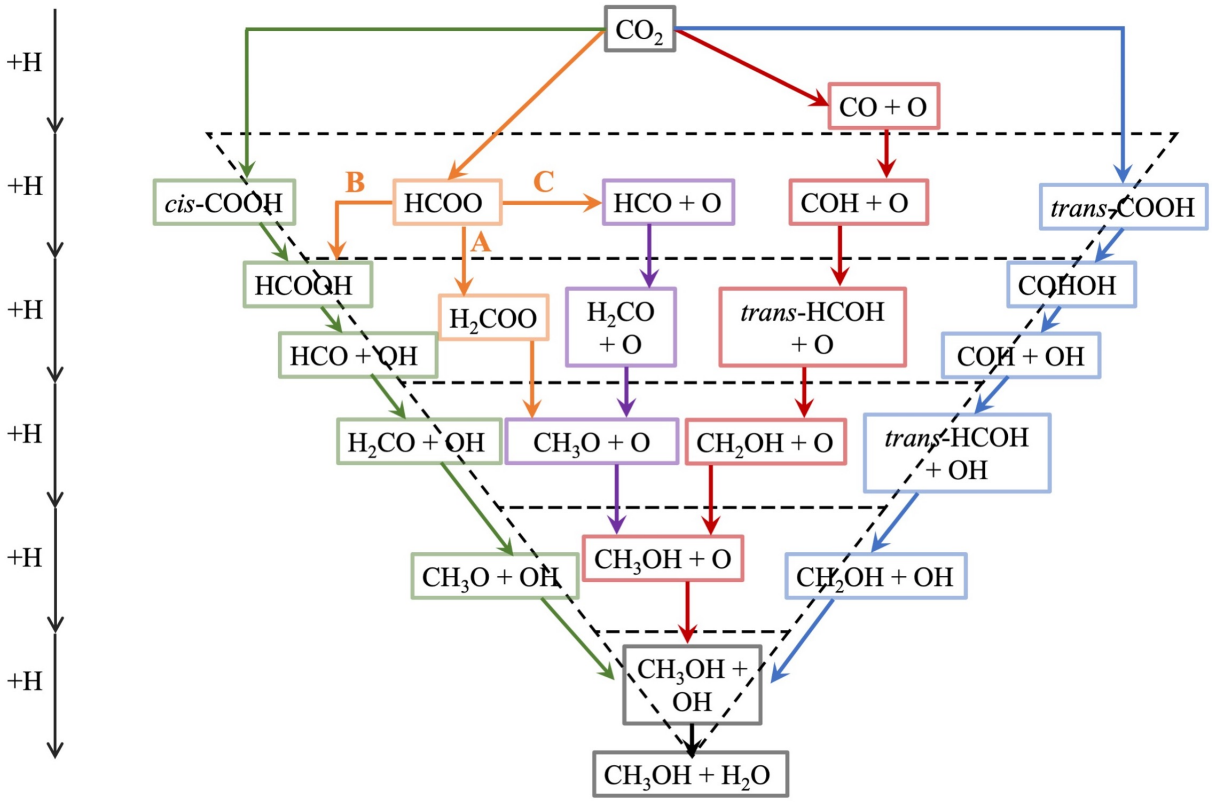

Figure 1.7: Reaction pathways of CO_2 hydrogenation to MeOH on Cu as the catalyst. Pathways coloured green, orange, purple, red, and blue indicate the *cis*-COOH, formate (1 and 2), formate-3, RWGS and *trans*-COOH pathways. The various pathways are differentiated based on the intermediate formed after the addition of the first H^+ atom. Reprinted with permission from [2]. Copyright (2021) by Springer Nature (Switzerland AG).

nism, differentiated by the first intermediates, formate ($HCOO^*$), carbon monoxide (CO), and *trans*–COOH, respectively. These intermediates effectively control the overall rate of the reaction, as their formation is the rate-determining step in the respective mechanism.

1.3.3 Electrooxidation of ethanol

Ethanol (EtOH), a C_2 fuel can be produced from biomass waste, urban residues and can also be a product of CO_2RR. EtOH is a better fuel than MeOH because of its low toxicity, possesses a high energy density [51](6.3 kWh/L compared to 4.8 kWh/L for MeOH) and provides 12 electrons upon complete oxidation. However, the low rate of ethanol oxidation

reaction (EOR) is a major hindrance in large-scale application of direct ethanol fuel cell (DEFCs) [51, 52] to generate electricity. C-C bond cleavage is the rate-limiting step of the reaction; also most Pd based catalysts have poor poison tolerance.

In acidic media [53–58], EtOH can either be partially oxidised to acetic acid (CH_3COOH) *via* an acetaldehyde (CH_3CHO) intermediate, giving out 4 electrons along the C_2 pathway; or follow the C_1 route in which EtOH oxidises completely to CO_2 *via* CO intermediate, providing 12 electrons in the process. In alkaline medium, EOR occurs *via*

- reactive intermediate pathway: HO^* and CH_3CO^* intermediates combine to produce an acetate molecule (partial oxidation).
- poisoning intermediate pathway: CH_3CO^* intermediate dissociates to give $^*CO$ and $^*CH_3$ which poison the active sites of the catalyst [59] thus reducing its reusability.

1.3.4 Direct synthesis of H_2O_2

Hydrogen peroxide (H_2O_2), an industrially valuable green oxidising agent [60–62], has the highest content of active nascent oxygen and gives out H_2O as a by-product. Due to its benign nature, H_2O_2 finds applications in a variety of processes such as pulp and textile bleaching [63], wastewater treatment, and in low concentrations as an antiseptic [64]. Commercially, most of the H_2O_2 is generated *via* anthraquinone auto-oxidation (AO) process [65]. The cyclic AO method is an organic route involving: a) hydrogenation of anthraquinone over a Pd-Ni catalyst; b) oxidation of the hydrogenated anthraquinone; c)extraction and purification of H_2O_2.

Though widely used, the energy-intensive AO process has various drawbacks [66,67] which include, side reactions leading to poisoning of the catalyst, degradation of anthraquinone molecules, and difficulties in separation and transportation of H_2O_2 due to organic impurities. It also generates chemically polluted liquid and solid waste along with emission of

harmful chemicals like mesitylene isomers.

Direct synthesis of H_2O_2 (DSHP) provides a straightforward pathway to generate H_2O_2 by a $2e^-$ reduction of O_2 molecule [68, 69]. Although hydrogenation of O_2 to H_2O_2 is an exothermic reaction (-120.5 kJ mol^{-1}), selectivity of the catalyst is crucial because of other competing reactions, like the Oxygen Reduction Reaction (ORR) being more spontaneous (-237.2 kJ mol^{-1}) [20]. Moreover, the unstable nature of the peroxide bond causes H_2O_2 to decompose (-116.7 kJ mol^{-1}) into H_2O and O_2, or undergo reduction (-354.0 kJ mol^{-1}) to yield H_2O [20]. Pd based catalysts, [61,70,71] in particular Pd-Au and Pd-Sn based catalysts, have been extensively explored for DSHP [61,70,72–76]. However, the cost and scarcity of Pd limits the large scale use of these catalysts.
DSHP occurs in the following steps:

$$* + O_2 + H_2 \rightarrow {}^*O_2 + H_2 \tag{1.11}$$

$${}^*O_2 + H_2 \rightarrow {}^*O_2 + {}^* H + \frac{1}{2}H_2 \tag{1.12}$$

$${}^*O_2 + {}^* H + \frac{1}{2}H_2 \rightarrow {}^*OOH + \frac{1}{2}H_2 \tag{1.13}$$

$${}^*OOH + \frac{1}{2}H_2 \rightarrow {}^*OOH + {}^* H \tag{1.14}$$

$${}^*OOH + {}^* H \rightarrow {}^*H_2O_2 \tag{1.15}$$

$${}^*H_2O_2 \rightarrow * + H_2O_2 \tag{1.16}$$

1.3.5 Electrochemical nitrogen reduction reaction

An essential chemical in most fertilizers vital for sustained global food supply, ammonia (NH_3) is a vital ingredient in our agricultural dependent society [77–79]. Its role as a C-free energy carrier is also being extensively explored [80]. Currently, industrial synthesis of NH_3 relies on the century old *Haber-Bosch* process [81], a thermochemical catalytic reaction in which 1 mole of N_2 reacts with 3 moles of H_2 over an Fe-based catalyst [82].

The reaction is carried out at 600-700 K under high pressure (100-200 atm), making it one of the most energy-intensive processes [83]. The *Haber-Bosch* process uses 1-2 % of the world's total energy production and contributes to 1.5 % of global CO_2 emissions, more than any other chemical-synthesis process [83].

Electrochemical N_2 reduction reaction (eNRR), an alternate route to generate NH_3, has captured attention of many scientists owing to its C-free footprint and ambient reaction conditions [84, 85]. eNRR is a heterogeneous electrocatalytic reaction involving six proton-coupled electron transfer (PCET) steps to hydrogenate N_2 to NH_3. Although hydrogenation of N_2 to NH_3 is exothermic (-46.1 kJ mol^{-1}) [86], the inherent inertness of the rigid N≡N triple bond ($E_{dissociation}$ = 945 kJ mol^{-1}) [87]is the kinetic bottleneck for most catalyst employed for eNRR. Furthermore, highly selective catalysts are critical for eNRR to suppress kinetically brisk competing reactions like HER [88, 89].

Mechanistically, eNRR can occur *via* three different pathways [89] depending on the orientation of intermediates adsorbed on the surface of a catalyst: End-on adsorbed N_2 can proceed *via* distal or alternating pathway, while a side-on adsorbed N_2 follows the enzymatic route. Along distal pathway, the dangling N-atom gets fully hydrogenated to NH_3 (Fig. 1.8), following which the $^*N$ undergoes 3 PCET steps releasing a second NH_3 molecule. In the alternating route, both N-atoms are targeted alternatingly by incoming protons and the first NH_3 is released after the 5^{th} PCET step. Similar alternate hydrogenation of $^*N_2$ occurs along the enzymatic mechanism, the only difference being side-on orientation of various N_xH_y intermediates (Fig. 1.8).

1.4 Overview of the thesis

This thesis focuses on first-principles theoretical analysis of several heterogeneous catalytic reactions having direct implications to global problems associated with climate change.

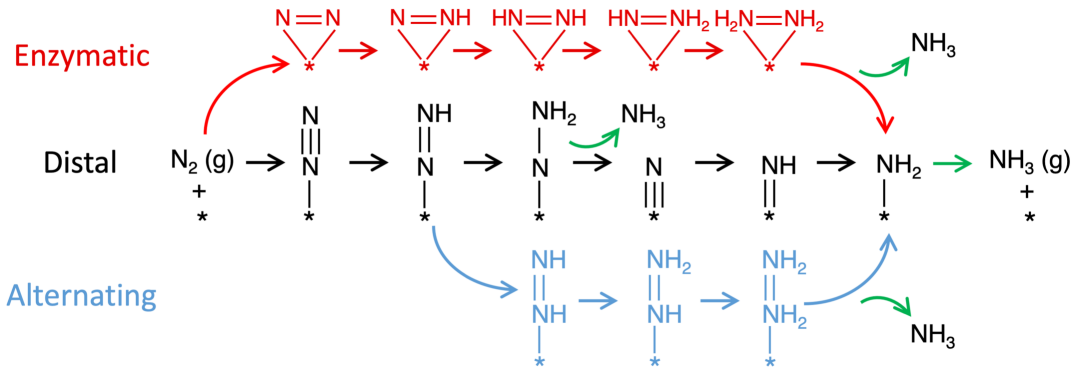

Figure 1.8: Intermediates along the enzymatic, distal, and alternating pathways for electrochemical reduction of nitrogen (eNRR). * signifies the catalytic surface and * above an intermediate denotes its adsorbed state.

We showcase the effectiveness and versatility of DFT calculations in identifying and predicting various mechanisms at play, responsible for enhancing the activity of catalysts and connect our findings with experiments wherever possible. The catalytic materials studied here are inexpensive and constitute earth-abundant elements. We have looked at materials with high catalytically active surface area: 2D materials like MoS_2, graphene, borophene and various facets of 3D bulk materails like Ni_2P (111), Pd_2Ge (111), MC (100) and (111). The central theme of the work presented in this thesis is to develop, understand and optimize cost-effective catalysts for reactions significant to renewable energy conversion and storage. We start with introducing a few fundamental concepts governing catalysis, followed by description of various chemical reactions studied in our work. In Chapter 2, we give a brief description of the formalism and first-principles methods used in this thesis. The rest of the thesis is divided into three sections, based on the catalytic reactions studied.

Part I: Splitting the H_2O molecule

Electrolysis of water, known for over 240 years, is a sustainable and environment friendly method to generate H_2, the fuel of tomorrow. It is comprises of two half-cell reactions, the anodic HER and cathodic OER. A catalyst comprising of earth-abundant elements

to efficiently catalyze HER has captured the imagination of scientists for decades but designing an efficient candidate for widespread application still remains a challenge. Also, the oxidation half reaction, OER is generally responsible for the low reaction rates of water splitting due to high kinetic barriers associated with its $4e^-$ transfer process. In Chapters 3-5, we focus on elucidating the mechanisms behind enhancement of catalytic activity in metal phosphides, sulfides and carbides towards the cathodic part of water splitting (HER) and/or the anodic half-cell reaction (OER).

In Chapter 3, we exploit chemical ordering and substitutional doping as means to tailor the activity of two catalysts towards alkaline HER. In Chapter 3(a), we introduce amorphicity in a Co-Mo-P based catalyst and identify active sites for evolution of H_2. We pinpoint the role played by each element in catalyzing the reaction and highlight the significance of amorphicity for the activity of the catalyst. In Chapter 3(b) we use substitutional Ni/Co to stabilize the metastable 1T polymorph of molybdenum disulfide (MoS_2). Ni/Co substituents cause a local structural distortion of the 1T lattice transforming it to a lower energy 1T" polytype. We further obtain a close to optimal Gibbs free energy of H-adsorption (ΔG^H_{ads}) for Ni/Co substituted MoS_2, a widely accepted descriptor for HER, showing their viability to evolve H_2. In Chapter 4, we demonstrate increase in catalytic activity of a metal phosphide, Ni_2P, towards water splitting and metal carbides, WC and MoC, towards HER, with substitutional alloying. Surface oxygen further ameliorates the catalytic activity of Mn-substituted Ni_2P (Chapter 4a) while Ni-dopants alter the electronic structure of tungsten and molybdenum carbide (Chapter 4b), leading to superior HER activity. In Chapter 5, we use DFT calculations to design and predict a novel catalyst comprising of graphene and 1H-MoS_2 forming an out-of-plane heterostructure and illustrate how the site-specific activity towards HER is tuned with substitutional N. Chemically inequivalent N, substituted in graphene monolayer, alter the electronic and catalytic properties of the heterostructures and graphitic N-substituents exhibit high affinity to evolve H_2 with optimum ΔG^H_{ads} and work function (ϕ).

Part II: Conversion of CO_2 into fuels and their utilization

In Chapters 6 and 7, we explore two intermetallic catalysts to convert the greenhouse gas CO_2 into a value added fuel, CH_3OH and utilizing such fuels (CH_3CH_2OH) to generate power using a fuel cell. We present a thorough analysis of the catalytic activity of an intermetallic catalyst based on Ni-In, towards hydrogenation of CO_2 to CH_3OH. We investigate eight distinct pathways for CO_2 reduction and show the catalyst, Ni_3In, to be highly selective towards one particular product, CH_3OH. We also calculate activation barriers along the two thermodynamically most feasible pathways and identify the formate pathway to be kinetically favoured. In Chapter 7, we provide mechanistic insights into a manyfold increase in the activity of Pd_2Ge towards ethanol electrooxidation reaction (EOR) observed upon Ni-substitution. We show an optimization of adhesion strength for the main intermediates occurring along the EOR pathway to be the cause of enhancement of the activity.

Part III: Designing catalysts for industrial processes

The third part of thesis comprises of Chapters 8 and 9, in which we design and predict novel two catalysts based on 2D materials for synthesis of commercially value-added products, H_2O_2 and NH_3. We use 1H-MoS_2 as the base material and tune its catalytic activity by introducing two surface modifications, for direct synthesis of hydrogen peroxide (DSHP). We show the synergy between substitutional Au and S-vacancies work in tandem to facilitate the partial reduction of O_2, to H_2O_2 without significant energy input. The catalyst also exhibits high selectivity towards DSHP and suppresses the competing oxygen reduction reaction (ORR). Finally in Chapter 9, we report a highly efficient metal-free catalyst for electrochemical reduction of nitrogen, based on 2D boron sheets. C-decorated α borophene is show to execute the electrochemical nitrogen reduction reaction (eNRR) at a vanishingly low onset potential making it an attractive candidate for experimental

exploration. Along with high efficiency, our borophene based catalyst also showcases high selectivity towards eNRR over a competing reaction, HER. We trace the origin of the high catalytic performance of our catalysts to two novel descriptors which can facilitate high throughput screening of catalysts for eNRR.

Chapter 2

Methods and Formalism

Most properties of a material can be explained by the interaction between electrons, ions and the interaction among themselves. Quantum theory very accurately describes the behavior of these atomic and subatomic particles. The success of quantum theory has made it possible for scientists to explain and predict various properties of a material in solid state physics. Nearly all physical properties of a material can be determined from the derivatives of (difference between) the energy as a function of an external perturbation. In order to obtain the total energy of a system containing electrons and ions, one needs to solve the Schrödinger equation (SE). The Hamiltonian of a system which takes into account electron-electron, electron-nuclear and nuclear-nuclear interactions is defined as [90]:

$$\begin{aligned} \hat{H} &= -\frac{\hbar^2}{2m_e}\sum_i \nabla_i^2 + \frac{1}{2}\sum_{i\neq j}\frac{e^2}{|\mathbf{r}_i-\mathbf{r}_j|} - \sum_{i,I}\frac{Z_I e^2}{|\mathbf{r}_i-\mathbf{R}_I|} \\ &- \sum_I \frac{\hbar^2}{2M_I}\nabla_I^2 + \frac{1}{2}\sum_{I\neq J}\frac{Z_I Z_J e^2}{|\mathbf{R}_I-\mathbf{R}_J|}, \end{aligned} \tag{2.1}$$

where m_e and e are the mass and charge of an electron respectively, and $\hbar$ is the reduced Planck constant. $\mathbf{r}_i$ is the position vector of i^{th} electron. $\mathbf{R}_I$, M_I and Z_I are

the position vector, mass and atomic number of the I^{th} nucleus, respectively. The first and fourth terms in Eq. (2.1) are the kinetic energy of electrons and nuclei respectively. Second, third and fifth terms represent electron-electron, electron-nuclei and nuclei-nuclei Coulomb interactions, respectively.

Though the many-body Hamiltonian (Eq. 2.1) looks simple, its solution is almost impossible for a material that consists of the large number of electrons and nuclei. Therefore, we solve Eq. (2.1) within the Born-Oppenheimer approximation (adiabatic approximation) [91]. This approximation has been made considering the fact that $M_I \sim 1836 * m_e$, the kinetic energy of nuclei is much lower than that of electrons, and can be ignored. Thus, electrons and nuclei can be treated as quantum and classical particles, respectively. Consequently, the total energy of a given set of atoms in a material is the sum of the nuclei-nuclei Coulomb interaction and electronic ground state energy. To estimate the electronic ground state energy, the form of many-body electronic Hamiltonian can be written as:

$$\hat{H}_e = \hat{T}_e + \hat{V}_{int} + \hat{V}_{ext}, \tag{2.2}$$

where $\hat{T}_e$, $\hat{V}_{int}$ and $\hat{V}_{ext}$ denote kinetic energy, electron-electron interactions and potential acting on the electrons due to nuclei, respectively. Given this total Hamiltonian of any system, one can write the time-independent SE as,

$$\hat{H}\psi(\mathbf{R},\mathbf{r}) = \epsilon\psi(\mathbf{R},\mathbf{r}), \tag{2.3}$$

where ϵ and $\psi(\mathbf{R},\mathbf{r})$ are the ground state energy eigenvalue and wavefunction of the electrons, respectively. $\mathbf{R}$ and $\mathbf{r}$ are the position vectors of nuclei and electrons in the materials respectively. Since, the electrons are fermions, $\psi(\mathbf{R},\mathbf{r})$ must be antisymmetric

under exchange of two electronic coordinates $\mathbf{r}_i$. Though Born-Oppenheimer approximation reduces the difficulty to determine the ground state for a given set of atoms and their positions, quantum mechanical solution of Eq. (2.3) for the large number of atoms is still a challenge. Therefore, determination of the ground state is quite hard and requires additional approximations.

Various other approximations have also been developed to solve it. Independent electron approximation is the oldest approximation which considers that interaction between the electrons can be ignored. Hartree approximation modified it further by treating the electrons as independent, but interacting only via the mean-field Coulomb potential. Hartree did not consider the asymmetric nature of electronic wave functions. Antisymmetric nature of electrons was considered in the Hartree-Fock Approximation.

2.1 Density Functional Theory

According to quantum mechanics wave function of a given system ψ, contains all the possible information about that system. The solution to this wave function is calculated by using the SE which for a single electron moving in a potential $\upsilon(\mathbf{r})$ is given by:

$$\left[-\frac{\hbar^2\nabla^2}{2m_e}+\upsilon(\mathbf{r})\right]\psi(\mathbf{r})=\epsilon\psi(\mathbf{r}) \tag{2.4}$$

For many electrons system, the SE becomes:

$$\left[\sum_i^N(-\frac{\hbar^2\nabla_i^2}{2m_e}+\upsilon(\mathbf{r}_i))+\sum_i U(\mathbf{r}_i,\,\mathbf{r}_j)\right]\psi(\mathbf{r}_1,\,\mathbf{r}_2\,\cdots,r_N)=\epsilon\psi(\mathbf{r}_1,\,\mathbf{r}_2\,\cdots,r_N) \tag{2.5}$$

where N is the number of electrons and is the electron-electron interaction. In quantum mechanics, the usual approach to SE is:

$$\upsilon(\mathbf{r}) \overset{\text{SE}}{\Longrightarrow} \psi(r_1, r_2 \cdots, r_N) \overset{\langle\psi|\cdots|\psi\rangle}{\Longrightarrow} observables \tag{2.6}$$

the system is specified by choosing $\upsilon(\mathbf{r})$ for which the SE is solved for wave function $\psi(r_1, r_2 \cdots, r_N)$. Expectation values of operators with this wave function is calculated to obtain various observables. One such observable is the particle density given by:

$$n(\mathbf{r}) = N \int d\mathbf{r}_2^3 \int d\mathbf{r}_3^3 \cdots \int d\mathbf{r}_N^3 \psi^*(\mathbf{r}_1, \mathbf{r}_2 \cdots, r_N)\psi(\mathbf{r}_1, \mathbf{r}_2 \cdots, r_N) \tag{2.7}$$

Density functional theory (DFT) uses this particle density as the key variable to calculate all other observables. It has excluded the problem of 3N-variables (N is the number of electrons and their associated 3 spatial variables) associated with many electron-wave function with a functional of electron density which reduces the number of variables to 3, and hence has reduces the complexity of many electron problem to a great extent. In other words, it allows one to map exactly the problem of strongly interacting electron gas onto that of a single particle moving in an effective potential arising from the rest. This approach can be summarized as follows:

$$n(\mathbf{r}) \Rightarrow \psi(r_1, r_2 \cdots, r_N) \Rightarrow \upsilon(\mathbf{r}) \tag{2.8}$$

2.1.1 Hohenberg-Kohn Theorems

DFT was developed by Hohenberg and Kohn in 1964 [92], Kohn and Sham in 1965 [93] replacing an interacting many-body problem into a set of single-particle problems treating charge density of electron gas as fundamental, including many-body effects in the exchange-correlation energy functional of density. The two theorems that constituted their ground breaking work can be stated as follows:

Theorem I: The external potential $V_{ext}(\mathbf{r})$ of any system of interacting particles can

be determined uniquely by the ground state particle density $n_0(\mathbf{r})$ within an additive constant.

Theorem II: For any given external potential $V_{ext}(\mathbf{r})$, the universal functional for energy $E[n]$ of the system can be defined in terms of particle density $n(\mathbf{r})$. The exact ground state energy of the system is the global minimum value of this functional, and the density n($\mathbf{r}$) that minimizes this functional is the exact ground state particle density $n_0(\mathbf{r})$.

Based on these two theorems, the $3N_e$ (N_e is number of electrons) variables in the problem are reduced to a problem involving function of only three variables of $n(\mathbf{r})$, and the total energy functional can be written:

$$E_{HK}[n] = F_{HK}[n] + \int d^3r V_{ext}(\mathbf{r})n(\mathbf{r}) + E_{II}, \tag{2.9}$$

$$F_{HK}[n] = T[n] + E_{int}[n], \tag{2.10}$$

where E_{II} is the nuclei-nuclei Coulomb interactions. Functional $F_{HK}[n]$ includes kinetic $T[n]$ and potential $E_{int}[n]$ energies of interacting particles system. Though these two theorems prove existence of an universal functional $F_{HK}[n]$ (only a functional of density $n(\mathbf{r})$), they do not provide a practical scheme for determining the ground state density $n_0(\mathbf{r})$, In 1965, Kohn and Sham proposed an anstaz for the ground state density $n_0(\mathbf{r})$ to simplify this.

2.1.2 Kohn-Sham ansatz

Kohn-Sham ansatz [93] is a mathematical assumption that replaces the ground state density of an original interacting many-body system by a system of auxiliary non-interacting particles. Thus, calculations of an original system can be performed on an auxiliary

non-interacting particles system with the total energy functional given by,

$$E_{KS} = T_s[n] + \int d\mathbf{r} V_{ext}(\mathbf{r}) n(\mathbf{r}) + E_{XC}[n] + E_H[n] + E_{II}. \tag{2.11}$$

Terms in Eq. (2.11) are described below:

$n(\mathbf{r})$ is charge density of auxiliary system determined by the sum of square of N_e non-interacting electrons′ wavefuctions ($\psi_i(\mathbf{r})$):

$$n(\mathbf{r}) = \sum_{i=1}^{N_e} |\psi_i(\mathbf{r})|^2, \ and \ N_e = \int d\mathbf{r} \ n(\mathbf{r}). \tag{2.12}$$

$T_s[n]$ is the kinetic energy of N_e non-interacting electrons, and given by,

$$T_s[n] = -\frac{\hbar^2}{2m_e} \sum_{i=1}^{N_e} \langle \psi_i(\mathbf{r}) | \nabla^2 | \psi_i(\mathbf{r}) \rangle. \tag{2.13}$$

$E_H[n]$ is the Hartree energy, classical interaction energy of the electron density interacting with itself, and define as,

$$E_H[n] = \frac{e^2}{2} \int \frac{n(\mathbf{r}) n(\mathbf{r}')}{|\mathbf{r} - \mathbf{r}'|} d\mathbf{r} d\mathbf{r}'. \tag{2.14}$$

$E_{XC}[n]$ is the exchange-correlation energy of electrons that takes into account of (i) difference in kinetic energy of the many-body interacting system and set of non-interacting system, and (ii) residual energy contributions due to the exchange asymmetry and correlations. E_{XC} is given by,

$$E_{XC}[n] = (T[n] - T_s[n]) + (E_{int}[n] - E_H[n]), \tag{2.15}$$

where $[n]$ denotes a functional of the electron density $n(\mathbf{r})$. The exact form of $E_{XC}[n]$ is unknown, and will be discussed shortly. In this approch, the Hamiltonian of an auxiliary non-interacting particles is called Kohn-Sham Hamiltonian (H_{KS}), and written as,

$$H_{KS} = -\frac{\hbar^2}{2m_e}\nabla^2 + V_{KS}(\mathbf{r}), \tag{2.16}$$

where $V_{KS}(\mathbf{r})$ is Kohn-Sham potential expressed as,

$$V_{KS}(\mathbf{r}) = V_{ext}(\mathbf{r}) + V_H(\mathbf{r}) + V_{XC}(\mathbf{r}), \tag{2.17}$$

where $V_{ext}(\mathbf{r})$, $V_H(\mathbf{r})$ and $V_{XC}(\mathbf{r}) = \frac{\partial E_{XC}[n]}{\partial n(\mathbf{r})}$ are external, Hartree and exchange-correlation potentials, respectively. Now, one can write single-particle Kohn-Sham equations as,

$$H_{KS}\psi_i(\mathbf{r}) = \epsilon_i\psi_i(\mathbf{r}), \tag{2.18}$$

the solution of Eq. (2.18) is a self-consistent iterative method, and illustrated in Fig. 2.1.

2.1.3 Exchange-Correlation Energy Functional

Electrons are Fermions, hence the wavefunction of many electron system should be asymmetric under exchange of any two electrons. This produces a spatial separation between the electrons that have the same spin causing a reduction in the Coulomb energy of the electronic system. This reduction in energy due to antisymmetric nature of wavefunction is known as the exchange energy, and this is referred to as the Hartree-Fock approximation. Coulomb energy of the system is also reduced at the cost of an increase in kinetic

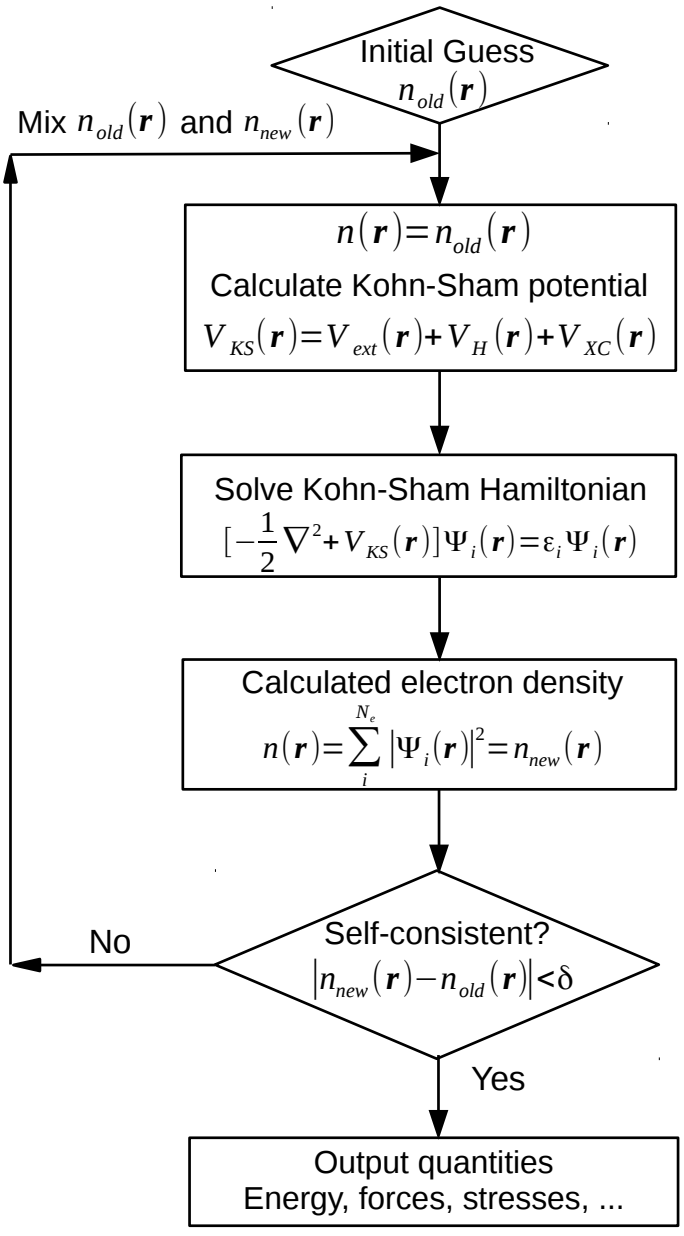

Figure 2.1: Flow chart for the iterative solution of Kohn-Sham equations.

energy when the electrons of the same spin are spatially separated. The difference between the many body energy of an electronic system and that calculated in the Hartree-Fock approximation is called the correlation energy. Formulation of a correct exchange-correlation functional is one of the bottlenecks in DFT due to electron-electron interactions involved. Kohn Sham replaces many electron problem by single electron equation. The exchange-correlation energy functional Kohn Sham approach can be defined as:

$$E_{XC}[n(\mathbf{r})] = T[n(\mathbf{r})] - T_{\circ}[n(\mathbf{r})] + E_{ee}[n(\mathbf{r})] - E_H[n(\mathbf{r})] \tag{2.19}$$

where, $\mathrm{T}_{\circ}[n(\mathbf{r})]$ and $\mathrm{E}_{ee}[n(\mathbf{r})]$ are exact kinetic and electron-electron interaction energies respectively. Since, exact value of E_{xc} is not known; so various approximations based on electron density have been introduced to describe it.

Local density approximation (LDA): In LDA, the exchange-correlation energy of an electronic system is constructed by assuming that the exchange-correlation energy per electron ($\epsilon_{XC}(\mathbf{r})$) at a point $\mathbf{r}$ in the electron gas is equal to the exchange-correlation energy per electron of a homogeneous electron gas that has the same density as the electron density at a point $\mathbf{r}$. Thus,

$$E_{XC}^{LDA}[n(\mathbf{r})] = \int \epsilon_{XC}(n(\mathbf{r}))n(\mathbf{r})d^3\mathbf{r} \tag{2.20}$$

and

$$\frac{\delta E_{XC}[n(\mathbf{r})]}{\delta n(\mathbf{r})} = \frac{\partial[n(\mathbf{r})\epsilon_{XC}]}{\partial n(\mathbf{r})} \tag{2.21}$$

where

$$\epsilon_{XC}^{LDA}(\mathbf{r}) = \epsilon_{XC}^{hom}[n(\mathbf{r})] \tag{2.22}$$

The LDA approximation proves to be very successful for many systems especially for those whose electron density is quite uniform such as bulk metals, ionic crystals etc. But

it fails to produce some properties (e.g. band gap) in semiconductors, strongly correlated systems due to fact that the excitation spectrum of homogeneous electron gas is gapless and exchange-correlation energy is regular [94]. LDA also fails to capture weak intermolecular bonds, hydrogen bonds etc. The Perdew-Zunger (PZ) [95], Perdew-Wang (PW) [96], and Vosko-Wilk-Nusair (VWN) [97] functionals are the LDA functionals used commonly in calculations, which interpolate between exact results available at high and low densities n.

Generalized gradient approximation (GAA): GGA is an improved version of the LDA in which several aspects which were not present in LDA like inhomogeneity of electrons, non-local exchange correlation effect, complete cancellation of self-energies of electrons are taken into account. The exchange correlation energy in GGA [90] can be written as:

$$E_{XC}^{GGA}[n(\mathbf{r})] = \int d^3\mathbf{r} n(\mathbf{r}) \epsilon_{XC}[n(\mathbf{r}), |\nabla n|, |\nabla^2 n|, \cdots] \tag{2.23}$$

GGA method turns out to be better than LDA in the sense that it improves binding energies, bond lengths and also improves the band gap of semiconductors over LDA. Perdew and Wang (PW91) [98] and Perdew, Burke and Ernzerhof (PBE) [99] are some of the functional within GGA.

2.1.4 Pseudopotential approximation

The core electrons in solids or molecules are tightly bound to the nucleus and are thus not involved in bonding. So, as an approximation core electrons are removed from the calculation, and the interaction of the valence electrons with the nucleus plus the core states is replaced by an effective screened potential. The solution of the atomic SE for the pseudopotential is a pseudo-wave function different from the true wave function. The pseudopotential is constructed in such a way that its scattering properties are similar to those of the all-electron potential. It requires less number of basis functions and hence is

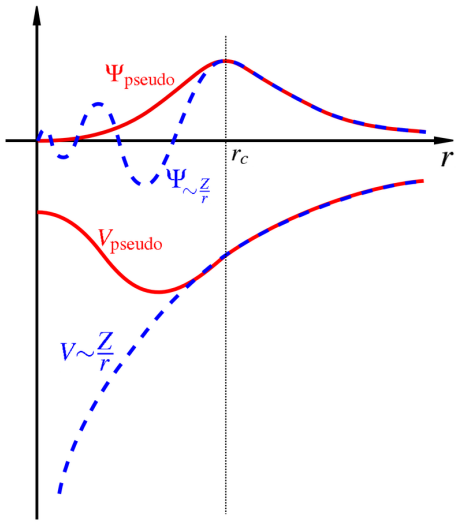

Figure 2.2: Schematic representation of an all electron potential (dotted line) and pseudopotential (solid line) along with corresponding wavefunction. Images by Sassospicco is licensed under CC BY-SA 1.0.

computationally efficient, without compromising much on the properties of system.

The behavior of pseudopotential in different regions of radius r (see Fig. 2.2) is defined by a cut-off radius (r_c). For $r \geq r_c$, all-electron and pseudo wavefunctions of valence electrons are identical. For $r < r_c$, energy eigenvalues and scattering properties are conserved by the pseudo-wavefunctions. If the charge density of each pseudo wavefunction is equal to the charge density of the actual wavefunction inside the region r $< r_c$, the pseudopotential is known as a norm-conserving pseudopotential [100]. This is generalized in ultrasoft pseudopotentials [101], where the total charge in $r < r_c$ region is conserved along with augmented charge density.

2.2 Nudged Elastic Band Method

One crucial aspect while studying chemical moieties is to find out lowest energy path in which a group of atoms rearrange themselves, moving from one configuration to another configuration. Such path is called as minimum energy path (MEP) and the potential energy maximum along MEP corresponds to saddle-point energy. Finding out saddle-

points and reaction paths are the key questions in Transition state theory [102] and many methods have been employed to achieve this. Some of these methods adopts local minimum on the potential energy surface as initial state and search of a path of slowest ascent [103, 104]. However, such ascent paths do not necessarily lead to saddle points. Another common strategy [105, 106] is to compute normal modes within the harmonic approximation of potential energy surface and follow each of these modes until saddle point is reached. Within this scheme, each step involves with evaluation and diagonalization of second derivative matrix and is thus computationally expensive. As an alternative, other methods such as the drag method or reaction coordinate method are proposed that need only computation of first derivative. Within these methods, linear interpolation between the initial and final configuration is done by assigning a subset of coordinates as the progress variable parameter. This degree of freedom is varied in equal interval going from initial to final state and minimization is done over remaining degrees of freedom. For example, at each step, minimization is performed over (3N-1) degrees of freedom if we are interested in a system consisting of N number of atoms in 3 dimension. These approaches are successful in many simple cases however, fail for complicated systems'.

Along the Nudged Elastic Band method (NEB) [107], optimization of an elastic band is performed by projecting the parallel component of the true force and the perpendicular component of the spring force. Using this force projection, dynamics of the path is decoupled from the particular distribution of images, given in discrete representation of the path. This decoupling scheme and discrete representation are two key ingredients and make sure the convergence to MEP. NEB has been used for a wide-range of applications, like to understand diffusion process at metal surface [108], dissociation of a molecule on a surface [109], contact formation between surface and metal tip [110].

Part I

Water Splitting

Chapter 3

Tuning the Catalytic Activity by Engineering Atomic Structure of Catalysts for Alkaline HER

3.1 Introduction

Hydrogen (H_2) is presently the best potential replacement available for the conventional energy sources due to its minimal ecological footprint. Currently, the main source of energy, fossil fuels have led to global climate change and are progressing towards their inevitable exhaustion. In this regards, mass production of H_2 molecule in a cost-effective manner is highly desirable. The most explored method of H_2 production is by electrochemical and photoelectrochemical splitting of water. Metals belonging to the platinum group are know to be the most efficient at executing the hydrogen evolution reaction (HER) [111], which is one of the half-cell reactions involved in water splitting. At present, the best available electrocatalyst, platinum, is often used as the standard to compare the performance of other catalysts. However, the expense associated with platinum group

metals and their low abundance minimize their widespread application as electrocatalysts for HER. Hence there is a global need to discover new cost-effective materials and optimize their ability to drive HER.

Water splitting consists of two half-cell reactions [23], HER which corresponds to reduction of two protons to evolve H_2, and oxygen evolution reaction (OER) in which a water molecule gets oxidized to give out oxygen (O_2). In order to achieve HER at an industrial scale, one medium should be able to carry out both HER and OER. Since many non-expensive OER catalysts operate in an alkaline medium, it is preferred to find catalysts which execute HER in the same medium efficiently [112, 113].

Doping different metals into materials which are catalytically active is a widely used strategy to tune the binding and transformation kinetics of key reaction intermediates. examples of such doping induced catalytic activity modulation include the doping of $NiO_x/Ni(OH)_2$ with Fe [114], NiFe layered double hydroxide with Co [115] and $CoFeO_x$ with W [116] for OER, and the doping of CoP/NiP systems with Fe and Mn for HER. [117] Substituting molybdenum (Mo), a metal with excellent hydrogen binding [118, 119] with cobalt (Co), an active water dissociation center [120], in amorphous CoP should lead to improved alkaline HER performance. Motivated by this hypothesis, Prof. Daniel Strongin's * group doped highly HER active CoP alloy with molybdenum using $MoCl_5$ as the Mo precursor.

3.2 Co-Mo-P based Amorphous Electrocatalyst†

Here we discuss a nonprecious metal-based catalyst for alkaline constituting cobalt (Co), molybdenum (Mo) and phosphorus (P) within the framework of density functional theory.

*Department of Chemistry, Temple University

†This work has been published as A. C. Thenuwara, L. Dheer, N. H. Attanayake, Q. Yan, U. V. Waghmare, and D. Strongin, Co-Mo-P Based Electrocatalyst for Superior Reactivity in the Alkaline Hydrogen Evolution Reaction, *ChemCatChem* **10**, 4832-4837 (2018) [40]. Reproduced with permission from the John Wiley and Sons.

We show that synergy between Mo and P effectively tunes the energetics of the HER reaction intermediates giving rise to the excellent catalytic activity of Co-Mo-P alloy in alkaline medium.

3.2.1 Computational details

Our first-principles calculations are based on density functional theory (DFT) as implemented in the Quantum ESPRESSO [121] code, employing plane-wave basis and ultrasoft pseudopotential [101] to represent the interaction between ionic cores and valence electrons. We adopt the exchange-correlation energy functional of Perdew-Burke-Ernzerhof (PBE) [99] obtained within a generalised gradient approximation (GGA). We smear the occupation numbers of electronic states with Fermi–Dirac distribution and a smearing width (k_BT) of of 0.04 eV. An energy cutoff of 40 Ry is used to truncate the plane-wave basis used in representation of Kohn-Sham wave functions, and 320 Ry to represent the charge density. Structures are determined through minimization of energy until the Hellmann-Feynman forces on each atom are smaller than 0.03 eV/Åin magnitude. In the supercell to model a monolayer, a parallel vacuum layer of 14 Åis introduced separating adjacent periodic images. Two supercells for Co-Mo-P alloy with different compositions are constructed (i) $Co_{28}Mo_4P_4$ and (ii) $Co_{12}Mo_2P_2$ (Fig 3.2). We sampled Brillouin-zone integrations on uniform grids of 5×5×1 k-points for $Co_{28}Mo_4P_4$ and 3×3×3 k-points for $Co_{12}Mo_2P_2$. Calculated lattice constants of Co (a_{Co} = 2.47 Å, c_{Co} = 3.93 Å) are in good agreement with the experimental values [122] (a°_{Co}= 2.5 Å, c°_{Co} = 4.07 Å).

3.2.2 Generating the Co-Mo-P alloy

Cobalt exists in a hexagonal closed packed (hcp) structure having $P6_3/mmc$ space group at room temperature. The bulk unit cell consists of two basis atoms. To generate the Co-Mo-P alloy we take a cobalt supercell (3×3×1) and dope molybdenum and phospho-

rus in molar ratio Co:Mo:P ∼ 78:11:11. We substitute molybdenum and phosphorus in 3×3×1 bulk cobalt matrix in varied configurations (Mo-P domain(s), isolated Mo and P atom(s)) and compute the energetically most stable structure (see Fig 3.1). We consider the following doping configurations:

1. $Co_{14}Mo_2P_2$ (Bulk 1): Two Mo-P domains.
2. $Co_{14}Mo_2P_2$ (Bulk 2): One Mo-P domain and one isolated Mo and P atom.
3. $Co_{14}Mo_2P_2$ (Bulk 3): One Mo-Mo domain and two isolated P atoms.
4. $Co_{14}Mo_2P_2$ (Bulk 4): Two isolated Mo and P atoms.

We use the following expression to calculate the formation energy (E_{form}) of the supercell:

$$E_{form} = E_{Co-Mo-P} - [n_{Co}E_{Co} + n_{Mo}E_{Mo} + n_P E_P] \tag{3.1}$$

where, $E_{Co-Mo-P}$, E_{Co}, E_{Mo} and E_P are the total energies of Co-Mo-P alloy, isolated Co, Mo and P atoms, respectively. Here, n_{Co}, n_{Mo} and n_P are the number of Co, Mo and P atoms, respectively, in the supercell. As is evident from Fig. 3.1 $Co_{14}Mo_2P_2$ (Bulk 3) is most stable out of the configurations considered here. Hence, Co matrix with one Mo-Mo domain and two isolated P atoms is taken as the default configuration in all further calculations.

3.2.3 Constructing amorphous structures

We simulate two model amorphous structures of Co-Mo-P with varied stoichiometries as follows:

1. $Co_{28}Mo_4P_4$: A 3×3×2 supercell with Co:Mo:P ∼ 78:11:11, and
2. $Co_{12}Mo_2P_2$: A 2×2×2 supercell with Co:Mo:P ∼ 75:12.5:12.5.

We employ the expanding lattice method [123] to generate amorphous structures. We

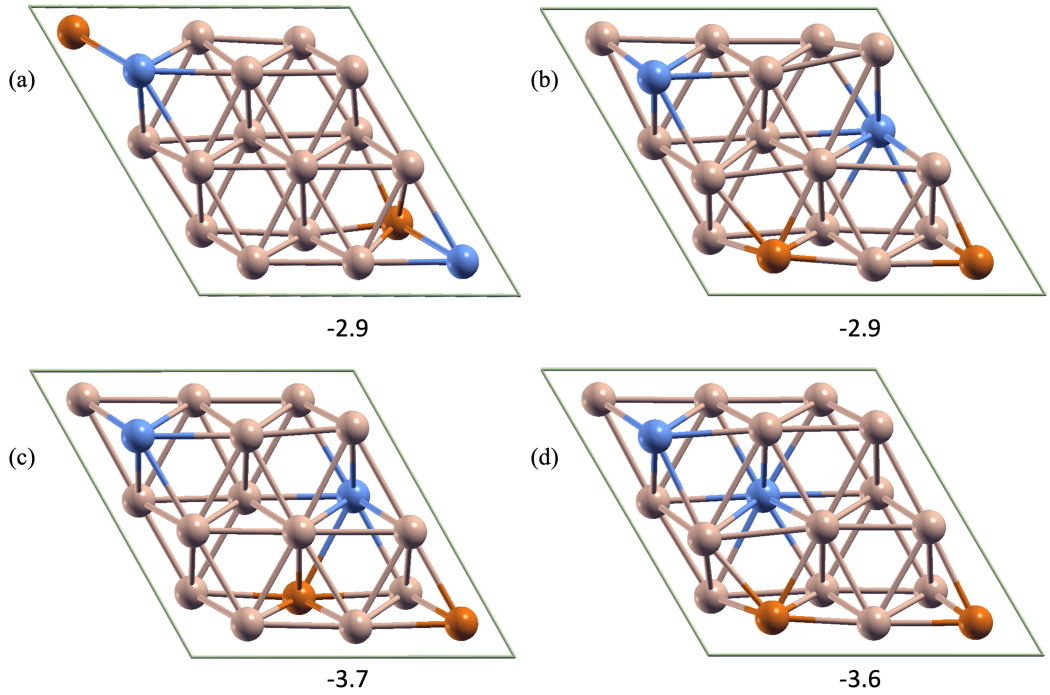

Figure 3.1: Generated $Co_{12}Mo_2P_2$ structures: (a) Bulk 1; (b) Bulk 2; (c) Bulk 3; (d) Bulk 4. Brown, orange and blue spheres represent Co, P and Mo atoms, respectively.

expand the volume of the constructed crystalline supercell by 50%, optimise the internal coordinates which results in formation of a nanoporous and a disordered system for different Co:Mo:P ratios. Each lattice parameter was increased by $\sqrt[3]{1.5}$ thus increasing the volume of supercells by 50%. On optimising these expanded supercells, we obtain a nanoporous ($Co_{28}Mo_4P_4$) and disordered ($Co_{12}Mo_2P_2$) system (Fig. 3.2).

3.2.4 Alkaline HER: reaction mechanism

H_2O molecule serves as the proton source in alkaline HER. Electron-coupled water dissociation (*Volmer* step) is the first step, followed by the reaction between adsorbed hydrogen atoms (*Tafel* step) or between adsorbed hydrogen and water (*Heyrovsky* step) to form H_2.

(3.2)

$$H_2O + M + e^- \rightarrow M.H_{ads} + OH^- \ (Volmer \text{ step}) 2M.H_{ads} \rightarrow H_2 + 2M \ (Tafel \text{ step}) \quad (3.3)$$

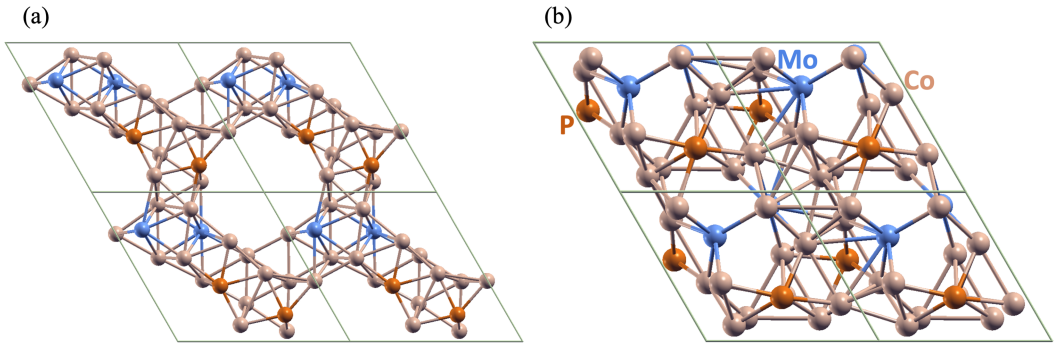

Figure 3.2: (2×2×1) Model amorphous structures of (a) $Co_{28}Mo_4P_4$ and (b) $Co_{12}Mo_2P_2$ obtained using the technique of expanded supercell and relaxation. Brown, orange and blue spheres represent Co, P and Mo atoms, respectively.

$$\mathrm{M.H}_{ads} + \mathrm{H_2O} \rightarrow \mathrm{H_2} + \mathrm{M} + \mathrm{OH^-} \ (\textit{Heyrovsky} \text{ step}) \tag{3.4}$$

3.2.5 Simulations of adsorption

To shed light on the enhancement in catalytic activity upon introduction of Mo in Co-P system, we examined the interaction of the reactant and intermediate species along the pathway of alkaline HER with the before-mentioned models of Co-Mo-P alloy. To quantify the strength of adsorption of H-atom, H_2O molecule and OH intermediate at various inequivalent surface sites on the model structures. To calculate energies of adsorption of various adsorbates, we use the following expression:

$$\Delta E_{ads} = E_{system+adsorbate} - (E_{system} + \mu_{adsorbate}) \tag{3.5}$$

where, ΔE_{ads} is the adsorption energy and $E_{system+adsorbate}$, E_{system} and $\mu_{adsorbate}$ are the total energies of adsorbate stabilized on Co-Mo-P system, Co-Mo-P system and chemical potentials of isolated adsorbate species (H-atom, OH and H_2O molecule), respectively. Here, $\frac{1}{2}\mu_{H_2}$ and μ_{H_2O} - $\frac{1}{2}\mu_{H_2}$, are taken as the chemical potentials of an isolated H-atom (μ_H) and OH (μ_{OH}), respectively. Gibbs free energy of adsorption (ΔG_{ads}) is computed

using the following expression:

$$\Delta G_{ads} = \Delta E_{ads} - T\Delta S_{adsorbate} + E^{ZPE}_{adsorbate} \tag{3.6}$$

where, ΔE_{ads} is the adsorption energy, $\Delta S_{adsorbate}$ is the standard molar entropy of adsorbate and $E^{adsorbate}_{ZPE}$ is the zero-point energy of the isolated adsorbate specie calculated from phonon frequencies. We take T as room temperature. i.e., 298 K. Here, $\Delta S_H = \frac{1}{2}S^{\circ}_{H_2}$ and $E^{ZPE}_H = \frac{1}{2}E^{ZPE}_{H_2}$ and $\Delta S_{OH} = S^{\circ}_{H_2O}$ - $\frac{1}{2}S^{\circ}_{H_2}$ and $E^{ZPE}_{OH} = E^{ZPE}_{H_2O}$ - $\frac{1}{2}E^{ZPE}_{H_2}$.

Upon adsorption of H_2O molecule at Mo-Co bridging site, we find that the water molecule splits into H^* and $^*OH$, where * denotes an adsorbed entity (Fig. 3.3a). The H^* attached to Co, which is what we find to be the preferred site of adsorption for H, which OH binds to a neighbouring Mo-Co bridging site. Thus, we identify the Mo-Co bridging site as the active site for splitting H_2O to yield H^* (*Volmer* step). Our simulations of adsorption also show that the O-atom of both OH and H_2O binds strongly to either a Mo or Co atomic site.

To understand the role of phosphorus in OH adsorption, we compare interaction of OH with (a) $Co_{14}Mo_2$ and (b) $Co_{14}P_2$ (Fig. 3.3c, d). We find that the ΔG^{OH}_{ads} and $\Delta G^{H_2O}_{ads}$ on $Co_{14}P_2$ are larger in magnitude than the respective adsorption energies on $Co_{14}Mo_2$. Being electronegative, P polarizes the metal atom in its vicinity inducing a positive charge. This electron deficient metal site is attractive for the adsorption of a nucleophilic specie like OH and H_2O (Fig. 3.3b inset). As a result $|\Delta G^{OH}_{ads}|$ and $|\Delta G^{H_2O}_{ads}|$ are much higher for $Co_{14}P_2$ than $Co_{14}Mo_2$, while intermediate strength of adhesion of OH and H_2O is observed for $Co_{12}Mo_2P_2$ (Fig. 3.3b). Thus, phosphorus site serves a key role in facilitating the *Heyrovsky* step. Analysis of projected density of states (PDOS) of OH and H_2O adsorbed on $Co_{12}Mo_2P_2$ shows the highest occupied molecule orbitals (HOMO) of adsorbates (OH and H_2O) are close to the bottom of the d-band of the catalyst (Fig. 3.4). As the HOMO of OH is degenerate and partly occupied, charge transfers from the catalyst metal to OH.

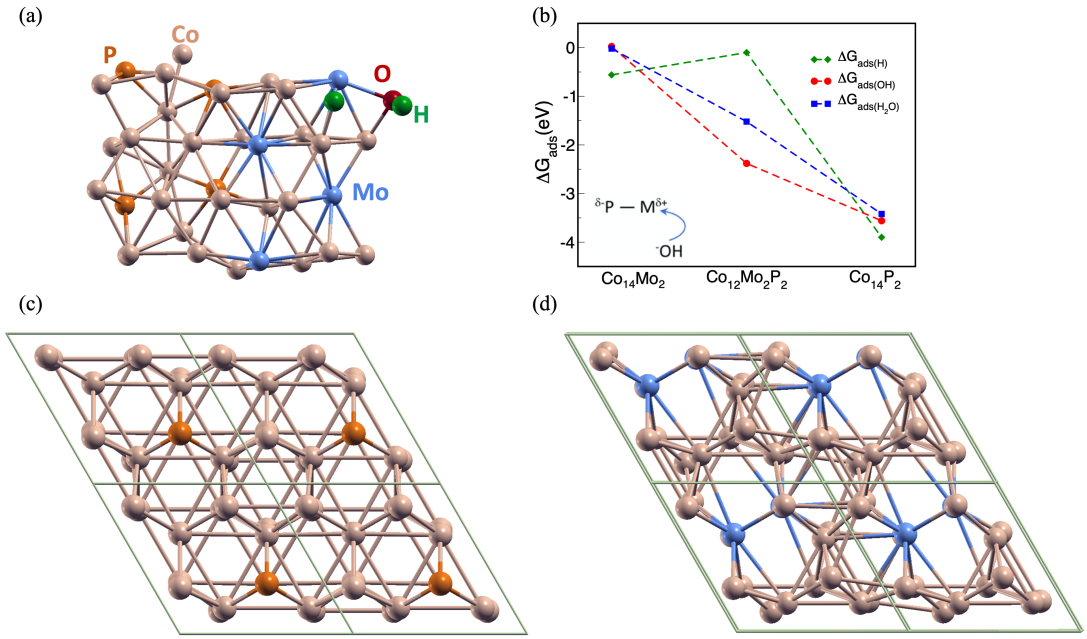

Figure 3.3: (a) Splitting of H_2O molecule upon adsorption at the Mo-Co bridging site of $Co_{28}Mo_4P_4$; (b) Energies of adsorption (ΔG_{ads}) of H, OH and H_2O. Inset: A schematic showing the mechanism of how electronegative P-atom ionizes metal (M) and enhances $^{-}$OH binding; Model amorphous structures of (c) $Co_{14}P_2$ and (d) $Co_{14}Mo_2$ obtained using the technique of expanded supercell and relaxation. Brown, orange and blue spheres represent Co, P and Mo atoms, respectively.

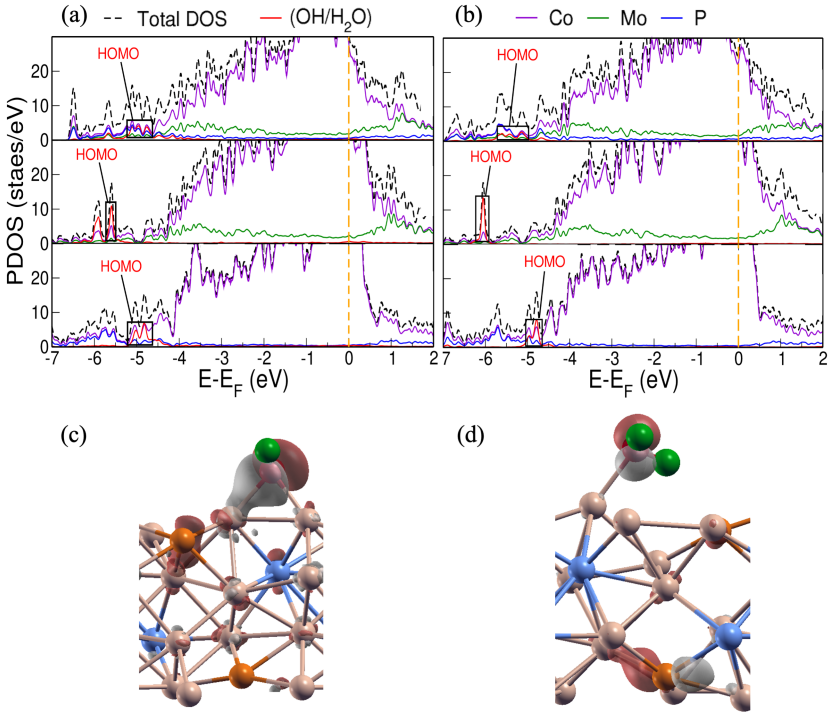

Figure 3.4: PDOS of (a) OH and (b) H_2O adsorbed on $Co_{12}Mo_2P_2$, $Co_{14}Mo_2$, $Co_{14}P_2$, top, middle and bottom panels, respectively; Iso-surfaces of wave functions depicting the interacting orbitals (HOMO) for (c) $OH^*Co_{12}Mo_2P_2$ and $H_2O^*Co_{12}Mo_2P_2$. Red and silver colors represent positive and negative iso-surfaces respectively. Co, Mo, P, O and H atoms are represented with brown, blue, orange, red and green spheres, respectively.

Also, the peak associated with the HOMO of OH splits and broadens due to covalent interaction with Mo and P states. The latter interaction is weak when there is no P in the system (e.g. $Co_{14}Mo_2$). As the HOMO of H_2O is fully occupied and lower in energy relative to the frontier bands of the catalyst, the interaction is weaker and associated HOMO peaks are sharper. In comparison with H-adsorption on $Co_{12}Mo_2P_2$, H binds more strongly to $Co_{14}Mo_2$ and even more strongly to $Co_{14}P_2$. Thus, Mo in the Co-Mo-P alloy weaken H-binding, facilitating the evolution of the product H_2 molecule (*Tafel* step). The chemical synergy between Mo and P gives rise to the excellent catalytic activity of Co-Mo-P alloy towards alkaline HER. As pointed out here, the alloy effectuates the steps of HER with each element playing an important role.

3.2.6 Effect of amorphicity on catalytic activity

To better understand why the amorphous (nanoporous and disordered) Co-Mo-P catalyst is superior to the compositionally similar crystalline catalyst towards alkaline HER, we computed and compared the energetics of reaction intermediates on a model crystalline structure (Fig. 3.5a) An analysis of energetics of adsorption (ΔG_{ads}) of H, OH and H_2O on amorphous-$Co_{12}Mo_2P_2$ and crystalline-$Co_{12}Mo_2P_2$ suggests the former exhibits higher activity towards catalyzing the evolution of H_2. Amorphous-$Co_{12}Mo_2P_2$ shows a stronger affinity towards all adorbates considered here (higher $|\Delta G_{ads}|$). For H_2O and OH, we identify Co-atom as the main adhesion site in amorphous-$Co_{12}Mo_2P_2$, while Mo-atom serves as the main adsorption site in crystalline-$Co_{12}Mo_2P_2$. H-atom binds strongly to Co irrespective of the type of structure. Perhaps one of the more significant results is that we find and optimal ΔG^H_{ads} of $\sim$ -0.1 eV on amorphous-$Co_{12}Mo_2P_2$, compared to ΔG^H_{ads} of $\sim$ 0.63 eV on the crystalline surface (Fig. 3.5b). This comparison suggests that the *Tafel* step is favored on the amorphous surface, consistent with superior HER activity of the amorphous surface.

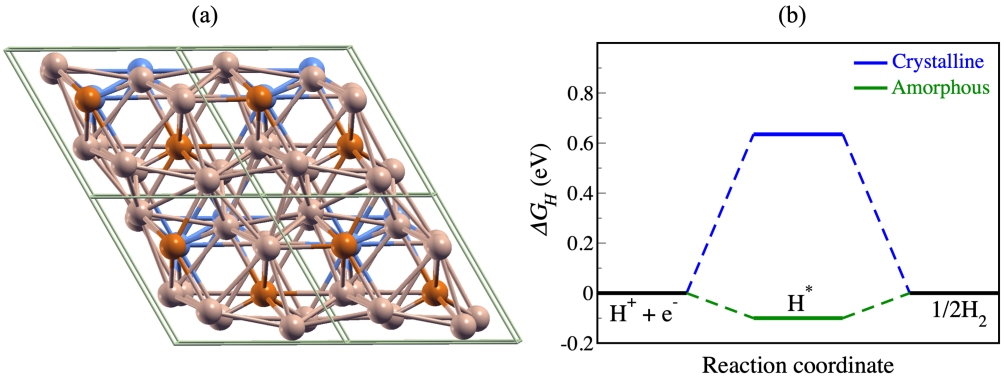

Figure 3.5: (a)(2×2×1) Model crystalline $Co_{12}Mo_2P_2$ structure; (b) ΔG^H_{ads} for amorphous and crystalline $Co_{12}Mo_2P_2$. Co, Mo, and P atoms are represented with brown, blue and orange spheres, respectively.

3.2.7 Conclusions

We simulate two model amorphous structures of Co-Mo-P alloy and examine their catalytic activity towards alkaline HER within the framework of density functional theory. We employ expanding lattice method to generate a nanoporous ($Co_{28}Mo_4P_4$) and a disordered ($Co_{12}Mo_2P_2$) system. To quantify the catalytic performance of Co-Mo-P alloy, we determine the strength of adsorption of reactants (H-atom and H_2O molecule) and intermediate (OH) occurring along the alkaline HER pathway at various surface sites. We identify Co as the preferred site of adsorption of H-atom in the alloy. Upon adsorption of an H_2O molecule at Mo-Co bridging site, we find the water molecule splits into H* and OH* which adhere to a neighbouring Co and Mo-Co bridging sites respectively. Thus, we propose the bridging Mo-Co as the active site for the *Volmer* step. We further compare the adhesion of OH and H_2O on $Co_{12}Mo_2P_2$ to that on $Co_{12}Mo_2$ and $Co_{12}P_2$ and find $\Delta G_{ads(OH)}$ and $\Delta G_{ads(H_2O)}$ to be higher on the latter. This effect is attributed to the high electronegativity of P atom which ionizes a nearby metal atom, making it an attractive site for electron-rich species (like OH and H_2O). Mo in the Co-Mo-P alloy is identified to be responsible to weaken the H-binding which is evident by a decrease in ΔG^H_{ads} for $Co_{12}Mo_2$ over $Co_{12}P_2$. Hence, phosphorus serves as the key site in facilitating the *Heyrovsky* step while molybdenum is responsible for the *Tafel* step. We further carried out

simulations of adsorption of H, OH and H_2O on crystalline-$Co_{12}Mo_2P_2$ which showed a weaker catalytic activity towards evolution of H_2 than its amorphous counterpart. The superior HER activity of the amorphous surface comes from a favourable *Tafel* step with an optimal ΔG^H_{ads} of $\sim$ -0.1 eV, compared to ΔG^H_{ads} of $\sim$ 0.63 eV on the crystalline surface.

3.3 Stabilizing the Metastable 1T-MoS_2 by Substitutional Ni and Co[†]

Molybdenum disulfide (MoS_2) has been shown to be a promising candidate as a catalysts for HER. Density functional theory (DFT) calculations reveal that undercoordinated edge S atoms and S-vacancies in 1H-MoS_2 exhibit an optimal $\Delta G^H_{ads} \sim 0$ eV. [124] Based on this, there have been several reports looking at MoS_2 morphologies which exhibit exposed edges site. [125–129] MoS_2 exists in various known polytypes (Fig. 3.6), of which the semiconducting 2H-MoS_2 phase (space group *P6/mmc*) is the ground state in which S atoms form a trigonal prismatic coordination around Mo and two S-Mo-S units per unit cell. Other metastable polytypes include 1T which exhibits an octahedrally coordinated S atoms around Mo (one S-Mo-S unit per unit cell) [130] and 3R which also shows a trigonal prismatic coordination but with three S-Mo-S units in the c-direction [131].

Although MoS_2 has shown promise in the catalytic proton reduction step, it has not been successful in reducing water under alkaline conditions owing to the high energy barrier associated with H_2O dissociation. [118] Prior reports has also shown that the basal plane of MoS_2 is inactive for the HER. It has been shown, however, that the metastable 1T polymorph of MoS_2 is active on both the undercoordinated edges and the basal plane. [132–134] In this study Prof. Daniel Strongin's* group realised that introduction of 3d

[†]This work has been published as N. H. Attanayake, L. Dheer, A. C. Thenuwara, S. C. Abeywaara, C. Collins, U. V. Waghmare, and D. Strongin, Ni- and Co-Substituted Metallic MoS_2 for the Alkaline hydrogen evolution Reaction, *ChemElectroChem* **7**, 3606-3615 (2020) [28]. Reproduced with permission from the John Wiley and Sons.

*Department of Chemistry, Temple University

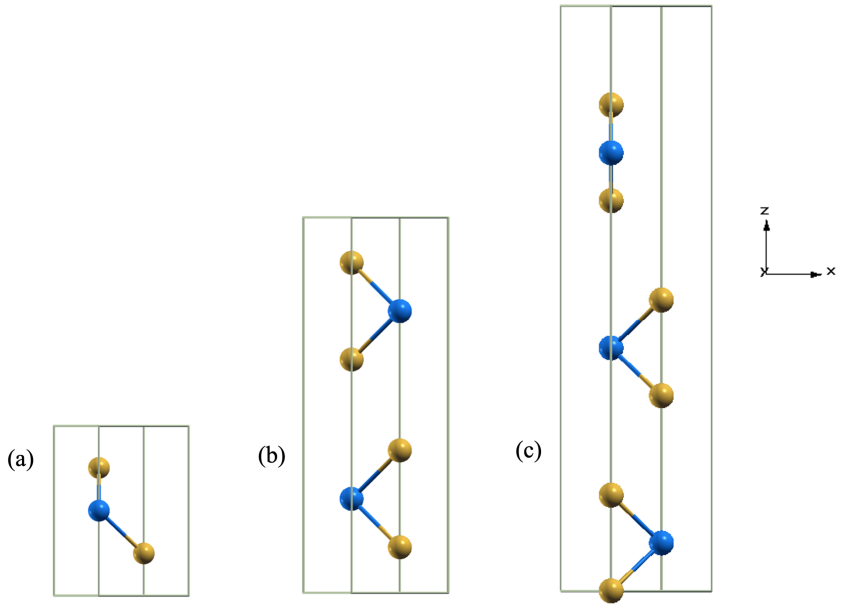

Figure 3.6: Polytypes of MoS_2: (a) 1T-MoS_2, (b) 2H-MoS_2, and (c) 3R-MoS_2. Mo and S atoms are represented with blue and gold spheres respectively.

transition metals such as Ni or Co into the basal plane of metallic MoS_2 would help in the water dissociation step since presence of Ni and Co is known to facilitate the dissociation of water during HER. We present a detailed density functional theoretical analysis of the effect of substitutional Ni and Co in 1T MoS_2 on the structural, electronic and catalytic properties of the TMDC.

3.3.1 Computational details

Our first-principles calculations are based on density functional theory (DFT) as implemented in the Quantum ESPRESSO code [121] employing plane-wave basis sets and ultra-soft pseudopotentials [101] to represent the interaction between ionic cores and valence electrons. We adopt the exchange-correlation energy functional of Perdew-Burke-Ernzerhof (PBE) [99] within a generalized gradient approximation (GGA), and smear occupation numbers of electronic states with Fermi–Dirac distribution and a smearing width (k_BT) of 0.04 eV. An energy cutoff of 30 Ry is used to truncate the plane-wave basis used in representation of Kohn-Sham wave functions, and of 240 Ry to represent the charge

density. We included van der Waals (vdW) interactions using Grimme scheme. [135] Structures were determined through minimization of energy until the Hellmann Feynman force on each atom is smaller than 0.03 eV/Å in magnitude. In the supercell to model a monolayer, a parallel vacuum layer of 14 Åis introduced separating adjacent periodic images. We sampled Brillouin-zone integrations on uniform grids of 9×9×1 k-points. The projected density of states of all the structures was obtained from a much denser 21×21×1 k-point mesh. Calculated lattice constant of 1T-MoS_2 (a = 3.22 Å) within typical GGA errors of the experimental value (a° = 3.19 Å). [118]

3.3.2 Stability of 1T-MoS_2 on Ni/Co substitution

To understand effects of Ni/Co substituents on structural, electronic and catalytic activity of 1T-MoS_2, we modelled a 5×4×1 supercell of 1T-MoS_2 ($Mo_{20}S_{40}$) with Ni and Co atom(s) substituting Mo atom(s). In these simulations, two substitutional concentrations were employed:

1. $Mo_{19}M_1S_{40}$: 5% substitutional doping
2. $Mo_{18}M_2S_{40}$: 10% substitutional doping

where M=Ni/Co. We estimated the formation energy of the substituted samples using:

$$E_{form} = \frac{E_{Mo_{20-m}M_mS_{40}} - [E_{M_{20}S_{40}} - mE_{Mo} + mE_M]}{m} \tag{3.7}$$

where, $E_{Mo_{20-m}M_mS_{40}}$, $E_{M_{20}S_{40}}$, E_{Mo} and E_M are the energies of Ni/Co substituted 1T-MoS_2, pristine 1T-MoS_2, isolated Mo and Ni/Co atoms respectively. Here, m is an integer giving the number of Mo atoms substituted with Ni/Co atoms.

Results of DFT calculations presented in Table 3.1 show that either Ni or Co substitution stabilizes the 1T-MoS_2 lattice, and formation energies per Ni/Co atom are higher (in magnitude) at a Ni or Co concentration of 10 at.% than at 5 at.%. Substitution of Ni or

Catalyst	E_{form}(eV)/atom	
	Ni	Co
$Mo_{19}M_1S_{40}$	-0.8	-0.84
$Mo_{18}M_2S_{40}$	-1.1	-1.3

Table 3.1: Formation energy of M=Ni/Co substitution in 1T-MoS_2 basal plane.

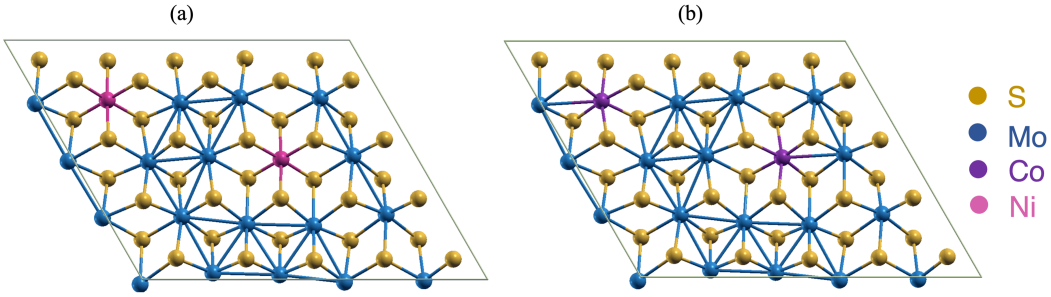

Figure 3.7: Optimized structures of (a) 10% Ni-substituted 1T-MoS_2, and (b) 10% Co-substituted 1T-MoS_2. Mo, S, Ni and Co atoms are represented by blue, gold, magenta and violet spheres, respectively.

Co at Mo sites in metallic phase of MoS_2 results in a local structural distortion around the 3d-transition metal substituents (Fig. 3.7), and consequent trimerization of Mo-atoms which resembles a distorted polytype of 1T-MoS_2 known as 1T" as presented in earlier works [19]. The pristine 1T" structure of MoS_2 is higher in energy than the 1H phase, but is about 0.2 eV/Mo-atom lower in energy than 1T. Upon structural distortion, the Mo-Mo bond lengths change locally from 3.25 Åin pristine 1T-MoS_2 and ranges from 2.7 to 3.7 Åin the Ni and Co substituted samples.

3.3.3 Electronic properties

Pristine MoS_2 in the high symmetry 1T phase is metallic in nature [136], evident from the calculated electronic structure (Fig. 3.8a). A 10 at.% substitution of Ni or Co for Mo in MoS_2 significantly changes the density of states (DOS) near the Fermi level (ϕ). In Co substituted 1T-MoS_2, we find states arising from Co just below ϕ (Fig. 3.8b), while the Ni states lie deeper in energy in the Ni substituted 1T-MoS_2. Secondly we calculate a drop in DOS for both Ni and Co substituted catalysts at ϕ, creating a pseudo gap that

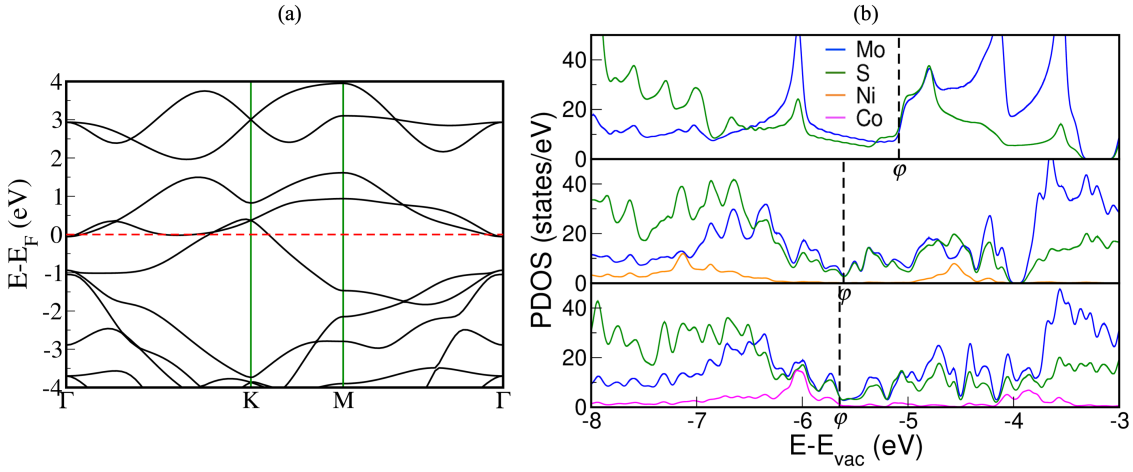

Figure 3.8: (a) Band structure of 1T-MoS_2, and (b) PDOS of pristine, 10% Ni and 10% Co-substituted 1T-MoS_2, top, middle and bottom panels, respectively.

is responsible for stabilization of the MoS_2 lattice.

3.3.4 Catalysis of alkaline HER

To assess the catalytic activity of pristine and Ni/Co substituted 1T-MoS_2 towards alkaline HER, we simulated the adsorption of reactant and intermediate species of the reaction at inequivalent surface sites. The strength of interaction between the monolayer and adsorbates (H, OH and H_2O) is determined using:

$$\Delta E_{ads} = \frac{E_{n\times adsorbate+Mo_{20-m}M_mS_{40}} - (E_{Mo_{20-m}M_mS_{40}} + n\mu_{adsorbate})}{n} \tag{3.8}$$

where, $E_{n\times adsorbate+Mo_{20-m}M_mS_{40}}$, $E_{Mo_{20-m}M_mS_{40}}$ and $\mu_{adsorbate}$ are the energies of adsorbate and pristine or Ni/Co substituted 1T-MoS_2 monolayer complex, pristine or Ni/Co substituted 1T-MoS_2 monolayer and chemical potentials of isolated adsorbate, respectively. $\frac{1}{2}\mu_{H_2}$ and μ_{H_2O} - $\frac{1}{2}\mu_{H_2}$, are taken as the chemical potentials of an isolated H-atom (μ_H) and OH (μ_{OH}), respectively. Here, n is an integer denoting the number of adsorbates interacting with the catalyst. We estimated the Gibbs free energy of H adsorption (ΔG^H_{ads}) using Eq. **??**. 1T-MoS_2 in its pristine state interacts strongly with the H-atom while

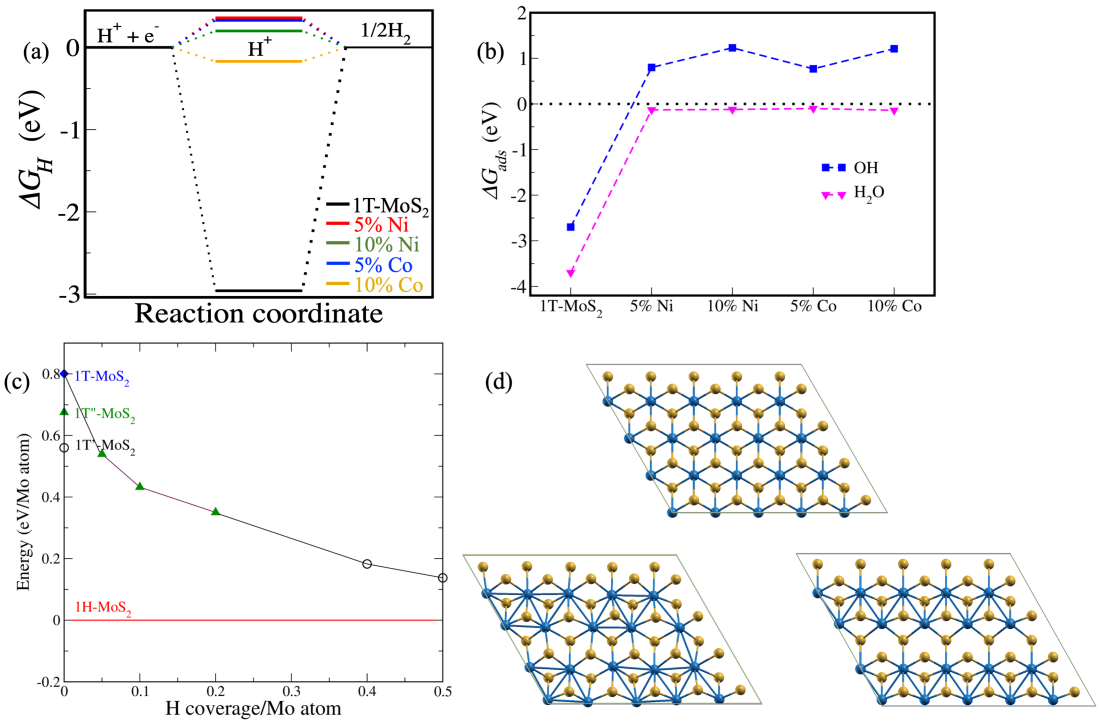

Figure 3.9: (a)ΔG^H_{ads} values relevant to the HER over pristine and Ni and Co substituted 1T-MoS_2; (b) Energies of adsorption of OH and H_2O; (c) Structural transformation of 1T phase to 1T" at lower H-coverage and further transformation to 1T' polytype at H-coverage $\geq$ 40%; (d) Optimised structures of pristine 1T-MoS_2 (top), 1T"-MoS_2 (left) and 1T'-MoS_2 (right). Mo, S, Ni and Co atoms are represented by blue, gold, magenta and violet spheres, respectively.

the Ni/Co substituted 1T-MoS_2 exhibit an optimal interaction strength (Fig. 3.9a). The high (in magnitude) adsorption energy for H-atom on pristine 1T-MoS_2 is comparable to the estimate reported by Tang *et al.* [137]. Nearly optimum ΔG^H_{ads} is obtained for 10% Ni-substituted 1T-MoS_2 ($\Delta G^H_{ads} \sim$ 0.2 eV) and 10% Co-substituted 1T-MoS_2 ($\Delta G^H_{ads} \sim$ -0.17 eV). Interestingly we observe a structural transition of the (pristine) 1T lattice on H-adsorption consistent with previous reports [137, 138]. We find that the 1T" lattice of Ni/Co-MoS_2 remains unchanged at low H-coverages (<40%), but transforms into 1T' phase at higher H-coverage ($\geq$40%) (Fig. 3.9c, d) . Both H_2O and OH exhibit a high binding affinity towards pristine 1T-MoS_2 (Fig. 3.9b) which is understandable in light of its high energy and metastable nature. From our simulations of adsorption of H_2O molecule on Ni and Co substituted 1T"-MoS_2, we find a weaker (in magnitude) interaction strength

at both 5% and 10% concentrations (Fig. 3.9b). Both Ni and Co substituted 1T"-MoS_2 interact repulsively with OH and exhibit a weak positive adsorption energy (Fig. 3.9b). It is likely that such a repulsive interaction leads to an enhanced catalytic activity of 1T"-MoS_2 upon Ni or Co substitution by limiting the poisoning of active sites by OH and thus enhancing water dissociation in alkaline HER [118].

3.3.5 Conclusions

We show that substitution of Ni or Co into 1T-MoS_2 locally distorts the lattice structure near the dopant site, giving the 1T"-like polytype, a lower energy than the 1T phase. Pristine 1T-MoS_2 exhibits high interaction strength with H-atom ($\Delta G^H_{ads} \sim$ -3 eV) which shifts to a close to optimum interaction for both Ni and Co substituted catalysts ($\Delta G^H_{ads} \sim$ 0.2 and -0.17 eV, respectively). Also on interaction with H-atom, the 1T-MoS_2 monolayer transforms into 1T" at lower coverages (<40%) which further transforms into 1T' phase at higher coverage ($\geq$40%). The proton source in alkaline HER, H_2O shows weak adhesion to Ni/Co substituted 1T-MoS_2 monolayers and attaches strongly to the pristine 1T-MoS2 ($\Delta G^H_{ads} \sim$ -3.6 eV). OH molecule, responsible for poisoning active sites of the catalyst, binds strongly to the pristine 1T-MoS_2 ($\Delta G^H_{ads} \sim$ -2.7 eV) but shows no affinity towards the Ni/Co substituted 1T-MoS2 ($\Delta G^H_{ads} > 0$ eV) further confirming their high catalytic activity.

Chapter 4

Tailoring Catalytic the Activity of Metal Phosphide and Carbides by Substitutional

4.1 Introduction

Hydrogen, owing to its high gravimetric energy density (143 kJ kg^{-1}) [22] and environmentally benign nature, can be an ideal potential alternative to fossil fuels. Electrocatalytic water splitting, empowered by renewable energy sources, is an efficient and sustainable methods to generate H_2 and can be easily coupled with fuel cell applications [139]. Thermodynamically uphill processes of hydrogen evolution (HER) at cathode and oxygen evolution (OER) at anode involves overpotentials, which determine the overall cell voltage (E_{cell}) governing an catalysts's practical viability. [140] Despite extensive reports over the last decade, both acidic and alkaline water electrolysis is still most efficiently catalyzed by noble metal-based catalysts (Pt for HER and Ir/Ru oxides for OER) [141], which are expensive and scarce [142] limiting their use.

Recently, transition metal phosphides (TMPs) have emerged as a promising electrocatalysts due to their unique electrochemical properties. TMPs have shown to catalyze water splitting efficiently with high activity, high stability, and close to 100% Faradaic efficiency in a wide pH range (0-14). Single TMPs are the most common class of phosphides. CoP was shown to exhibit high HER efficiency in acid media both experimentally and theoretically. [143] doping a second element is another common strategy to enhance catalytic activity. Iron is a commonly used doping element, which can significantly improves the catalytic performance of materials. [143] Mn is another transition metal used as a dopant. Chen *et al* fabricated Mn-doped NiP_2, that showcased higher HER activity due to low thermoneutral hydrogen adsorption. [144] Doping Mn into Co_2P greatly enhanced the OER activity due to modulation of the high oxophilic nature of Mn by Co with improved overpotential and turnover frequency. [145] FeMnP on nickel foam served as an efficient water splitting catalyst having a cell potential of 1.55 V to achieve a current density of 10 mA cm^{-2}. [146] Motivated by this Prof. Sebastian Peter's* group hypothesized Mn substitution in Ni_2P may effectively improve both the HER and OER activity and, hence, the overall performance towards water splitting. They applied a simple solvothermal strategy to improve the catalytic activity of $Ni_{2-x}Mn_xP$ nanostructures by varying Ni/Mn ratio.

4.2 Ni_2P with Substitutional Mn as Catalyst for Enhanced Water Splitting †

We present a comprehensive analysis using *first-principles* DFT calculations to show the effect of Mn substituents on the electronic and catalytic properties of Ni_2P (space group $P\bar{6}2m$).

*New Chemistry Unit, JNCASR

†This work has been published as S. Sarkar, L. Dheer, C. P. Vinod, R. Thapa, U. V. Waghmare, S. C. Peter, Stress-Induced Electronic Structure Modulation of Manganese-Incorporated Ni2P Leading to Enhanced Activity for Water Splitting, *ACS. Appl. Energy Mater.* **3**, 1271-1278 (2020) [33]. Reproduced with permission from the American Chemical Society

4.2.1 Computational details

Our first-principles calculations are based on density functional theory (DFT) as implemented in the Quantum ESPRESSO code [121] employing plane-wave basis sets and ultrasoft pseudopotentials [101] to represent the interaction between ionic cores and valence electrons. We adopt the exchange-correlation energy functional of Perdew Zunger [95] obtained within a local density approximation (LDA). We smear the discontinuity in occupation numbers of electronic states with Fermi–Dirac distribution having a smearing width (k_BT) of 0.04 eV. An energy cutoff of 40 Ry is used to truncate the plane-wave basis used in representation of Kohn-Sham wave functions, and of 320 Ry to represent the charge density. Optimized structures were determined through minimization of energy until the Hellmann-Feynman force on each atom is smaller than 0.03 eV/Å in magnitude. We use a supercell to model surfaces introducing a vacuum layer of 14 Åthickness parallel to the slab separating its adjacent periodic images. We sampled Brillouin-zone integrations on uniform grid of 5×5×1 k-points in the Brillouin zones of (111) surfaces Ni_2P and $Ni_{2-x}Mn_xP$. The projected density of states of each structure was obtained from calculations on a denser, 10×10×1, k-point mesh. Calculated lattice constant of bulk Ni_2P (a = 5.82 Å) is within the typical LDA errors with respect to its observed value (a = 5.825 Å). [143]

4.2.2 Mn-substitution in Ni_2P: formation energies

Ni_2P possesses a Fe_2P-type crystal structure (space group $P62m$) with four crystallographic sites: two of these sites, Wyckoff positions $3f$ and $3g$, are occupied by the Ni atoms and the other two, Wyckoff positions $2d$ and $1a$, are occupied by the P atoms. Thus, substituted atoms can occupy any of these four crystallographic sites. To check the site-specific stability of Mn substitution, we modelled a 2×1×1 of 2 layered (111) surface of Ni_2P with one Ni atom substituted at various sites in $Ni_{32}P_{16}$, and calculated formation

energy using:

$$E_{form} = \frac{E_{Ni_{32-x}Mn_{x+y}P_{16-y}(111)} - [E_{Ni_{32}P_{16}(111)} - xE_{Ni} - yE_P + (x+y)E_{Mn}]}{(x+y)} \quad (4.1)$$

where, $E_{Ni_{32-x}Mn_{x+y}P_{16-y}(111)}$, $E_{Ni_{32}P_{16}(111)}$, E_{Ni}, E_P and E_{Mn} are the energies Mn substituted Ni_2P (111) surface, pristine Ni_2P (111) surface, isolated Ni, P and Mn atoms, respectively. Here, x and y are integers giving number of Ni and P atoms substituted by Mn atoms respectively. As is evident from Fig. 4.1 and expected, Mn atomic substitution

(111) surface	E_{form}(eV)/Mn atom			
	$2d$	$1a$	$3g$	$3f$
$Ni_{32}M_1P_{15}$	0.35	0.20	-	-
$Ni_{31}M_1P_{16}$	-	-	-0.60	-0.08

Table 4.1: Formation energy of Mn substitution at various Wyckoff sites of (111) surface of Ni_2P.

at the Ni site is more stable than at P sites. Of the two Wyckoff sites of Ni, Mn substitution is more favorable to occur at the $3g$ site. We further simulated the (111) surface of $Ni_{2-x}Mn_xP$ with varied Mn substitution concentration and estimated the respective formation energies using Eq. 4.1. We find that $Ni_{1.5}Mn_{0.5}P$ (25% substitution) is the most stable among the configurations studied here (Fig. 4.1).

4.2.3 Catalysis of HER

To understand the HER activity of pristine Ni_2P and Mn-substituted $Ni_{2-x}Mn_xP$ (Fig. 4.2), we simulated adsorption of H atom at various inequivalent surface sites. The strength of its interaction with $Ni_{2-x}Mn_xP$ is determined using:

$$\Delta E_{ads} = E_{adsorbate+Ni_{32-x}Mn_xP_{16}} - (E_{Ni_{32-x}Mn_xP_{16}} + n\mu_{adsorbate}) \quad (4.2)$$

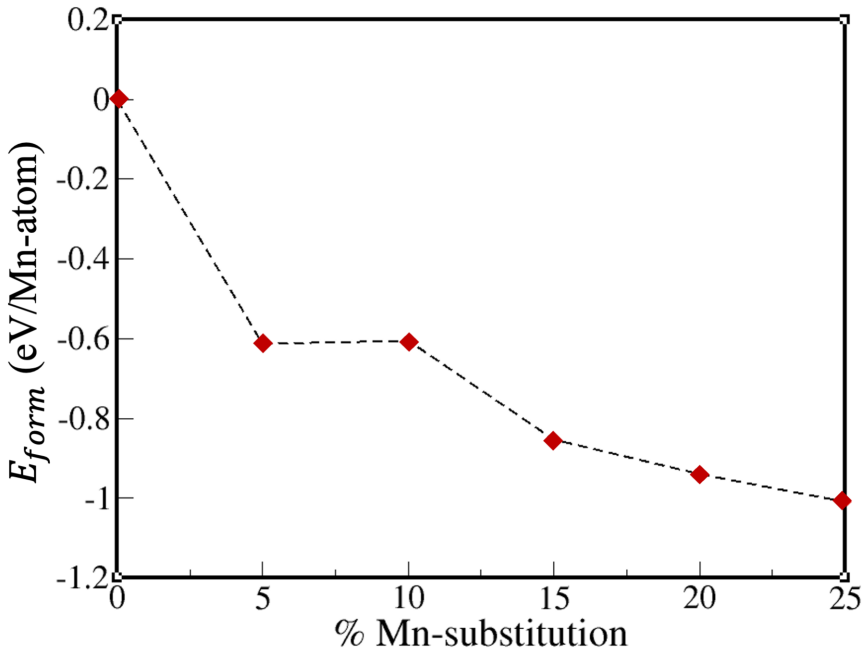

Figure 4.1: Formation energies of Mn substituted Ni_2P with varied Mn concentration.

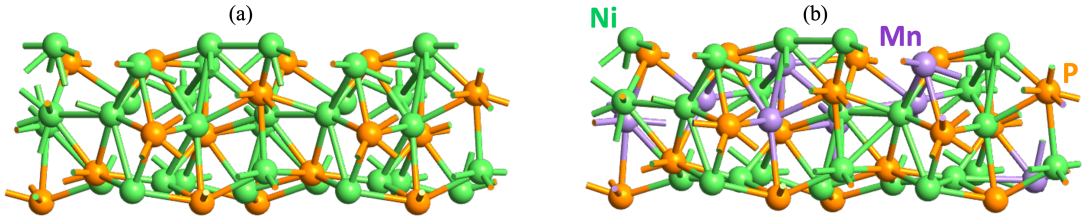

Figure 4.2: Optimised structures of (111) surfaces of (a) pristine Ni_2P and (b) $Ni_{1.5}Mn_{0.5}P$. Ni, Mn and P atoms are denoted by green, purple and orange spheres, respectively.

where, $E_{adsorbate+Ni_{32-x}Mn_xP_{16}}$, $E_{Ni_{32-x}Mn_xP_{16}}$ and $\mu_{adsorbate}$ are the energies of adsorbate on pristine/Mn-substituted Ni_2P (111) surface, pristine/Mn-substituted Ni_2P (111) surface and isolated adsorbate, respectively. We take $\frac{1}{2}\mu_{H_2}$ as the chemical potential of an isolated H-atom (μ_H). We further estimated the Gibbs free energy of H adsorption (ΔG^H_{ads}), which is a descriptor of catalytic activity toward HER [124] using:

$$\Delta G^H_{ads} = \Delta E^H_{ads} - T\Delta S_H + E^{ZPE}_H \tag{4.3}$$

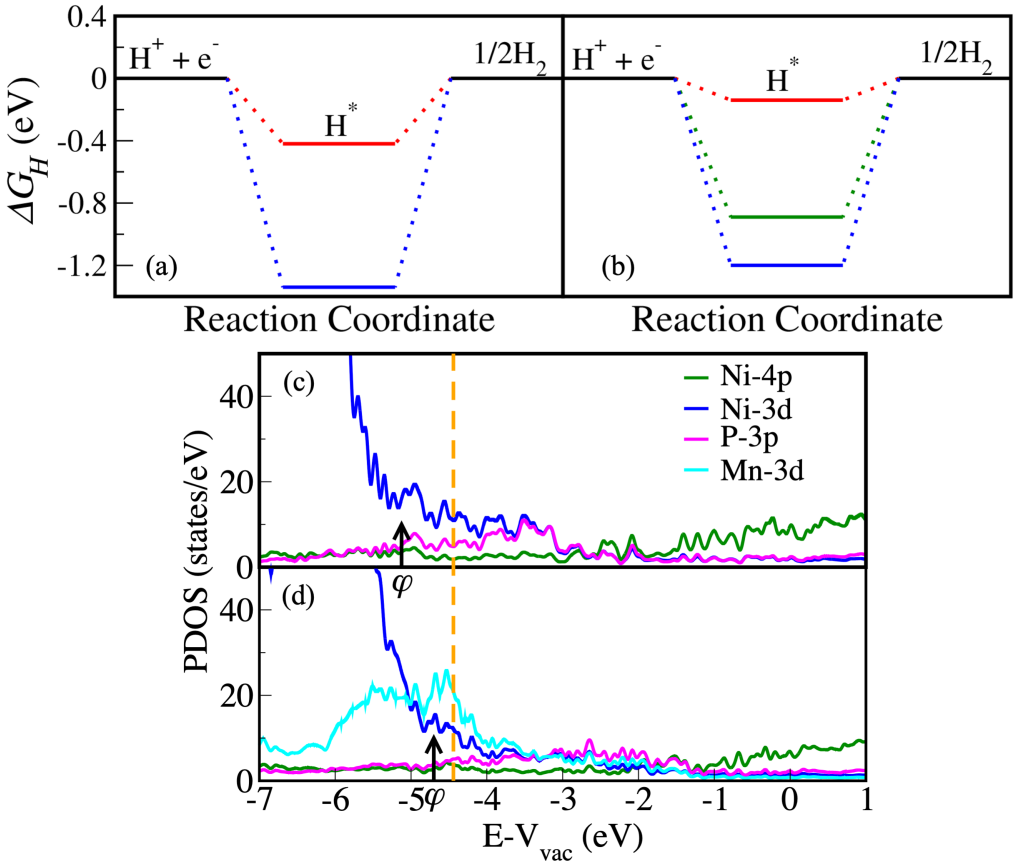

Figure 4.3: Free energy relevant to hydrogen evolution reaction over (a) Ni_2P and (b) $Ni_{1.5}Mn_{0.5}P$. Red, blue, and green lines correspond to adsorption at P, Ni, and Mn sites, respectively. Projected density of states (PDOS) of (111) surfaces of (c) Ni_2P and (d) $Ni_{1.5}Mn_{0.5}P$. Dashed orange line represents the hydrogen reduction potential, and black arrows indicate the Fermi energy or work function.

where, ΔE^H_{ads} is the H-adsorption energy (calculated using Eq. 4.2) T is room temperature. i.e., 298 K, $\Delta S_H = \frac{1}{2}S^\circ_{H_2}$, $S^\circ_{H_2}$ being the entropy of H_2 molecule and $E^{ZPE}_H = \frac{1}{2}E^{ZPE}_{H_2}$, $E^{ZPE}_{H_2}$ being the zero-point energy of an isolated H_2 molecule. Its vanishingly small value indicates optimal catalytic activity of the Mn substituted surface ($\Delta G^H_{ads} \sim$ - 0.14 eV; Fig. 4.3a). We further estimated the work function (ϕ), which was recently shown to be a relevant descriptor of catalytic activity of metals toward CO_2 reduction [147] using:

$$\phi = V_{vac} - E_F \tag{4.4}$$

where, V_{vac} and E_F is the vacuum energy estimated from the planar average of the electrostatic potential, and Fermi energy respectively. The work functions given by Fermi energies of pristine and Mn-substituted Ni_2P surfaces are just below the hydrogen reduction potential. Upon Mn substitution, there is a reduction in ϕ of the catalyst (see Fig. 4.3c, d and Table 4.2), supporting its enhanced activity toward HER.

Catalyst	ϕ
Ni_2P	5.12
$Ni_{1.5}Mn_{0.5}P$	4.78

Table 4.2: Work function of pristine and Mn substituted (111) surfaces of Ni_2P.

4.2.4 Catalysis of OER

OER in alkaline media involves four steps [148] along the reaction path:

$$2H_2O\ (l) + * \rightarrow HO^* + H^+ + e^- + H_2O\ (l) \tag{4.5}$$

$$HO^* + H^+ + e^- + H_2O(l) \rightarrow O^* + 2(H^+ + e^-) + H_2O\ (l) \tag{4.6}$$

$$O^* + 2(H^+ + e^-) + H_2O\ (l) \rightarrow HOO^* + 3(H^+ + e^-) \tag{4.7}$$

$$HOO^* + 3(H^+ + e^-) \rightarrow * + O_2\ (g) + 4(H^+ + e^-) \tag{4.8}$$

To understand the mechanism of the catalytic activity of Mn-substituted and pristine Ni_2P catalysts toward OER, we simulated adsorption of OH, O, and OOH intermediates occurring during the OER at various surface sites and estimated the Gibbs free energies (ΔG) of each step along the reaction pathway at T = 298 K using:

$$\Delta G = \Delta E - T\Delta S + \Delta E^{ZPE} - neU \tag{4.9}$$

where, ΔE, ΔS, ΔE^{ZPE}, n and U are the changes in enthalpy (obtained from DFT total energy), entropy, zero-point energy, number of electrons transferred and the applied potential respectively. Zero-point energies for the adsorbed and the free molecules are computed using DFT calculations, while the entropic contributions for free molecules are taken from the thermodynamic tables [149]. To identify the potential rate-determining step, we estimate free energy change at each reaction step using the scheme developed by Rossmeisl *et al* [148] .The theoretical overpotentials for pristine and Mn-substituted Ni_2P catalysts at standard conditions are obtained using [148]:

$$\eta^{OER} = \left(\frac{G^{OER}}{e}\right) - 1.23V \tag{4.10}$$

where G^{OER} is the Gibbs free energy change of the potential-determining step, i.e., the particular step in the OER reaction mechanism to have the largest ΔG. For pristine Ni_2P and $Ni_{1.5}Mn_{0.5}P$, the final reaction step, i.e., desorption of *OOH to evolve O_2, is the potential determining step. As is evident from the free energy diagrams (Fig. 4.4a), Mn-substituted Ni_2P catalyst has a notably lower theoretical overpotential ($\eta^{Ni_{1.5}Mn_{0.5}P}$ = 1.78 V) than the pristine Ni_2P catalyst (η^{Ni_2P} = 2.62 V) leading to its improved OER catalytic activity. Analysis of the projected density of states (PDOS) of OOH*Ni_2P and OOH*$Ni_{1.5}Mn_{0.5}P$ (see Fig. 4.4c-h) shows that the interaction of $Ni_{1.5}Mn_{0.5}P$ with OOH intermediate is weaker than that of pristine Ni_2P catalyst, which facilitates the evolution to O_2 molecule more efficiently. The peak associated with the highest occupied molecular orbital (HOMO) of OOH splits and broadens due to covalent interaction with Ni and P orbitals of Ni_2P. For OOH*$Ni_{1.5}Mn_{0.5}P$, the HOMO peak of the OOH intermediate is sharper, indicating weaker interaction with the surface.

4.2.5 Effect of O-coverage on OER activity

Metal phosphides are prone to formation of metal oxide (M-O) during electrocatalytic reactions. This leads to modification of their surfaces by oxygen incorporation, which improves the catalytic activity by facilitating charge transfer and increasing the electrochemically active surface area of the catalyst [150]. Wu *et al* reported [151] that oxygen-incorporated Ni_2P outperformed both $Ni(OH)_2$ and pure Ni_2P in its catalytic activity for OER. To see the effect of an oxygen rich environment on the surface of pristine/Mn-

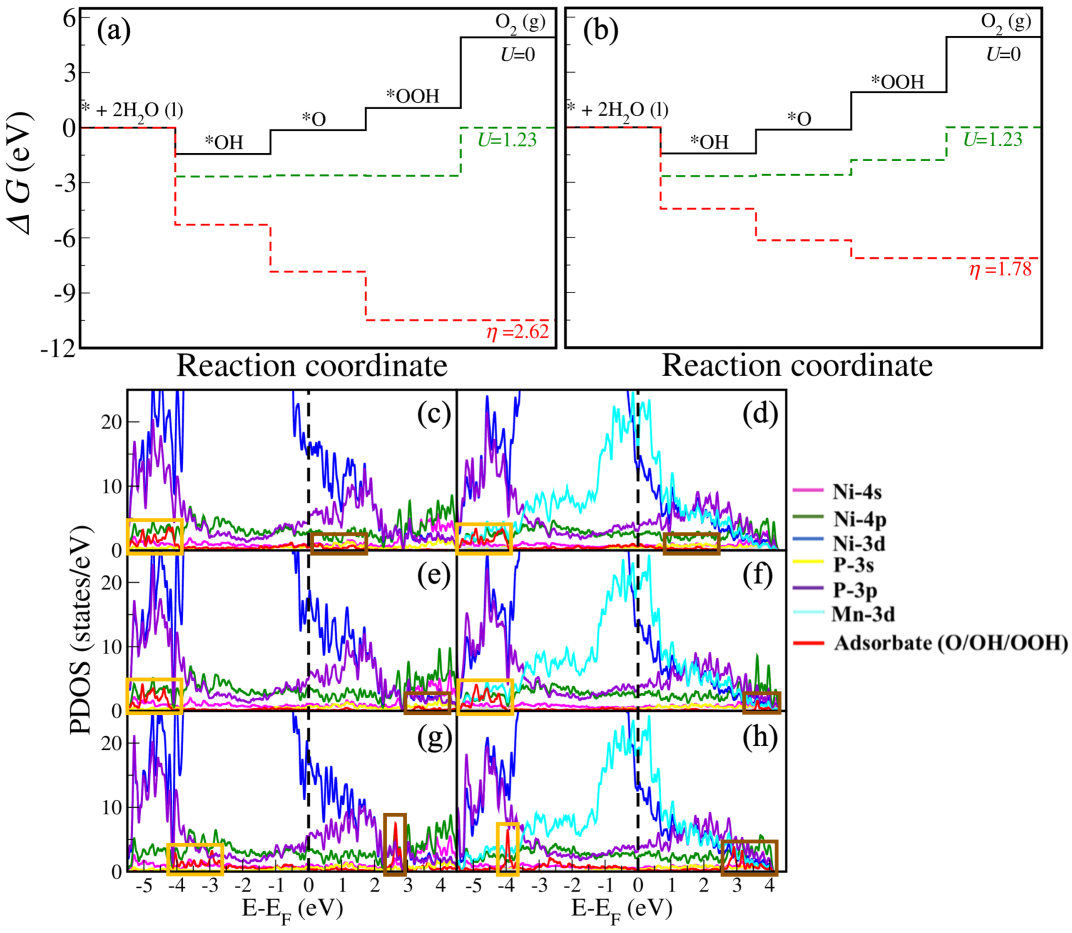

Figure 4.4: Standard free energy of intermediates along the path of oxygen evolution at U = 0 V and U = 1.23 V and the potential for which the potential-determining step becomes downhill, when catalyzed on (a) Ni_2P, (b) $Ni_{1.5}Mn_{0.5}P$. PDOS of OH adsorbed on (c) Ni_2P, (d) $Ni_{1.5}Mn_{0.5}P$; O adsorbed on (e) Ni_2P, (f) $Ni_{1.5}Mn_{0.5}P$; OOH adsorbed on (g) Ni_2P and (h) $Ni_{1.5}Mn_{0.5}P$. The golden and brown boxes denote the HOMO and LUMO of the adsorbates, respectively.

substituted Ni_2P catalysts, we simulated an O_2 molecule in the vicinity of metal atoms (Mn/Ni for $Ni_{1.5}Mn_{0.5}P$ and Ni for pristine Ni_2P). Both pristine and Mn-substituted Ni_2P surfaces exhibit high affinity toward oxygen, resulting in the formation of M-O (M = Mn/Ni) complex (Fig 4.5a). We further obtained the interaction strength of M-O covered (M = Mn/Ni) Mn-substituted Ni_2P surfaces (Fig 4.5b-d and Fig 4.6c-e) and the OER intermediates as a function of M-O species concentration. Using Eq. 4.9, we estimated the ΔG for each step at 298 K and examined the free energy diagrams of reactions for OER.

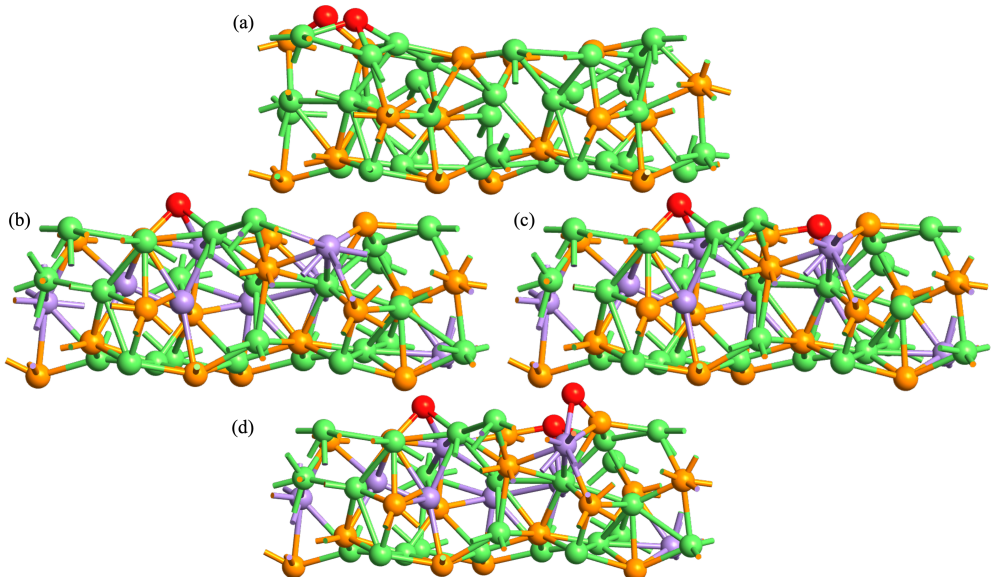

Figure 4.5: Optimized structures of (a) Ni_2P and $Ni_{1.5}Mn_{0.5}P$ surface with (b) one, (c) two and (d) three M-O centers (M=Mn/Ni). Purple, green, orange and red spheres correspond to Mn, Ni, P and O atoms, respectively.

As is evident in Fig 4.6b, the presence of M-O species on the surface further improves the catalytic activity of Mn-substituted Ni_2P catalyst, reducing the overpotential (η) to 1.52 V (see Fig 4.6d). We find a similar effect of catalytic activity of the pristine Ni_2P surface (Fig 4.6a) for which η reduces from 2.62 to 2.1 V upon formation of M-O centers at its surface.

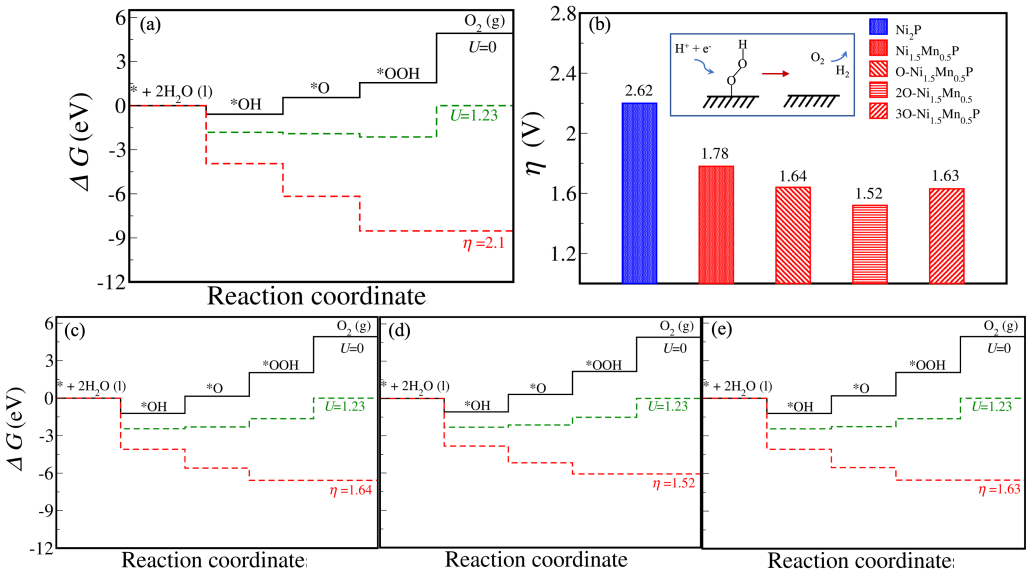

Figure 4.6: Standard free energy of intermediates along the path of oxygen evolution at U = 0 V and U = 1.23 V and the potential for which the potential-determining step becomes downhill, when catalyzed on (a) 2O-Ni_2P, (c) 1O-$Ni_{1.5}Mn_{0.5}P$, (d) 2O-$Ni_{1.5}Mn_{0.5}P$ and (e) 3O-$Ni_{1.5}Mn_{0.5}P$; (b) Reduction in overpotential upon introduction of M–O species in Ni_2P and $Ni_{1.5}Mn_{0.5}P$.

4.2.6 Conclusions

In summary we show an increase in the catalytic activity of Ni_2P on Mn substitution towards the overall water splitting. We find Mn substitution is stable in the (111) surface of Ni_2P and the energy gain increases with Mn concentration. $Ni_{1.5}Mn_{0.5}P$ exhibits close to optimal ΔG^H_{ads} of - 0.14 eV while pristine Ni_2P adsorbs H-atoms strongly ($\Delta G^H_{ads} \sim$ - 0.42 eV). Upon Mn substitution, the work function (ϕ) of Ni_2 also reduces from 5.12 eV to 4.78 eV further supporting its enhanced activity towards evolution of H_2. We also observe a reduction in the theoretical overpotential (η) towards OER upon Mn substitution in the (111) surface of Ni_2P ($\eta^{Ni_{1.5}Mn_{0.5}P}$ = 1.78 V and η^{Ni_2P} = 2.62 V) leading to its increased OER catalytic activity. Desorption of the *OOH to evolve O_2 is identified as the potential determining step for both pristine and Mn-substituted Ni_2P. We also show presence of M–O species on Ni_2P surfaces which further improves the catalytic activity of Mn-substituted Ni_2P catalyst, reducing η to 1.52 V. A similar effect on the activity of

pristine (111) surface of Ni_2P is observed for which η reduces to 2.1 V upon introduction of M–O centers.

4.3 Promotional Effect of Ni Substitution in Metal Carbides for HER †

Earth-abundant transition metal (TM) based phosphides [153, 154], carbides [155, 156], nitrides [157], borides [158], chalcogenides [159,160] have strongly emerged as a new class of low-cost and efficient electrocatalysts for HER and OER [161, 162]. Mo and W carbides [163] stand out owing to their noble metal-like electronic structure around the Fermi level [164], high electrochemical stability, and adaptability to various structural engineering techniques [139]. Some interesting approaches to improve the activities of pristine Mo and W carbide include, shape size modulation [165], active site enhancement, interface engineering [166], incorporating heteroatoms [167], alloying with secondary metals [168]. However, very few works exist for structurally engineered Mo and W carbides exhibiting highly efficient HER. Prof. Sebastian Peter's* group synthesized Ni substituted Mo and W carbide nanoparticles as potential HER catalysts as Ni is known for its superior HER activity in both acidic and alkaline media, valence electron-rich surface, and high charge-transfer characteristics. [169] We present first-principles theoretical analysis of enhancement of the catalytic activity of molybdenum and tungsten carbides (MoC and WC) towards HER on Ni substitution.

†This work has been published as S. Roy, D. Bagchi, L. Dheer, S. Ch. Sarma, V. Rajaji, C. Narayana, U. V. Waghmare, S. C. Peter, Mechanistic insights into the promotional effect of Ni substitution in non-noble metal carbides for highly enhanced water splitting, *Appl. Catal. B: Environ.* **298**, 120560 (2021) [152]. Reproduced with permission from Elsevier B.V.

*New Chemistry Unit, JNCASR

4.3.1 Computational details

Our first-principles calculations are based on density functional theory (DFT) as implemented in the Quantum ESPRESSO code [121] employing plane-wave basis and ultrasoft pseudopotentials [101] to represent the interaction between ionic cores and valence electrons. We adopt the exchange-correlation energy functional of Perdew-Zunger [95] obtained within a local density approximation (LDA). We smear the discontinuity in occupation numbers of electronic states with Fer-mi–Dirac distribution having a smearing width (k_BT) of 0.04 eV. An energy cutoff of 50 Ry is used to truncate the plane-wave basis used in the representation of Kohn-Sham wave functions and of 400 Ry to represent the charge density. Optimized structures were determined through minimization of energy until the Hellmann-Feynman force on each atom is smaller than 0.03 eV/Åin magnitude. We use a supercell to model surfaces, introducing a vacuum layer of 14.5 Åthickness parallel to the slab separating its adjacent periodic images. Each supercell contains a slab of 6 atomic planes of which, the bottom three atomic planes were kept fixed, and the top 3 were allowed to relax. We sampled Brillouin-zone integrations on a uniform grid of 6×6×1 k-points in the Brillouin zones of (100) and (101) surfaces of pristine and Ni substituted WC and MoC. The projected density of states of each structure was obtained from calculations on a denser, 15×15×1, k-point mesh. Calculated lattice constants of bulk WC (a_{WC} = 2.89 Å)and MoC (a_{MoC} = 2.88 Å) are within the typical LDA errors with respect to their observed values [122] (a_{WC} = 2.906 Åand a_{MoC} = 2.9 Å).

4.3.2 Energetics of WC and MoC with Ni substitution

Both WC and MoC occur in a hexagonal crystal structure (space group $P\bar{6}2m$) with two crystallographic sites: $1a$ and $1f$ Wyckoff sites occupied by W/Mo and C atoms, respectively. To assess feasibility of Ni substitution, we modelled a 3x3 supercell of (100) surfaces and a 3×2 supercell of (101) surfaces of WC and MoC, substituting Ni atoms at

the surface and in bulk like layers (Fig. 4.7), at the $1a$ site in $M_{54}C_{54}$ and $M_{32}C_{32}$ (M = W/Mo) respectively, and estimated formation energies using:

$$E_{form} = \frac{E_{M_{1-x}Ni_xC(100)/(101)} - [E_{M_C(100)/(101)} - xE_{Ni} + xE_M]}{x} \tag{4.11}$$

where $E_{M_{1-x}Ni_xC(100)/(101)}$, $E_{M_C(100)/(101)}$, E_{Ni} and E_M are the energies of Ni substituted (100)/(101) surface of MC, pristine MC (100)/(101) surface, and Ni and M atoms (M = Mo/W), respectively. Here, x is giving the fraction of M atoms substituted with Ni atoms.

	E_{form}(eV)/Ni atom			
Catalyst	100		101	
	10% Ni	20% Ni	10% Ni	20% Ni
WC	-0.57	-0.66	-1.01	-1.80
MoC	-0.69	-0.98	-1.01	-1.29

Table 4.3: Formation energy per Ni-atom substituted in (100) and (101) surfaces of MC (M = W/Mo).

As is evident from Table 4.3, Ni substitution at M sites ($1a$ Wyckoff site) of both (100) and (101) surfaces of MC is energetically favorable, and its stability improves with concentration.

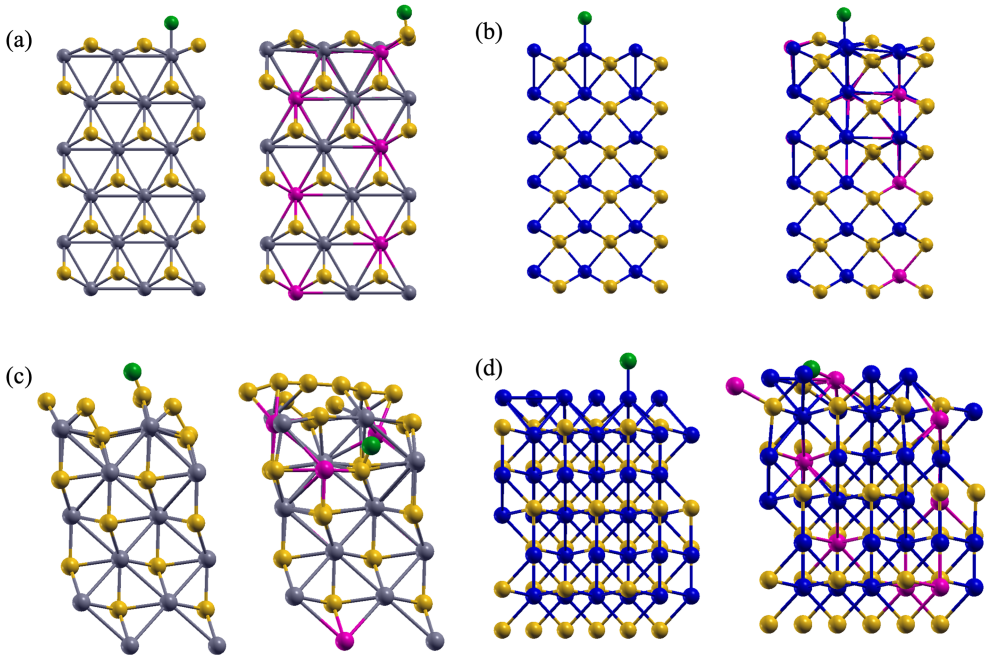

Figure 4.7: Optimized structures on H adsorbed on pristine (left) and Ni(20%) substituted (right) surfaces of (a) MoC (100), (b) WC (100) (c) MoC (101), (d) WC (101), surfaces. Magenta, blue, grey, yellow and green spheres correspond to Ni, W, Mo, C and H atoms respectively.

4.3.3 Catalysis of HER

To test the catalytic activity of surfaces of pristine and Ni substituted MC (M = W/ Mo), we have simulated adsorption of H-atom at various surface sites and determined the strength of its interaction with $M_{1-x}Ni_xC$ is determined using:

$$\Delta E_{ads} = E_{adsorbate+M_{1-x}Ni_xC} - (E_{M_{1-x}Ni_xC} + \mu_{adsorbate}) \tag{4.12}$$

where, $E_{adsorbate+M_{1-x}Ni_xC}$, $E_{M_{1-x}Ni_xC}$, $\mu_{adsorbate}$ are the energies of adsorbate locally stabilized on pristine/Ni-substituted MC (100) and (101) surfaces, pristine/Ni-substituted MC (100) and (101) surfaces and the adsorbate atom taken as, $\frac{1}{2}\mu_{H_2}$ respectively. We have estimated the Gibbs free energy of H adsorption (ΔG^H_{ads}), a descriptor of catalytic activity of surface towards HER using Eq. 4.12. Interaction of H with the surface having

vanishingly small ΔG^H_{ads} points to the optimal catalytic activity of the surface. Our simulations show that the interaction of adsorbate (H-atom) with (100) and (101) surfaces of pristine MC (Fig. 4.8) is relatively strong. For 10% Ni substituted MC, we find a slight reduction in the activity of the catalyst towards HER. However, the 20% Ni substituted MC surfaces exhibit a nearly optimum interaction with hydrogen. Out of the surfaces considered here, 20% Ni substituted WC (100), and MoC (101) surfaces exhibit the most optimal interaction of H-atom with, $\Delta G^H_{ads} \sim 0.3$ eV and 0.4 eV respectively.

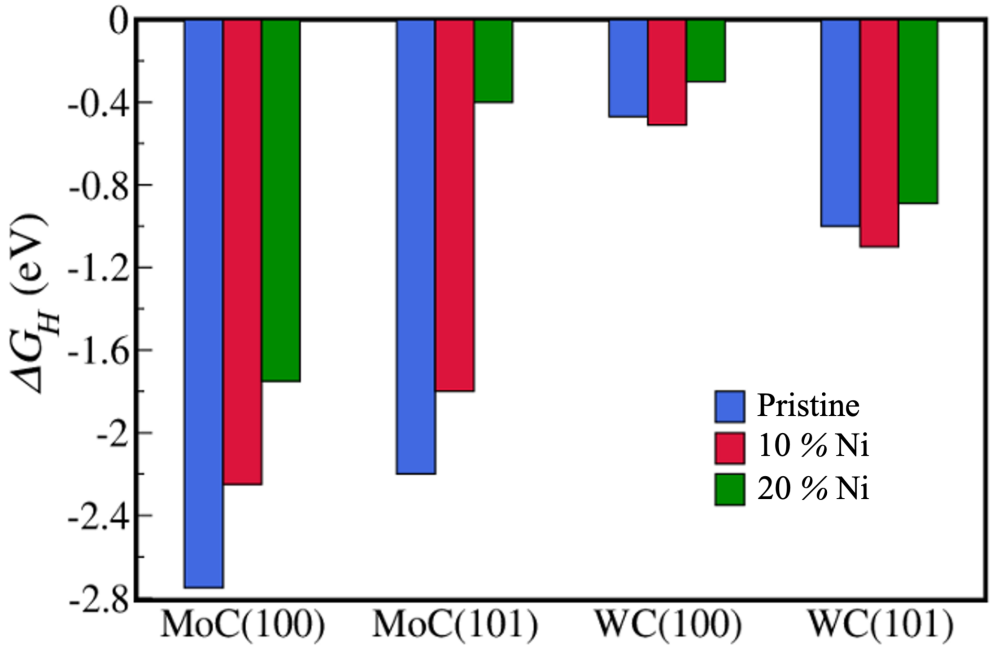

Figure 4.8: Free energy of hydrogen adsorption (ΔG_H) on pristine and Ni substituted (100) and (101) surfaces of MC (M = W/Mo). Blue, red, and green lines correspond to H-adsorption on pristine, 10% Ni-substituted, and 20% Ni-substituted surfaces, respectively.

4.3.4 Insights from electronic structure

The chemical nature of interaction between H and surfaces has been uncovered using the projected density of states (PDOS) (Fig. 4.9). For pristine (100) surface of MoC, the adsorbate orbital is degenerate (Fig. 4.9a), partially occupied, and has energy just below the Fermi level (E_F). The broad and split peak associated with the highest occupied atomic orbital (HOAO) of H shows a covalent interaction with the surface. PDOS of

H-atom adsorbed on pristine MoC (101) surface exhibits a sharp HOAO peak at an energy below E_F (Fig. 4.9b), denoting a more ionic nature of its interaction with the surface involving charge transfer. The HOAO of H-atom adsorbed on 20% Ni substituted (100) and (101) surfaces is deeper in energy than that on pristine surfaces (Fig. 4.9a, b), showing that H-atom interacts more weakly with the Ni-substituted surfaces. HOAO of H adsorbed on pristine (100)/(101) surfaces of WC, occurs at an energy just below E_F and is partially occupied, being degenerate with the W-6s and C-2s orbitals of the catalyst (Fig. 4.9c, d). As a result, it resonates and facilitates charge transfer from the catalysts' surfaces. H-atom adsorbed on 20% Ni substituted (100) exhibits a much broader HOAO peak, while the HOAO peak of H adsorbed on 20% Ni (101) lies much lower in energy, as expected. We estimated work functions (ϕ), a descriptor relevant to the catalytic activity of metals towards water reduction reaction [58], of the pristine, 20% Ni substituted (100) and (101) surfaces using Eq. 4.4. ϕ reduces upon with Ni substitution (Table 4.4),

	ϕ(eV)			
Catalyst	100		101	
	Pristine	20% Ni	Pristine	20% Ni
WC	5.85	5.63	5.71	5.40
MoC	5.41	4.54	4.81	4.62

Table 4.4: Work functions of pristine and Ni-substituted (100) and (101) surfaces of MC (M=W/Mo).

shifting the E_F close to HER potential (4.44 eV), thus increasing the catalytic activity of the metal carbides (WC and MoC) towards evolution of H_2.

4.3.5 Conclusions

We show that the catalytic activity of metal carbides (WC and MoC) increases with Ni substitution. Alloying the (100) and (101) surfaces of MC (M=W/Mo) with Ni is energetically favorable and its stability improves with Ni concentration. A close to optimal ΔG^H_{ads} is observed for 20% Ni substituted (100) and (101) surfaces of MC (M = W/Mo)

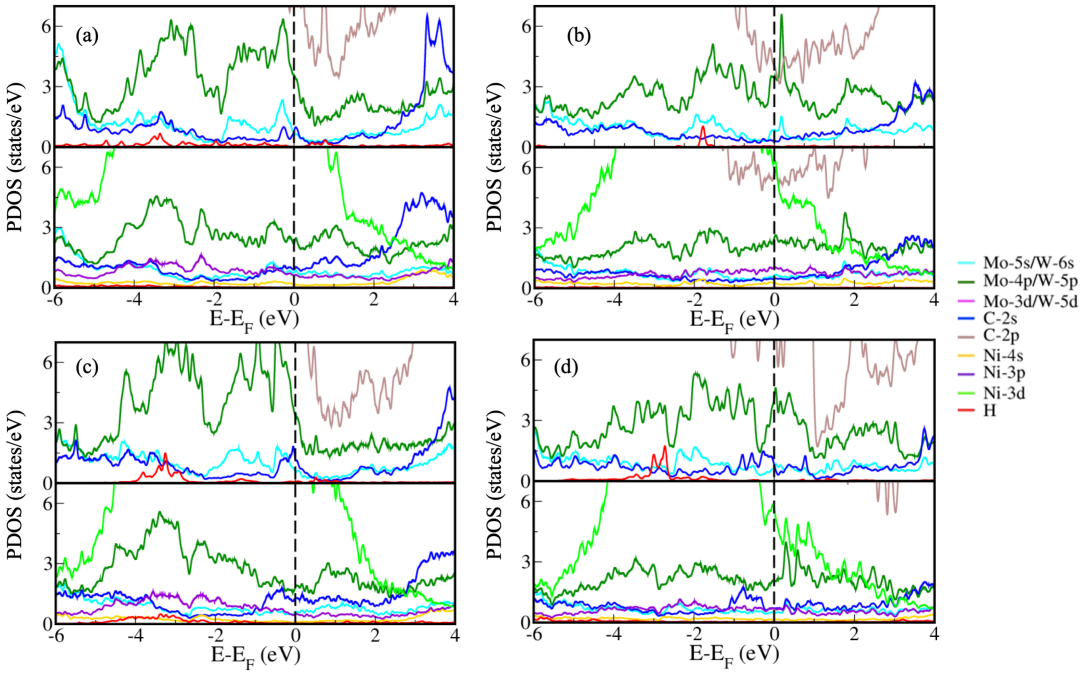

Figure 4.9: Projected density of states (PDOS) of structures with H-adsorbed on pristine (top) and 20% Ni-substituted surfaces (bottom) of (a) MoC (100), (b) MoC (101), (c) WC (100) and (d) WC (101) surfaces. Dashed black lines represent the Fermi level (E_F).

indicating an enhanced activity towards HER. The work function (ϕ) of the metal carbides (WC and MoC) reduces upon Ni substitution further supporting the increased HER activity.

Chapter 5

Site-Specific Activity of vdW Heterostructures of 1H-MoS_2 and Graphene with Substitutional N for Catalysis of HER[†]

5.1 Introduction

Graphene [170], a 2-dimensional sheet of sp^2 hybridized carbon atoms, initiated intense research activity in the field of 2D materials. In addition to exhibiting exceptional in-plane tensile strength [171] and a large specific surface area, graphene also exhibits properties such as high electrical and thermal conductivities [172, 173], good transparency [174], due to its unique electronic structure and high in-plane stiffness [175]. Being atomically thick, graphene serves as a perfect candidate to form hetero-structure with other 2D

[†]This work has been published as L. Dheer, S. Bhattacharjee, S. C. Lee, U. V. Waghmare, Van der Waals hetero-structures of 1H-MoS2 and N-substituted graphene for catalysis of hydrogen evolution reaction, *Mater. Res. Express* **6**, 124006 (2019) [30]. Reproduced with permission from the Institute of Physics.

materials. Another well studied 2D material is molybdenum disulfide (MoS_2) [176], a member of the family of Transition Metal Dichalcogenides (TMDCs). MoS_2 is widely used in solid-state lubrication, photovoltaic devices, and rechargeable batteries. [177] Bulk 2H-MoS_2 comprises of S-Mo-S monolayers which are held together by van der Waals interactions. [178]

Recently, exciting research has emerged in exploration of hetero-structures formed by stacking or adjoining different 2D materials together. [179] These 2D crystals can be coupled in a horizontal fashion creating an in-plane interface or by stacking them on top of one another forming a vertical hetero-structure. An attractive feature of these hetero-structures is that each layer acts as a bulk 2D materials and an interface simultaneously. [180] These vertical hetero-structures are held together by van der Waals interactions and are known to showcase novel interface-induced physical and chemical properties. [181] A particularly well-studied hetero-structure is graphene:MoS_2 hetero-structure [181–184] which was fabricated by Cheng *et al* [185]. This stacked hetero-structure has recently been exploited for its catalytic activity towards the hydrogen evolution reaction (HER). HER is the reduction involved in the water splitting reaction and gives hydrogen (H_2) as the product [111]. H_2, is an attractive fuel for storage of energy in the form of chemical energy. One of the challenges in use of H_2 is the scarcity of earth abundant materials to catalyse the conversion of protons (H^+) to H_2.

Li *et al* [186] showed that graphene layer as a support couples electrically with MoS_2 hence affecting the charge density distribution in MoS_2. The stacking leads to an in-built electric field in the hetero-structure resulting in excess negative charge on MoS_2 monolayer which improves its electrocatalytic activity towards HER. Similarly, a significant increase in the activity of inert MoS_2 surface was reported when graphene oxide (GO) was used as a support. [187] The catalytic activity of MoS_2 basal plane was influenced by the oxygen concentration in the GO. N-doping in the GO substrates further enhanced the catalytic

activity giving a $\Delta G_H \sim$ -0.014 eV. A recent report by Birjou *et al* [181] discussed the p-type doping effect of MoS_2 which promotes the H_2 adsorption on the graphene side of the graphene:MoS_2 hetero-structures.

Substitutional N-doping in graphene [188] is known to tune the electronic spectrum and enhance its properties for various applications [189]. While there have been many theoretical and experimental works on graphene:MoS_2 hetero-structures, [181,190–192] effects of N substitution in graphene on the catalytic and electronic properties of the hetero-structure have not been investigated yet.

Here, a detailed theoretical analysis of nitrogen (N)-doped graphene:MoS_2 bilayered hetero-structures,considering three different chemical types of N substituent: (i) Graphitic (G), (ii) Pyridinic (Pn), and (iii) Pyrrolic(Pr) is presented. Our focus is on the effects of chemical nature of N on the catalytic activity of graphene:MoS_2 hetero-structure. It is observed that the chemical type of substitutional N greatly influences the frontier electronic states of a hetero-structure whereas the interlayer binding and distance are about the same. Work function (ϕ) of the hetero-structure is thus dependent on the chemical type of N substituent; G N-atoms lower the i (n-type doping) while Pn and Pr N-atoms increase the ϕ (p-type doping) of the hetero-structure. Pr N-doped graphene:MoS2 hetero-structure is a direct narrow gap semiconductor with a band gap (E_g) value of $\sim$ 266 meV. Catalytic activity of graphene:MoS_2 towards HER enhances with N-substitution as the Gibbs free energy for hydrogen adsorption reduces from $\Delta G_H \sim$ 1.27 eV for pristine hetero-structure to $\Delta G_H \sim$ -0.2 eV and 0.295 eV for pyrrolic and graphitic N-doped graphene:MoS_2 hetero-structures.

5.2 Computational details

Our first-principles calculations are based on density functional theory (DFT) as implemented in the Quantum ESPRESSO [121] code, employing plane-wave basis and ultra-

soft pseudopotential [101] to represent the interaction between ionic cores and valence electrons. We use the exchange-correlation energy functional of Perdew-Burke-Ernzerhof (PBE) [99] within a generalised gradient approximation (GGA). We smear the occupation numbers of electronic states with Fermi–Dirac distribution and a smearing width (k_BT) of of 0.04 eV. We included van der Waals (vdW) interactions using Grimme scheme [135]. An energy cutoff of 40 Ry on the plane-wave basis is used in representation of Kohn-Sham wave functions, and of 320 Ry to represent the charge density. Structures are determined through minimization of energy until the Hellmann-Feynman forces on each atom are smaller than 0.03 eV/Åin magnitude. Hetero-structures between MoS_2 and N-substituted Gr are obtained using Virtual NanoLab (VNL). Each supercell comprises of 5×5 unit cells graphene stacked over 4×4 unit cells of MoS_2 amounting to a small lattice mismatch of 2.7%. A vacuum layer of 15 Åthickness is introduced parallel to the interface separating adjacent periodic images of the hetero-structure. We sampled Brillouin-Zone integrations on uniform grid of 5×5×1 K-points. The projected density of states for the hetero-structures was obtained from a much denser (11×11×1) k-point mesh. Calculated lattice constants of both 1H-MoS_2 (a_{MoS_2} = 3.19 Å) and graphene monolayer (a_{Gr} = 2.46 Å) are in good agreement with the respective experimental values [122, 193] ($a^{\circ}_{MoS_2}$= 3.16 Åand a°_{Gr} = 2.46 Å).

5.3 Constructing the hetero-structures

Lattices of MoS_2 and graphene monolayer have a nontrivial size mismatch. To construct a model hetero-structure, we place a 5×5 supercell of graphene on a 4×4 supercell of 1H-MoS_2 (Fig. 5.1a), with a C atom of graphene placed on top of one of the Mo atom of the MoS_2 sheet. It was previously shown that relative in-plane translation of graphene over the MoS_2 monolayer neither affects the energetics, nor the electronic properties of the system. [190] This is because local chemical environment of atoms averages out due to use of large supercell containing 5x5 units of graphene and 4x4 units of MoS_2. To determine

the properties of N-graphene:MoS_2 hetero-structure we considered three configurations: the 'graphitic' N corresponds to simply replacing a C atom by N atom in the graphene layer (Fig. 5.1b). In G N-graphene:MoS_2 we replace 6% C atoms of the graphene sheet with N atoms and place them far from each other to keep the interaction between the N atoms weak. The 'pyridinic' and 'pyrrolic' N, atoms which contribute one and two electrons each respectively to the π conjugated system. Pn N-graphene:MoS_2 comprises of three pyridine rings with 6% N-substitution and 2% vacancies in the graphene sheet creating a pyridine-like local chemical environment for N atoms (Fig. 5.1c). Similarly, the Pr N-graphene:MoS_2 structure is obtained with two N atoms inducing pyridine rings and one N atom forming a 5-membered pyrrole ring (Fig. 5.1d). A hydrogen (H) atom bonding with N atom is introduced to satisfy the valency of pyrrolic N substituent.

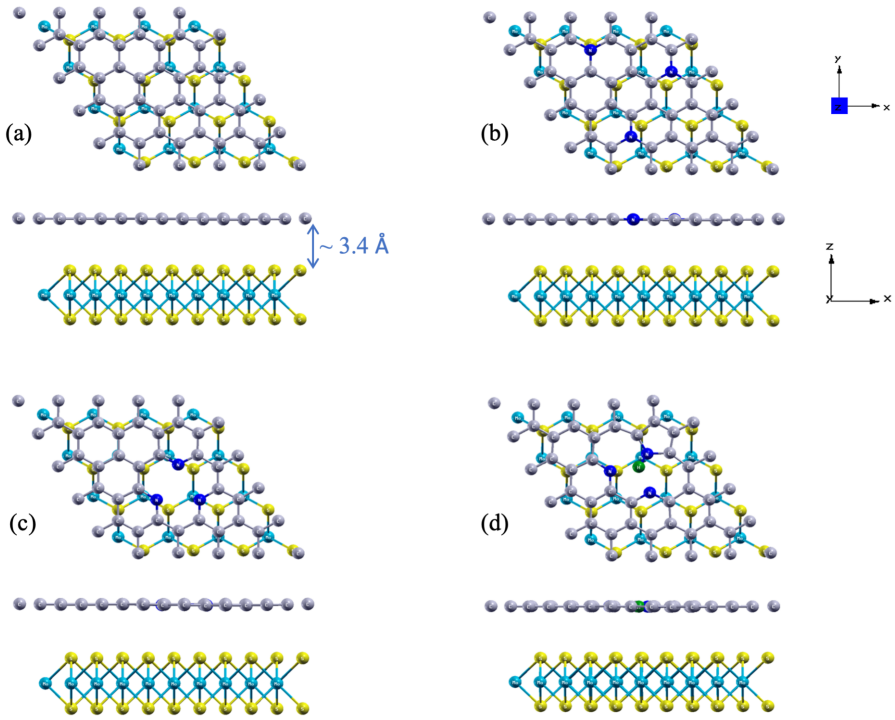

Figure 5.1: Top and side view of constructed hetero-structure, (a) Pristine graphene:MoS_2, (b) graphitic N-graphene:MoS_2, (c) pyridinic N-graphene:MoS_2, and (d) pyrrolic N-graphene:MoS_2. Grey, blue, cyan, yellow and green spheres represent C, N, Mo, S and H atoms respectively.

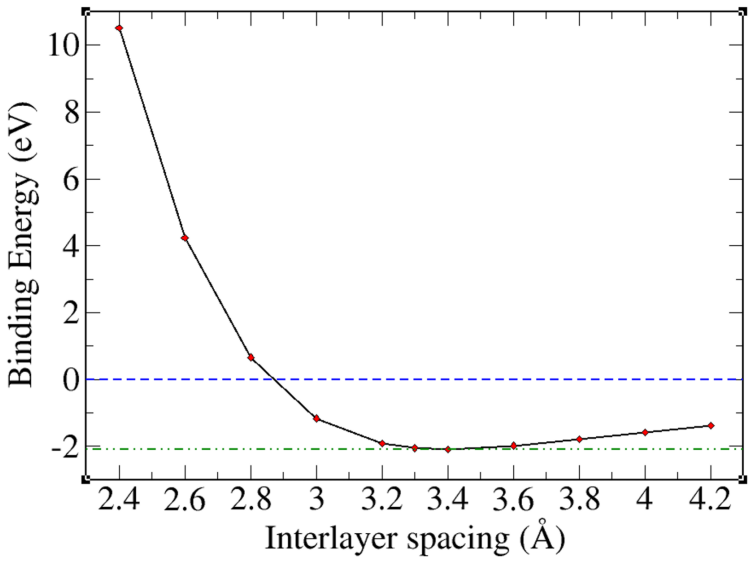

Figure 5.2: Binding energy (E_b) vs interlayer spacing between the two monolayers.

5.3.1 Interlayer spacing

The optimum interlayer spacing between the two monolayers is obtained by minimizing binding energy (E_b) between the N-doped/pristine graphene and MoS_2 monolayers:

$$E_b = E_{N-Graphene/pris:MoS_2} - (E_{N-Graphene/pris} + E_{MoS_2}) \tag{5.1}$$

where, $E_{N-Graphene/pris:MoS_2}$, $E_{N-Graphene/pris}$, and E_{MoS_2} are the energies of the hetero-structure, isolated N-doped/pristine graphene monolayer (5×5) and isolated 1H-MoS_2 (4×4), respectively. It is evident that the optimum separation is about 3.4 Å(Table 5.1) which is in good agreement with earlier reports [190] (Fig. 5.2). The vdW forces are almost solely responsible for the adhesion between the monolayers. Regardless of the chemical nature of substituted N, E_b changes by only about 10% showing that N-doping does not strongly affect the strength of adhesion of graphene sheet on MoS_2.

Hetero-structure	E_b/N_{MoS_2}(meV)	
	With vdW	Without vdW
Pristine graphene:MoS_2	-127	-4.7
Graphitic graphene:MoS_2	-131	-8.5
Pyridinic graphene:MoS_2	-123	-8.6
Pyrrolic graphene:MoS_2	-126	-8.6

Table 5.1: Interlayer binding energy (E_b) per MoS_2 formula units (N_{MoS_2}) calculated with vdW and without including vdW interactions.

5.4 Electronic properties

To understand the effect of chemical nature of N on the electronic properties of these graphene:MoS_2 hetero-structures, we determine the electronic structure and projected density of states (PDOS). Electronic structure of pristine graphene:MoS_2 hetero-structure is a simple superposition of electronic structures of each component. Graphene retains the linear dispersion of its bands and the Dirac point falls in the energy gap of 1H-MoS_2 (Fig. 5.3a). Interestingly, the Dirac point of graphene shows a tiny gap ($\sim$ 2.8 meV), consistent with previous reports [190,194] The orbitals of the C atoms of graphene contribute to states at energies between those of Mo-4d and S-3p orbitals as seen in the PDOS of the hetero-structure. Electronic structure of the graphene:MoS_2 hetero-structure changes with the chemical nature of N-substituents remarkably. Replacing three C atoms of 5×5 supercell of graphene with N atoms (graphitic N-substitution, Fig. 5.6b) results in donation of electrons causing the Fermi level E_F to shift up, imparting n-type character to the hetero-structure. States arising from N-substituents can be seen just above the E_F in the PDOS (Fig. 5.3b). With a small gap ($\sim$ 0.1 eV) opening up at the Dirac point, dispersion of bands at the Dirac point is parabolic in nature. This is evident in all the N-doped hetero-structures studied here irrespective of the chemical identity of N-atom.

Our configuration of graphitic N-substitution differs from that with pyridinic (Pn) N in the sense that in the former, N atoms are intentionally kept away from each other so as to lessen the N-N interaction. In Pn-N substitution, three N atoms are placed in close

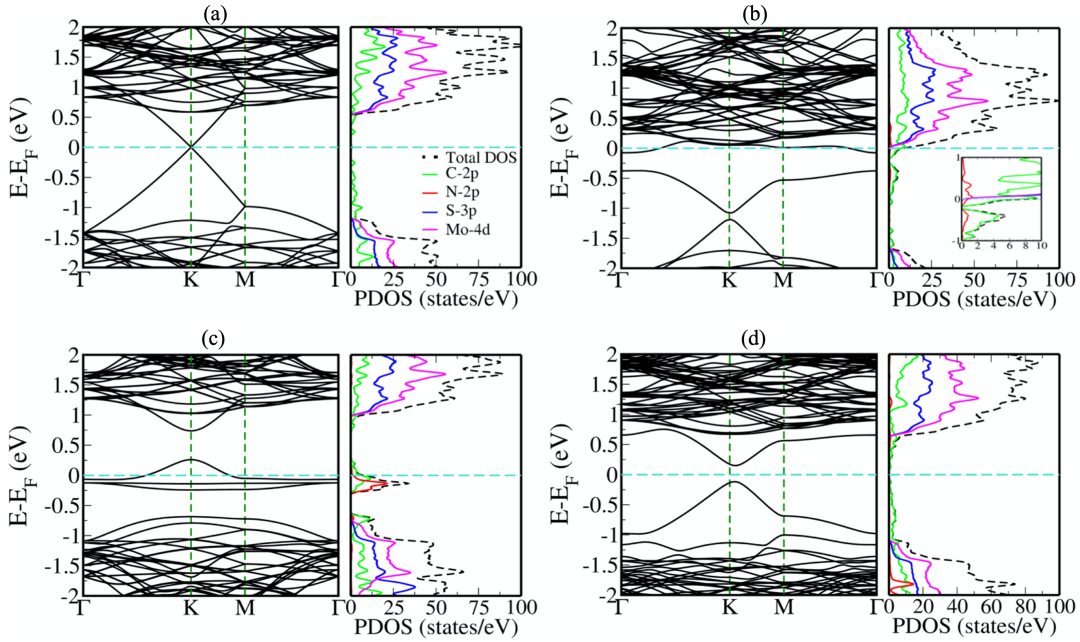

Figure 5.3: Electronic structure and projected density of states (PDOS) of (a) Pristine graphene:MoS_2, (b) graphitic N-graphene:MoS_2, (c) pyridinic N-graphene:MoS_2, and (d) pyrrolic N-graphene:MoS_2. An overlapping electronic structure of graphene and MoS_2 is observed (a), n-type character in graphitic N-doped graphene:MoS_2 (b), defect bands of N and p-type character in the valence band of graphene (c), and a gap opened up in graphene bands in (d). Doted cyan line denotes the Fermi level.

vicinity to each other and a vacancy defect is introduced at the centre of these dopants breaking the π conjugation and creating a pyridine ring like environment (Fig. 5.6c). Here, two of the five valence electrons of N participate in σ bonding with the neighboring C atoms while one contributes to π state within the pyridine ring. The remaining two electrons form a lone pair as the π conjugation is absent due to the vacancy adjacent to the dopants, and this lone pair gives rise to two new bands just below E_F. The Pn-N doping shifts the E_F down relative to the Dirac point, imparting effectively a p-type character to the hetero-structure (Fig. 5.3c). A gap ($\sim$ 0.48 eV) opens up at the Dirac point and the dispersion of resulting bands is parabolic.

Pr N-graphene:MoS_2 hetero-structure consists of two pyridine rings and one pyrrole ring in the supercell of graphene lattice (Fig. 5.6d). Pyrrolic-N atom uses three of its five valence electrons in σ bonding, two with C atoms and one with H atom, the remaining

two electrons are delocalized, imparting the pyrrole ring its aromatic nature. Therefore, the pyrrolic-N atom lends two electrons to the π conjugated system, imparting an n-type character to the system. Whereas two Pn- N atoms present in the sheet promote p-doping with downward shift in E_F as explained earlier. The opposite effects of the two types of N atoms cancel each other out resulting in a small band gap opening at the Dirac point, and thus Pr N-graphene:MoS_2 hetero-structure is a direct narrow band gap semiconductor with a E_F of $\sim$ 266 meV (Fig. 5.3d).

5.4.1 Work function

Further the work function (ϕ) which is defined as the minimum amount of energy required to remove an electron from a material to vacuum, and was recently shown to be relevant to the reactivity of the a catalyst is calculated. To estimate work functions of pristine, graphitic, and pyridinic N-graphene:MoS_2 hetero-structures the following expression is used:

$$\phi = V_{vac} - E_F \tag{5.2}$$

and for pyrrolic N-graphene:MoS_2

$$\phi = V_{vac} - E_{VBM} \tag{5.3}$$

where E_{VBM} and V_{vac} is the energy of the valence band maximum and vacuum energy respectively. ϕ (Table 5.2) is used to align the energies of band edges with respect to vacuum and hydrogen evolution potential (HER) to assess the suitability of these graphene:MoS_2 hetero-structures as catalysts for hydrogen evolution. Doping graphene with graphitic N-atoms reduces the ϕ of the hetero-structure, while Pn and Pr N-substitutions increase the ϕ. The hydrogen evolution potential (HER) is just below E_F of graphitic N-graphene:MoS_2, suggesting it to be a viable electrocatalyst for HER (Fig. 5.5). Pristine, Pn N-substituted and Pr N-substituted graphene:MoS_2 hetero-structures, due to ap-

propriate band edge energies, are predicted to be photocatalysts for HER (Fig. 5.5). To check the viability of the pristine and the N-substituted graphene:MoS_2 hetero-structures as photocatalysts, we obtained their optical conductivities. All the four hetero-structures show absorbance in the visible part of the spectrum, mainly blue-violet light, showing their suitability to use solar energy (Fig. 5.4a).

Hetero-structure	ϕ (eV)
Pristine graphene:MoS_2	4.5
Graphitic graphene:MoS_2	3.8
Pyridinic graphene:MoS_2	4.97
Pyrrolic graphene:MoS_2	4.7

Table 5.2: Work-functions of various graphene:MoS_2 heterostructures.

To understand the role of MoS_2 in the hetero-structures, we align the projected band edge energies of pristine and N-doped graphene monolayers on the SHE potential scale. As is evident here, MoS_2 support shifts E_F down and increases the work function of the pristine as well as N-substituted graphene monolayers (Fig. 5.5). To understand electronic properties at the graphene:MoS_2 interface of the hetero-structures, we examine the planar average charge density difference. Charge transfer across the interface between two monolayers (pristine/N-graphene and 1H-MoS_2) is evident as an excess negative charge accumulates on the 1H-MoS_2 monolayer (Fig. 5.4b). This leads to built-in electric field at the interface, consistent with the observation made by Li *et al.* Interestingly, the trend in charge transfer characteristics correlates with the ϕ of four hetero-structures studied here, i.e., higher the charge accumulation on the MoS_2 monolayer, lower the ϕ. For graphitic N-graphene:MoS_2, a relatively larger charge transfers from N-graphene to the MoS_2 monolayer, reflected in charge accumulation on the MoS_2 lattice, correlating with its low ϕ (Fig. 5.4b).

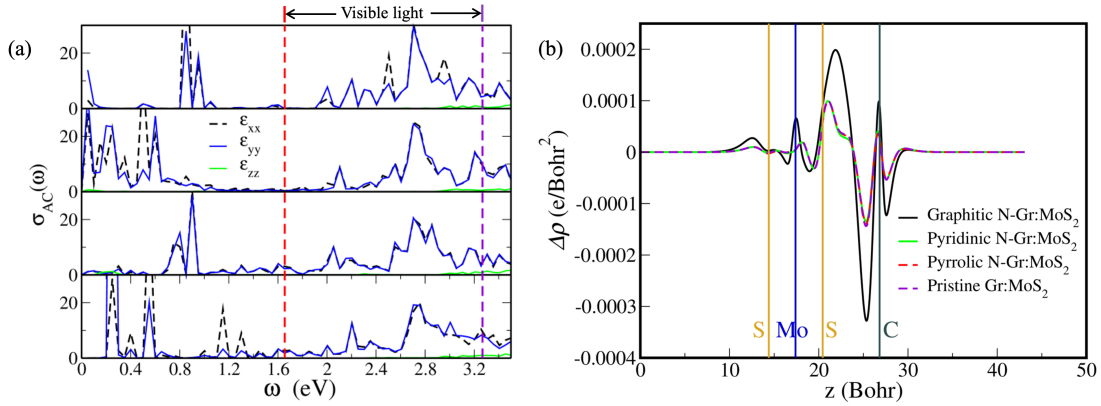

Figure 5.4: Imaginary part of dielectric constant of Pristine graphene:MoS_2, graphitic N-graphene:MoS_2, pyridinic N-graphene:MoS_2, and pyrrolic N-graphene:MoS_2 (top to bottom) as a function of frequency; (b) Calculated planar average charge density difference ($\Delta\rho$) as a function of distance along z-axis of the graphene:MoS_2 and N-doped graphene:MoS_2 hetero-structures.

5.5 Simulations of adsorption

To quantify the catalytic performance of the hetero-structures, the strength of adsorption of H-atom, H_2O molecule and OH at various adsorption sites on the N:graphene side of four hetero-structures is obtained. The interaction strength between the adsorbate and the surface is evaluated using:

$$\Delta E_{ads} = E_{complex} - (E_{hetero-structure} + \mu_{adsorbate}) \tag{5.4}$$

where, ΔE_{ads} is the adsorption energy and $E_{complex}$ $E_{hetero-structure}$ and $\mu_{adsorbate}$ are the total energies of adsorbate-heterostructure complex, hetero-structure, and chemical potentials of isolated adsorbate species (H-atom, OH and H_2O molecule), respectively. Here, $\frac{1}{2}\mu_{H_2}$ and μ_{H_2O} - $\frac{1}{2}\mu_{H_2}$, are taken as the chemical potentials of an isolated H-atom (μ_H) and OH (μ_{OH}), respectively. Doping graphene with N strengthens the hydrogen adsorption and the effect varies with the chemical nature of N dopant. Analysis of the PDOS of H-atom adsorbed on pristine and N-doped graphene:MoS_2 hetero-structure reveal the nature of interaction between the highest occupied molecular orbital (HOMO) of the adsorbate

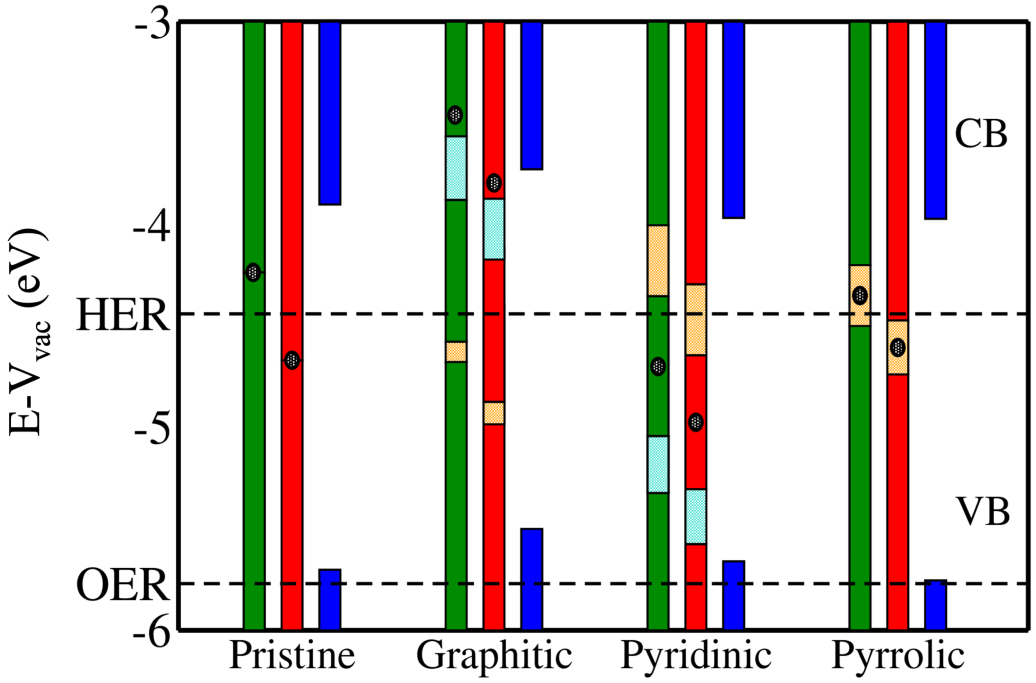

Figure 5.5: Energies of electronic band edges of N-substituted graphene monolayers (green) and of hetero-structures projected on to graphene (red) and MoS_2 (blue) aligned to vacuum and hydrogen evolution potential (HER) and oxygen reduction potential (OER). Black circles denote the Fermi energy. Yellow and cyan panels represent the band gaps at the K and Gamma points. Vacuum potential is set to 0 eV.

(H) with the bands of the catalyst (Fig. 5.8). The HOMO peak of adsorbate on pristine graphene:MoS_2 hetero-structure lies at E_F showing its weak interaction with the C-2p orbital of the substrate. In graphitic N-graphene:MoS_2, the HOMO of adsorbed H-atom is fully occupied and lies below the E_F. Also, the associated peak (HOMO) in PDOS splits and becomes broad showing its covalent interaction with the graphitic N-substituents. The HOMO peak of H-atom adsorbed on pyridinic N-graphene:MoS_2 hetero-structure is sharp and lies just above E_F, resonant with the N states, resulting in weaker adsorption. Relatively high ΔE^H_{ads} at sites 2, 3 and 4 of pyridinic N graphene:MoS_2 hetero-structure are due to the vacancy defect present in the graphene ring. H-atom adsorbs strongly at the N-atom vacancy site, and increases (in magnitude) the energy of adsorption (Fig. 5.7). The HOMO peak of H-atom attached to the pyrrolic N (dashed dark green peak) and the HOMO of adsorbed H, both lie much deeper in energy and resonate with the pyrrolic

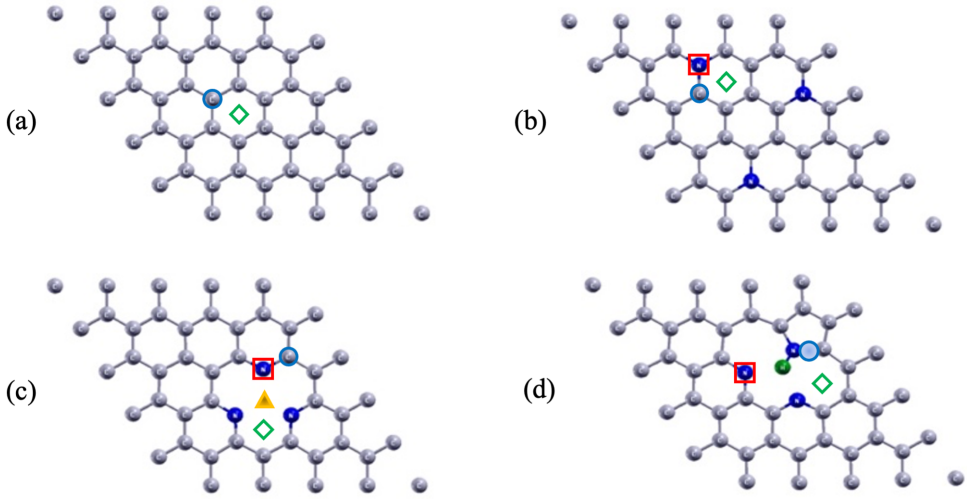

Figure 5.6: Schematic representation of (a) pristine graphene, (b) graphitic N-graphene, (c) pyridinic N-graphene, and (d) pyrrolic N-graphene. Carbon, nitrogen and hydrogen atoms are represented by grey, blue and green spheres respectively. Surface sites represented by blue-empty/filled circle, green diamond, red square and orange filled triangle, denote C-atom/C-N bridging site (site 1), hollow site at the center of the benzene ring (site 2), N-atom (site 3), and hollow site at the vacancy defect (site 4).

N-atom. The adsorbed H-atom, prefers to bind to the electron rich N site which leads to the H-atom attached to the pyrrolic N being pushed out of plane. This is also shown in the iso-surfaces of wave functions where the HOMO of the adsorbed H-atom is interacting with the N-2p orbital which enhances the strength of adsorption (Fig. 5.8b). The binding of H_2O to the graphene:MoS_2 hetero-structures remains relatively unaltered on introduction of N-substituents. Poisoning of the catalytically active sites by OH (in alkaline media) is unlikely for both pristine and N-substituted hetero-structures since ΔE_{ads}^{OH} is positive for all cases considered here (Table 5.3).

Adsorption of H_2O molecule on N-graphene monolayer was also simulated to get deeper understanding of role of MoS_2 on catalytic nature of the hetero-structure. The adsorption of H_2O molecule at the considered adsorption sites 1, 2 and 3 of Pn N-graphene was simulated. The interaction between the adsorbate and monolayer is weaker in magnitude as compared to hetero-structure.

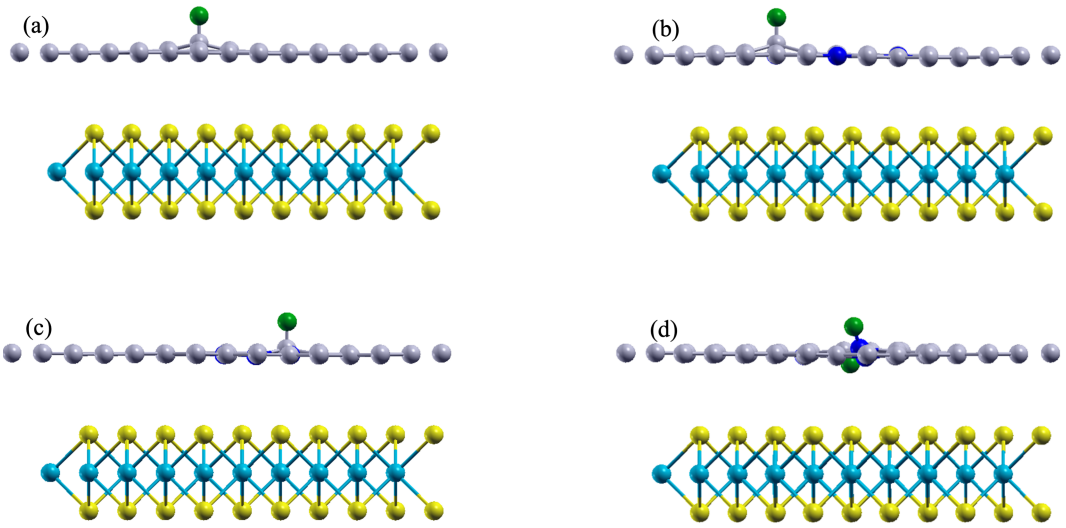

Figure 5.7: Optimized structures of H-adsorbed (a) pristine N-graphene:MoS_2, (b) graphitic N-graphene:MoS_2, (c) pyridinic N-graphene:MoS_2 and (d) pyrrolic N-graphene:MoS_2 at adsorption site 1. Grey, blue, cyan, yellow and green spheres represent C, N, Mo, S and H atoms respectively.

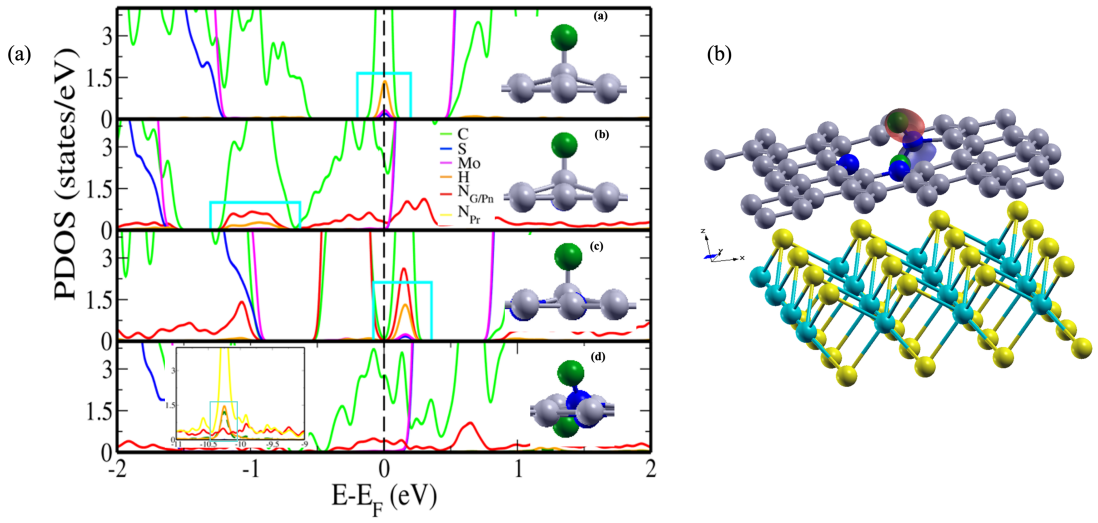

Figure 5.8: Projected density of states (PDOS) of H-atom adsorbed on (a) Pristine graphene:MoS_2, graphitic N-graphene:MoS_2, pyridinic N-graphene:MoS_2, and pyrrolic N-graphene:MoS_2 (top to bottom) at adsorption site 1. Inset shows optimized structures of H-adsorbed on respective hetero-structures. Dotted black line denotes the Fermi level. (b) Iso-surfaces of wave functions showing the highest occupied molecular orbital of H-atom interacting with N-2p orbital of the pyrrolic N-doped graphene:MoS_2 hetero-structure. Red and blue colors represent positive and negative iso-surfaces respectively. Cyan boxes show the HOMO of adsorbed H-atom. C, N and H atoms are represented by grey, blue and green spheres respectively.

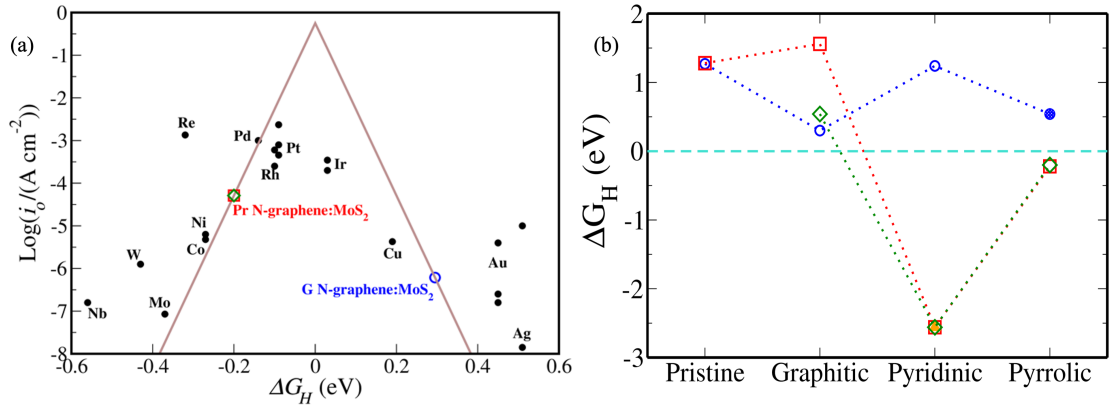

Figure 5.9: (a) Volcano plot of DFT-calculated Gibbs free energies of H adsorption and experimentally measured exchange current, Log (i_o). Plot recreated using data from [4]. The blue circle and red square/green diamond correspond to ΔG_H for graphitic and pyrrolic N-graphene:MoS_2 respectively; (b) ΔG_H at various sites of graphene:MoS_2 and N-doped graphene:MoS_2 hetero-structures.

Gibbs free energy of H adsorption (ΔG_H) has been widely used as a descriptor of catalytic activity towards HER, and its value close to zero is optimal. [124] To calculate ΔG_H, we use:

$$\Delta G_H = \Delta E^H_{ads} - T\Delta S_H + E^{ZPE}_H \tag{5.5}$$

where, ΔE^H_{ads} is the H-adsorption energy, $\Delta S_H = \frac{1}{2}S^\circ_{H_2}$, $S^\circ_{H_2}$ being the standard molar entropy of H_2 molecule and $E^H_{ZPE} = \frac{1}{2}E^{ZPE}_{H_2}$, $E^{ZPE}_{H_2}$ being the zero-point energy of an isolated H_2 molecule. At T as room temperature. i.e., 298 K, ΔG_H at site 1 of graphitic N-graphene:MoS_2 hetero-structure is $\sim$ 0.295 eV, while at sites 2 and 4 of pyrrolic N-graphene:MoS_2 hetero-structure is $\sim$ -0.20 eV (Fig. 5.9a). For H-adsorption on pristine graphene:MoS_2 hetero-structure, $\Delta G_H \sim$ 1.27 eV (Fig. 5.9b), which is comparable to the estimate reported recently by Birjou *et al.* [181] (ΔG_H = 1.45 eV).

5.6 Conclusions

It is concluded that the electronic properties of graphene:MoS_2 hetero-structures can be tuned with different chemical types of N-doping. The graphitic N-doped hetero-structure

Hetero-structure	Adsorption Site	ΔE_{ads} (eV)		
		H	OH	H_2O
Pristine graphene:MoS_2	1	1.33	2.26	-0.13
	2	1.34	2.8	-0.42
Graphitic graphene:MoS_2	1	0.36	0.9	-0.13
	2	0.6	1.26	-0.14
	3	1.6	2.04	-0.14
Pyridinic graphene:MoS_2	1	1.3	2.28	-0.17
	2	-2.5	1.62	-0.45
	3	-2.5	1.62	-0.45
Pyrrolic graphene:MoS_2	1	0.6	1.9	-0.17
	2	-0.14	2.83	-0.08
	3	-0.16	2.85	-0.21

Table 5.3: Energies of adsorption (ΔE_{ads}) of H, OH and H_2O on pristine and N-doped graphene:MoS_2 hetero-structures at various adsorption sites.

exhibits optimal band edge positions for reduction of H^+ to evolve H_2. Calculated Gibbs free energies of H adsorption (ΔG_H) show that N dopants strengthen the adsorption of H-atom on the hetero-structure, and nearly optimum interaction energies are obtained for graphitic and pyrrolic N-graphene:MoS_2 hetero-structures, $\Delta G_H \sim 0.295$ eV and $\Delta G_H \sim$ -0.20 eV, respectively. It is also show that using 1H-MoS_2 as a support strengthens the adhesion between the adsorbate (H_2O) and hetero-structure, and also imparts a p-type character to the hetero-structure. The graphene:MoS_2 hetero-structures are shown to be photocatalysts for HER due to suitable band edge energies and absorbance in the visible part of solar spectrum. Another subtle result is that a tiny gap ($\sim$ 2.8 meV) opens up at the Dirac point of pristine graphene over 1H-MoS_2, consistent with the reported value.These results offer useful insights into deciphering and enhancing catalytic activity of vdW hetero-structures by substitutional doping.

Part II

Carbon Dioxide Reduction and Utilization

Chapter 6

Selective Conversion of CO_2 to Methanol on Ni_3In[†]

6.1 Introduction

Anthropogenic carbon dioxide (CO_2) emissions have increased the CO_2 concentration in the atmosphere from pre-industrial levels of 280 ppm to 412 ppm in 2020. [12] Efficiently transforming CO_2 into useful fuels can revolutionize large-scale renewable energy storage while mitigating environmental damage due to carbon emissions. [196, 197] One potential strategy to curtail the alarming CO_2 levels in the atmosphere is to use scalable thermocatalytic hydrogenation of captured CO_2 to produce energy dense fuels of importance to the material value chain. Methanol (MeOH), is one such fuel because of its high octane number. [198] It can be directly used as additive to gasoline in internal combustion engines or its derivatives such as dimethyl ether (DME). [199, 200] It is also an essential starting material for the production of several multicarbon products, including alcohols, ethers, esters,

[†]This work has been published as A. Cherevotan, J. Raj, L. Dheer, S. Roy, S. Sarkar, R. Das, C. P. Vinod, S. Xu, P. Wells, U. V. Waghmare, S. C. Peter *ACS. Energy Letters* **6**, 509-516 (2021) [195]. Reproduced with permission from the American Chemical Society.

olefins, and alkanes. [201, 202] The catalytic conversion of CO_2 to methanol (CTM) via a thermochemical route of hydrogenation has been investigated since the early 1990s. [203] Currently, $CuO/ZnO/Al_2O_3$(CZA) is the state-of-the-art catalyst used for CTM in high pressuretemperature regimes. [204] Many advances in catalyst design have been made to facilitate the hydrogenation of CTM. [205–209]

A relatively new area in CTM catalyst engineering has seen the advent of transition-metal-based bimetallic or intermetallic catalysts (IMCs). [210, 211] Even in the state-of-the-art CZA system, interfacial Cu-Zn alloy is speculated to be the active site for CTM under the reaction conditions. [212–214] Given the role bimetallic alloys in various catalytic processes, such as CuZn in CTM, recent studies have explored the possibilities of their ordered IM variants. [215–217] In this work, Prof. Sebastian Peter's* group discovered a novel non-noble metal based IMC comprising Ni and In atoms, Ni_3In, through in situ. stabilization of kinetic NiIn phase that selectively yields MeOH as the product.

6.2 Computational details

Our first-principles calculations are based on density functional theory (DFT) as implemented in the Quantum ESPRESSO code [121] employing plane-wave basis and ultra-soft pseudopotentials [101] to represent the interaction between ionic cores and valence electrons. We adopt the exchange-correlation energy functional of Perdew-Burke-Ernzerhof (PBE) [99] obtained within a generalized gradient approximation (GGA). We smear the discontinuity in occupation numbers of electronic states with Fermi–Dirac distribution having a smearing width (k_BT) of 0.04 eV. An energy cutoff of 50 Ry is used to truncate the plane-wave basis used in representation of Kohn-Sham wave functions, and of 400 Ry to represent the charge density. Optimized structures were determined through minimization of energy until the Hellmann-Feynman force on each atom is smaller than

*New Chemistry Unit, JNCASR

0.03 eV/Å in magnitude. We use a supercell (2×2) to model the (111) surface of Ni_3In ($Ni_{48}In_{16}$) introducing a vacuum layer of 15 Åthickness parallel to the slab separating its adjacent periodic images. Each supercell contains a slab of 4 atomic planes of which, the bottom 2 atomic planes were kept fixed and the top 2 were allowed to relax (FIg. 6.1). We sampled Brillouin-zone integrations on uniform grid of 6×6×1 k-points in the Brillouin zone of (111) surface of Ni_3In. The projected density of states of each structure was obtained from calculations on a denser, 15×15×1, k-point mesh. Calculated lattice constants of bulk Ni_3In are within the typical GGA errors with (a_{Ni_3In} = 3.74 Å) respect to their observed values [122] ($a^{\circ}_{Ni_3In}$ = 3.73 Å). Relative energies of the intermediate steps were plotted taking pristine Ni_3In (111) surface + CO_2 + $3H_2$ as the reference. We simulated adsorption of various intermediates occurring during the CO_2 reduction reaction (CO_2RR) and calculated their adsorption energies using

$$\Delta E_{ads} = E_{adsorbate+Ni_3In} - (E_{Ni_3In} + \mu_{adsorbate}) \tag{6.1}$$

where, $E_{adsorbate+Ni_3In}$, E_{Ni_3In}, $\mu_{adsorbate}$ are the energies of adsorbate locally stabilized on Ni_3In (111) surface, bare Ni_3In (111) surface and the adsorbate molecule, respectively. The transition states (TSs) were obtained using the nudged elastic band (NEB) [107] method. Five images were used in all the NEB calculations in this paper. All transition states were fully relaxed until the Hellmann–Feynman forces acting on the atoms were within 0.05 eVÅ^{-1}.

6.3 CO_2 reduction to CH_3OH on Ni_3In

Ni_3In possesses a cubic crystal structure (space group $Pm\bar{3}m$) with In at the corners of the cube (1a Wyckoff site), and Ni atoms lying on the face centres (3c Wyckoff site). To probe the underlying mechanism of CTM on Ni_3In, we modelled a 2×2 supercell of the (111) surface of Ni_3In ($Ni_{48}In_{16}$) (Fig. 6.1). Eight CO_2 hydrogenation pathways

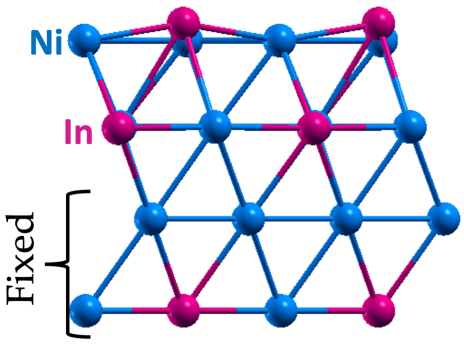

Figure 6.1: Optimised structure of (111) surface of Ni_3In. Ni and In atoms are represented by blue and magenta spheres respectively.

(HCOO, CO hydrogenation,*trans*-COOH, and *cis*-COOH) (see Fig. 1.7) were analyzed by determining their reaction energies to pinpoint the most feasible pathway for CTM conversion on Ni_3In. All intermediates occurring on various CO_2 reduction pathways, with the exceptions of CH_3O and *bi*-HCOO, stabilize in configurations of adsorption at the surface Ni sites (Fig. 6.2) indicating Ni atoms to be the active centers of (111) surface of Ni_3In. Energy landscape plots show that the initial and final steps, i.e., adsorption of CO_2 and desorption of CH_3OH, are both non spontaneous and exhibit an energy cost of ∼0.11 and ∼0.25 eV respectively. The thermodynamically most feasible CO_2 reduction pathway has the lowest energy barrier associated with the potential-determining step (PDS). In the context of a thermocatalytic reaction, PDS gives a measure of thermodynamic energy barrier. As is evident in Fig. 6.3, the CO hydrogenation pathway is energetically most expensive, and formation of $^*CO$ molecule from adsorbed $^*CO_2$ species is the PDS (ΔE = 0.9 eV). For the *trans*-COOH pathway, hydrogenation of $^*COH$ to form **trans*-HCOH is the PDS with an energy barrier of 0.82 eV. Both *cis*-COOH and formate pathways exhibit similar energy barriers of 0.25 eV, wherein the final step, i.e., desorption of CH_3OH, is the potential-determining step. To conclusively determine the most feasible pathway, we estimated the energy of second elementary step in *cis*-COOH and formate pathways, i.e.

$$CO_2 + 3H_2 \rightarrow {}^*bi - HCOO + H + 2H_2 \tag{6.2}$$

$$CO_2 + 3H_2 \rightarrow {}^{*}trans - COOH + H + 2H_2 \tag{6.3}$$

Formation of *bi*-HCOO from CO_2 adsorbed on the (111) surface of Ni_3In is quite spontaneous ($\Delta E = 0.53$ eV) and more exothermic than that of its competing intermediate, *trans*-COOH, occurring in the *cis*-COOH pathway ($\Delta E = 0.32$ eV). Also, both intermediates show a bidentate attachment to the (111) surface; however, the chemical bonds formed by the adsorbates with Ni_3In are distinct: Ni-O and In-O in the case of *bi*-HCOO (Fig. 6.2); Ni-C and Ni-O bonds (Fig. 6.2) in the case of *trans*-COOH. The fact that In does not bind with *trans*-COOH suggests that Ni_3In will prefer *bi*-HCOO.

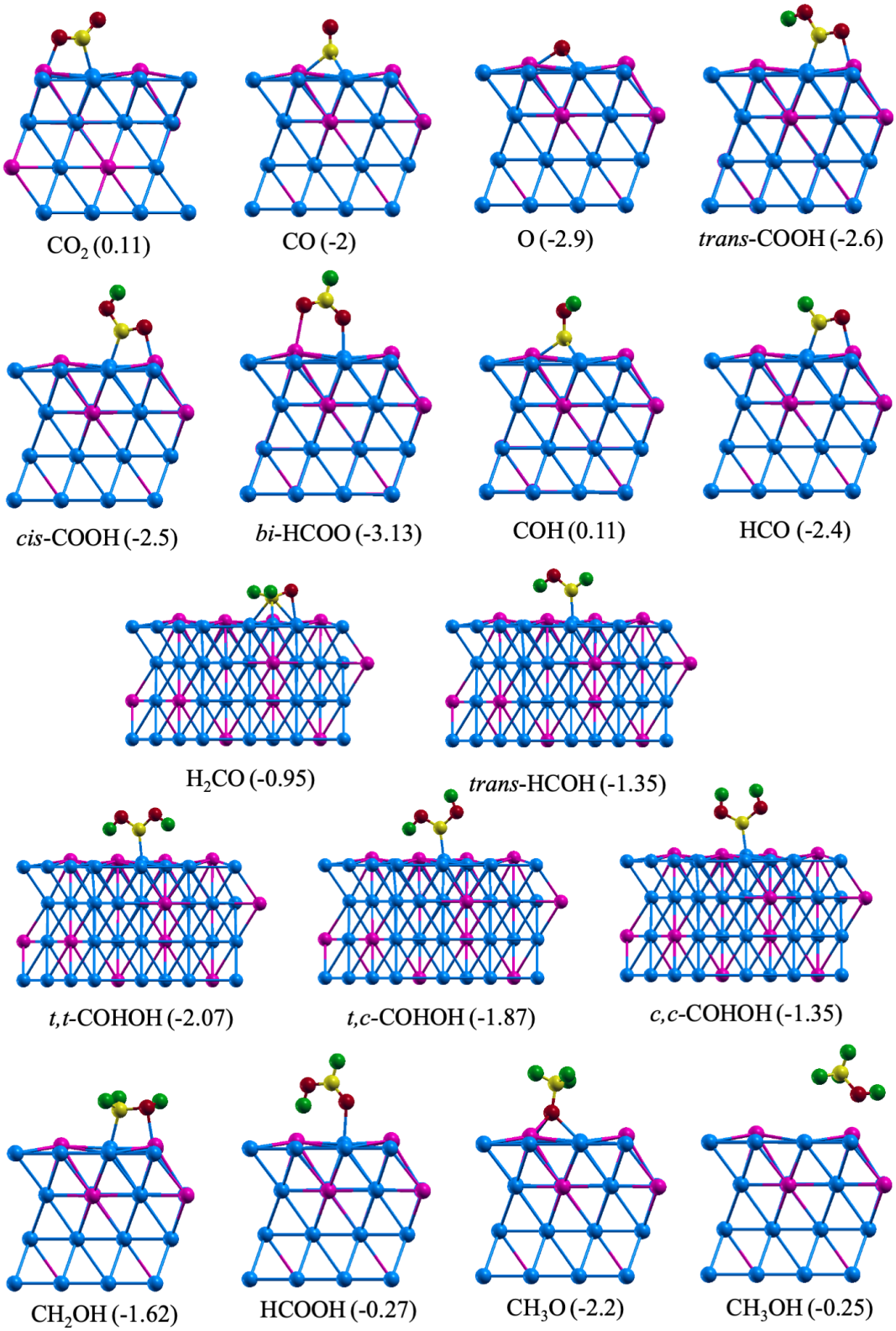

Figure 6.2: Optimized structures and binding energies of various intermediates occurring via various CO_2 hydrogen pathways on Ni_3In (111) surface. Magenta, blue, red, green and yellow spheres correspond to In, Ni, O, H and C atoms respectively. Binding energies are in eV.

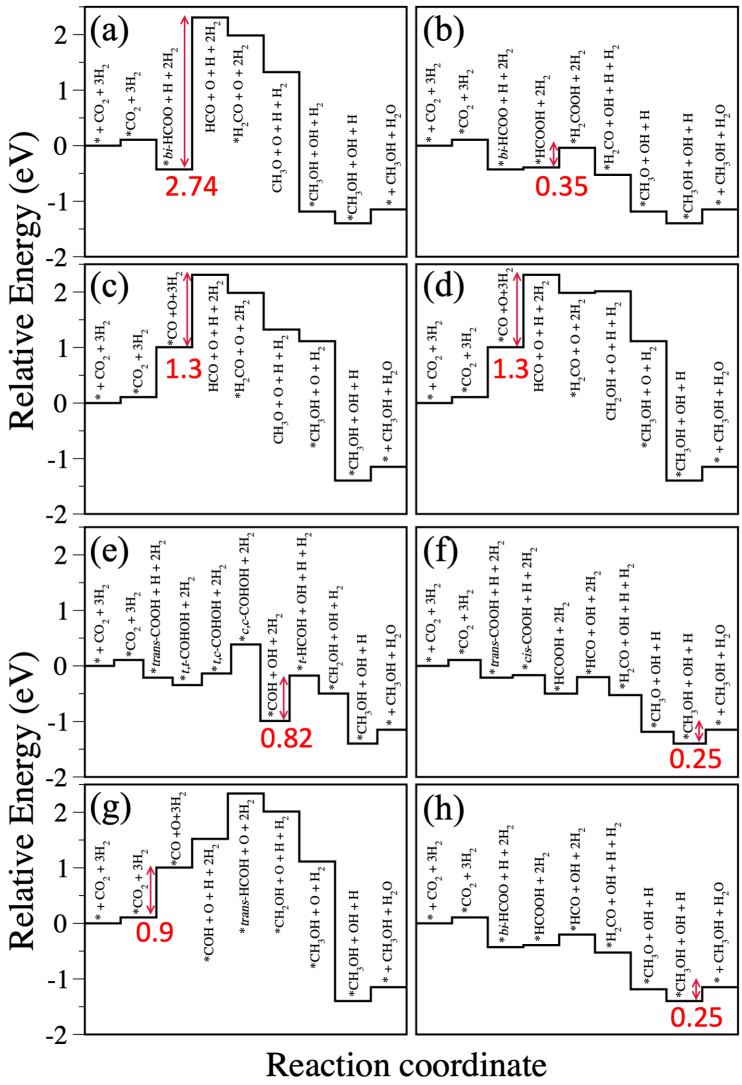

Figure 6.3: Relative energy diagrams of CO_2 to methanol conversion on Ni_3In occurring via (a) HCOO (2), (b) HCOO (3), (c) CO-hydrogenation (2), (d) CO-hydrogenation (3), (e) *trans*-COOH, (f) *cis*-COOH, (g) Co-hydrogenation and (h) *bi*-HCOO pathway. Red double headed arrows represent the energetically most expensive elementary step along each pathway. All values are in eV.

6.4 Insights from electronic structure

To shed light on the nature of bonding between intermediates and the catalyst, we examine the projected density of states (PDOS) of the first intermediates occurring along the formate and *cis*-COOH pathways of CO_2 reduction on the (111) surface of

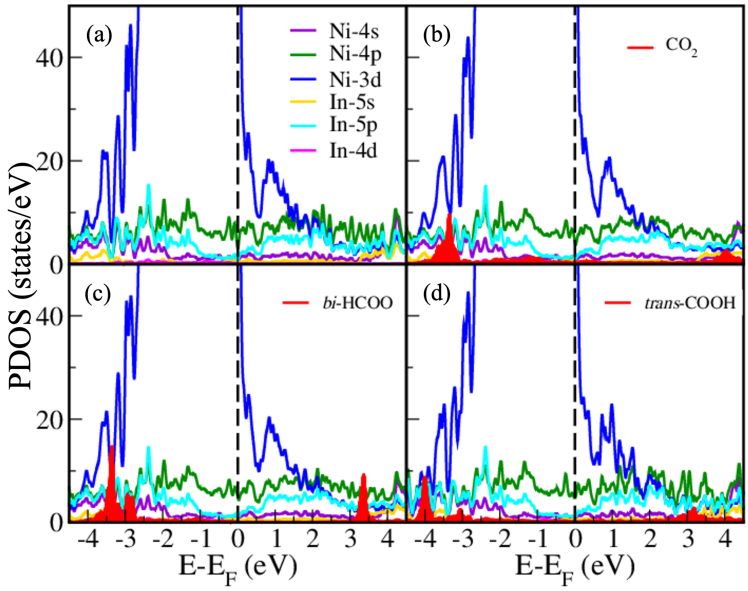

Figure 6.4: PDOS of (a) pristine Ni_3In (111) surface and (b) CO_2, (c) *bi*-HCOO and (d) *trans*-COOH adsorbed on Ni_3In (111) surface. Dashed black line represents the Fermi energy.

Ni_3In: *bi*-HCOO*Ni_3In and *trans*COOH*Ni_3In, respectively (Fig. 6.4). The PDOS of *bi*-HCOO*Ni_3In and *trans*-COOH*Ni_3In reveal the highest occupied molecular orbitals (HOMO) of the adsorbates lie close to the bottom of the 3d-bands of Ni. HOMO of **bi*-HCOO exhibits a sharp peak close to -3.5 eV, (similar to HOMO of $^*CO_2$) accompanied by another smaller peak at a slightly higher energy. The degeneracy in the HOMO peaks is because of charge transfer from the surface to the adsorbate (Fig. 6.4), which is also evident from the Lowdin charges that show a reduction the occupancy of Ni-3d and In-5s orbitals and an increased occupancy of O-2p orbitals of both the O-atoms of HCOO (Table 6.1). Also, HOMO of *bi*-HCOO splits and broadens because of its covalent interaction with the In-5p and Ni-4p orbitals of the catalyst, which are in resonance. HOMO of **trans*-COOH lies deeper in energy and resonates with Ni-3d, Ni-4p and In-5p orbitals of the surface. Lowdin charge analysis shows a charge transfer from the Ni_3In surface to the adsorbate. We find a decrease in the number of electrons in Ni-3d states due to transfer to C-2s and C-2p orbitals (Table 6.1).

Sample	Atom	Valence e⁻s			Total valence e⁻s	Valence e⁻s in PP
		s	p	d		
	Ni	0.42	0.99	8.8	10.21	$4s^2 3d^8$ (10)
Ni_3In	In	0.8	1.46	9.94	12.2	$5s^2 4d^{10} 5p^1$ (13)
Isolated	C	0.74	2.46	0	3.2	$2s^2 2p^2$ (4)
CO_2	O	1.66	4.61	0	6.17	$2s^2 2p^4$ (6)
	Ni_C	0.42	**1.09**	**8.76**	10.27	$4s^2 3d^8$ (10)
Ni_3In	Ni_O	0.4	1.03	**8.72**	10.15	$4s^2 3d^8$ (10)
CO_2	In	0.79	1.44	9.94	12.17	$5s^2 4d^{10} 5p^1$ (13)
adsorbed	C	**0.88**	2.61	0	3.49	$2s^2 2p^2$ (4)
	O	1.63	4.64	0	6.27	$2s^2 2p^4$ (6)
Ni_3In	Ni_{O1}	0.4	1.06	**8.72**	10.15	$4s^2 3d^8$ (10)
bi-HCOO	In_{O2}	**0.73**	1.44	9.94	12.17	$5s^2 4d^{10} 5p^1$ (13)
adsorbed	O1	1.66	**4.73**	0	6.39	$2s^2 2p^4$ (6)
	O2	1.61	**4.71**	0	6.32	$2s^2 2p^4$ (6)
	Ni_C	0.4	**1.19**	**8.72**	10.34	$4s^2 3d^8$ (10)
Ni_3In	Ni_O	0.39	1.02	**8.74**	10.15	$4s^2 3d^8$ (10)
*trans*COOH	In	0.79	1.44	9.95	12.17	$5s^2 4d^{10} 5p^1$ (13)
adsorbed	C	**0.97**	2.6	0	3.57	$2s^2 2p^2$ (4)
	O	1.63	4.34	0	6.26	$2s^2 2p^4$ (6)

Table 6.1: Calculated Lowdin charges of Ni, In, C and O atoms for (a) pristine (111) surface of Ni_3In, (b) isolated CO_2 molecule, and (c) CO_2, (d) *bi*-HCOO and (e) *trans*-COOH adsorbed on the (111) surface of Ni_3In, respectively.

6.5 Kinetics of CTM

To comment on the kinetics of the CTM conversion on the present catalyst, we determined the activation energy barriers for each elementary step along the *cis*-COOH and *bi*-HCOO pathways using the nudged elastic band (NEB) method. These pathways are very similar and differ only in the initial intermediates. From this analysis, we find the following step to be the rate-determining step with activation energy barrier of 1.2 eV (Fig. 6.5):

$$^*HCO + {}^*OH + 2H_2 \rightarrow {}^*H_2CO + {}^*OH + H + H_2 \tag{6.4}$$

However, the formation of the first intermediate, i.e., *trans*-COOH and *bi*-HCOO along the carboxylic acid and formate pathways, respectively, have different activation energy barriers associated with them. Formation of *bi*-HCOO from adsorbed CO_2 has an activation energy of 0.57 eV, while the *trans*-COOH intermediate requires crossing of energy barrier of 0.83 eV to form. Hence, the activation energy barrier and the thermodynamic reaction energies of the second elementary step in carboxylic acid and formate pathways conclusively show the latter to be more feasible. Therefore, CTM conversion on Ni_3In is most feasible via the formate pathway because of its low energy barrier and thermodynamically spontaneous hydrogenation of CO_2 to yield *bi*-HCOO.

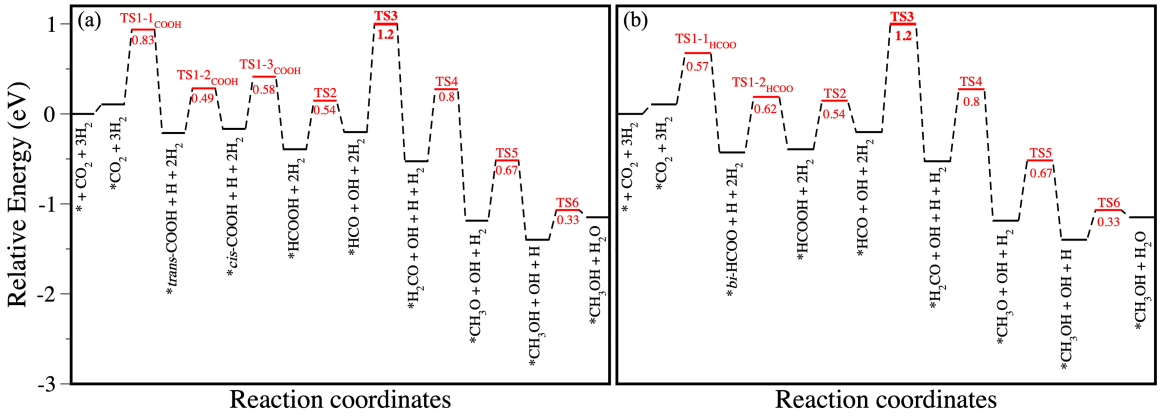

Figure 6.5: Relative activation energy diagrams of CO_2 to methanol conversion on Ni_3In occurring via (a) *cis*-COOH and (b) *bi*-HCOO pathway. Black and red bars denote the intermediates and transition states along the CO_2 hydrogenation pathways. TS3 (transition state 3) is the kinetic bottleneck along both pathways, while the desorption of CH_3OH is the thermodynamically most energy demanding step (denoted by blue double headed arrows). All values are in eV.

6.6 Conclusions

In conclusion, we show Ni_3In exhibits excellent catalytic activity towards hydrogenation of CO_2 and selectively generates MeOH as the product. We analyzed eight reaction pathways for CO_2 reduction to MeOH and showed *cis*-COOH and formate pathway to be thermodynamically most feasible with an energy cost of 0.25 eV. Desorption of the product

(MeOH) is identified as the potential determining step for both *cis*-COOH and formate pathways. We further show that formation of the first hydrogenated intermediate along the formate pathway (*bi*-HCOO) is more exothermic than the intermediate along the *cis*-COOH pathway (*trans*-COOH) . We examined the projected density of states (PDOS) of *bi*-HCOO*Ni$_3$In and *trans*-COOH*Ni$_3$In, which further show that *trans*-COOH interacts only with Ni atoms on the surface while *bi*-HCOO exhibits charge transfer from both Ni and In atoms. Finally, we calculated the activation energies along *cis*-COOH and formate pathways and show the latter to be more feasible for CTM.

Chapter 7

Efficient Electrooxidation of CH_3CH_2OH on Ni-doped Pd_2Ge[†]

7.1 Introduction

The demand for energy has been tremendously increased because of high population and industrial growth. It is essential to find alternative resources to control global energy demands and minimize global warming. Liquid fuels such as methanol, ethanol, and glycerol are regarded as the promising alternatives because alcohol fuels are easily transportable and easy to handle, have outstanding efficiency, and can be produced from abundant biomass. [219–222] Ethanol is preferred over methanol for energy conversion because it is less toxic, highly abundant, and cost-effective; it has high energy density (methanol 4.8 kWh/L, ethanol 6.3 kWh/L) at low potential; and it can offer 12 electrons in a single oxidation reaction because of C-C bond cleavage of ethanol. The energy produced from a direct ethanol fuel cell (DEFC) is theoretically higher than the novel direct methanol

[†]This work has been published as A. R. Rajamani, P. C. Ashly, L. Dheer, S. Ch. Sarma, S. Sarkar, D. Bagchi, U. V. Waghmare, S. C. Peter, *ACS. Appl. Energy Mater.* **2**, 7132-7141 (2019) [218]. Reproduced with permission from the American Chemical Society.

fuel cell (DMFC). [223–225] However, ethanol being a C2 molecule, its electrocatalysis is constrained with sluggish oxidation kinetics because of difficulty in CC bond cleavage and ultimately poor poison tolerance. [226]

Electrooxidation of ethanol can be done in either acidic or alkaline medium. Over the past decade, extensive attention has been given to the electrooxidation in acidic media, and significant progress has been made in their development. [227] Recently, enormous attention has also been paid to ethanol oxidation in alkaline media. Pd-based catalysts are less expensive and have comparable or even better electrocatalytic activities than Pt-based catalysts. [228–231] In a previous work, Prof. Sebastian Peter's group studied the electrocatalytic activity of Pd_2Ge intermetallic catalyst for ethanol oxidation reaction (EOR), which showed better activity than Pd/C. [232] In this work, Prof. Sebastian Peter's* group synthesized $Pd_{2-x}Ni_xGe$ (x = 0, 0.2, 0.4, and 0.5) with varied Pd/Ni compositions by a solvothermal method. Optimization of Pd/Ni composition and structural arrangement of Ni substitution in Pd sites gives high ethanol electrooxidation activity and tolerance against intermediate products. In this chapter, we aim to understand the role of Ni-substituents in experimentally observed enhanced catalytic activity of $Pd_{2-x}Ni_xGe$.

7.2 Computational details

Our first-principles calculations are based on density functional theory (DFT) as implemented in the Quantum ESPRESSO code [121] employing plane-wave basis sets and ultrasoft pseudopotentials [101] to represent the interaction between ionic cores and valence electrons. We adopt the exchange correlation energy functional of Perdew-Zunger [95] obtained within a local density approximation (LDA). We smear occupation numbers of electronic states with Fermi-Dirac distribution and a smearing width (k_BT) of 0.04 eV. An energy cutoff of 40 Ry is used to truncate the plane-wave basis used in representa-

*New Chemistry Unit, JNCASR

tion of Kohn-Sham wave functions, and 320 Ry is used to represent the charge density. Structures were determined through minimization of energy until the Hellmann-Feynman force on each atom is smaller than 0.03 eV/Åin magnitude. In the supercell to model a surface, a vacuum layer of 14 Å is introduced parallel to the slab separating adjacent periodic images. We sampled Brillouin zone integrations on uniform grids of 5×5×1 k-points in calculation of the (111) surface Pd_2Ge and $Pd_{2-x}Ni_xGe$. The projected density of states for all the structures was obtained from a much denser 10×10×4 k-point mesh. The calculated lattice constant of bulk Pd_2Ge (a = 6.67 Å) is within the typical LDA error of the observed value (a = 6.7 Å). [233] To assess catalytic activity, we determined energies of adsorption of OH and CH_3CO at various sites of $Pd_{2-x}Ni_xGe$ surfaces.

7.3 Results and discussion

Pd_2Ge has a hexagonal Fe_2P type structure (space group $P\bar{6}2c$) with four crystallographic sites: two Pd atoms occupy Wyckoff sites $3f$ and $3g$, and two Ge atoms occupy the other two Wyckoff sites $2a$ and $1b$. Thus, substituted atoms can occupy any of these four crystallographic sites. To check the site-specific stability of Ni substitution, we modeled the (111) surface of Pd_2Ge with one Ni atom substituted at various sites in $Pd_{28}Ge_{12}$ (Pd_2Ge), and calculated the formation energy using:

$$E_{form} = \frac{E_{Pd_{28-x}Ni_{x+y}Ge_{12-y}} - [E_{Pd_{28}Ge_{12}} + (x+y)E_{Ni} - xE_{Pd} - yE_{Ge}]}{(x+y)} \tag{7.1}$$

where, $E_{Pd_{28-x}Ni_{x+y}Ge_{12-y}}$, $E_{Pd_{28}Ge_{12}}$, E_{Pd}, E_{Ge}, E_{Ni} are the energies of the Ni-substituted Pd_2Ge (111) surface, pristine Pd_2Ge (111) surface, isolated Pd, Ge, and Ni atoms, respectively. Here, x and y are integers giving number of Pd and Ge atoms substituted by Ni atoms, respectively.

As is evident from Table 7.1, Ni substitution at Pd site (Wyckoff sites $3f$ and $3g$) is far

	E_{form}(eV)/Ni atom			
(111) surface	$2a$	$1b$	$3g$	$3f$
$Pd_{28}Ni_1Ge_{11}$	-0.36	-0.62	-	-
$Pd_{27}Ni_1Ge_{12}$	-	-	-2.97	-2.83

Table 7.1: Formation energy per Ni substitution at various Wyckoff sites of (111) surface of Pd_2Ge.

more stable than at Ge sites (Wyckoff sites $2a$ and $1b$). Of the two Wyckoff sites of Pd, Ni substitution is more favorable to occur at the $3g$ site. We further simulated the (111) surface of $Pd_{28-x}Ni_xGe_{12}$ with varied Ni substitution concentration (x = 1-7) and estimated the respective formation energies using Eq. 7.1 and find that $Pd_{1.6}Ni_{0.4}Ge$ is the most stable configuration for Ni-substituted Pd_2Ge (Table 7.2).

		E_{form}(eV)/Ni atom
(111) surface	% substitution	Ni (site $3g$)
$Pd_{27}Ni_1Ge_{12}$	3.6	-2.97
$Pd_{26}Ni_2Ge_{12}$	7.1	-2.86
$Pd_{25}Ni_3Ge_{12}$	10.7	-3.04
$Pd_{24}Ni_4Ge_{12}$	14.3	-3.02
$Pd_{23}Ni_5Ge_{12}$	17.9	-3.30
$Pd_{22}Ni_6Ge_{12}$	21.4	-3.23
$Pd_{21}Ni_7Ge_{12}$	25	-2.97

Table 7.2: Formation energy per Ni substitution in (111) surface of Pd_2Ge at various concentrations.

7.3.1 Catalysis of EOR

The electrooxidation of ethanol in alkaline media can be represented in Eqs. 7.2 and 7.3. Liang [226] proposed that formation of CH_3COOH is the rate determining step (RDS).

$$M-(CH_3CO)_{ads} + M-(OH)_{ads} \rightarrow M-CH_3COOH + M \tag{7.2}$$

$$M-CH_3COOH + OH^- \rightarrow M + CH_3COO^- + H_2O \tag{7.3}$$

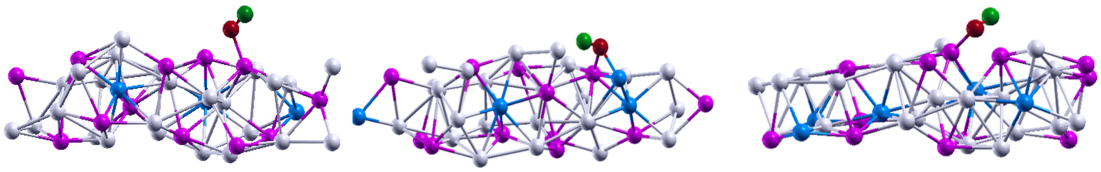

Figure 7.1: Adsorption of OH on $Pd_{1.8}Ni_{0.2}Ge$ (left), $Pd_{1.7}Ni_{0.3}Ge$ (middle) and $Pd_{1.6}Ni_{0.4}Ge$ (right) surfaces. Magenta, silver, blue, red, yellow and green spheres correspond to Ge, Pd, Ni, O, C and H atoms respectively.

where M is the catalyst. CH_3CO and OH are thus the main intermediate species occurring during the reaction, and OH facilitates the desorption of CH_3CO releasing acetate as the main product. [226] Hence, a good catalyst for ethanol oxidation should bind strongly to OH and weakly to CH_3CO. To test the catalytic activity of doped Pd_2Ge nanocomposites, OH intermediate was bonded through the O atom (Fig. 7.1) and CH_3CO at various sites in the initial configurations of the most active Pd_2Ge-based catalysts, that is, $Pd_{1.8}Ni_{0.2}Ge$ (10% Ni substitution) and $Pd_{1.6}Ni_{0.4}Ge$ (18% Ni substitution), and also for intermediate concentration of 14% Ni substitution, $Pd_{1.7}Ni_{0.3}Ge$. For CH_3CO, we kept the molecule in two orientations: (i) bonding through CO, oriented parallel to the surface of the catalyst (Fig. 7.2a); and (ii) bonding through O and H atoms (Fig. 7.2b). In energetically most favorable configurations, OH preferentially binds to Ge atom with GeO bond lengths of 1.8 and 1.9 Å in $Pd_{1.6}Ni_{0.4}Ge$ and $Pd_{1.8}Ni_{0.2}Ge$, respectively (Fig. 7.1). OH interacts more weakly with $Pd_{1.7}Ni_{0.3}Ge$ (14% Ni) than the other concentrations (10% and 18%) of Ni, binding to both Ni and Ge sites with GeO and NiO bond lengths of 1.9 Å (Fig. 7.1). The reason for this will be clear later in our discussion of electronic structure. In contrast, CH_3CO exhibits relatively weak binding in both orientations on Ni-substituted Pd_2Ge surfaces (Table. 7.3) than on pristine Pd_2Ge nanoparticles, indicating a significant improvement in catalytic activity. Interaction of $Pd_{1.7}Ni_{0.3}Ge$ (14% Ni) with CH_3CO is slightly stronger than for the other two surfaces. The stronger adhesion of CH_3CO on $Pd_{1.7}Ni_{0.3}Ge$ leads to poisoning of active sites on its surface and hence its lower catalytic activity. As evident from the calculated adsorption energies -OH binds much more

strongly than CH_3CO on both Ni substituted ($Pd_{1.8}Ni_{0.2}Ge$ and $Pd_{1.6}Ni_{0.4}Ge$) surfaces.

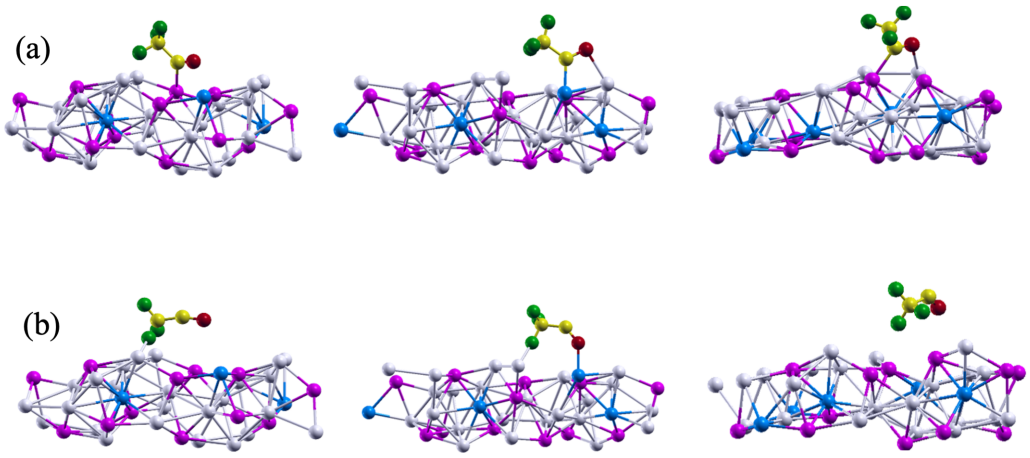

Figure 7.2: Adsorption of CH_3CO bonding through (a) C–O and (b) O–H on $Pd_{1.8}Ni_{0.2}Ge$ (left), $Pd_{1.7}Ni_{0.3}Ge$ (middle) and $Pd_{1.6}Ni_{0.4}Ge$ (right) surfaces. Magenta, silver, blue, red, yellow and green spheres correspond to Ge, Pd, Ni, O, C and H atoms respectively.

Catalyst	ΔE_{ads} (kJmol^{-1})	
	OH	CH_3CO
$Pd_{1.8}Ni_{0.2}Ge$	-481	-221
$Pd_{1.7}Ni_{0.3}Ge$	-437	-285
$Pd_{1.6}Ni_{0.4}Ge$	-462	-220

Table 7.3: Energies of adsorption (ΔE_{ads}) of OH radical and CH_3CO on Ni-substituted Pd_2Ge surfaces.

7.3.2 Insights form electronic structure

The nature of these interactions can be understood from the projected density of electronic states (PDOS) (Fig. 7.3), where the highest occupied molecular orbital (HOMO) of OH lies close to the bottom of Pd-4p, Pd4d, Ge-4p, and Ni-3d bands of the catalyst. Covalent bonding interaction of OH with the catalyst surface is evident from its sharp HOMO peak resonating with the Pd-4d, Pd-4p, and Ge-4p orbitals of $Pd_{1.8}Ni_{0.2}Ge$ and $Pd_{1.6}Ni_{0.4}Ge$ surfaces and with Ni-3d, Pd-4p, and Ge-4p orbitals of $Pd_{1.7}Ni_{0.3}Ge$. The relative position of these HOMO peaks determines the strength of interaction between the adsorbate and catalyst surface. The HOMO for OH adsorbed on $Pd_{1.7}Ni_{0.3}Ge$ (14%

Ni) lies deeper in energy than the other two concentrations (10 and 18%) of Ni (Fig. 7.3a and 7.2b); hence, OH interacts more weakly with $Pd_{1.7}Ni_{0.3}Ge$. Orbitals of OH interacting with the frontier orbitals of the catalyst are degenerate and partially occupied and readily receive an electron (charge transfer) from the catalyst (Fig. 7.3a). The interaction of the lowest unoccupied molecular orbital (LUMO) of CH_3CO with the surface states dominates over the interaction of its HOMO, which is fully occupied and has a sharp peak at deeper energy. The latter indicates weaker covalent interaction of CH_3CO with the catalyst surface (Fig. 7.3b). In contrast, the LUMO of CH_3CO is close to the Fermi level (E_F) and resonates with d-orbitals of Pd and Ni atoms of the catalyst. It leads to broadening of the LUMO peak in PDOS. Interaction of LUMO with 3d orbitals of Ni, evident in its contribution to states well below E_F (Fig. 7.3b), is responsible for its stronger adhesion to Ni sites of $Pd_{1.7}Ni_{0.3}Ge$ (14% Ni).

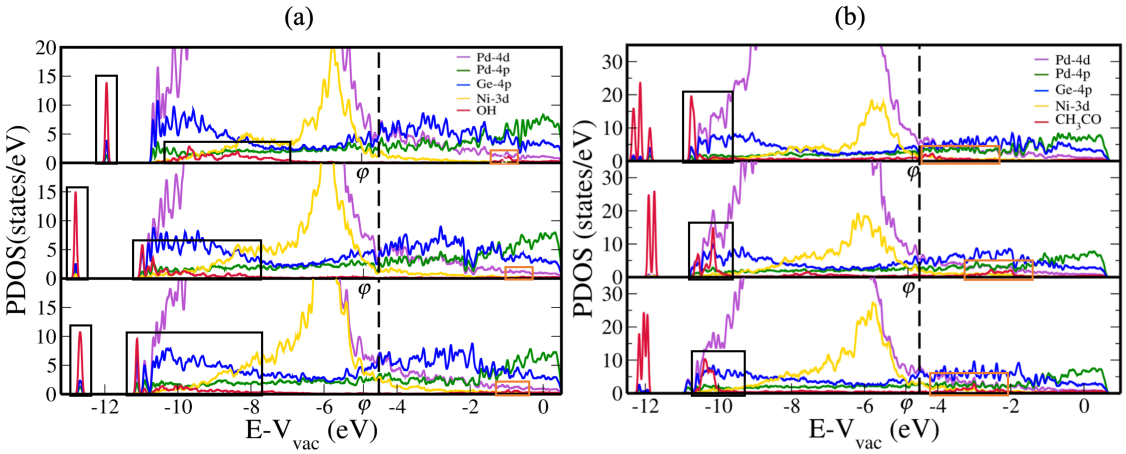

Figure 7.3: PDOS of (a) OH and (b) CH_3CO on $Pd_{1.8}Ni_{0.2}Ge$ (top), $Pd_{1.7}Ni_{0.3}Ge$ (middle) and $Pd_{1.6}Ni_{0.4}Ge$ (bottom) surfaces. Black and orange boxes denote the HOMO and LUMO of the adsorbates (OH and CH3CO), respectively. Dashed black line represents the ethanol redox potential.

Work function was recently shown to be a relevant descriptor of catalytic activity of metals toward CO_2 reduction.46 We estimated the work function (ϕ) for the pristine and (111)

surface of Ni substituted Pd_2Ge using the following expression:

$$\phi = V_{vac} - E_F \tag{7.4}$$

where V_{vac} is the vacuum energy estimated from the planar average of the electrostatic potential. The redox potential of ethanol oxidation is 4.5 eV. The work function of both pristine and Ni-substituted Pd_2Ge surfaces (Table. 7.4 and Fig. 7.3) are close and below the redox potential of ethanol oxidation, further confirming their suitability for catalyzing this reaction.

Catalyst	ϕ
Pd_2Ge	4.90
$Pd_{1.8}Ni_{0.2}P$	4.88
$Pd_{1.7}Ni_{0.3}P$	4.90
$Pd_{1.6}Ni_{0.4}P$	4.92

Table 7.4: Work function of (111) surfaces of pristine and Ni-substituted Pd_2Ge.

7.4 Conclusions

We show that Ni-substitution in Pd_2Ge optimizes the adhesion strength of CH_3CO and OH intermediates, thus enhancing its activity towards EOR. The OH intermediate prefers to bind at the Ge site on $Pd_{1.6}Ni_{0.4}Ge$ while CH_3CO exhibits a weak binding on Ni-substituted Pd_2Ge as compared to OH. Also, the work function (ϕ) for both pristine and Ni-substituted Pg_2Ge surfaces lie close to the ethanol oxidation potential further supporting their catalytic activity towards EOR.

Part III

Catalysis of Commercially Vaule-added Products

Chapter 8

Synergistic Role of Substitutional Au and S-Vacancies in MoS_2 for Catalyzing DSHP

8.1 Introduction

The simplest member of the peroxide family, hydrogen peroxide (H_2O_2), is an unstable molecule which decays exothermically (-116.7 kJmol^{-1}) [20] to produce water and O_2. It has, for long been used as an oxidizing agent, [60–62] in pulp and textile bleaching [63] and in low concentrations as an antiseptic. [64] Most commercial H_2O_2 is synthesized via the anthraquinone auto-oxidation (AO) process. [65] The cyclic AO process includes hydrogenation of anthraquinone on Pd-Ni catalyst, oxidation of the hydrogenated anthraquinone and extraction and purification of H_2O_2. [66] Though efficient, the AO process has various disadvantages, [66, 67] which include, side reactions leading to poisoning of the catalyst, degradation of anthraquinone molecules, difficulties in separation and transportation of H_2O_2 due to organic impurities. In contrast, the direct synthesis of

hydrogen peroxide (DSHP) is a single reactor process, comprising of controlled, partial hydrogenation of O_2 using a catalyst. [68,69] Although hydrogenation of O_2 to H_2O_2 is an exothermic reaction (-120.5 kJmol^{-1}), selectivity of the catalyst is crucial since other competing reactions, for instance, formation of H_2O, through the Oxygen Reduction Reaction, is more spontaneous (-237.2 kJmol^{-1}). [20] Moreover, since the peroxide bond is unstable, H2O2 can decompose (-116.7 kJmol^{-1}) into H_2O and O_2, or undergo reduction (-354.0 kJmol^{-1}) to yield H_2O. [20] Therefore, an ideal catalyst for DSHP should interact with O_2 optimally so as to activate the O=O bond moderately and not split the molecule. So far, various materials have been explored as catalysts for DSHP including TiO_2, [234–239] transition metal complexes, [240–244] CdS, [234, 245] and g-C_3N_4. [246–252] Several reports have focused on Pd based catalysts, [61,70,71] in particular Pd-Au and Pd-Sn based catalysts. [61, 70, 72–76] Hutchings and co-workers showed that a homogeneous alloy of AuPd on carbon support exhibited excellent selectivity and activity towards DSHP. [71] However, the cost and scarcity of Pd hinders its use at large scale. Our aim is to develop a catalyst comprising primarily of cheaper and earth abundant elements, with expensive elements present in small concentrations.

In this direction, we consider the possibility of using molybdenum disulfide (MoS_2), a transition metal dichalcogenide with tuneable chemistry which has been extensively studied in catalysis (in conjunction with single atom catalysis), since both Mo and S are inexpensive, abundantly found elements. While the basal plane of 2H-MoS_2 is known to be relatively inert, [124, 253] incorporation of sulfur (S) vacancies and transition metal doping greatly improves its catalytic activity towards Hydrogen Evolution Reaction (HER), [28, 30, 253] Oxygen Evolution Reaction (OER) [254] and Oxygen Reduction Reaction (ORR). [255] In the context of DSHP, HER and ORR are particularly relevant. Initial steps of HER and ORR involving H adsorption and O_2 activation, respectively, are also the first steps in DSHP (Fig. 8.3). Hence catalysts which are used for HER and ORR could be tuned to selectively catalyze DSHP. MoS_2 is known to be an excellent catalyst for HER with its

S-vacancies, [39] and edge sites being the active sites. [124] A recent study by Wang *et al.* has reported effects of various transition metal substituents in MoS_2 (1H-MoS_2) on its activity for ORR and find copper substituted MoS_2 to exhibit the highest activity. [255] While this indicates excellent activation of the O_2 molecule, DSHP is facilitated by moderate activation of O_2. The same work also found that gold (Au) substituted 1H-MoS_2 shows relatively weaker activation of the O_2 molecule, i.e., slight elongation of the O=O bond with weak adhesion to the monolayer. This property of Au-substituted MoS_2, which is sub-optimal for ORR, can be exploited for DSHP.

In this work, we show Au-substituted 1H-MoS_2 with S-vacancies (Au_xMoS_{2-x-v}) to be an efficient catalyst for DSHP. The selective reduction of O_2 to yield H_2O_2 occurs without any thermodynamically uphill reaction step on Au_xMoS_{2-x-v}. Calculation of transition states (TS) show relatively low activation barriers. Further, analysis of electronic structures provides mechanistic insights into the catalytic activity of Au_xMoS_{2-x-v} towards DSHP.

8.2 Computational details

Our first-principles calculations are based on density functional theory (DFT) as implemented in the Quantum ESPRESSO [121] code employing a plane-wave basis set and PAW pseudopotentials [256] to represent the interaction between ionic cores and valence electrons. We adopt the exchange-correlation energy functional of Perdew-Burke-Ernzerhof (PBE) [99] within a generalized gradient approximation (GGA), and occupation numbers of electronic states have been smeared with Fermi–Dirac distribution and a smearing width (k_BT) of 0.04 eV. Additionally, van der Waals (vdW) interactions using the Grimme scheme [135] have been included to account for weak interactions. A kinetic energy cutoff of 55 Ry on the plane-wave basis is used in representation of the Kohn-Sham wave functions, and a cutoff of 440 Ry to represent the charge density. Structures of reactants, products and intermediates are determined through minimization of energy until

the Hellmann-Feynman forces on each atom are smaller than 0.03 eV/Å in magnitude. The transition states (TS) were obtained using the nudged elastic band (NEB) method. Seven images were used in all NEB calculations. All TSs were relaxed until the Hellmann–Feynman forces acting on the atoms were within 0.05 eV/Å. A supercell consisting of 4×4 units of 1H-MoS_2 is used to model the various catalysts and a vacuum layer of 15 Åthickness is introduced separating adjacent periodic images. The catalysts studied in this work are shown in Fig. 8.1 and the stoichiometry of the supercells in given in Table 8.1. Brillouin-zone integrations were sampled on a uniform grid of 6×6×1 k-points. The projected density of states (PDOS) of each structure was obtained from calculations on a denser, 18×18×1 mesh of k-points. Calculated lattice constants of bulk MoS_2 (a = 3.19 Å, c = 12.45 Å) are within the typical GGA errors with respect to experimentally observed values [122] (a° = 3.16 Å, c° = 12.29 Å).[51]

	Label	% Au	Stoichiometric formula
1	1H-MoS_2	-	$Mo_{16}S_{32}$
2		2.08	$AuMo_{16}S_{31}$
3	Au_xMoS_{2-x}	4.17	$Au_2Mo_{16}S_{30}$
4		2.08	$AuMo_{15}S_{32}$
5	$Au_xMo_{1-x}S_2$	4.17	$Au_2Mo_{14}S_{32}$
6		2.04	$AuMo_{16}S_{32}$
7	Ad-Au_xMoS_2	4	$Au_2Mo_{16}S_{32}$
8	MoS_{2-v}	-	$Mo_{16}S_{31}$
9		2.13	$AuMo_{16}S_{30}$
10	Au_xMoS_{2-x-v}	4.26	$Au_2Mo_{16}S_{29}$

Table 8.1: Au:MoS_2 catalysts considered here, with the stoichiometric formula in a supercell.

8.3 Configurations of Au:MoS_2: stability

MoS_2 is known to exist in three polytypes–2H-MoS_2, 3R-MoS_2 and 1T-MoS_2 (H, R and T indicate, hexagonal, rhombohedral and tetragonal structure, respectively, while the numbers preceding the letters indicate the thickness of periodic cell in terms of number of

MoS_2 units). Of these, the semiconducting 2H-MoS_2 is thermodynamically most stable, and has two S-MoS layers with an interlayer separation of ∼3 Å. The catalysts considered (Fig. 8.1) here are generated using a 4×4 supercell of monolayer of 2H-MoS_2, with various modifications including, Au-substitution at S and Mo sites, Au-adatom, and S vacancies (see Table 8.1 for stoichiometry of the supercells). The formation energies of various Au-doped MoS_2 monolayers are calculated using:

$$E_{form} = \frac{E_{Mo_{16-x}Au_{x+y+z}S_{32-y}} - [E_{Mo_{16}S_{32}} + (x+y+z)E_{Au} + xE_{Mo} - yE_S]}{(x+y+z)} \tag{8.1}$$

where, $E_{Mo_{16-x}Au_{x+y+z}S_{32-y}}$, $E_{Mo_{16}S_{32}}$, E_{Au}, E_{Mo} and E_S are the energies of Au substituted/adatom surface of 1H-MoS_2, pristine 1H-MoS_2, isolated Au, Mo and S atoms, respectively. Here x, y are integers, giving the number of Au substituents on Mo and S sites respectively. Integer z represents number of Au-adatoms present in the surface.

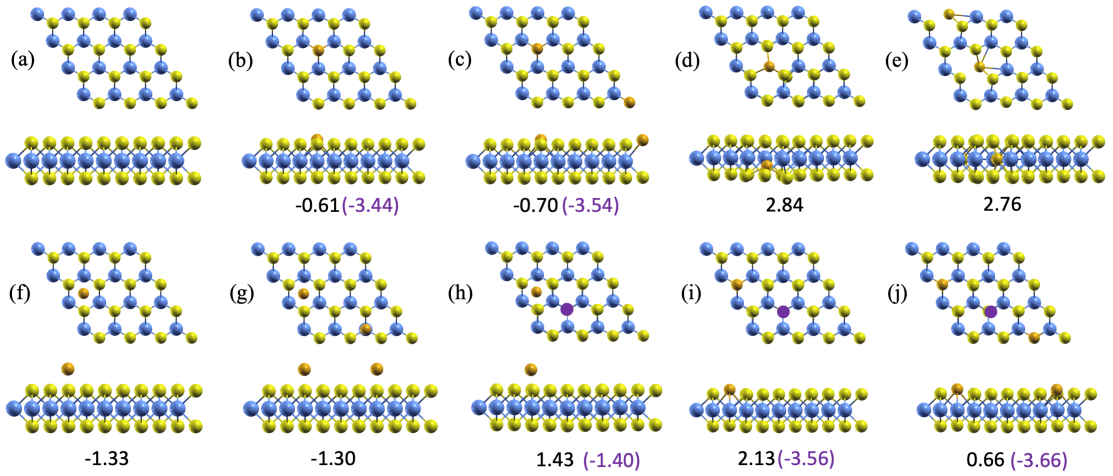

Figure 8.1: Formation energies and structures of 4x4 supercells of MoS_2 with Au (substitution or adatom) and S-vacancies (a) pristine MoS_2, Au_xMoS_{2-x} (2.08%) (c) Au_xMoS_{2-x} (4.17%), (d) $Au_xMo_{1-x}S_2$ (2.08%), (e) $Au_xMo_{1-x}S_2$ (4.17%), (f) ad-Au_xMoS2 (2.04%), (g) ad-Au_xMoS2 (4.00%), (h) MoS_{2-v}, (i) Au_xMoS_{2-x-v} (2.13%) and (j) Au_xMoS_{2-x-v} (4.26%). Values in eV/Au-atom. Negative values indicate favourable formation. Blue, yellow, and gold spheres represent Mo, S and Au. Purple circles indicate S vacancies. Concentrations given as Au atom percentage.

Their negative values (see Fig. 8.1) indicate that the formation of respective configuration

is spontaneous. We find Au-substitution at S sites (Au_xMoS_{2-x}) and Au-adatom (ad-Au_xMoS_2) to be spontaneous, while Au substitution at Mo sites ($Au_xMo_{1-x}S_2$) is non-spontaneous. On this basis, we can eliminate $Au_xMo_{1-x}S_2$ as a suitable configuration. Also, MoS_2, which is typically grown on metal supports such as Au, Ag and Cu, is known to form with S vacancies. [253, 257] Therefore, we have estimated the formation energies of Au_xMoS_{2-x-v} taking 1H-MoS_{2-v} as reference (values within parenthesis in Fig. 8.1):

$$E_{form} = \frac{E_{Mo_{16}Au_{x+y+z}S_{32-y-v}} - [E_{Mo_{16}S_{32-y-v}} + (x+y+Z)E_{Au} - xE_Mo]}{(x+y+Z)} \tag{8.2}$$

where, $E_{Mo_{16}Au_{x+y+z}S_{32-y-v}}$, and $E_{Mo_{16}S_{32-y-v}}$ are the energies of Au substituted 1H-MoS_{2-v} and 1H-MoS_{2-v}. . Integer v represents number of Au-adatoms present in the surface. While the formation of Au_xMoS_{2-x} was already found to be favorable with respect of MoS_2 (-0.61 eV and -0.70 eV for 2% and 4% of Au, respectively),it is more favorable when the reference is MoS_{2-v}. The formation of Au_xMoS_{2-x-v}, when synthesized from MoS2 is unfavorable (2.13 eV and 0.66 eV for 2% and 4%, respectively), however, when synthesized from MoS_{2-v}, its synthesis is favorable (-3.56 eV and -3.66 eV for 2% and 4%, respectively). Another configuration of Au:MoS2 we have considered is the ad-Au_xMoS_{2-v} (Fig. 8.1h). Like Au_xMoS_{2-x-v}, it shows an unfavorable formation energy taking MoS_2 as reference (1.43 eV) but a favorable formation energy when synthesized from MoS_{2-v} (-1.40 eV). Overall, when pristine MoS_2 is considered, the most favorable doped surfaces are the ad-Au_xMoS2 surfaces, however, MoS_{2-v} favors the formation of Au_xMoS_{2-x-v} over both ad-Au_xMoS_2 and ad-Au_xMoS_{2-v}.

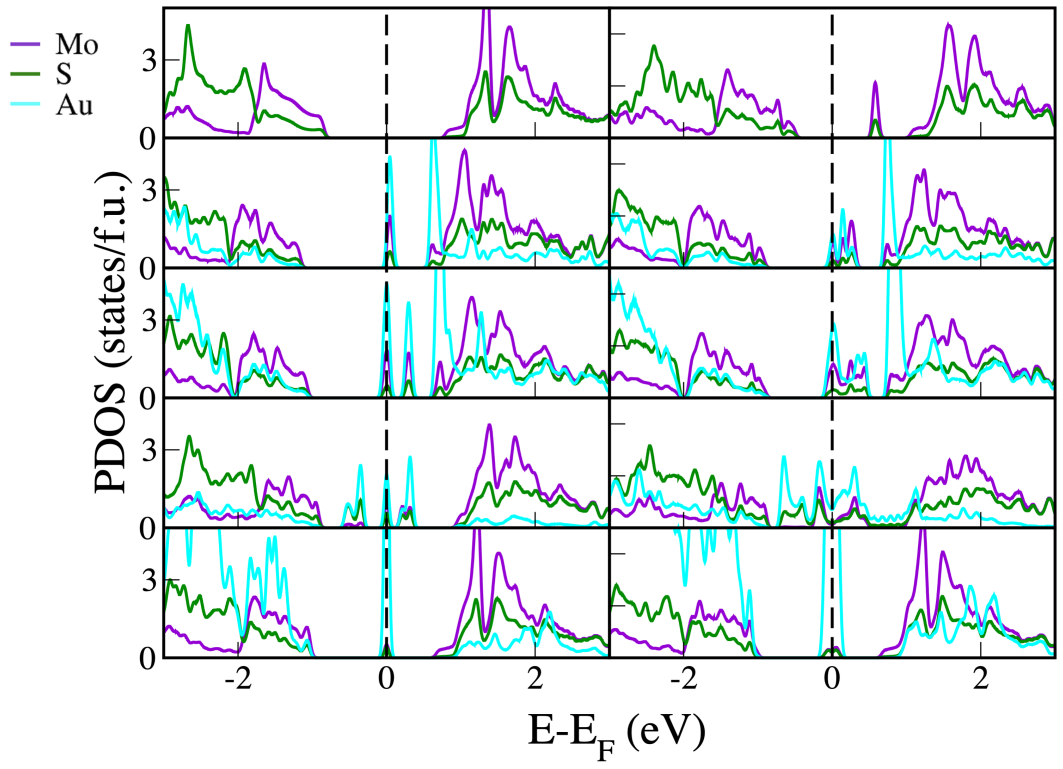

Figure 8.2: Projected density of states (PDOS) of (a) pristine MoS_2, Au_xMoS_{2-x} (2.08%) (c) Au_xMoS_{2-x} (4.17%), (d) $Au_xMo_{1-x}S_2$ (2.08%), (e) $Au_xMo_{1-x}S_2$ (4.17%), (f) ad-Au_xMoS2 (2.04%), (g) ad-Au_xMoS2 (4.00%), (h) MoS_{2-v}, (i) Au_xMoS_{2-x-v} (2.13%) and (j) Au_xMoS_{2-x-v} (4.26%).

The projected density of states (PDOS) (Fig. 8.2), highlight changes in the electronic structure of 1H-MoS_2 on Au substitution or adatom and S-vacancy. S-vacancy reduces the band gap from 1.62 eV in pristine 1H-MoS_2 to 1.05 eV in 1H-MoS_{2-v}. As is evident in Fig. 8.2b, this reduction is due to appearance of mid-gap states arising from S-vacancy defects. Au-doping in MoS_2, irrespective of whether it is substitutional or adatom, makes the monolayer semi-metallic. It is also clear (see Fig. 8.2c-j) that the semi-metallicity is due to the Au-6s states appearing at the Fermi level (E_F). Effects of Au substitution or adatom is site specific on electronic structure and energetics of 1H-MoS_2. While Au_xMoS_{2-x} and ad-Au_xMoS_2 are stabilized, $Au_xMo_{1-x}S_2$ is not, suggesting distinct chemical environment and activity of Au in the three configurations.

8.4 Adsorption of key intermediates: screening catalysts for DSHP

The first step along the reaction pathway of DSHP (Fig. 8.3) involves adsorption of O_2 and H on the surface of the catalyst. Of these, O_2 adsorption is crucial in determining selectivity of catalyst towards H_2O_2 versus ORR. Weak to moderate adsorption of O_2 on the catalyst ensures optimal activation of O=O bond needed for H_2O_2 production. Conversely, strong adhesion may lead to complete reduction of O_2 yielding H_2O (ORR). Further, strong adsorption energies also may also lead to poisoning of active sites by O_2 molecules and cause surface reconstruction, which would hinder repeated use of the catalyst. As indicated by positive adsorption energies (Eq. 8.3), O_2 does not adhere to 1H-MoS_2, and there is insignificant change in the O_2 bond length (Fig. 8.4). This is expected since the basal plane of MoS_2 is known to be catalytically inert.

$$\Delta E_{ads} = E_{adsorbate+E_{Mo_{1-x}Au_{x+y+z}S_{2-y}}} - (E_{Mo_{1-x}Au_{x+y+z}S_{2-y}} + \mu_{adsorbate}) \tag{8.3}$$

where, ΔE_{ads} is the adsorption energy and $E_{adsorbate+Mo_{1-x}Au_{x+y+z}S_{2-y}}$, $E_{Mo_{1-x}Au_{x+y+z}S_{2-y}}$ and $\mu_{adsorbate}$ are the total energies of adsorbate stabilized on Au-substituted/adatom MoS_2, Au-substituted/adatom MoS_2, and chemical potentials of isolated adsorbate species, respectively. Here, $\frac{1}{2}\mu_{H_2}$, ($\mu_{H_2O_2}$ - $\frac{1}{2}\mu_{H_2}$) and ($2\mu_{H_2O_2}$ - $2\mu_{H_2}$ + 4.92) are taken as the chemical potentials of an isolated H-atom (μ_H), OOH (μ_{OOH}) and O_2 molecule respectively.

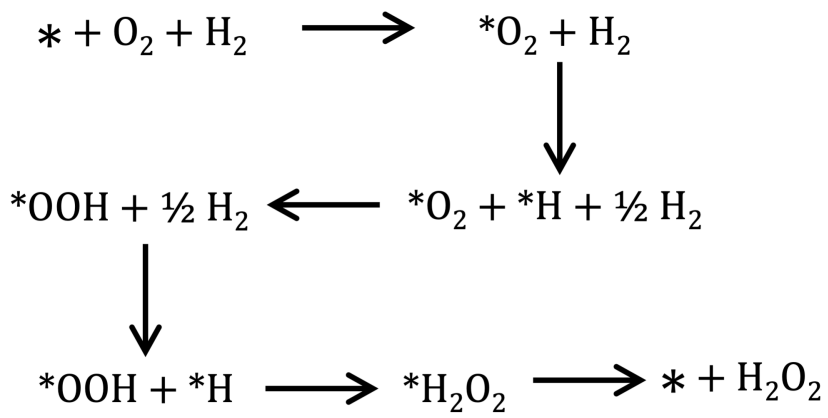

Figure 8.3: Intermediates along the reaction pathway of direct synthesis of hydrogen peroxide (DSHP). * indicates the adsorbent and * above an intermediate indicates its state after adsorption.

To achieve optimal O_2 adsorption, we introduce Au doping in MoS_2, since Au is known to adsorb O_2 moderately. [255] However, the type of Au doping (substitution or adatom) and the site of doping having distinct effects on (S or Mo) O_2 adsorption. Adsorption energies and percentage of bond elongation of O_2 (shown in Fig. 8.4) show that Au_xMoS_{2-x} and (2% Au) ad-Au_xMoS_2 would be ideal to catalyze DSHP owing to moderate activation of O=O bond. Ad-Au_xMoS_2 (4% Au) and $Au_xMo_{1-x}S_2$, on the other hand, show high adsorption energies, and accompanying bond elongation. In fact, the O_2 molecule splits when adsorbed on $Au_xMo_{1-x}S_2$. Interestingly, O_2 molecule does not split on 4% ad Au_xMoS_2 despite its high energy of adsorption: -2.60 eV. A closer inspection of the structure indicates major reconstruction leading to a bidentate adhesion of the adsorbent with Au-adatoms (Fig. **??**). It is likely that this reconstruction is the cause of a high O_2 adsorption energy. Therefore, we eliminate this surface as a potential catalyst for DSHP. Further, a combination of positive formation energy (Fig. 8.1), and high O_2 adsorption energy conclusively support the disqualification of $Au_xMo_{1-x}S_2$ as a catalyst for DSHP. It is worth noting, however, that ad-Au_xMoS_2 and $Au_xMo_{1-x}S_2$ would be ideal catalysts for ORR. While Zhang *et al* showed that Au_xMoS_{2-x} would not be suitable for ORR, our study finds that a modification of the doping site, to $Au_xMo_{1-x}S_2$, can make a dramatic

difference in O_2 activation.

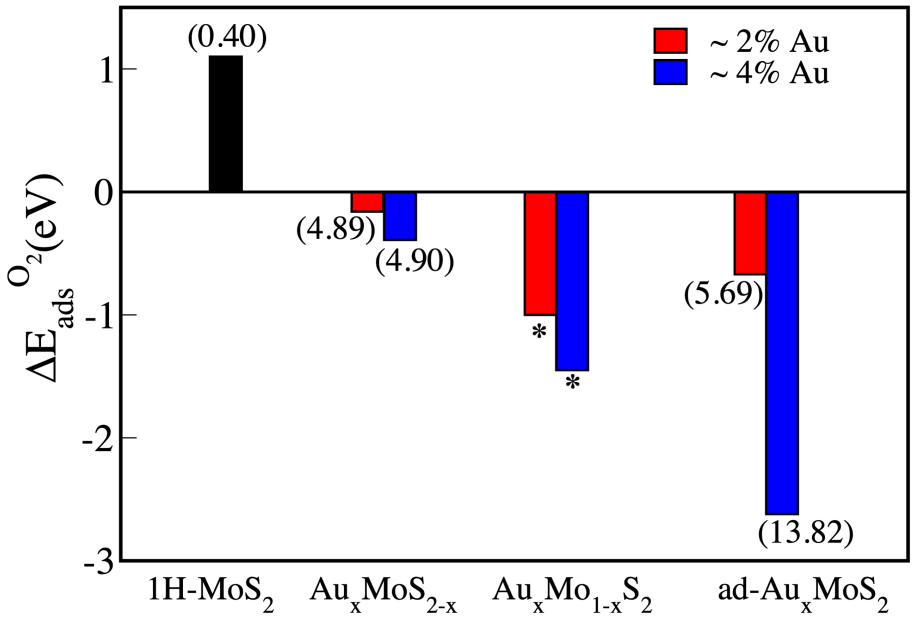

Figure 8.4: Energies of adsorption of O_2 on various catalysts, along with consequent percentage deviation in bond length of O_2, given in parenthesis. * indicates splitting of the O_2 molecule. Negative adsorption energies imply attractive interactions. O_2 adsorbed on S site in pristine, and Au site in Au:MoS_2, respectively.

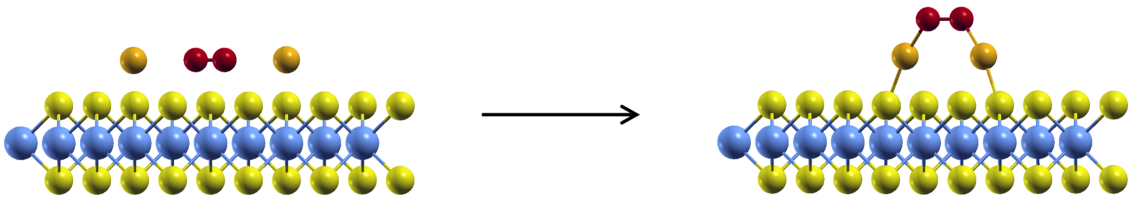

Figure 8.5: Initial (left) and final (right) structures of O_2 adsorbed on ad-Au$_x$MoS$_2$ (4% Au). Blue, yellow, and gold spheres represent Mo, S and Au.

We also simulated adsorption of O_2 at S sites of Au:MoS_2, and obtain positive adsorption energies (Table 8.2), providing further validation that Au plays a crucial role in stabilizing the O_2^* intermediate. Based on these results, we eliminate ad-Au$_x$xMoS$_2$, Au$_x$Mo$_{1-x}$S$_2$ and MoS_2 as possible candidates as catalysts for DSHP. However, we continue to perform calculations on pristine 1H-MoS_2, using it as a reference for comparison and analysis.

H adsorption is the next step in DSHP. Since, H_2O_2 decomposes in alkaline medium[1,10],

	Catalyst	% Au	ΔE_{ads} (eV)
1	Au_xMoS_{2-x}	2.08	0.96
2		4.17	0.85
3	$Au_xMo_{1-x}S_2$	2.08	0.58
4		4.17	0.20

Table 8.2: Energies of adsorption (in eV) of O_2 on S sites of Au-substituted MoS_2. Positive values indicate unfavorable interaction.

DSHP is usually carried out in acidic conditions. An additional advantage of this is that the acidic medium provides protons for the reduction of O_2 to H_2O_2. Therefore, the catalyst for DSHP is not required to catalyze dissociation of H2. Extensive work on Hydrogen Evolution Reaction (HER) on MoS_2 has uncovered the importance of S-vacancies in pristine MoS_2 for the favorable adsorption of H, [148, 253, 257] which is corroborated by our calculations (Fig. 8.6). To verify if S-vacancies facilitate H adsorption in Au substituted MoS_2, we introduced one S-vacancy per supercell in Au_xMoS_{2-x} and simulated adsorption of H-atom. We find that S-vacancies indeed stabilize H adsorption in Au_xMoS_{2-x}. Thus, these Au:MoS_2 based catalysts screened for the first step of DSHP are also favorable to the key step of adsorption of H-intermediate, provided, S-vacancies are also present.

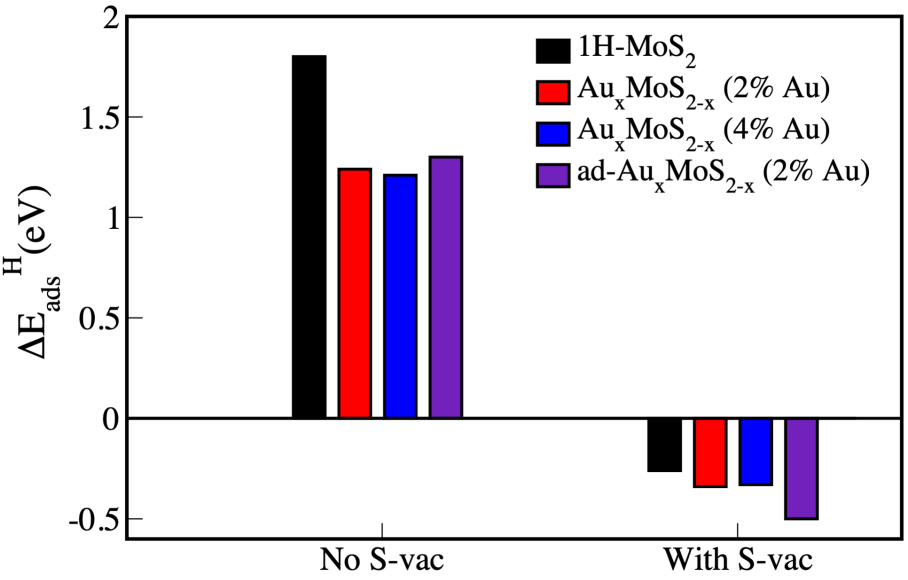

Figure 8.6: Energies of adsorption of H, adsorbed on vacancy sites, on various catalysts. Negative values imply attractive interactions.

8.5 DSHP reaction pathway: role of S-vacancies and selectivity

Adsorption of O_2 and H result in the formation of the –OOH intermediate. H_2O_2 is then formed by the adsorption of an additional H atom (Fig. 8.3). We now determine energetics of each intermediate step occurring along the pathway of DSHP reaction (Fig. 8.3) on these catalysts. We compute the reaction energy of each step with respect to the reactants. For Au-substituted MoS_2 monolayers (Au_xMoS_{2-x}), the second step, i.e., adsorption of H-atom is the potential-determining step (see left panel of Fig. 8.7). S-vacancies in Au-substituted 1H-MoS_2 (Au_xMoS_{2-x-v}), result in marked reduction in this barrier and hence tremendous increase in the catalytic activity. The energy profile of the reaction (right panel of Fig. 8.7) shows that all elementary reaction steps are barrierless for Au_xMoS_{2-x-v}. Further, optimized structures of the intermediates (Fig. 8.8) adsorbed on Au_xMoS_{2-x-v} reveal that the catalyst undergoes only weak reconstruction, implying that it should be stable over a greater number of reuse cycles. Interestingly, inclusion of S-vacancy has

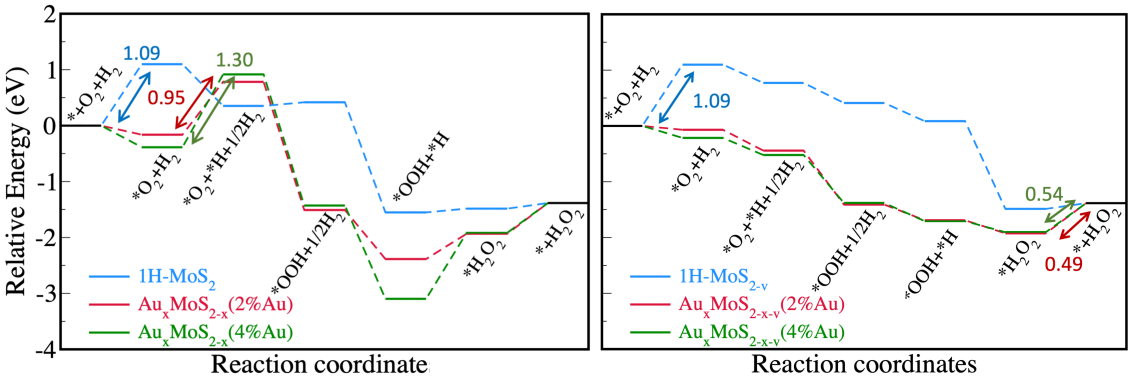

Figure 8.7: Energies of intermediates along reaction pathway of direct synthesis of hydrogen peroxide on catalysts based on MoS_2 without (left panel) and with (right panel) S-vacancies. The double headed arrows indicate the reaction step with highest energy barrier. All energies are in eV.

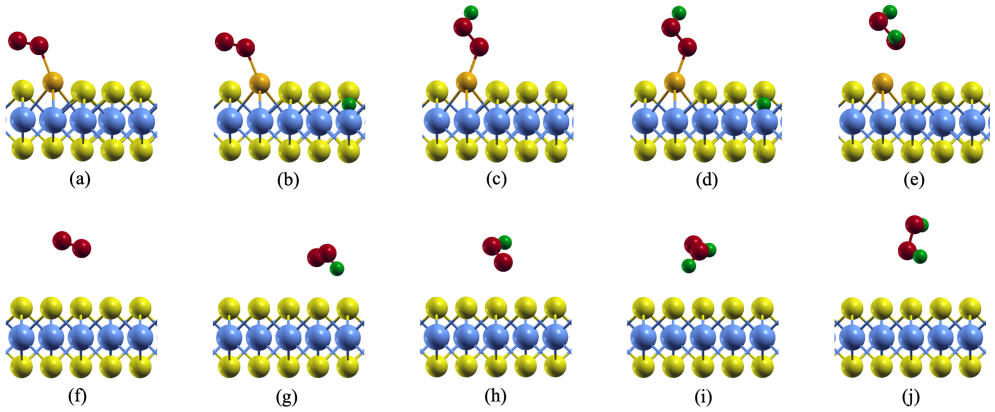

Figure 8.8: Optimized structures of intermediates occurring along direct synthesis of hydrogen peroxide on Au_xMoS_{2-x-v} (2% Au) (a-e), and on 1H-MoS_2 (f-j).

little impact on catalytic activity of MoS_2 since the energetically uphill step involves adsorption of O_2 which remains unaffected. For Au_xMoS_{2-x-v}, the release of the product (H_2O_2) is an endothermic step. However, one expects the energy gained by the catalyst on adsorbing H and O_2, to compensate for the energy barrier that needs to be crossed for desorption of H_2O_2. Our analysis of kinetics of DSHP on Au_xMoS_{2-x-v} (2% Au) is based on results of nudged elastic band (NEB) calculations (Fig. 8.11), and transition states and kinetic energy barriers are determined. Reaction steps involving adsorption of a free molecule or atom (O_2 or H) on the surface occur without any barriers. Along the DSHP reaction pathway, kinetic barriers are encountered for the two hydrogenation steps,

formation of *OOH and *H_2O_2 intermediates: 0.56 eV and 0.80 eV, respectively. These may be compared with the barrier of 0.87 eV reported as the activation energy barrier for DSHP on 11 mol% Au doped Pd (111) by Li and Yoshizawa. [20] The catalyst here has a dual advantage of having a moderately lower barrier, and being composed of earth abundant elements with small amounts of Au doping.

A key requirement of DSHP is the activation of O_2 bond without cleaving it. This is a challenge in the first step, when O_2 is adsorbed onto the surface, and also in subsequent steps. Following the formation of the *OOH intermediate, its O=O bond can split to give *O+*OH intermediates leading to undesired ORR, instead of forming *H_2O_2. We find O=O bond cleavage in *OOH to have a kinetic barrier of 0.93 eV, higher than that for the formation of *H_2O_2 (0.80 eV) implying favorable selectivity of Au_xMoS_{2-x-v} towards DSHP over ORR. Thus, Au-substitution and S vacancies synergistically render selectivity of Au_xMoS_{2-x-v} towards partial reduction of O_2 (to H_2O_2) over its complete reduction to give H_2O.

We considered the viability of 2% Au ad-Au_xMoS_2 as a catalyst for DSHP owing to a reasonable bond length of *O_2 on the surface (see Fig. 8.4). As S-vacancies are critical for adsorbing H-atoms (Fig. 8.6), we compute the energy of each elementary step along DSHP relative to reactants (Fig. 8.9), and find that all the reaction steps are downhill on 2% Au ad-Au_xMoS_{2-v}, with the exception of final uphill step having barrier three times the energy barrier seen on Au_xMoS_{2-x-v} (2% Au) to desorb H_2O_2. Further, we used NEB calculations to determine the kinetics and find that the third reaction step, *O2 + *H $\rightarrow$ *OOH, is the rate-determining step with a barrier of 1.72 eV. Such a high kinetic barrier shows that 2% Au ad-Au_xMoS_{2-v} is not an ideal catalyst for DSHP.

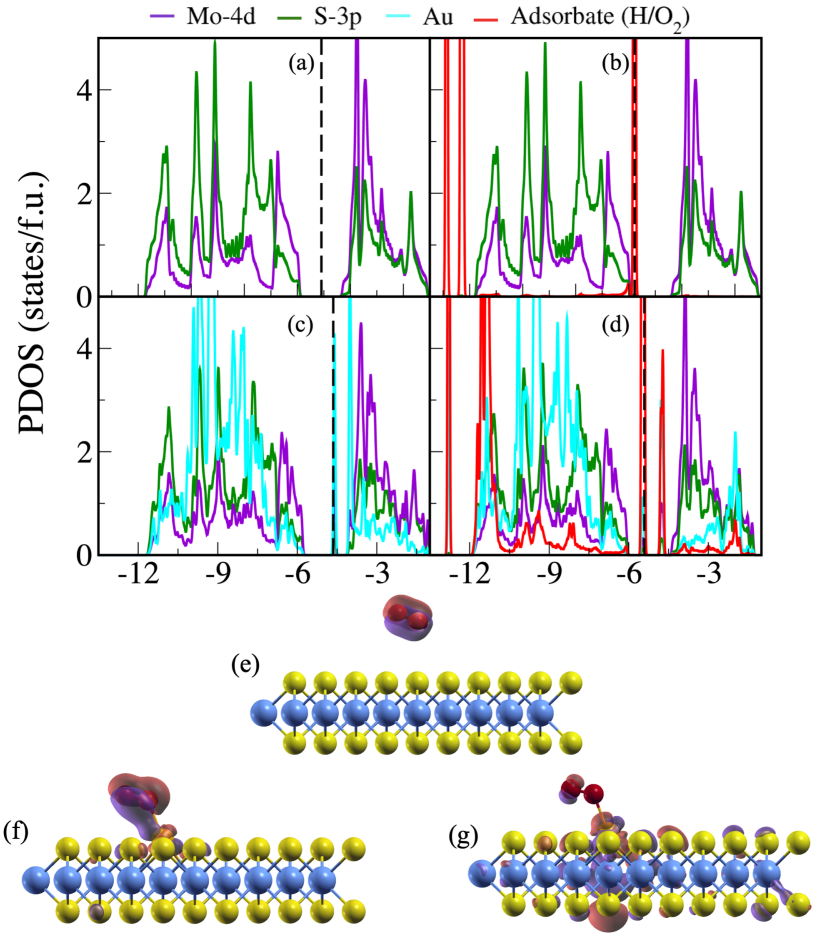

Figure 8.10: Projected density of states (PDOS) of (a) 1H-MoS_2, (b) 1H-MoS_2 with adsorbed O_2, (c) Au_xMoS_{2-x} (2% Au), and (d) Au_xMoS_{2-x} (2% Au) with adsorbed O_2. Iso-surfaces of wave functions depicting (e) highest occupied molecular orbitals (HOMO) of $^*O_2$ on pristine MoS_2, (f) sharp HOMO like peak (in the range $\sim$ -12 to -11 eV) of $^*O_2$ on Au_xMoS_{2-x} (2% Au), and (g) covalent interaction ($\sim$ -10 to -8 eV) of $^*O_2$ with surface states of Au_xMoS_{2-x} (2% Au). Red and purple colors represent positive and negative iso-surfaces, respectively.

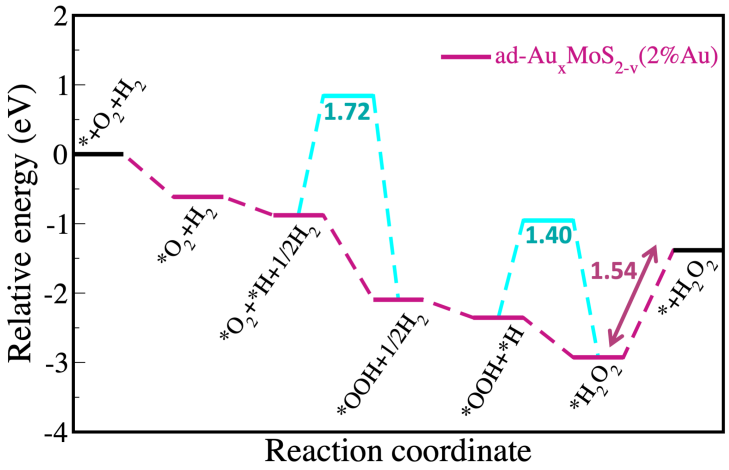

Figure 8.9: Relative energy diagram for direct synthesis of hydrogen peroxide (DSHP) on 2% ad-Au_xMoS_{2-v}. Cyan curves indicate kinetic barriers along the DSHP pathway. Double headed magenta arrow indicates the reaction step with highest thermodynamic energy barrier. All energies are in eV.

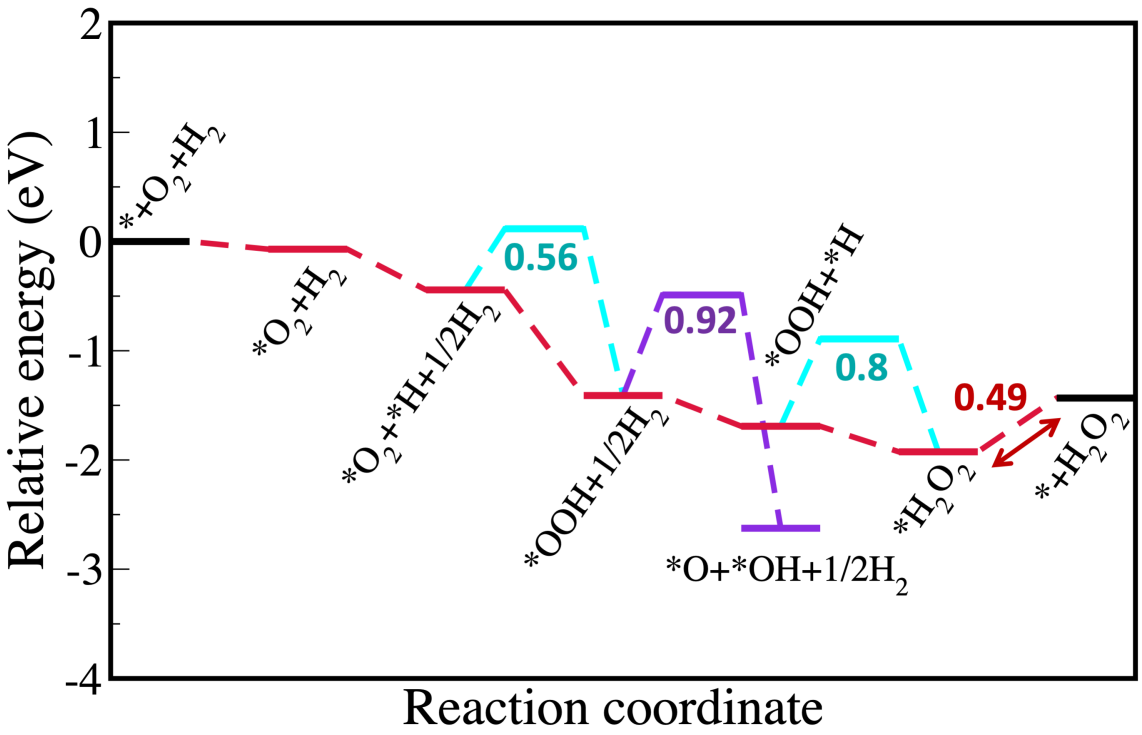

Figure 8.11: Relative activation energy diagram for direct synthesis of hydrogen peroxide (DSHP) on 2% Au_xMoS_{2-x-v}. Cyan curves indicate barriers along the DSHP pathway and purple curves indicate barriers for cleavage of O—O bond from the *OOH intermediate.

8.6 Analysis of electronic structure: mechanistic insights

We note that S-vacancies and Au-substitution, were introduced in MoS_2 monolayer to facilitate H adsorption and O_2 activation, respectively. Analysis of the PDOS of catalysts, and their interaction with key intermediates confirms this. Comparison of adsorption of O_2 on 1H-MoS_2 and Au_xMoS_{2-x} (Fig. 8.10a-d), shows that the highest occupied molecular orbital (HOMO) of O_2 retains its localized nature on 1H-MoS_2 and appears at the Fermi level. Upon substitution of Au at S-sites of 1H-MoS_2, HOMO of O_2 gets delocalized due to interaction with the surface states, primarily with Au-orbitals. This is also supported by visualizing the iso-surfaces of HOMO of O_2 adsorbed on 1H-MoS_2 (Fig. 8.10c) and Au_xMoS_{2-x} (2% Au) (Fig. 8.10f and g). Analysis of PDOS of H-atom adsorbed on

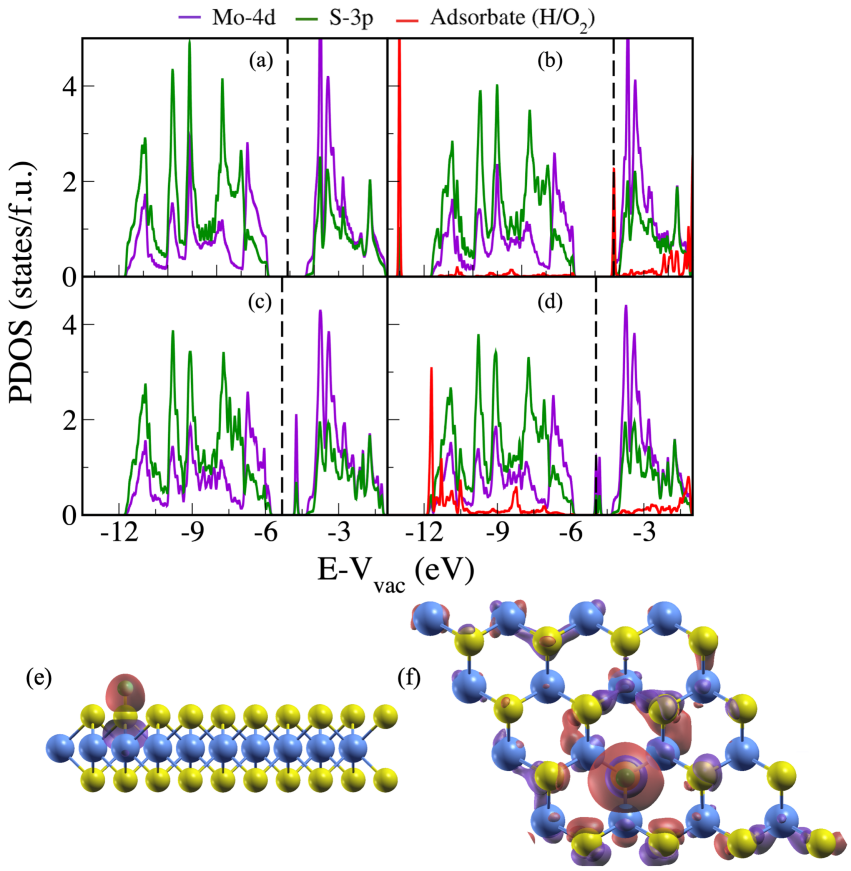

Figure 8.12: Projected density of states (PDOS) of (a) 1H-MoS_2, (b) 1H-$MoS_2$with adsorbed H, (c) 1H-MoS_{2-v}, and (d) 1H-MoS_{2-v} with adsorbed H. Iso-surfaces of wave functions depicting (e) discrete highest occupied molecular orbitals (HOMO) of H* on pristine 1H-MoS_2, (f) somewhat extended HOMO-like peak ($\sim$ -12 to -10 eV) of H* on 1H-MoS_{2-v}. Red and purple colors represent positive and negative iso-surfaces, respectively.

pristine 1H-MoS_2 and 1H-MoS_{2-v} (Fig. 8.12a-d), shows similar trends. HOMO of H-atom remains sharp and discrete (see Fig. 8.12b) indicating weak interaction. However, for H-atom adsorbed on MoS_{2-v}, HOMO of H broadens over a wide energy range, overlapping with the frontier states of the catalyst (see Fig. 8.12d) showing a covalent interaction. This is also evident in iso-surfaces of HOMO of H-atom adsorbed on pristine 1H-MoS_2 (Fig. 8.12e) and 1H-MoS_{2-v} (Fig. 8.12f). Finally, we examine the PDOS of Au_xMoS_{2-x-v} (2% Au) monolayer with O_2 and H adsorbed to ensure that both modifications continue to facilitate stabilization of respective adsorbates without affecting the other. As is evident in Fig. 8.13b, we identify signatures of optimal interaction of the orbitals of O_2 with Au

states. s-orbital of H-atom exhibits a covalent type bonding with the catalyst's surface states arising from S-vacancy. The synergy between Au-substitution at S-sites and S-vacancies in MoS_2 thus gives rise to superior catalytic activity and selectivity towards DSHP.

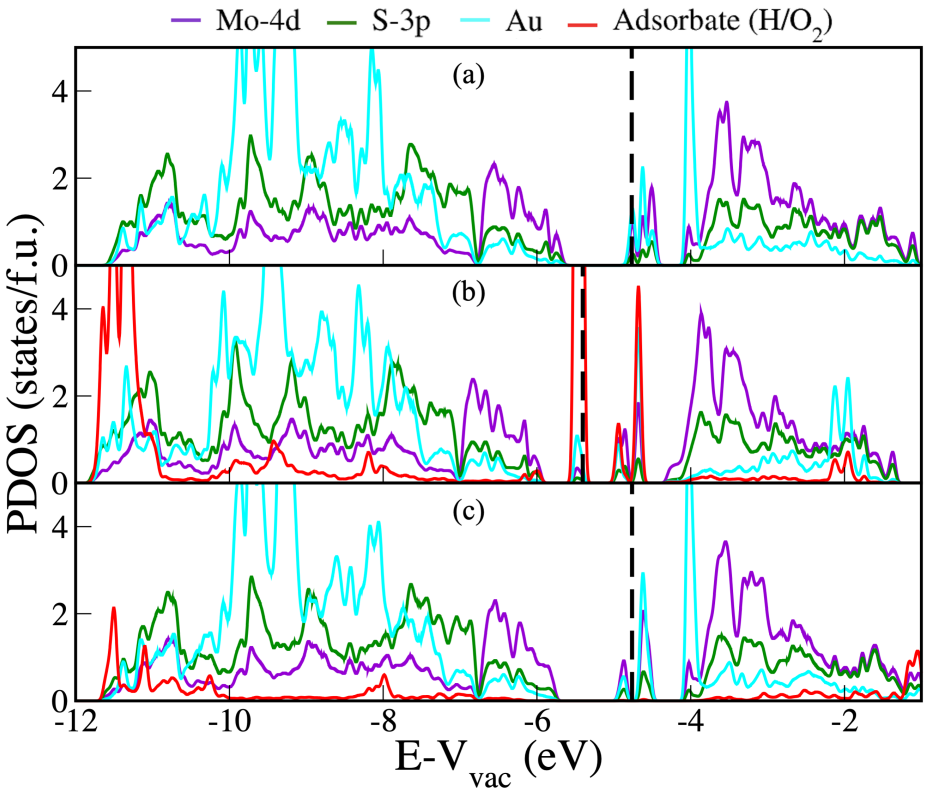

Figure 8.13: Projected density of states (PDOS) of $2\%Au_xMoS_{2-x-v}$, (a) without any adsorbates, with adsorbed (b) O_2, and (c) H. Black dashed lines denote the Fermi level.

8.7 Conclusions

Au_xMoS_{2-x-v} (MoS_2 monolayer with substitutional Au at S sites and S-vacancies) is proposed for the efficient catalysis of DSHP. Using first-principles density functional theory calculations, Au_xMoS_{2-x-v} is found to catalyze the complete reaction pathway of DSHP without any significant energy barriers. Mechanistically, Au substitution and S-vacancies have two different and crucial roles to play: while the former facilitates optimal activation of O_2, the latter assists H adsorption. Electronic mechanism of optimal adhesion of O_2

and H to Au_xMoS_{2-x-v} uncovered from analysis of electronic structure of the intermediates involved in the reaction pathway. Weak adsorption of O_2 and subsequent moderate activation of the O=O bond, indicate the high selectivity of Au_xMoS_{2-x-v} towards DHSP over ORR. Interestingly, Au substituted at Mo-sites ($Au_xMo_{1-x}S_2$) and Au-adatom (Ad Au_xMoS_2), exhibit strong O_2 adsorption and are expected to be selective towards ORR over DSHP. Optimized structures of intermediates along the reaction pathway show weak reconstruction of the catalyst structure implying its stability through large number of reuse cycles. Au_xMoS_{2-x-v}, with a reasonable formation energy, is expected to be feasible in terms of synthesis. Calculations of TSs and energy barriers indicate that hydrogenation of $^*OOH$ to H_2O_2 is favored over cleavage of the O=O bond making the catalyst selective for DSHP. Finally, Au_xMoS_{2-x-v}, is composed of earth-abundant elements (Mo and S) with small concentrations of Au. Our work shows how combining complementary strategies of vacancies and substitutional doping, can be effective in design of catalysts with good catalytic activity and selectivity. In the proposed catalyst, Au-substitution and S-vacancies work synergistically for the efficient catalysis of DSHP.

Chapter 9

Borophene based Metal-Free Catalysts for Electrochemical Reduction of Nitrogen

9.1 Introduction

Nitrogen trihydride (NH_3), more commonly known as ammonia, is an essential ingredient in most fertilizers. [77–79] Owing to its high hydrogen density and carbon-free footprint, its role as an energy carrier is also being explored. [80] NH_3 ranks second in tonnage of annual production and is only preceded by sulfuric acid. [258] Synthesis of NH_3 from nitrogen (N_2) relies on the thermocatalytic Haber-Bosch process, in which 1 mole of N_2 reacts with 3 moles of hydrogen (H_2) over an iron based catalyst. [81, 82] The reaction is carried out at high temperatures (600-700 K) and pressures ranging from 100-200 atm, making the process heavily energy demanding. [83] Electrocatalytic N_2 reduction reaction (eNRR) serves as a sustainable and carbon-free alternative to the Haber Bosch process to produce NH_3 owing to its ambient reaction conditions. [84, 85] The stride to identify

low-cost, highly efficient and selective catalysts which execute eNRR at a reasonable energy cost has resulted in intense research activity in the past decade. eNRR is a heterogeneous catalytic reaction involving six proton-coupled electron transfer (PCET) steps to produce NH_3 from N_2. Although hydrogenation of N_2 to NH_3 is exothermic11 (-46.1 $kJmol^{-1}$) [86], activation of the N_2 molecule remains a hurdle due to the inherent inertness of the strong triple bond [87] (dissociation energy = 945 $kJmol^{-1}$). Following this, the first hydrogenation step, ($^*N_2 + H \rightarrow {}^*NNH$), is generally the highest energy-demanding step. Furthermore, a catalyst with high selectivity towards eNRR is critical to suppress the competing hydrogen evolution reaction (HER). [88, 89] Thus, an ideal catalyst for eNRR should sufficiently activate N_2, catalyze the reaction at a low limiting potential (U_L), while mitigating HER. eNRR can proceed via three distinct routes: distal, alternating, and enzymatic. [89] These pathways differ from each other depending on the orientation of adhesion of N_2 (and other N_xH_y intermediates) on the surface of the catalyst.

Various materials have been explored as catalysts for NRR, including transition metals (TMs) like Mo, Fe, Rh, Ru, [259, 260] Au nanoparticles, [261–263] Ag nanodots, [264] Au/TiO_2, [265] Co nanotubes, [266] and other TM and noble-metal-based catalysts. In recent years, TMs embedded on substrates like BN, [267] MoS_2, [268, 269] borophene, [88, 270] graphene, [271] graphitic carbon (g-C_3N_4) [272, 273] have been extensively studied as catalysts for eNRR. These, metal-based catalysts are prone to poisoning, expensive, and offer poor selectivity, limiting their widespread usage. Metal-free catalysts, on the contrary, are cost-effective, environment-friendly, possess high durability, and are less susceptible to poisoning. Exploration of metal-free catalysts for eNRR thus holds great scientific and socioeconomic significance. Recently, several reports have focused on developing non-metallic catalysts for eNRR. Liu et al. synthesized a series of N-doped porous carbon catalysts [274] at different temperatures, which, owing to their intrinsic defects, exhibit high activity towards eNRR. Legare et al. showed the presence of B-to-N_2 back-donation of π electrons, similar to the π-backbonding in many TM-based catalysts for

eNRR, which facilitates weakening of the N≡N bond leading to subsequent activation of the $^*N_2$ adsorbate. This paved the way for extensive work exploring B atoms as active centers [275] for eNRR. Yu *et al* studied Boron-doped graphene [276] (BG) and showed an abundance of electron-deficient B centers, which serve as active sites for hydrogenation of N_2, a weak Lewis base. Sun and co-workers modelled 21 B-based NRR catalysts and identified B-adsorbed graphene (G-A) and B-substituted MoS_2 (h-S1) to be highly active towards eNRR [277]. They demonstrated a charge transfer from B-atoms to $N_2$2 leads to high selectivity towards NRR over HER and low NRR reaction barriers of 0.31 eV and 0.46 eV for GA and h-S1, respectively. Using first-principles calculations Ling *et al.* explored B embedded graphitic-carbon nitride (B/g-C_3N_4) for photocatalytic N_2 fixation and computed an onset potential of 0.20 V NRR, the lowest reported for a metal-free catalyst [272]. The introduction of B-atoms was also linked to reduction of the band-gap from 2.98 eV for pure g-C_3N_4 to 1.12 eV for B/g-C_3N_4, thus enhancing the IR and visible light absorption.

Borophene, the 2D allotrope of boron, was theoretically predicted by Tang *et al.* [278] over a decade ago and further explored by Wu *et al* [279] and Yakobson and co-workers [280]. Polymorphs of 2D boron sheets, can be generated by introducing hexagonal holes in various patterns within a triangular grid of boron atoms. These holes are characterized by the global density parameter (η) [279], which is defined as the ratio of hexagonal holes in a unit cell of a boron sheet to the number of atomic sites. The intrinsic holes present in the borophene sheets are essentially defects in a triangular lattice which may showcase some novel chemical applications. [281] Experimentally, two planar (β_{12}, χ_3) and one buckled polymorph of borophene were recently synthesized on Ag (111) substrate using molecular beam epitaxy in ultrahigh vacuum. [282,283] Consequently, numerous studies highlighting various applications of borophene sheets as gas sensors [284–286] H_2 storage material [80], electrodes for Li and Na-ion batteries [287, 288] have emerged. Catalytic performance of pristine and metal-decorated borophenes for various reactions like hydrogen evolution

reaction [289, 290] (HER), CO_2 capture, [291] CO_2 reduction, [292] oxygen evolution and oxygen reduction [293] has also been extensively studied. Theoretical studies focusing on catalysis of eNRR on pristine and TM anchored borophenes have gained attention in recent years. A single atom catalyst (SAC) comprising of Mo active centers was shown to exhibit high selectivity and activity towards NRR at a low U_L of -0.26 V on a β_{12} borophene substrate. [270] Sun and co-workers also showed that Ru embedded α borophene catalyzes NRR at a low energy barrier of 0.42 eV [294]. We aimed to test whether a similar catalytic performance can be obtained by replacing the metal atoms in borophene-based catalysts with a non-metal moiety.

We evaluated the catalytic performance of four borophene sheets, α ($\eta = \frac{1}{9}$), β_{12} ($\eta = \frac{1}{6}$), χ_3 ($\eta = \frac{1}{5}$) and δ_4 ($\eta = \frac{1}{4}$) with one B atom per supercell substituted by carbon. α borophene is predicted to be the most stable polymorph of borophene, making it a prime candidate for experimental isolation of a free-standing 2D boron sheet. β_{12}, χ_3 polymorphs have been experimentally isolated over an Ag (111) substrate, [282, 283] which motivated us to explore them as catalysts for eNRR. borophene features a high hexagonal hole density , and two inequivalent B-atoms, both four coordinated and only differing slightly in terms of the local chemical environment. We performed a thorough screening of 8 metal-free borophene based catalysts (4 pristine and 4 C-substituted) for eNRR *via* all three possible mechanisms, distal, alternating, and enzymatic. The 2D-boron catalysts are labelled on the basis of coordination number (cn) of the active site considered, for instance, C-atom substituted at a five coordinated site of χ_3 borophene is denoted by C@5cn_χ_3. Using comprehensive density functional theory (DFT) calculations, we show C@6cn_α exhibits a minimal U_L of -0.25 V for eNRR along the alternating pathway, suppresses HER, and efficiently activates N_2, thus meeting all three essential conditions for an ideal eNRR catalyst. Other catalysts like B-6cn_α, B@5cn_β_{12}, and B@4'cn_δ_4 also exhibit low limiting potentials ($|U_L| < 0.6$ V), surpassing some of the metal-based catalysts in the literature. We show these borophene-based catalysts stabilize the first

hydrogenated intermediate along the reaction pathway of eNRR, NNH, thus efficiently catalyzing the reaction. Charge transfer from the 2D-boron sheets to N_2 weakens the triple bond and activates the molecule leading to ease in hydrogenation. Additionally, C@6cn_α exhibits exothermic adsorption of N_2 and suppresses the competing HER making it an ideal metal-free catalyst for ammonia synthesis.

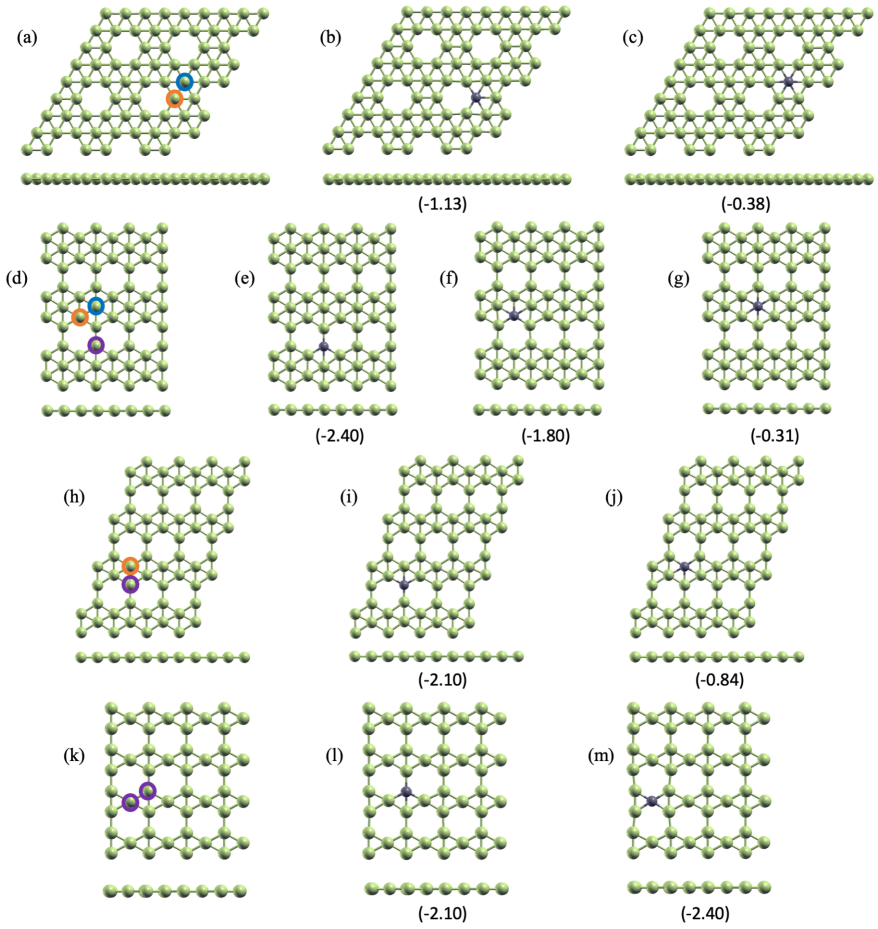

Figure 9.1: Optimized structures (top and side views) of pristine and C-substituted borophene sheets consisting of 3x3 supercell of α (a-c), 4x3 supercell of β_{12} (d-g), 4x3 supercell of χ_3 (h-j), 4x3 supercell of δ_4 (k-m) forms. Formation energies (in parenthesis) of C-substituted monolayers (b) C@5cn_α, (c) C@6cn_α, (e) C@4cn_β_{12}, (f) C@5cn_β_{12}, (g) C@6cn_β_{12}, (i) C@4cn_χ_3, (j) C@5cn_$_3$, (l) C@4cn_δ_4, and (m) C@4'cn_δ_4 are given in eV/C-atom. A negative formation energy corresponds to a stable substitution. Green and grey spheres represent B and C atoms, respectively. Purple, orange and blue circles in pristine borophene sheets mark B-atoms at 4cn, 5cn and 6cn sites, respectively.

9.2 Computational details

Our first-principles calculations are based on density functional theory (DFT) as implemented in the Quantum ESPRESSO [121] code employing a plane-wave basis set and PAW [256] pseudopotentials to represent the interaction between ionic cores and valence electrons. We adopt the exchange correlation energy functional of Perdew-Burke-Ernzerhof (PBE) [99] within a generalized gradient approximation (GGA), and occupation numbers of electronic states have been smeared with Fermi–Dirac distribution and a smearing width (k_BT) of 0.04 eV. Additionally, van der Waals (vdW) interactions using the Grimme scheme [135] have been included to account for weak interactions. A kinetic energy cutoff of 40 Ry on the plane-wave basis is used in the representation of the Kohn Sham wave functions, and a cutoff of 320 Ry to represent the charge density. Structures are determined through minimization of energy until the Hellmann-Feynman forces on each atom are smaller than 0.03 eV/Å in magnitude. The transition states (TS) were obtained using the nudged elastic band (NEB) method [107]. Five images were used in all NEB calculations. All TSs were relaxed until the Hellmann–Feynman forces acting on the atoms were within 0.05 eV/Å. Supercells consisting of 3×3, 4×3, 4×4 and 4×4 units of α, β_{12}, χ_3 and δ_4 borophene, respectively, are used to model the various catalysts, and a vacuum layer of 20 Åthickness is introduced separating adjacent periodic images. The catalysts studied in this work are shown in Fig. 9.1, and the stoichiometry of the supercells is given in Table 9.1. Brillouin-zone integrations were sampled on a uniform grid of 6×6×1, 5×5×1, 5×3×1, and 5×5×1 k points for α, β_{12}, χ_3 and δ_4 borophene sheets, respectively. The projected density of states (PDOS) of each structure was calculated using 18×18×1, 15×15×1, 15×9×1, and 15×15×1 k-mesh for α, β_{12}, χ_3 and δ_4 borophene sheets, respectively. Calculated lattice constants of bulk α, β_{12}, χ_3 and δ_4 borophene are listed in Table 9.2 and are well within the typical GGA errors with respect to experimentally observed values [279]. The interaction strength between adsorbate

	Label	% C	Stoichiometric formula
1	α	-	B_{72}
2	C@α	1.39	$B_{71}C$
3	β_{12}	-	B_{60}
4	Cβ_{12}	1.67	$B_{59}C$
5	χ_3	-	B_{64}
6	C@χ_3	1.56	$B_{63}C$
7	δ_4	-	B_{48}
8	C@δ_4	2.08	$B_{47}C$

Table 9.1: Borophene monolayers considered in this work, with the stoichiometric formula of the supercell.

Borophene	Calculated		Experimental	
	a(Å)	b(Å)	a(Å)	b(Å)
α	5.057	5.057	5.05	5.05
β_{12}	2.927	5.07	2.91	5.04
χ_3	2.91	4.445	2.9	4.437
δ_4	2.95	3.32	2.93	3.28

Table 9.2: Calculated and experimental lattice parameters of various borophene monolayers considered in this work.

and the borophene monolayer is evaluated using:

$$\Delta E_{ads} = E_{complex} - (E_{monolayer} + \mu_{adsorbate}) \tag{9.1}$$

where, $E_{complex}$, $E_{monolayer}$, $\mu_{adsorbate}$ are the energies of adsorbate-borophene monolayer complex, pristine/C-substituted borophene monolayer and chemical potential of isolated adsorbate. Following convention has been followed for energies of isolated adsorbates:

- $\mu_{N_2} = E_{N_2}$
- $\mu_N = E_{N_2H_2}$ - $\frac{1}{2}E_{H_2}$

where, $E_{N_2H_2}$, E_{N_2} and E_{H_2} are the DFT calculated energies of isolated N_2H_2, N_2 and H_2 molecules respectively.

The Gibbs free energies (ΔG) of each step along the reaction pathway at $T = 298$ K is

determined using:

$$\Delta G = \Delta E - T\Delta S + \Delta E^{ZPE} - neU \tag{9.2}$$

where, ΔE, TΔS, ΔE^{ZPE}, n and U are the changes in enthalpy (from DFT total energy), zero-point energy, entropy, number of electrons transferred and the applied potential respectively.

Limiting potential (U_L), defined as the externally applied voltage at which all reaction steps are spontaneous is calculated as:

- $U_L^{NRR} = \frac{-\Delta G_{MAX}}{e}$
- $U_L^{HER} = \frac{-|\Delta G^H_{ads}|}{e}$

where, $-\Delta G_{MAX}$ and ΔG^H_{ads} is the Gibbs free energy of the potential determining step for NRR and Gibbs free adsorption energy of H-atom, respectively.

9.3 Structural and electronic properties of borophene sheets

2D boron sheets are predicted to exist in multiple buckled and planar polytypes with different η values. These monolayers are classified into five categories based on the local coordination of B atoms. [279] Here, we present a detailed study of four borophene sheets, α, β_{12}, χ_3 and δ_4 (Fig. 9.1) as catalysts for eNRR and study the effect of C-substitution on their catalytic activity. Formation energies (E_{form}) of C-substituted boron monolayers are estimated using

$$E_{form} = E_{C@Borophene} - [E_{Borophene} - E_B + E_C] \tag{9.3}$$

where, $E_{C@Borophene}$, $E_{Borophene}$, E_B, E_C are the energies of C-substituted borophene monolayer, pristine borophene monolayer, isolated B and C atoms, respectively.$E_{form} < 0$ corresponds to a stable substitution. The planar structure of all four borophenes remains unaltered upon C-substitution (Fig. 9.1). Interestingly, C-substitution is more favorable at a site with lower cn. We explore this further using electronic structures of pristine and C-substituted borophenes.

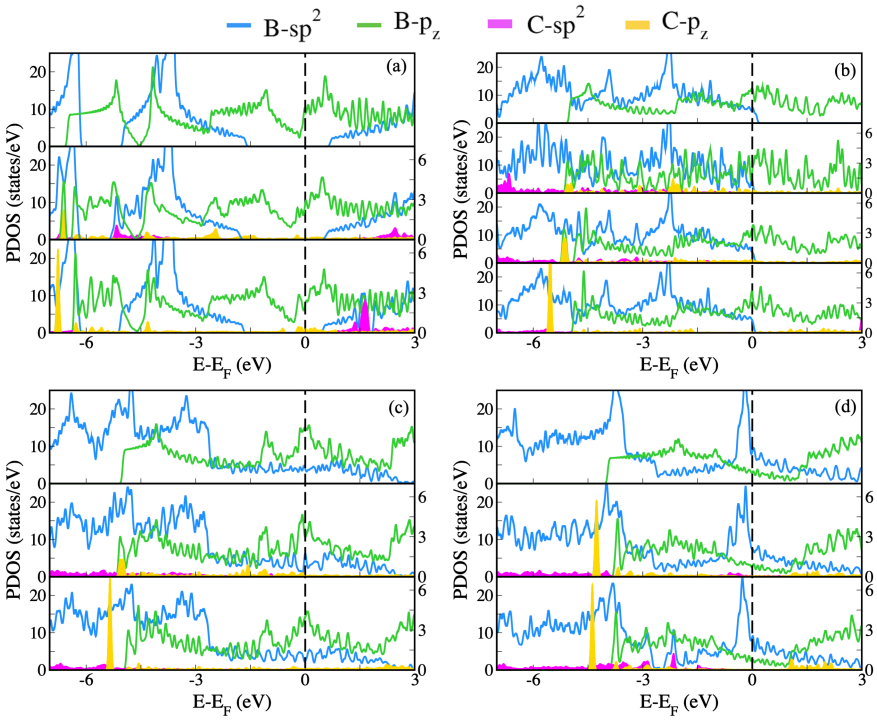

Figure 9.2: Density of states (PDOS) projected onto the in-plane (sp^2 hybridized states) and out-of-plane orbitals (p_z orbitals) of pristine and C-substituted (a) α, (b) β_{12}, (c) χ_3 and (d) δ_4 forms of borophenes (E_F=0). Top part of each panel has the PDOS of pristine borophene sheet while the others show PDOS of C-substituted borophenes with increasing coordination of the substituted C (middle and top parts). Alternate y-axis represents the PDOS of C-substituent.

Analysis of density of states (PDOS) projected onto the in-plane (sp^2 hybridized states) and out-of-plane orbitals (p_z orbitals) highlights the effect of C-substituents on the electronic structure of α, β_{12}, χ_3 and δ_4 borophene sheets. The metallic nature of borophene sheets is retained upon the introduction of C-atom in the lattice (Fig. 9.2). Substituting

one B-atom per supercell of borophene with C, brings an extra electron in the system, leading the Fermi level (E_F) to shift up. This n-type doping due to C-substituents stabilizes the otherwise electron-deficient borophene sheets. This is evident in PDOS of C-substituted borophenes in which the B-sp^2 states shift lower in energy indicative of a stabilization effect (Fig. 9.2); however, the nature of interaction of C orbitals differ with the local chemical environment in the borophene sheet. This effect is most prominent in borophene, where the in-plane bonding states are partially unoccupied (Fig. 9.2b top panel), leading to a less stable configuration as compared to the fully occupied sp^2 bonding states in α. It was recently shown that the 6-coordinated B-atoms in the β_{12} borophene majorly show a π bonding character, while B-atoms with lower cn (4cn and 5cn) contribute to the in-plane (σ) bonds. [295, 296] A similar trend is followed by C-substituents based on the local coordination of the substitution site. States arising from C-p_z orbitals become more notable as we go from C@4cn_β_{12} to C@6cn_β_{12} (Fig. 9.2b). Thus, a C with a lower cn (4cn) interacts with the in-plane sp^2 hybridized states of the lattice while a C@6cn primarily exhibits a π (p_z) type bonding. Since σ interaction provides more stability than π, energy gained by β_{12} sheets upon C-substitution decreases as we go from 4cn to 6cn (Fig. 9.1e-g, and Fig. 9.22b). This trend also emerges in the other borophene sheets with multiple coordination environments (α and χ_3) (Fig. 9.1b, c and i, j and Fig. 9.2a, c). In the δ_4 polymorph, all B-atoms are 4-coordinated but are not chemically equivalent, labelled here as 4cn and 4'cn. Despite having the same cn, a B-atom at the 4cn site forms three equivalent bonds (forming a triangle) however, the fourth bond is slightly smaller. All bonds formed by 4'cn B-atom are equivalent and have the same bond length. Thus, substituting a C-atom at the two inequivalent sites (4cn and 4'cn) leads to a comparable gain in energy. The stabilizing effect of C-substitution in borophene sheets supports the viability of their experimental synthesis.

9.4 Reaction pathways of eNRR

To assess the catalytic performance of these borophene sheets towards eNRR, we simulated the adsorption of various intermediates occurring along the three reaction pathways at all possible inequivalent surface sites, starting with N_2. The primary difference between the distal, alternating, and enzymatic pathways is the orientation of N_2 adsorbed on the catalyst's surface. End-on adsorbed N_2 can proceed via the distal or alternating pathway, while a side-on adsorbed N_2 takes the enzymatic route (Fig. 1.8). Along the distal pathway, the dangling N-atom gets fully hydrogenated to NH_3, following which the N-atom attached to the surface of the catalyst (*N) undergoes three PCET steps releasing the second ammonia molecule. Whereas, both N atoms are targeted alternatively by incoming protons in the alternating pathway, and the first NH_3 is released at the 5^{th} PCET step. Similar alternate hydrogenation of N occurs via the enzymatic pathway, the only difference being that each intermediate is oriented in a side-on fashion. All three pathways start with adsorption of N_2 and activation of N≡N, vital for the subsequent steps. N_2 adsorption on most borophene sheets is non spontaneous in almost all cases irrespective of the orientation (Table 9.3), exhibiting an energy cost ranging from 0.2 eV to 1.0 eV. C@6cn_α, however, stabilizes the $^*N_2$ adsorbate, and -0.75 eV of energy is gained of upon adsorption. Other catalysts like C@5cn_α, B@6cn_α, and C@4cn_δ_4 have a low N_2 activation cost ($\sim$0.2 eV) associated with them. N_2 adsorption is followed by 6 PCET steps, generating various N_xH_y intermediates, eventually yielding NH_3 as the product.

9.5 Energetics of the reaction pathways

A total of 54 eNRR scenarios constituting of all inequivalent surface sites were compared using free energy diagrams (Fig. 9.3, 9.4, 9.5, 9.6), among which C@6cn_α, B@6cn_α, B@5cn_χ_3, and B@4'cn_δ_4 exhibit a low U_L ($|U_L| < 0.6$ V) (Fig. 9.7). N_2 reduction

Borophene	Adsorption Site	$\Delta G_{ads}^{N_2}$ (eV)		N≡N bond length (Å)	
		End-on	Side-on	End-on	Side-on
α	B@5cn	0.21	0.23	1.13	1.11
	B@6cn	0.24	0.22	1.14	1.11
	C@5cn	-0.07	-0.04	1.11	1.11
	C@6cn	-0.74	-0.63	1.13	1.11
β_{12}	B@4cn	0.46	0.33	1.13	1.11
	B@5cn	0.58	0.33	1.13	1.11
	B@6cn	0.35	0.33	1.11	1.11
	C@4cn	0.34	0.33	1.11	1.11
	C@5cn	0.33	0.34	1.11	1.11
	C@6cn	0.33	0.31	1.11	1.11
χ_3	B@4cn	0.67	0.33	1.13	1.11
	B@5cn	0.91	0.33	1.13	1.11
	C@4cn	0.34	0.34	1.11	1.11
	C@5cn	0.33	0.32	1.11	1.11
δ_4	B@4cn	1.00	0.34	1.13	1.11
	B@4'cn	1.00	0.35	1.13	1.11
	C@4cn	0.20	0.22	1.11	1.11
	C@4'cn	0.30	0.30	1.11	1.11

Table 9.3: Adsorption energies and bond length for N_2 in end-on and side-on orientation on B/C sites of pristine/C-substituted borophenes.

on C@6cn_α and B@4'cn_δ_4 prefers the distal pathway while on B@6cn_α and B@5cn_χ_3 the reaction follows alternating and enzymatic pathways, respectively. The addition of a second H, i.e., formation of $^*NNH_2$ from $^*NNH$, is the potential determining step (PDS) for C@6cn_α while hydrogenation of $^*N_2$ is PDS for the other three catalysts. B@6cn_α and B@5cn_χ_3 catalyze N_2 reduction with U_L of -0.33 V and -0.40 V, respectively; however, the adsorption of N_2 on these monolayers requires a small energy input (0.24 eV and 0.33 eV, respectively). B@4'cn_δ_4 also showcases a reasonable U_L of -0.55 V for the distal hydrogenation of N_2, but significant energy (∼1.00 eV) is needed to facilitate N_2 adsorption on the monolayer. C@6cn_α adsorbs N_2 exothermically (-0.75 eV) and exhibits the lowest U_L (-0.25 V) of all catalysts studied here to produce NH_3 via the distal pathway.

Introducing a C-atom in 3×3 supercell of α borophene not only reduces the U_L for eNRR but also facilitates adsorption of N_2 molecule. Additionally, the desorption of the second NH_3 requires high energy input in most cases, making it the rate-determining step (RDS). However, in an experimental setup, protons from acidic solutions combine with NH_3 to produce NH_4^+ ions making the final step essentially spontaneous.

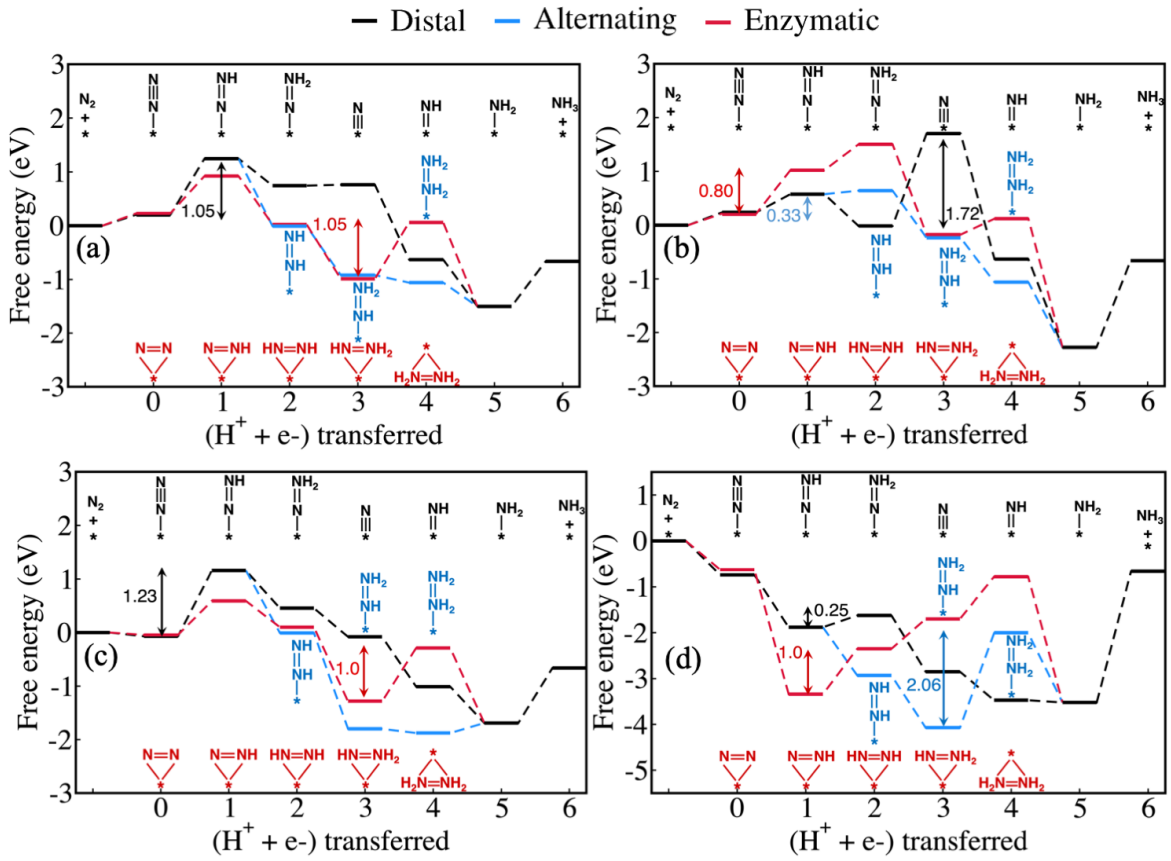

Figure 9.3: Free energy profiles for electrochemical nitrogen reduction via distal, alternating and enzymatic pathways on (a) B@5cn_α, (b) B@6cn_α, (c) C@5cn_α, and (d) C@6cn_α. All energies in eV.

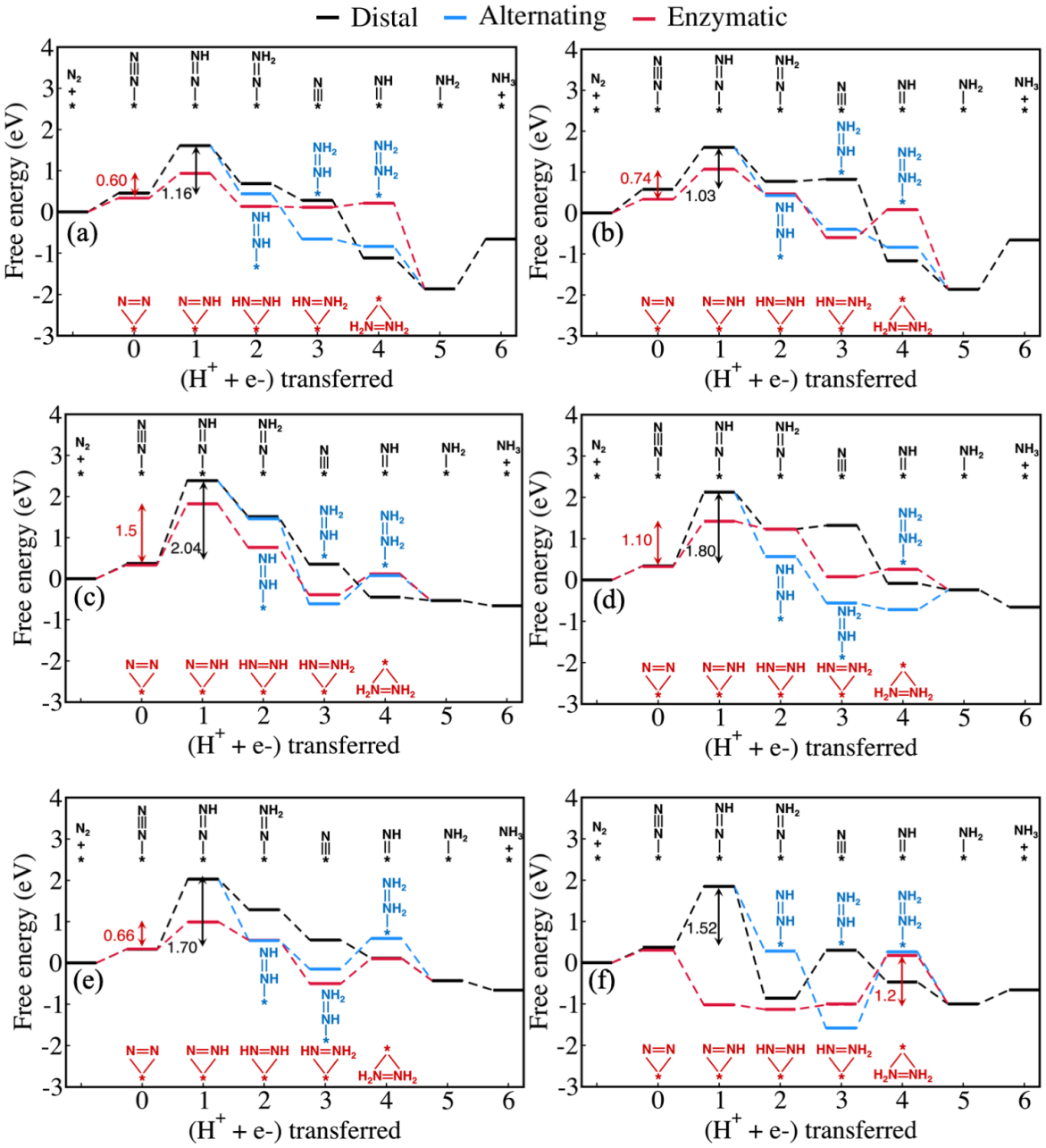

Figure 9.4: Free energy profiles for electrochemical nitrogen reduction via distal, alternating and enzymatic pathways on (a) b@4cn_β_{12}, (b) B@5cn_β_{12}, (c) B@6cn_β_{12}, (d) C@4cn_β_{12}, (e) C@5cn_β_{12}, and (f) C@6cn_β_{12}. All energies in eV.

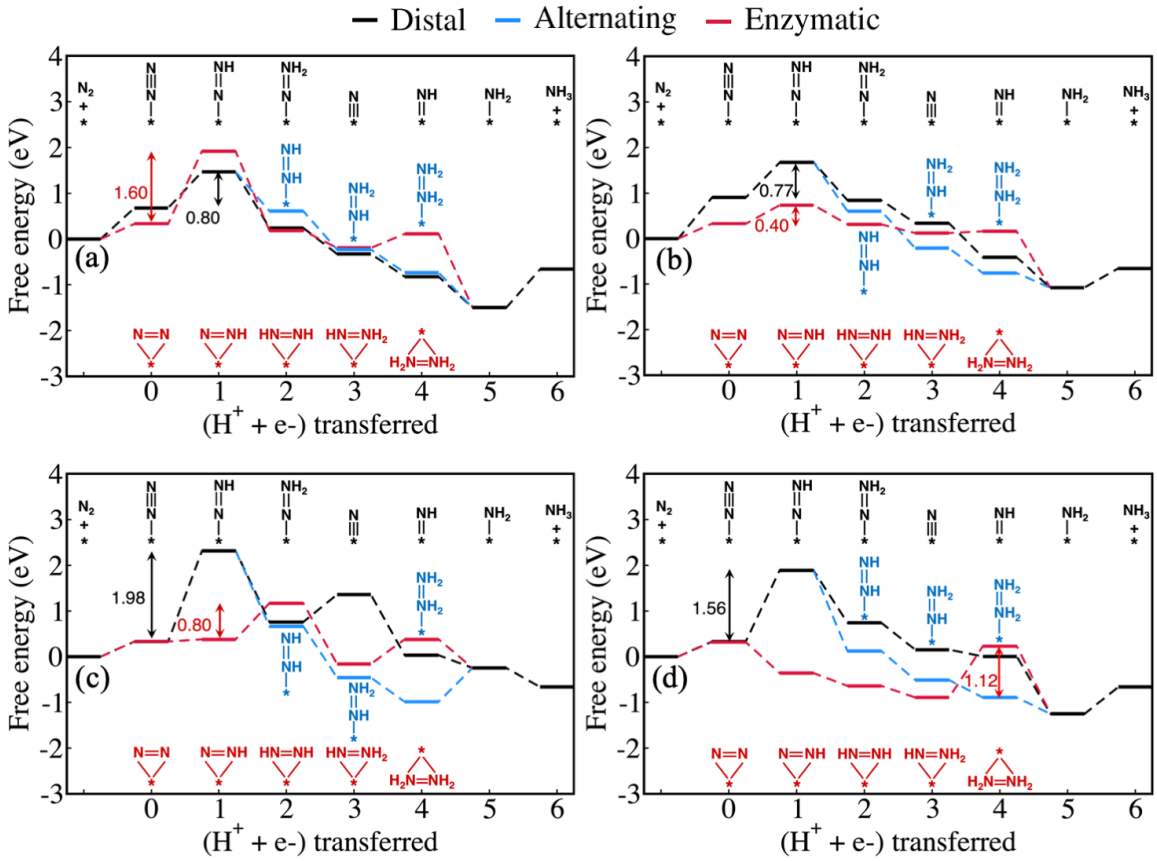

Figure 9.5: Free energy profiles for electrochemical nitrogen reduction via distal, alternating and enzymatic pathways on (a) B@4cn_χ_3, (b) B@5cn_χ_3, (c) C@4cn_χ_3, and (d) C@5cn_χ_3. All energies in eV.

We explore the energetics of each hydrogenation step along the three reaction pathways of eNRR (Fig. 1.8), taking C@6cn_α as an example (Fig. 9.8). N_2 adsorbs exothermically on C@6cn_α in both side-on (-0.62 eV) and end-on (-0.75 eV) configurations, the latter being more spontaneous. Here, $^*N_2$ (end-on) binds to a neighboring B-site with a bond length of 1.48 Å, and the NN bond length elongates from 1.11 Å (isolated N_2) to 1.14 Å. Along the distal pathway, the formation of various N_xH_y intermediates (*NNH, *N, *NH, $^*NH_2$) is exothermic by -1.14 eV, -1.22 eV, -0.62 eV, and -0.05 eV, respectively. The second hydrogenation step ($^*NNH + H^+ + e^- \rightarrow {}^*NNH_2$) is uphill by 0.25 eV and thus serves as the PDS. Along the alternating pathway, second H^+ attacks the *N of *N-*NH forming *NH-*NH.

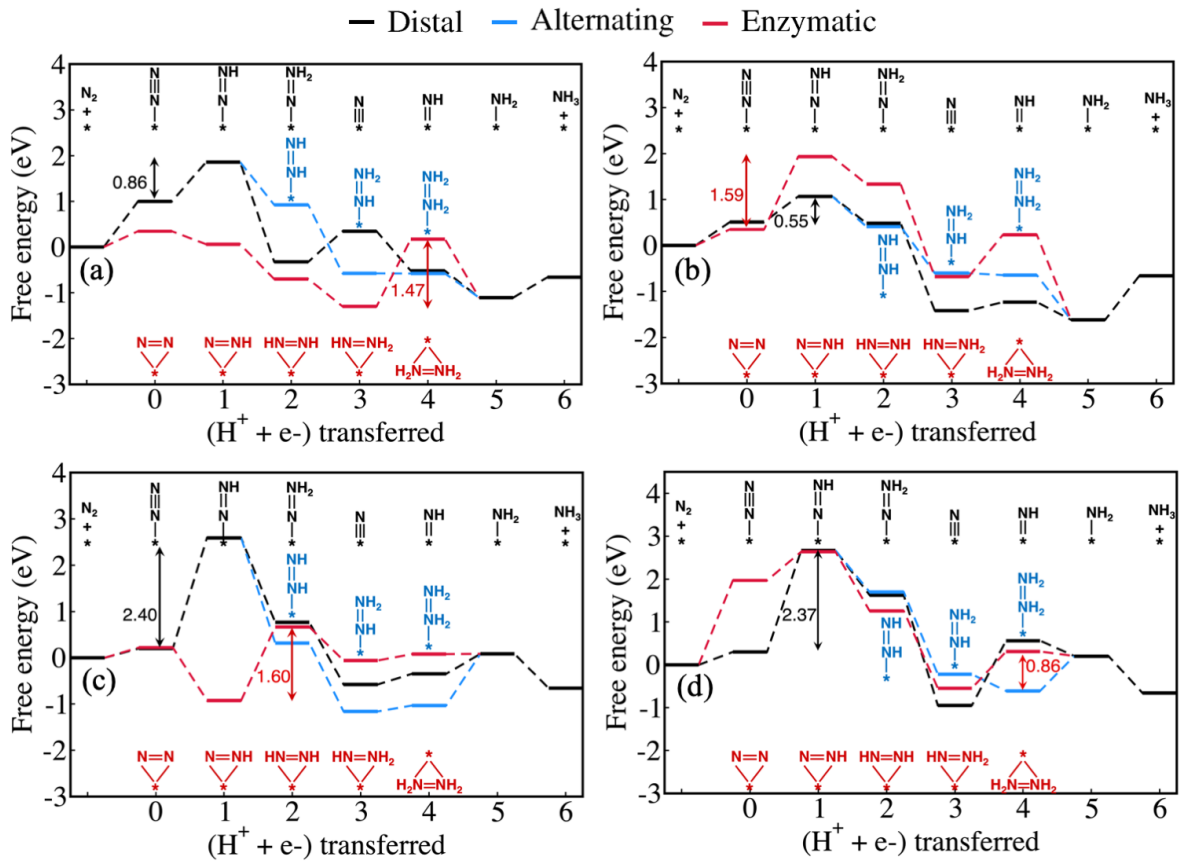

Figure 9.6: Free energy profiles for electrochemical nitrogen reduction via distal, alternating and enzymatic pathways on (a) B@4cn_δ_4, (b) B@4'cn_δ_4, (c) C@4cn_δ_4, and (d) C@4'cn_δ_4. All energies in eV.

The fourth PCET (*NH-*NH_2 + $H^+ + e^- \rightarrow$ *NH_2-*NH_2) along the alternating pathway requires a high energy input of 2.06 eV, making the reaction unfeasible on C@6cn_α via this route. Finally, in the enzymatic pathway, N_2 adsorbs in a side-on orientation on the surface of the catalyst. Formation of *N-*NH and *NH2 is exothermic by -2.74 eV and -2.70 eV, respectively, while *NH-*NH, *NH-*NH_2, and *NH_2-*NH_2 intermediates require energy of 1.00 eV, 0.65 eV, and 0.92 eV. PDS along the enzymatic pathway is *N-*NH + $H^+ + e^- \rightarrow$ *NH-*NH with a ΔG of 1.00 eV, comparable to the bulk Ru catalyst. [297] Thus, reduction of N_2 to NH_3 is most feasible on C@6cn_α *via* the distal pathway.

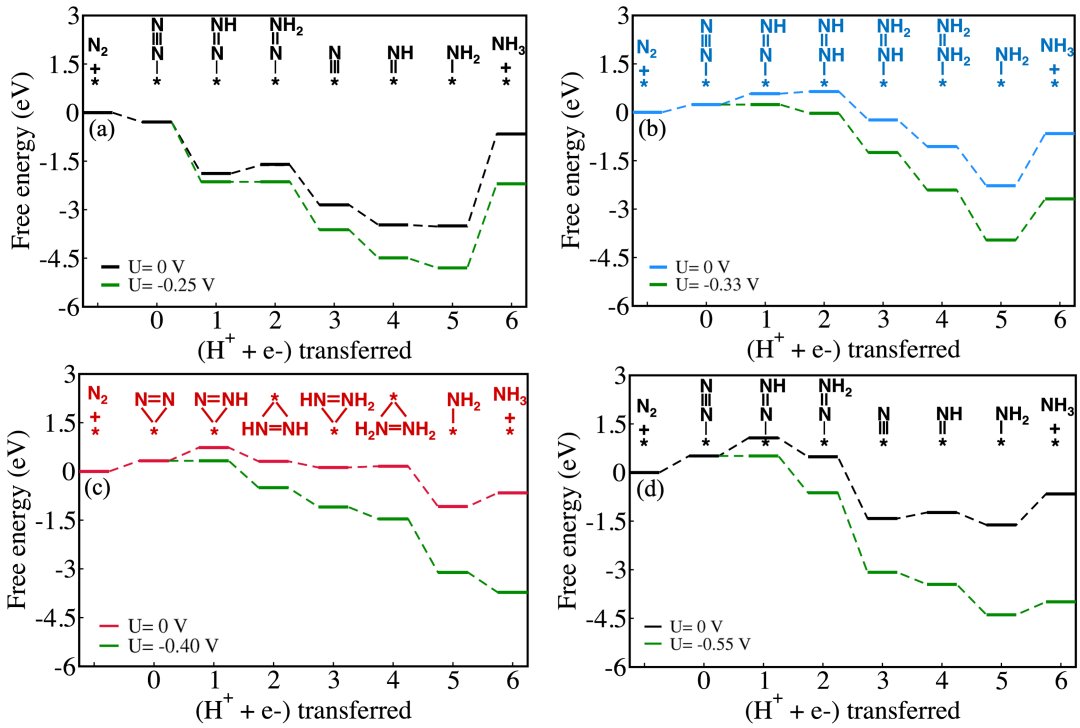

Figure 9.7: Free energy profiles of electrochemical nitrogen reduction on (a) C@6cn_α, (b) B@6cn_β_{12}, (c) B@5cn_χ_3, and (d) B@4'cn_δ_4. Reactions in (a) and (d) proceed along the distal pathway, while (b) and (c) follow alternating and enzymatic routes, respectively. The green curves show eNRR at applied potential, different for each catalyst.

9.6 Selectivity

Along with the ability of a catalyst to execute eNRR at low U_L, its selectivity towards NRR over the competing hydrogen evolution reaction (HER), is also crucial. To comment on the HER activity of the borophene sheets, we simulated adsorption of H-atom and calculated its Gibbs free energy of adsorption (ΔG^H_{ads}), a well-known descriptor for HER. [124] ΔG^H_{ads} close to zero is considered optimal for an efficient catalyst for HER. Fig. 9.9 shows the difference between U_L for eNRR and HER as a function of U_L (eNRR) [298], illustrating both the activity and selectivity of a catalyst towards eNRR. As discussed earlier, C@6cn_α, and B@6cn_α, B@5cn_χ_3 , and B@4'cn_δ_4 execute eNRR at low U_L ($|U_L| < 0.6$ V) (Fig. 9.7); however, only the former two also exhibit high selectivity towards eNRR over HER (Fig. 9.9). C@6cn_α demonstrates least affinity for HER and

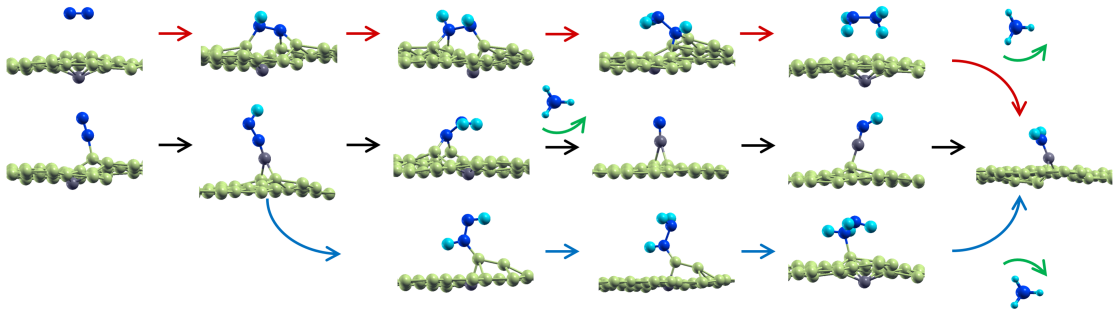

Figure 9.8: Optimized structures of intermediates occurring along the enzymatic (red), distal (black), and alternating (blue) reduction of N_2 on C@6cn_α. Green, grey, blue and cyan spheres represent B, C, N and H atoms, respectively.

exceptional activity towards eNRR making it an ideal catalyst for N_2 reduction. Finally, we explore the underlying mechanisms for the activity of these borophene based catalysts towards eNRR.

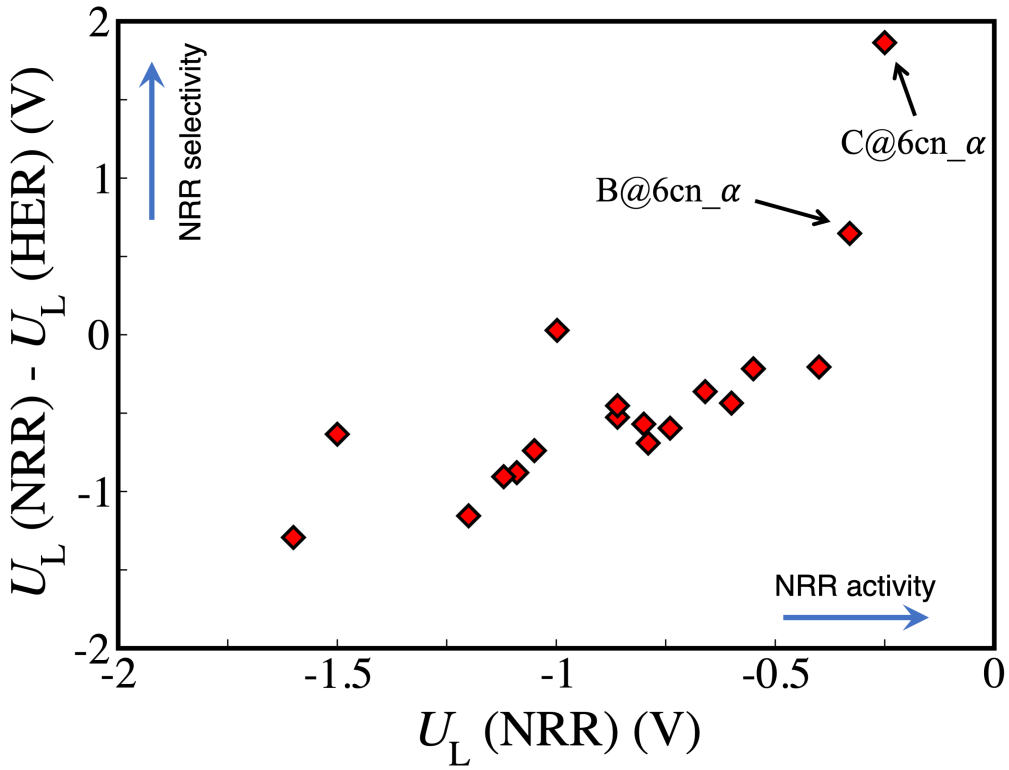

Figure 9.9: Selectivity of borophene catalysts with respect to NRR and HER described using limiting potential (U_L). U_L(NRR) – U_L(HER) as a function of U_L(NRR) give measures of activity (x-axis) and selectivity (y-axis) of various borophene catalysts towards eNRR.

9.7 Mechanistic insights

Across the 54 eNRR scenarios considered here, activation of $^*N_2$ and its hydrogenation to $^*NNH$ emerge as the two critical criteria for a highly efficient catalyst. Transition-metal based catalysts, owing to a combination of filled and empty d-orbitals, are well known to accept and back-donate electrons from and to N_2, [259, 275, 298] respectively, resulting in excellent eNRR catalytic activity. Back-donation of electrons to the unoccupied anti-bonding orbital ($1\pi^*$) of N_2 weakens its triple bond and promotes its adsorption leading to NN bond activation on the surface of the catalyst. Boron possesses filled and empty p-orbitals and exhibits a similar 'acceptance-donation' interaction with N_2. To understand the charge transfer between $^*N_2$ and our catalysts, we calculated Bader charges [299] of $^*N_2$ adsorbed on borophene sheets with respect to isolated N_2 molecule. In most cases, we observed a transfer of electrons from borophene sheets to the molecule accompanied by an elongation of the N*equiv*N bond. These excess electrons occupy the antibonding π^* orbitals of $^*N_2$, activating its triple bond. We note that U_L decreases (in magnitude) logarithmically with number of electrons gained by $^*N_2$ on our catalysts. For a small amount of charge transfer ($\Delta e < 0.05$ e$^-$) from borophene sheets to $^*N_2$, there is sharp decrease in $|U_L|$ (Fig. 9.10a), followed by a linear pattern (0.05 e$^-$ $< \Delta e$). Our most efficient catalyst, C@6cn_α, showcases a high charge transfer ($\sim$0.6 e$^-$) to the $^*N_2$ molecule, resulting in a highly activated triple bond. $\Delta G_{ads}^{N_2}$ further supports this observation with C@6cn_α showcasing spontaneous N_2 adsorption (-0.75 eV). B@6cn_α, B@5cn_χ_3, and B@4'cn_δ_4 catalysts exhibit a significant charge transfer ($\Delta e > 0.5$ e$^-$) to $^*N_2$ but adsorb N_2 endothermically, albeit with a small energy input. This is expected as the loss of electrons from electron-deficient pristine borophene sheets destabilizes them further, making the process uphill. The partial density of states (PDOS) also substantiates the backdonation of electrons from borophene sheets to the anti-bonding orbital ($1\pi^*$) of N_2. The lowest unoccupied molecular orbital (LUMO) of $^*N_2$ broadens and new states appear just

below the E_F, resonant with the $2p_z$ states of B and C. Compared to the sharp LUMO of an isolated N_2 molecule, 1π orbital of $^*N_2$ gets partially occupied when adsorbed on C@6cn_α (Fig. 9.10b), and B@6cn_α (Fig. 9.10c). Thus, Δe can be used as a quantitative descriptor for the degree of N_2 activation and can be used for screening a broad range of catalysts for eNRR.

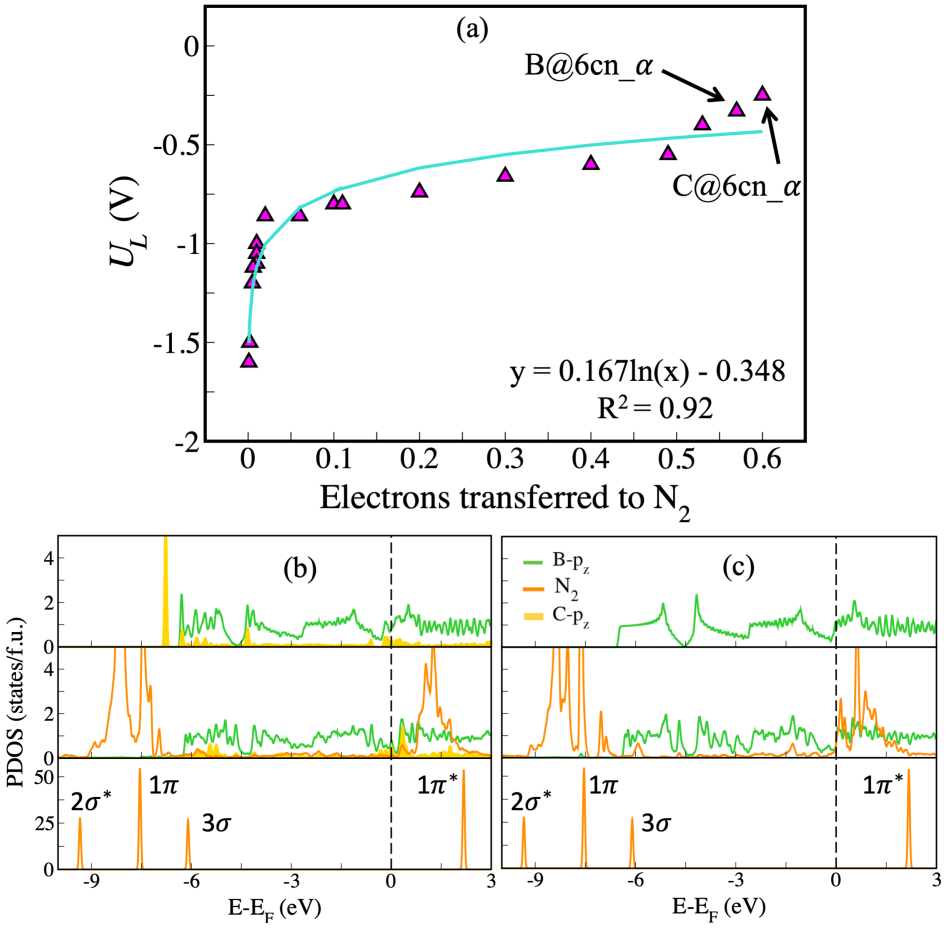

Figure 9.10: Limiting potential (U_L) of various configurations and sites of borophene sheets for electrochemical N_2 reduction as a function of (a) number of electrons transferred to N_2 upon adsorption. Density of states (PDOS) projected onto the out-of-plane orbitals (p_z orbitals) of (b) $^*N_2$ B@6cn_α, and (c) C@6cn_α. Top, middle and bottom panel show the PDOS for borophene monolayer, $^*N_2$ adsorbed on the monolayer, and isolated N_2 molecule, respectively (E_F=0).

As mentioned earlier, activation of the triple bond in an N_2 molecule is generally the bottleneck for most NRR catalysts, and thus the first hydrogenation step ($^*N_2 + H^+ +$

$e^- \rightarrow {}^*NNH$) is widely accepted as the PDS. To facilitate this step, activation of ${}^*N_2$ and stabilization of ${}^*NNH$ moiety are equally important. To comment on the latter, we calculated the Gibbs free adsorption energy of ${}^*NNH$ (ΔG_{ads}^{NNH}). The limiting potential (U_L) for each catalyst along its most efficient eNRR pathway correlates linearly with ΔG_{ads}^{NNH} (see Fig. 9.11), further validating their viability to efficiently catalyze N2 reduction. Both C@6cn_α, and B@6cn_α show a high stabilization of ${}^*NNH$ intermediate, thus facilitating the first hydrogenation step. This directly connects with excess electrons on ${}^*N_2$ (discussed above) as a negatively charged ${}^*N_2$ would attract incoming protons and undergo hydrogenation to form ${}^*NNH$. ΔG_{ads}^{NNH} can thus be employed, in tandem with Δe as a descriptor of the ability of various NRR catalysts to execute the first hydrogenation step, which in most cases, is the PDS. A combination of spontaneous adsorption of ${}^*N_2$ ($\Delta G_{ads}^{N_2}$ = -0.75 eV), a consequence of Δe from the catalyst to N_2, stable adsorption of ${}^*NNH$, high selectivity over HER and a vanishingly small U_L (-0.25 V) make C@6cn_α a prime candidate for catalyzing eNRR.

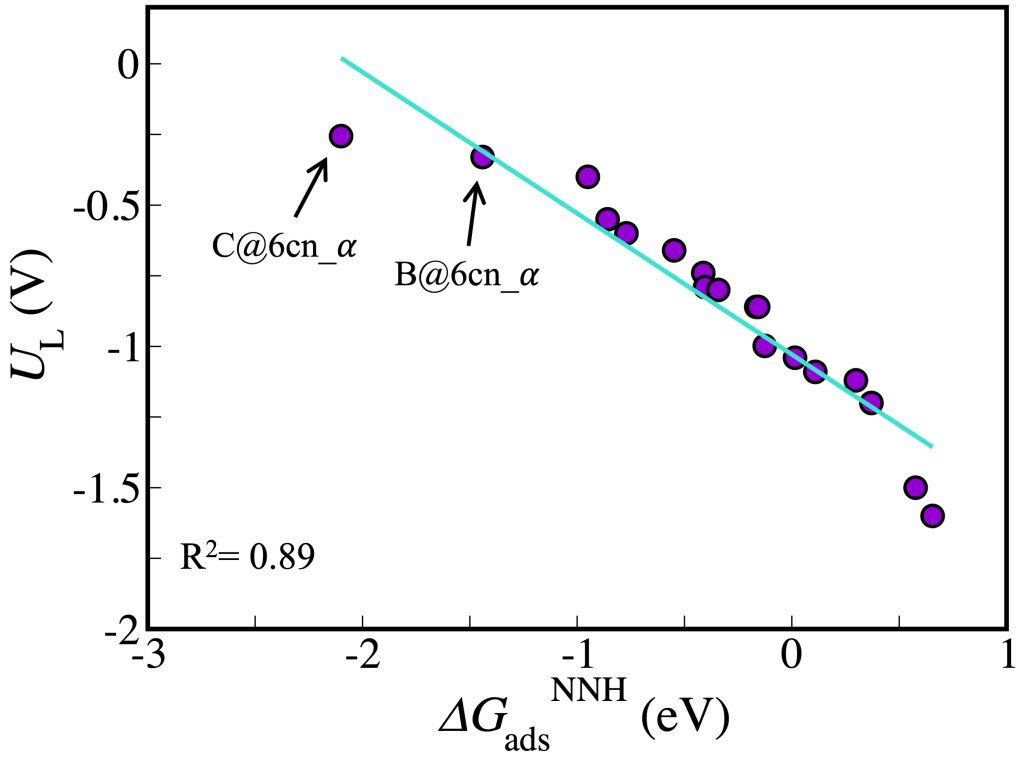

Figure 9.11: Limiting potential (U_L) of various borophene sheets for electrocatalytic N_2 reduction as a function of ΔG_{ads}^{NNH}.

9.8 Kinetics of eNRR

Kinetics of a catalytic reactions determines the practical viability of the catalyst. We use NEB calculations to determine the activation barriers for each elementary step along the distal pathway of N_2 reduction on our most efficient catalyst, C@6cn_α. Reaction steps involving adsorption/desorption of a free molecule (N_2/NH_3) on the surface occur without any barriers. Kinetic barriers are encountered for the 4 hydrogenation steps, formation of NNH, NNH_2, NH and NH_2, 0.27 eV, 0.51 eV, 0.40 eV and 0.56 eV, respectively. The rate determining step (RDS) is hydrogenation of NH to form NH_2 with a barrier of 0.56 eV Fig. 9.12. This is much lower than the activation barrier reported on B-doped graphene and B-substituted MoS_2 by Sun *et. al.* indicating excellent kinetics can be expected from our borophene based catalyst.

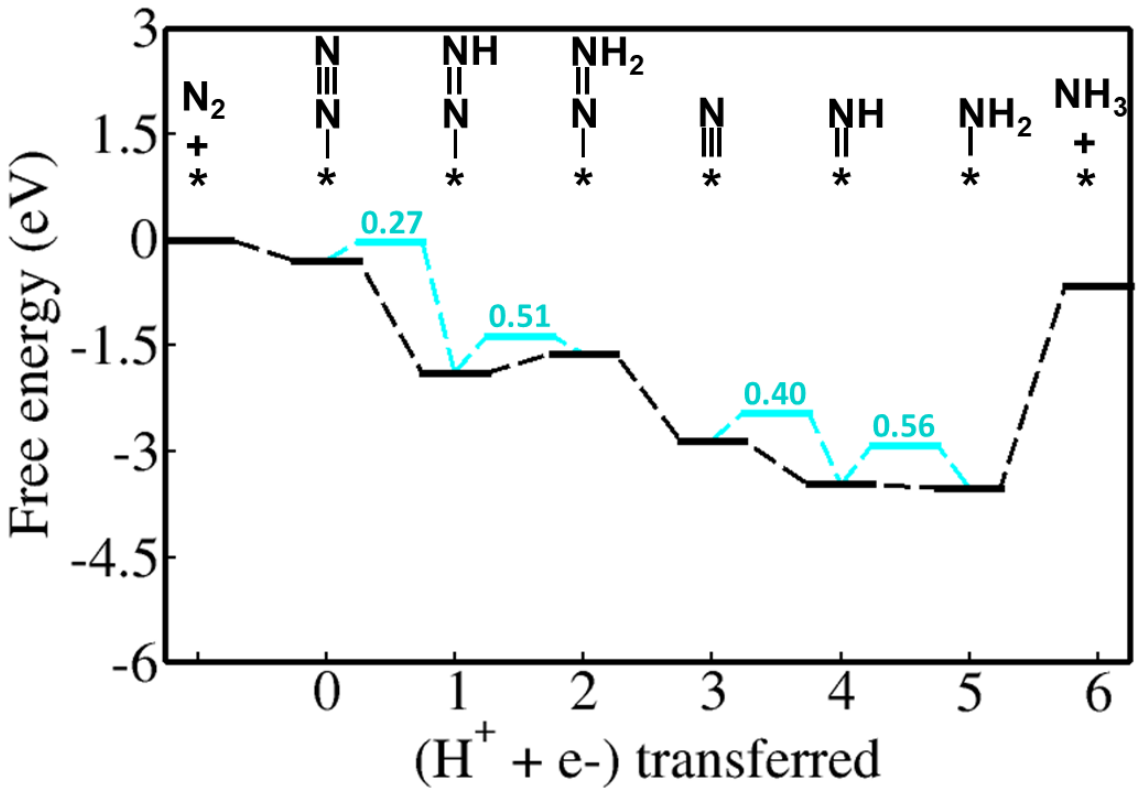

Figure 9.12: Relative energy diagram for electrocatalytic N_2 reduction *via* the distal pathway on C@6cn_α. Cyan curves indicate kinetic barriers. All energies are in eV.

9.9 Conclusions

In summary, we report a set of α borophene based metal-free catalysts with superior activity towards eNRR. We show carbon substitution in borophene sheets is energetically favorable, and its stability reduces with increase in the coordination number of the substituted atomic site. Using comprehensive first-principles density functional theory calculations, we present two candidates, C@6cn_α, and B@6cn_α, to be highly selective towards eNRR against HER. High charge transfer to the anti-bonding $1\pi^*$ orbital of N_2 from these catalysts facilitates adhesion and activation of the NN bond. This excess charge on $^*N_2$ further promotes the first hydrogenation step leading to stabilization of the *NNH intermediate. Thus, a combination of charge transferred to $^*N_2$ (Δe) and stabilization of *NNH (ΔG_{ads}^{NNH}) on borophene sheets, directly govern the activity of the

catalyst and function as descriptors which can be employed in high throughput screening of high-performance materials. C@6cn_α and B@6cn_α electrochemically catalyze N_2 reduction at small limiting potentials of -0.25 V and -0.33 V, via the alternating and distal pathways, respectively. Calculations of TSs and activation energy barriers show hydrogenation of NH to NH_2 is the RDS with a low barrier of 0.56 eV. to High N_2 activation, excellent HER suppression, and vanishingly small limiting potentials for eNRR render C@6cn_α and B@6cn_α as a robust metal-free catalysts, ideal for electrochemical production of NH_3.

Chapter 10

Summary

The central theme of this thesis has been to explicate the underlying mechanisms leading to enhancement in the catalytic performance of various materials. The chemical reactions studied here are not only crucial to tackling problems of energy and environment, but are also fundamentally interesting as they offer fundamental mechanistic insights into catalysis of various processes. We study these heterogeneous catalytic reactions within the framework of first-principles density functional theoretical calculations and demonstrate how surface modifications can be used to alter the electronic structure of materials, leading to enhanced catalytic activity.

Deviation from the bulk structure of a crystal can lead to important changes in its physical properties. We show chemical disorder and substitutional alloying can be effectively used to tune the catalytic performance of two earth-abundant metal catalysts for HER in alkaline environment. We study evolution of H_2 on a Co-Mo-P catalyst by introducing structural amorphicity and identify Mo-Co bridging site to be an active site for dissociation of the water molecule, facilitated by the electronegative P-atom. We further show desorption of the product (H_2) is accelerated by the Mo-atoms in the system. We presented analysis of another catalyst for alkaline HER comprising of the metastable 1T

polytype of MoS_2 stabilized by substitutional Ni/Co. We show that a local structural distortion occurs in the 1T lattice upon substitution with Ni/Co atoms which transforms it to a more stable 1T" polymorph. Ni/Co substituted catalysts exhibit optimal Gibbs free energy of H-adsorption (ΔG^H_{ads}), supporting their superior HER performance. Pristine 1T-MoS_2 interacts rather strongly with H ($\Delta G^H_{ads} \sim$ -2.9 eV), and the 1T lattice decays to a lower energy 1T" at low H-coverages ($< 40\%$). With increasing the H-coverage ($\geq 40\%$), the 1T" polymorph further decays to the more stable 1T' structure.

We presented analysis of the enhancement in catalytic activity of a metal phosphide, Ni_2P, towards the over water splitting reaction and two metal carbides, WC and MoC, towards HER, with substitutional doping of a 3d TM. Mn-substituted Ni_2P catalyzes both HER and OER with higher efficiencies than the pristine Ni_2P. An optimal $\Delta G^H_{ads} \sim$ -0.14 eV and work function of 4.78 eV showcases the high catalytic activity of $Ni_{1.5}Mn_{0.5}P$ towards HER. Presence of surface oxygen (M–O) species, reduces the OER overpotential of $Ni_{1.5}Mn_{0.5}P$ supporting its high catalytic activity towards evolution of O_2. Ni substituents in WC and MoC alter their electronic structure, pushing the Fermi level close to SHE potential, making them viable HER electrocatalysts.

We showed how site-specific catalytic activity can be tuned by chemical character of N-atoms substituted in the graphene monolayer of a graphene:MoS_2 heterostructure. Graphitic, pyridinic and pyrrolic N dopants lead to different electronic and catalytic properties of the heterostructure. We predicted graphitic N-substituted graphene:MoS_2 heterostructure to exhibit superior HER activity owing to an optimal ΔG^H_{ads} and suitable band edge energies relative to redox potential, making it a suitable for electrocatalytic HER.

Our analyses of catalytic performance of these materials towards the two half-cell reactions of water splitting lack the effects due to various solvents used experimentally. In future work, it would be interesting to study the liquid phase interactions and how they influence

the activity of catalysts studied here. Also, it would be desirable to comment on the kinetic aspect of HER and OER on the catalytic materials explored here.

We presented studies of catalytic activity of two intermetallics to reduce the greenhouse gas CO_2 to CH_3OH, a value added fuel, and also activity to oxidize such fuels (CH_3CH_2OH) to generate electricity using a fuel cell. Using comprehensive density-functional theoretical calculations, we presented analysis of the mechanisms of catalytic activity of Ni_3In towards the 6 electron reduction of CO_2 to generate CH_3OH. Through detailed investigation of eight discrete pathways, we showed that CO_2 reduction on Ni_3In proceeds preferentially via the formate pathway. We further calculated the activation barriers along the formate pathway and conclusively determined the potential determining and rate determining steps. In future, it would be interesting to calculate the thermodynamic and activation energy barriers of CO_2 reduction to other possible products like CH_4 and even C_2 products like EtOH. This would give a clearer picture into the underlying mechanism governing the selectivity of Ni_3In catalyst towards CH_3OH.

We also studied the role of Ni-substituents in the amelioration of catalytic activity of Pd_2Ge for electrooxidation of ethanol. We find that optimization of adsorption energies of CH_3CO and OH intermediates on Ni-substituted Pd_2Ge surface dictate its superior electrocatalytic activity as compared to that of pristine Pd_2Ge. For future work, it would be really interesting to extend our investigations to include all steps involving the catalytic electrooxidation of ethanol instead of focusing on the energies of adsorption of the key intermediates.

We also predicted two novel catalysts with a goal to produce two chemicals of great industrial value, H_2O_2 and NH_3. For catalyzing the synthesis of the former, we demonstrate how substitutional Au and S-vacancies tune the catalytic activity of 1H-MoS_2 (Au_xMoS_{2-x-v}). The 2 electron reduction of O_2 to generate H_2O_2, occurs on Au_xMoS_{2-x-v} without any significant energy input and the catalyst also offers high selectivity over the competing

reaction, ORR. Both substitutional Au and S-vacancy operate synergistically to catalyze the direct synthesis of H_2O_2 (DSHP) and play distinctly crucial roles: the former facilitates optimal activation of O_2, while the latter facilitates H adsorption. Au_xMoS_{2-x-v} catalyses DSHP at a reasonable activation energy barrier of 0.80 eV, significantly lower than other reported catalysts. We also report a metal-free catalyst based on 2D boron sheets and show it to be highly active in catalyzing electrochemical nitrogen reduction reaction (eNRR) at a exceptionally low onset potential. These borophene based catalysts also exhibit high selectivity towards eNRR over the competing and kinetically swift HER, making them attractive candidates for producing NH_3. The prime candidate material to catalyze eNRR also possesses a minimal kinetic barrier of 0.56 eV, further confirming the superior catalytic activity of our borophene based catalysts. Uncovering the mechanisms, we identify two novel descriptors namely, amount of charge transferred to $^*N_2$ and ΔG_{ads}^{NNH}, which can be employed in high-throughput screening of non-metallic catalysts for eNRR.

The next step in these studies would be to validate these results experimentally. Here we provide a detailed road-map towards synthesis of two industrially important chemical, H_2O_2 and NH_3. It would be fascinating to see these predicted catalysts take shape into real materials and analyze their performance. Also, we would like to see the applicability of the two novel descriptors described in Chapter 9 on other metal-free candidate materials to catalyze eNRR and assess their scope.

We have summarized the ideas in this thesis in a schematic (see Fig. 10.1) showcasing commonality and central theme across the topics covered. Specifically, we demonstrate various tuning parameters in different materials that can be used to engineer their catalytic activity, and uncover the mechanisms leading to enhancement in the catalytic activity towards chemical reactions relevant to energy, environment and industry.

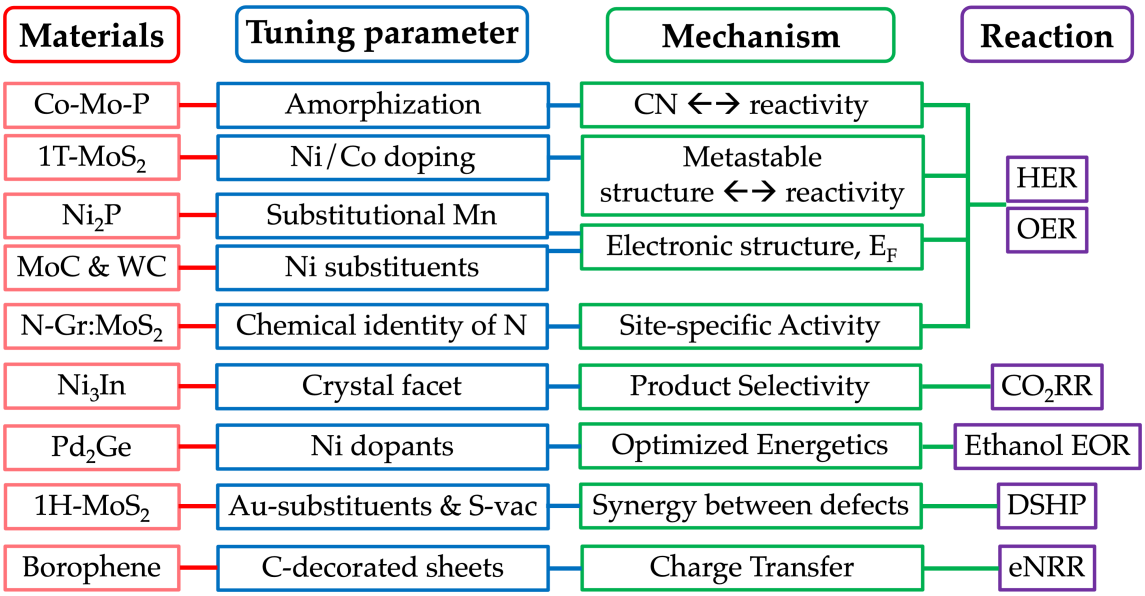

Figure 10.1: Schematic summary of ideas presented in the thesis.

References

[1] Steven J Davis, Nathan S Lewis, Matthew Shaner, Sonia Aggarwal, Doug Arent, Inês L Azevedo, Sally M Benson, Thomas Bradley, Jack Brouwer, Yet-Ming Chiang, et al. Net-zero emissions energy systems. *Science*, 360(6396), 2018.

[2] Meghna A Manae, Lakshay Dheer, and Umesh V Waghmare. Co2 utilization through its reduction to methanol: Design of catalysts using quantum mechanics and machine learning. *Transactions of the Indian National Academy of Engineering*, pages 1–11, 2021.

[3] Nian-Tzu Suen, Sung-Fu Hung, Quan Quan, Nan Zhang, Yi-Jun Xu, and Hao Ming Chen. Electrocatalysis for the oxygen evolution reaction: recent development and future perspectives. *Chemical Society Reviews*, 46(2):337–365, 2017.

[4] Jens Kehlet Nørskov, Thomas Bligaard, Ashildur Logadottir, JR Kitchin, Jingguang G Chen, S Pandelov, and U Stimming. Trends in the exchange current for hydrogen evolution. *Journal of The Electrochemical Society*, 152(3):J23, 2005.

[5] JJ Berzelius. Quelques idées sur une nouvelle force agissant dans les combinaisons des corps organiques. *Ann. Chim*, 61:146–151, 1836.

[6] AJB Robertson. The early history of catalysis. *Platinum Metals Review*, 19(2):64–69, 1975.

[7] Bård Lindström and Lars J Pettersson. A brief history of catalysis. *Cattech*, 7(4):130–138, 2003.

[8] Andreas Libavius. *Alchemia*. Johannes Sautrius, Frankfurt, 1597.

[9] S. Green. *Industrial Catalysis*. Macmillan Company, New York, 1928.

[10] Gerhard Ertl, Helmut Knözinger, Jens Weitkamp, et al. *Handbook of heterogeneous catalysis*, volume 2. VCH Weinheim, 1997.

[11] Tony Eggleton. Climate change: The physical picture. *Climate Change Impacts on Fisheries and Aquaculture, 2 Volumes: A Global Analysis*, 1:1, 2017.

[12] J Blunden and DS Arndt. State of the climate in 2019. *Bulletin of the American Meteorological Society*, 101(8):S1–S429, 2020.

[13] JCJ Bart and RPA Sneeden. Copper-zinc oxide-alumina methanol catalysts revisited. *Catalysis Today*, 2(1):1–124, 1987.

[14] Malte Behrens, Felix Studt, Igor Kasatkin, Stefanie Kühl, Michael Hävecker, Frank Abild-Pedersen, Stefan Zander, Frank Girgsdies, Patrick Kurr, Benjamin-Louis Kniep, et al. The active site of methanol synthesis over cu/zno/al2o3 industrial catalysts. *Science*, 336(6083):893–897, 2012.

[15] Bert Metz, Ogunlade Davidson, HC De Coninck, Manuela Loos, and Leo Meyer. *IPCC special report on carbon dioxide capture and storage*. Cambridge: Cambridge University Press, 2005.

[16] G. Weatherbee. Hydrogenation of co2 on group viii metals: Ii. kinetics and mechanism of co2 hydrogenation on nickel. *Journal of Catalysis*, 77:460–472, 1982.

[17] Th Kammler and J Küppers. Methanation of carbon on ni (100) surfaces at 120 k with gaseous h atoms. *Chemical physics letters*, 267(3-4):391–396, 1997.

[18] Andrea Alvarez, Atul Bansode, Atsushi Urakawa, Anastasiya V Bavykina, Tim A Wezendonk, Michiel Makkee, Jorge Gascon, and Freek Kapteijn. Challenges in the greener production of formates/formic acid, methanol, and dme by heterogeneously catalyzed co2 hydrogenation processes. *Chemical reviews*, 117(14):9804–9838, 2017.

[19] Marianna Bellardita, Agatino Di Paola, Elisa García-López, Vittorio Loddo, Giuseppe Marcì, and Leonardo Palmisano. Photocatalytic co2 reduction in gas-solid regime in the presence of bare, sio2 supported or cu-loaded tio2 samples. *Current Organic Chemistry*, 17(21):2440–2448, 2013.

[20] Jun Li and Kazunari Yoshizawa. Mechanistic aspects in the direct synthesis of hydrogen peroxide on pdau catalyst from first principles. *Catalysis Today*, 248:142–148, 2015.

[21] Davi de Carvalho Diniz Melo, Jamil AA Anache, Edson Wendland, Valéria Peixoto Borges, Diego G Miralles, Brecht Martens, Joshua Fisher, Rodolfo LB Nobrega, Alvaro Moreno, Osvaldo MR Cabral, et al. Are remote sensing evapotranspiration models reliable across south american climates and ecosystems? *Earth and Space Science Open Archive ESSOAr*, 2021.

[22] Min Zeng and Yanguang Li. Recent advances in heterogeneous electrocatalysts for the hydrogen evolution reaction. *Journal of Materials Chemistry A*, 3(29):14942–14962, 2015.

[23] Carlos G Morales-Guio, Lucas-Alexandre Stern, and Xile Hu. Nanostructured hydrotreating catalysts for electrochemical hydrogen evolution. *Chemical Society Reviews*, 43(18):6555–6569, 2014.

[24] John Bockris. Energy: the solar-hydrogen alternative. *New York*, 1975.

[25] Rasmus Frydendal, Elisa A Paoli, Brian P Knudsen, Björn Wickman, Paolo Malacrida, Ifan EL Stephens, and Ib Chorkendorff. Benchmarking the stability

of oxygen evolution reaction catalysts: the importance of monitoring mass losses. *ChemElectroChem*, 1(12):2075–2081, 2014.

[26] Youngmin Lee, Jin Suntivich, Kevin J May, Erin E Perry, and Yang Shao-Horn. Synthesis and activities of rutile iro2 and ruo2 nanoparticles for oxygen evolution in acid and alkaline solutions. *The journal of physical chemistry letters*, 3(3):399–404, 2012.

[27] Marijan Vuković. Oxygen evolution reaction on thermally treated iridium oxide films. *Journal of applied electrochemistry*, 17(4):737–745, 1987.

[28] Nuwan H Attanayake, Lakshay Dheer, Akila C Thenuwara, Sasitha C Abeyweera, Coby Collins, Umesh V Waghmare, and Daniel R Strongin. Ni-and co-substituted metallic mos2 for the alkaline hydrogen evolution reaction. *ChemElectroChem*, 7(17):3606–3615, 2020.

[29] Manjeet Chhetri, Somak Maitra, Himanshu Chakraborty, Umesh V Waghmare, and CNR Rao. Superior performance of borocarbonitrides, b x c y n z, as stable, low-cost metal-free electrocatalysts for the hydrogen evolution reaction. *Energy & Environmental Science*, 9(1):95–101, 2016.

[30] Lakshay Dheer, Satadeep Bhattacharjee, Seung Cheol Lee, and Umesh V Waghmare. Van der waals hetero-structures of 1h-mos2 and n-substituted graphene for catalysis of hydrogen evolution reaction. *Materials Research Express*, 6(12):124006, 2020.

[31] Summayya Kouser, Anagha Thannikoth, Uttam Gupta, Umesh V Waghmare, and CNR Rao. 2d-gas as a photocatalyst for water splitting to produce h2. *Small*, 11(36):4723–4730, 2015.

[32] Anand Roy, Manjeet Chhetri, Suchitra Prasad, Umesh V Waghmare, and CNR Rao. Unique features of the photocatalytic reduction of h2o and co2 by new catalysts

based on the analogues of cds, cd4p2x3 (x= cl, br, i). *ACS applied materials & interfaces*, 10(3):2526–2536, 2018.

[33] Shreya Sarkar, Lakshay Dheer, CP Vinod, Ranjit Thapa, Umesh V Waghmare, and Sebastian C Peter. Stress-induced electronic structure modulation of manganese-incorporated ni2p leading to enhanced activity for water splitting. *ACS Applied Energy Materials*, 3(2):1271–1278, 2020.

[34] Peter CK Vesborg, Brian Seger, and IB Chorkendorff. Recent development in hydrogen evolution reaction catalysts and their practical implementation. *The journal of physical chemistry letters*, 6(6):951–957, 2015.

[35] Xiaoxin Zou and Yu Zhang. Noble metal-free hydrogen evolution catalysts for water splitting. *Chemical Society Reviews*, 44(15):5148–5180, 2015.

[36] Ming Gong, Di-Yan Wang, Chia-Chun Chen, Bing-Joe Hwang, and Hongjie Dai. A mini review on nickel-based electrocatalysts for alkaline hydrogen evolution reaction. *Nano Research*, 9(1):28–46, 2016.

[37] Joseph H Montoya, Linsey C Seitz, Pongkarn Chakthranont, Aleksandra Vojvodic, Thomas F Jaramillo, and Jens K Nørskov. Materials for solar fuels and chemicals. *Nature materials*, 16(1):70–81, 2017.

[38] Akila C Thenuwara, Elizabeth B Cerkez, Samantha L Shumlas, Nuwan H Attanayake, Ian G McKendry, Laszlo Frazer, Eric Borguet, Qing Kang, Richard C Remsing, Michael L Klein, et al. Nickel confined in the interlayer region of birnessite: an active electrocatalyst for water oxidation. *Angewandte Chemie*, 128(35):10537–10541, 2016.

[39] Akila C Thenuwara, Samantha L Shumlas, Nuwan H Attanayake, Yaroslav V Aulin, Ian G McKendry, Qiao Qiao, Yimei Zhu, Eric Borguet, Michael J Zdilla, and

Daniel R Strongin. Intercalation of cobalt into the interlayer of birnessite improves oxygen evolution catalysis. *ACS Catalysis*, 6(11):7739–7743, 2016.

[40] Akila C Thenuwara, Lakshay Dheer, Nuwan H Attanayake, Qimin Yan, Umesh V Waghmare, and Daniel R Strongin. Co-mo-p based electrocatalyst for superior reactivity in the alkaline hydrogen evolution reaction. *ChemCatChem*, 10(21):4832–4837, 2018.

[41] Tianyi Kou, Tyler Smart, Bin Yao, Irwin Chen, David Thota, Yuan Ping, and Yat Li. Theoretical and experimental insight into the effect of nitrogen doping on hydrogen evolution activity of ni3s2 in alkaline medium. *Advanced Energy Materials*, 8(19):1703538, 2018.

[42] Nasir Mahmood, Yunduo Yao, Jing-Wen Zhang, Lun Pan, Xiangwen Zhang, and Ji-Jun Zou. Electrocatalysts for hydrogen evolution in alkaline electrolytes: mechanisms, challenges, and prospective solutions. *Advanced Science*, 5(2):1700464, 2018.

[43] Sladjana Maslovara, Dragana Vasić Anićijević, Snežana Brković, Jelena Georgijević, Gvozden Tasić, and Milica Marčeta Kaninski. Experimental and dft study of cocumo ternary ionic activator for alkaline her on ni cathode. *Journal of Electroanalytical Chemistry*, 839:224–230, 2019.

[44] Jamesh Mohammed-Ibrahim and Xiaoming Sun. Recent progress on earth abundant electrocatalysts for hydrogen evolution reaction (her) in alkaline medium to achieve efficient water splitting–a review. *Journal of Energy Chemistry*, 34:111–160, 2019.

[45] R Narasimman, Manmohansingh Waldiya, K Jalaja, Suresh K Vemuri, Indrajit Mukhopadhyay, and Abhijit Ray. Self-standing, hybrid three-dimensional-porous mos2/ni3s2 foam electrocatalyst for hydrogen evolution reaction in alkaline medium. *International Journal of Hydrogen Energy*, 46(11):7759–7771, 2021.

[46] Shaoqu Xie, Wanli Zhang, Xingying Lan, and Hongfei Lin. Co2 reduction to methanol in the liquid phase: A review. *ChemSusChem*, 13(23):6141–6159, 2020.

[47] VK Saraswat and Ripunjaya Bansal. India's leapfrog to methanol economy. *NITI AAYOG*, 2017.

[48] Choon Fong Shih, Tao Zhang, Jinghai Li, and Chunli Bai. Powering the future with liquid sunshine. *Joule*, 2(10):1925–1949, 2018.

[49] Yawei Li, Siew Hwa Chan, and Qiang Sun. Heterogeneous catalytic conversion of co 2: a comprehensive theoretical review. *Nanoscale*, 7(19):8663–8683, 2015.

[50] Qingli Tang, Zhemin Shen, Liang Huang, Ting He, Hertanto Adidharma, Armistead G Russell, and Maohong Fan. Synthesis of methanol from co 2 hydrogenation promoted by dissociative adsorption of hydrogen on a ga 3 ni 5 (221) surface. *Physical Chemistry Chemical Physics*, 19(28):18539–18555, 2017.

[51] JD Lović, Nevenka R Elezović, BM Jović, Piotr Zabinski, Lj Gajić-Krstajić, and Vladimir D Jović. Electrodeposited agpd alloy coatings as efficient catalysts for the ethanol oxidation reaction. *International Journal of Hydrogen Energy*, 43(39):18498–18508, 2018.

[52] Wenxin Du, Guangxing Yang, Emily Wong, N Aaron Deskins, Anatoly I Frenkel, Dong Su, and Xiaowei Teng. Platinum-tin oxide core–shell catalysts for efficient electro-oxidation of ethanol. *Journal of the American Chemical Society*, 136(31):10862–10865, 2014.

[53] Sheng Dai, Tzu-Hsi Huang, Xingxu Yan, Chao-Yu Yang, Tsan-Yao Chen, Jeng-Han Wang, Xiaoqing Pan, and Kuan-Wen Wang. Promotion of ternary pt–sn–ag catalysts toward ethanol oxidation reaction: Revealing electronic and structural effects of additive metals. *ACS Energy Letters*, 3(10):2550–2557, 2018.

[54] Ye Wang, Shouzhong Zou, and Wen-Bin Cai. Recent advances on electro-oxidation of ethanol on pt-and pd-based catalysts: from reaction mechanisms to catalytic materials. *Catalysts*, 5(3):1507–1534, 2015.

[55] Hui-Fang Wang and Zhi-Pan Liu. Selectivity of direct ethanol fuel cell dictated by a unique partial oxidation channel. *The Journal of Physical Chemistry C*, 111(33):12157–12160, 2007.

[56] ZX Liang, TS Zhao, JB Xu, and LD Zhu. Mechanism study of the ethanol oxidation reaction on palladium in alkaline media. *Electrochimica Acta*, 54(8):2203–2208, 2009.

[57] C Lamy, EM Belgsir, and JM Leger. Electrocatalytic oxidation of aliphatic alcohols: Application to the direct alcohol fuel cell (dafc). *Journal of Applied Electrochemistry*, 31(7):799–809, 2001.

[58] Weijiang Zhou, Zhenhua Zhou, Shuqin Song, Wenzhen Li, Gongquan Sun, Panagiotis Tsiakaras, and Qin Xin. Pt based anode catalysts for direct ethanol fuel cells. *Applied Catalysis B: Environmental*, 46(2):273–285, 2003.

[59] Lin Chen, Lilin Lu, Hengli Zhu, Yueguang Chen, Yu Huang, Yadong Li, and Leyu Wang. Improved ethanol electrooxidation performance by shortening pd–ni active site distance in pd–ni–p nanocatalysts. *Nature communications*, 8(1):1–9, 2017.

[60] V Russo, R Tesser, E Santacesaria, and M Di Serio. Chemical and technical aspects of propene oxide production via hydrogen peroxide (hppo process). *Industrial & Engineering Chemistry Research*, 52(3):1168–1178, 2013.

[61] Jennifer K Edwards, Simon J Freakley, Richard J Lewis, James C Pritchard, and Graham J Hutchings. Advances in the direct synthesis of hydrogen peroxide from hydrogen and oxygen. *Catalysis Today*, 248:3–9, 2015.

[62] Kazuhiko Sato, Masao Aoki, and Ryoji Noyori. A" green" route to adipic acid: Direct oxidation of cyclohexenes with 30 percent hydrogen peroxide. *Science*, 281(5383):1646–1647, 1998.

[63] Raghu Nandan Gurram, Mohammad Al-Shannag, Nicholas Joshua Lecher, Shona M Duncan, Eric Lawrence Singsaas, and Malek Alkasrawi. Bioconversion of paper mill sludge to bioethanol in the presence of accelerants or hydrogen peroxide pretreatment. *Bioresource technology*, 192:529–539, 2015.

[64] Michael Vincent Urban, Thomas Rath, and Christine Radtke. Hydrogen peroxide (h2o2): a review of its use in surgery. *Wiener Medizinische Wochenschrift*, 169(9):222–225, 2019.

[65] Rledl Hans-Joachim and Pfleiderer Georg. Production of hydrogen peroxide, May 16 1939. US Patent 2,158,525.

[66] Sungeun Yang, Arnau Verdaguer-Casadevall, Logi Arnarson, Luca Silvioli, Viktor Čolić, Rasmus Frydendal, Jan Rossmeisl, Ib Chorkendorff, and Ifan EL Stephens. Toward the decentralized electrochemical production of h2o2: a focus on the catalysis. *Acs Catalysis*, 8(5):4064–4081, 2018.

[67] Sumanth Ranganathan and Volker Sieber. Recent advances in the direct synthesis of hydrogen peroxide using chemical catalysis—a review. *Catalysts*, 8(9):379, 2018.

[68] Jose M Campos-Martin, Gema Blanco-Brieva, and Jose LG Fierro. Hydrogen peroxide synthesis: an outlook beyond the anthraquinone process. *Angewandte Chemie International Edition*, 45(42):6962–6984, 2006.

[69] Chanchal Samanta. Direct synthesis of hydrogen peroxide from hydrogen and oxygen: An overview of recent developments in the process. *Applied Catalysis A: General*, 350(2):133–149, 2008.

[70] Jack H Lunsford. The direct formation of h2o2 from h2 and o2 over palladium catalysts. *Journal of catalysis*, 216(1-2):455–460, 2003.

[71] Jennifer K Edwards, Benjamin Solsona, Edwin Ntainjua, Albert F Carley, Andrew A Herzing, Christopher J Kiely, and Graham J Hutchings. Switching off hydrogen peroxide hydrogenation in the direct synthesis process. *Science*, 323(5917):1037–1041, 2009.

[72] Jennifer K Edwards, Simon J Freakley, Albert F Carley, Christopher J Kiely, and Graham J Hutchings. Strategies for designing supported gold–palladium bimetallic catalysts for the direct synthesis of hydrogen peroxide. *Accounts of chemical research*, 47(3):845–854, 2014.

[73] Jennifer K Edwards, Adrian Thomas, Albert F Carley, Andrew A Herzing, Christopher J Kiely, and Graham J Hutchings. Au–pd supported nanocrystals as catalysts for the direct synthesis of hydrogen peroxide from h 2 and o 2. *Green Chemistry*, 10(4):388–394, 2008.

[74] Edwin Ntainjua, Jennifer K Edwards, Albert F Carley, Jose Antonio Lopez-Sanchez, Jacob A Moulijn, Andrew A Herzing, Christopher J Kiely, and Graham J Hutchings. The role of the support in achieving high selectivity in the direct formation of hydrogen peroxide. *Green Chemistry*, 10(11):1162–1169, 2008.

[75] Edwin Ntainjua N, Marco Piccinini, James C Pritchard, Jennifer K Edwards, Albert F Carley, Jacob A Moulijn, and Graham J Hutchings. Effect of halide and acid additives on the direct synthesis of hydrogen peroxide using supported gold–palladium catalysts. *ChemSusChem: Chemistry & Sustainability Energy & Materials*, 2(6):575–580, 2009.

[76] Jennifer K Edwards, Albert F Carley, Andrew A Herzing, Christopher J Kiely, and Graham J Hutchings. Direct synthesis of hydrogen peroxide from h 2 and o 2 using

supported au–pd catalysts. *Faraday Discussions*, 138:225–239, 2008.

[77] Vaclav Smil. Detonator of the population explosion. *Nature*, 400(6743):415–415, 1999.

[78] R Service. Ammonia—a renewable fuel made from sun, air, and water—could power the globe without carbon. *Science*, page aau7489, 2018.

[79] Jan Willem Erisman, Mark A Sutton, James Galloway, Zbigniew Klimont, and Wilfried Winiwarter. How a century of ammonia synthesis changed the world. *Nature Geoscience*, 1(10):636–639, 2008.

[80] Asbjørn Klerke, Claus Hviid Christensen, Jens K Nørskov, and Tejs Vegge. Ammonia for hydrogen storage: challenges and opportunities. *Journal of Materials Chemistry*, 18(20):2304–2310, 2008.

[81] Fritz Haber. Neue arbeitsweisen. *Naturwissenschaften*, 11(36):753–756, 1923.

[82] Timur Kandemir, Manfred E Schuster, Anatoliy Senyshyn, Malte Behrens, and Robert Schlögl. The haber–bosch process revisited: on the real structure and stability of "ammonia iron" under working conditions. *Angewandte Chemie International Edition*, 52(48):12723–12726, 2013.

[83] Masaaki Kitano, Yasunori Inoue, Youhei Yamazaki, Fumitaka Hayashi, Shinji Kanbara, Satoru Matsuishi, Toshiharu Yokoyama, Sung-Wng Kim, Michikazu Hara, and Hideo Hosono. Ammonia synthesis using a stable electride as an electron donor and reversible hydrogen store. *Nature chemistry*, 4(11):934–940, 2012.

[84] Robert Schlögl. Catalytic synthesis of ammonia—a "never-ending story"? *Angewandte Chemie International Edition*, 42(18):2004–2008, 2003.

[85] Grigorii Soloveichik. Electrochemical synthesis of ammonia as a potential alternative to the haber–bosch process. *Nature Catalysis*, 2(5):377–380, 2019.

[86] Gerhard Ertl. Elementary steps in heterogeneous catalysis. *Angewandte Chemie International Edition in English*, 29(11):1219–1227, 1990.

[87] Sandro Gambarotta and Jennifer Scott. Multimetallic cooperative activation of n2. *Angewandte Chemie International Edition*, 43(40):5298–5308, 2004.

[88] Lu Xu, Li-Ming Yang, and Eric Ganz. Electrocatalytic reduction of n2 using metal-doped borophene. *ACS Applied Materials & Interfaces*, 13(12):14091–14101, 2021.

[89] Huimin Liu, Li Wei, Fei Liu, Zengxia Pei, Jeffrey Shi, Zhou-jun Wang, Dehua He, and Yuan Chen. Homogeneous, heterogeneous, and biological catalysts for electrochemical n2 reduction toward nh3 under ambient conditions. *ACS Catalysis*, 9(6):5245–5267, 2019.

[90] Richard M Martin. *Electronic structure: basic theory and practical methods*. Cambridge university press, 2020.

[91] Max Born and Robert Oppenheimer. Zur quantentheorie der molekeln. *Annalen der physik*, 389(20):457–484, 1927.

[92] P Hohenberg and W Kohn. Physical review, 136. *B864*, 1964.

[93] W Kohn and LJ Sham. Self-consistent equations including exchange and correlation effects physical review. 140. *A1133*, 1965.

[94] Jorge Kohanoff. *Electronic structure calculations for solids and molecules: theory and computational methods*. Cambridge university press, 2006.

[95] John P Perdew and Alex Zunger. Self-interaction correction to density-functional approximations for many-electron systems. *Physical Review B*, 23(10):5048, 1981.

[96] John P Perdew and Yue Wang. Accurate and simple analytic representation of the electron-gas correlation energy. *Physical review B*, 45(23):13244, 1992.

[97] Seymour H Vosko, Leslie Wilk, and Marwan Nusair. Accurate spin-dependent electron liquid correlation energies for local spin density calculations: a critical analysis. *Canadian Journal of physics*, 58(8):1200–1211, 1980.

[98] John P Perdew. Unified theory of exchange and correlation beyond the local density approximation. *Electronic structure of solids' 91*, 11, 1991.

[99] John P Perdew, Kieron Burke, and Matthias Ernzerhof. Generalized gradient approximation made simple. *Physical review letters*, 77(18):3865, 1996.

[100] DR Hamann, M Schlüter, and C Chiang. Norm-conserving pseudopotentials. *Physical Review Letters*, 43(20):1494, 1979.

[101] David Vanderbilt. Soft self-consistent pseudopotentials in a generalized eigenvalue formalism. *Physical review B*, 41(11):7892, 1990.

[102] George H Vineyard. Frequency factors and isotope effects in solid state rate processes. *Journal of Physics and Chemistry of Solids*, 3(1-2):121–127, 1957.

[103] Charles J Cerjan and William H Miller. On finding transition states. *The Journal of chemical physics*, 75(6):2800–2806, 1981.

[104] Wolfgang Quapp. A gradient-only algorithm for tracing a reaction path uphill to the saddle of a potential energy surface. *Chemical physics letters*, 253(3-4):286–292, 1996.

[105] Hugh Taylor and Jack Simons. Imposition of geometrical constraints on potential energy surface walking procedures. *The Journal of Physical Chemistry*, 89(4):684–688, 1985.

[106] Jon Baker. An algorithm for the location of transition states. *Journal of Computational Chemistry*, 7(4):385–395, 1986.

[107] Graeme Henkelman, Blas P Uberuaga, and Hannes Jónsson. A climbing image nudged elastic band method for finding saddle points and minimum energy paths. *The Journal of chemical physics*, 113(22):9901–9904, 2000.

[108] Marie Villarba and Hannes Jónsson. Diffusion mechanisms relevant to metal crystal growth: Pt/pt (111). *Surface science*, 317(1-2):15–36, 1994.

[109] Greg Mills and Hannes Jónsson. Quantum and thermal effects in h 2 dissociative adsorption: Evaluation of free energy barriers in multidimensional quantum systems. *Physical review letters*, 72(7):1124, 1994.

[110] Mads R Sørensen, Karsten W Jacobsen, and Hannes Jónsson. Thermal diffusion processes in metal-tip-surface interactions: contact formation and adatom mobility. *Physical review letters*, 77(25):5067, 1996.

[111] Min Zeng and Yanguang Li. Recent advances in heterogeneous electrocatalysts for the hydrogen evolution reaction. *Journal of Materials Chemistry A*, 3(29):14942–14962, 2015.

[112] M Gong, DY Wang, CC Chen, BJ Hwang, and H Dai. A mini review on nickel-based electrocatalysts for alkaline hydrogen evolution reaction. nano res 9 (1): 28–46, 2016.

[113] Joseph H Montoya, Linsey C Seitz, Pongkarn Chakthranont, Aleksandra Vojvodic, Thomas F Jaramillo, and Jens K Nørskov. Materials for solar fuels and chemicals. *Nature materials*, 16(1):70–81, 2017.

[114] Daniel Friebel, Mary W Louie, Michal Bajdich, Kai E Sanwald, Yun Cai, Anna M Wise, Mu-Jeng Cheng, Dimosthenis Sokaras, Tsu-Chien Weng, Roberto Alonso-Mori, et al. Identification of highly active fe sites in (ni, fe) ooh for electrocatalytic water splitting. *Journal of the American Chemical Society*, 137(3):1305–1313, 2015.

[115] Akila C Thenuwara, Nuwan H Attanayake, Jie Yu, John P Perdew, Evert J Elzinga,

Qimin Yan, and Daniel R Strongin. Cobalt intercalated layered nife double hydroxides for the oxygen evolution reaction. *The Journal of Physical Chemistry B*, 122(2):847–854, 2018.

[116] Bo Zhang, Xueli Zheng, Oleksandr Voznyy, Riccardo Comin, Michal Bajdich, Max García-Melchor, Lili Han, Jixian Xu, Min Liu, Lirong Zheng, et al. Homogeneously dispersed multimetal oxygen-evolving catalysts. *Science*, 352(6283):333–337, 2016.

[117] T Liu, X Ma, D Liu, S Hao, G Du, Y Ma, AM Asiri, X Sun, L Chen, and ACS Catal. 7, 98–102; b) h. *Huang, C. Yu, C. Zhao, X. Han, J. Yang, Z. Liu, S. Li, M. Zhang, J. Qiu, Nano Energy*, 34:472–480, 2017.

[118] Jian Zhang, Tao Wang, Pan Liu, Shaohua Liu, Renhao Dong, Xiaodong Zhuang, Mingwei Chen, and Xinliang Feng. Engineering water dissociation sites in mos 2 nanosheets for accelerated electrocatalytic hydrogen production. *Energy & Environmental Science*, 9(9):2789–2793, 2016.

[119] Jian Zhang, Tao Wang, Pan Liu, Zhongquan Liao, Shaohua Liu, Xiaodong Zhuang, Mingwei Chen, Ehrenfried Zschech, and Xinliang Feng. Efficient hydrogen production on moni 4 electrocatalysts with fast water dissociation kinetics. *Nature communications*, 8(1):1–8, 2017.

[120] Ram Subbaraman, Dusan Tripkovic, Kee-Chul Chang, Dusan Strmcnik, Arvydas P Paulikas, Pussana Hirunsit, Maria Chan, Jeff Greeley, Vojislav Stamenkovic, and Nenad M Markovic. Trends in activity for the water electrolyser reactions on 3 d m (ni, co, fe, mn) hydr (oxy) oxide catalysts. *Nature materials*, 11(6):550–557, 2012.

[121] Paolo Giannozzi, Stefano Baroni, Nicola Bonini, Matteo Calandra, Roberto Car, Carlo Cavazzoni, Davide Ceresoli, Guido L Chiarotti, Matteo Cococcioni, Ismaila Dabo, et al. Quantum espresso: a modular and open-source software project

for quantum simulations of materials. *Journal of physics: Condensed matter*, 21(39):395502, 2009.

[122] David R Lide. *CRC handbook of chemistry and physics*, volume 85. CRC press, 2004.

[123] Cristina Romero, Juan C Noyola, Ulises Santiago, Renela M Valladares, Alexander Valladares, and Ariel A Valladares. A new approach to the computer modeling of amorphous nanoporous structures of semiconducting and metallic materials: A review. *Materials*, 3(1):467–502, 2010.

[124] Berit Hinnemann, Poul Georg Moses, Jacob Bonde, Kristina P Jørgensen, Jane H Nielsen, Sebastian Horch, Ib Chorkendorff, and Jens K Nørskov. Biomimetic hydrogen evolution: Mos2 nanoparticles as catalyst for hydrogen evolution. *Journal of the American Chemical Society*, 127(15):5308–5309, 2005.

[125] Nuwan H Attanayake, Sasitha C Abeyweera, Akila C Thenuwara, Babak Anasori, Yury Gogotsi, Yugang Sun, and Daniel R Strongin. Vertically aligned mos 2 on ti 3 c 2 (mxene) as an improved her catalyst. *Journal of Materials Chemistry A*, 6(35):16882–16889, 2018.

[126] Jesse D Benck, Thomas R Hellstern, Jakob Kibsgaard, Pongkarn Chakthranont, and Thomas F Jaramillo. Catalyzing the hydrogen evolution reaction (her) with molybdenum sulfide nanomaterials. *Acs Catalysis*, 4(11):3957–3971, 2014.

[127] Desheng Kong, Haotian Wang, Judy J Cha, Mauro Pasta, Kristie J Koski, Jie Yao, and Yi Cui. Synthesis of mos2 and mose2 films with vertically aligned layers. *Nano letters*, 13(3):1341–1347, 2013.

[128] Guoqing Li, Du Zhang, Qiao Qiao, Yifei Yu, David Peterson, Abdullah Zafar, Raj Kumar, Stefano Curtarolo, Frank Hunte, Steve Shannon, et al. All the catalytic

active sites of mos2 for hydrogen evolution. *Journal of the American Chemical Society*, 138(51):16632–16638, 2016.

[129] Daniel Merki and Xile Hu. Recent developments of molybdenum and tungsten sulfides as hydrogen evolution catalysts. *Energy & Environmental Science*, 4(10):3878–3888, 2011.

[130] Fernando Wypych and Robert Schöllhorn. 1t-mos 2, a new metallic modification of molybdenum disulfide. *Journal of the Chemical Society, Chemical Communications*, (19):1386–1388, 1992.

[131] F Jellinek, Go Brauer, and H Müller. Molybdenum and niobium sulphides. *Nature*, 185(4710):376–377, 1960.

[132] Chun Kiang Chua, Adeline Huiling Loo, and Martin Pumera. Top-down and bottom-up approaches in engineering 1 t phase molybdenum disulfide (mos2): Towards highly catalytically active materials. *Chemistry–A European Journal*, 22(40):14336–14341, 2016.

[133] Thomas F Jaramillo, Kristina P Jørgensen, Jacob Bonde, Jane H Nielsen, Sebastian Horch, and Ib Chorkendorff. Identification of active edge sites for electrochemical h2 evolution from mos2 nanocatalysts. *science*, 317(5834):100–102, 2007.

[134] Mark A Lukowski, Andrew S Daniel, Fei Meng, Audrey Forticaux, Linsen Li, and Song Jin. Enhanced hydrogen evolution catalysis from chemically exfoliated metallic mos2 nanosheets. *Journal of the American Chemical Society*, 135(28):10274–10277, 2013.

[135] Stefan Grimme. Semiempirical gga-type density functional constructed with a long-range dispersion correction. *Journal of computational chemistry*, 27(15):1787–1799, 2006.

[136] Sharmila N Shirodkar and Umesh V Waghmare. Emergence of ferroelectricity at a metal-semiconductor transition in a 1 t monolayer of mos 2. *Physical review letters*, 112(15):157601, 2014.

[137] Qing Tang and De-en Jiang. Mechanism of hydrogen evolution reaction on 1t-mos2 from first principles. *Acs Catalysis*, 6(8):4953–4961, 2016.

[138] Matteo Calandra. Chemically exfoliated single-layer mos 2: Stability, lattice dynamics, and catalytic adsorption from first principles. *Physical Review B*, 88(24):245428, 2013.

[139] Ji-Sen Li, Yu Wang, Chun-Hui Liu, Shun-Li Li, Yu-Guang Wang, Long-Zhang Dong, Zhi-Hui Dai, Ya-Fei Li, and Ya-Qian Lan. Coupled molybdenum carbide and reduced graphene oxide electrocatalysts for efficient hydrogen evolution. *Nature communications*, 7(1):1–8, 2016.

[140] Yanna Guo, Jing Tang, Zhongli Wang, Yong-Mook Kang, Yoshio Bando, and Yusuke Yamauchi. Elaborately assembled core-shell structured metal sulfides as a bifunctional catalyst for highly efficient electrochemical overall water splitting. *Nano Energy*, 47:494–502, 2018.

[141] Debdyuti Mukherjee, P Muthu Austeria, and S Sampath. Two-dimensional, few-layer phosphochalcogenide, feps3: a new catalyst for electrochemical hydrogen evolution over wide ph range. *ACS Energy Letters*, 1(2):367–372, 2016.

[142] Dezhi Kong, Ye Wang, Yew Von Lim, Shaozhuan Huang, Jun Zhang, Bo Liu, Tupei Chen, and Hui Ying Yang. 3d hierarchical defect-rich nimo3s4 nanosheet arrays grown on carbon textiles for high-performance sodium-ion batteries and hydrogen evolution reaction. *Nano Energy*, 49:460–470, 2018.

[143] Jakob Kibsgaard, Charlie Tsai, Karen Chan, Jesse D Benck, Jens K Nørskov, Frank Abild-Pedersen, and Thomas F Jaramillo. Designing an improved transition metal

phosphide catalyst for hydrogen evolution using experimental and theoretical trends. *Energy & Environmental Science*, 8(10):3022–3029, 2015.

[144] Xiaodeng Wang, Hongpeng Zhou, Dingke Zhang, Mingyu Pi, Jiajia Feng, and Shijian Chen. Mn-doped nip2 nanosheets as an efficient electrocatalyst for enhanced hydrogen evolution reaction at all ph values. *Journal of Power Sources*, 387:1–8, 2018.

[145] Da Li, Habib Baydoun, Cláudio N Verani, and Stephanie L Brock. Efficient water oxidation using comnp nanoparticles. *Journal of the American Chemical Society*, 138(12):4006–4009, 2016.

[146] Zhenhuan Zhao, Desmond E Schipper, Andrew P Leitner, Hari Thirumalai, Jing-Han Chen, Lixin Xie, Fan Qin, Md Kamrul Alam, Lars C Grabow, Shuo Chen, et al. Bifunctional metal phosphide femnp films from single source metal organic chemical vapor deposition for efficient overall water splitting. *Nano Energy*, 39:444–453, 2017.

[147] Praveen Pankajakshan, Suchismita Sanyal, Onno E de Noord, Indranil Bhattacharya, Arnab Bhattacharyya, and Umesh Waghmare. Machine learning and statistical analysis for materials science: stability and transferability of fingerprint descriptors and chemical insights. *Chemistry of Materials*, 29(10):4190–4201, 2017.

[148] Isabela C Man, Hai-Yan Su, Federico Calle-Vallejo, Heine A Hansen, José I Martínez, Nilay G Inoglu, John Kitchin, Thomas F Jaramillo, Jens K Nørskov, and Jan Rossmeisl. Universality in oxygen evolution electrocatalysis on oxide surfaces. *ChemCatChem*, 3(7):1159–1165, 2011.

[149] P Peter Atkins and J De Paula. *Atkins' physical chemistry*. OUP Oxford, 2014.

[150] Anirban Dutta and Narayan Pradhan. Developments of metal phosphides as efficient oer precatalysts. *The journal of physical chemistry letters*, 8(1):144–152, 2017.

[151] Zejun Li, Xinyu Dou, Yingcheng Zhao, and Changzheng Wu. Enhanced oxygen evolution reaction of metallic nickel phosphide nanosheets by surface modification. *Inorganic Chemistry Frontiers*, 3(8):1021–1027, 2016.

[152] Soumyabrata Roy, Debabrata Bagchi, Lakshay Dheer, Saurav Ch. Sarma, Vincent Rajaji, Chandrabhas Narayana, Umesh V. Waghmare, and Sebastian C. Peter. Mechanistic insights into the promotional effect of ni substitution in non-noble metal carbides for highly enhanced water splitting. *Applied Catalysis B: Environmental*, 298:120560, 2021.

[153] Lucas-Alexandre Stern, Ligang Feng, Fang Song, and Xile Hu. Ni 2 p as a janus catalyst for water splitting: the oxygen evolution activity of ni 2 p nanoparticles. *Energy & Environmental Science*, 8(8):2347–2351, 2015.

[154] Deviprasath Chinnadurai, Rajmohan Rajendiran, Oi Lun Li, and Kandasamy Prabakar. Mn-co bimetallic phosphate on electrodeposited pani nanowires with composition modulated structural morphology for efficient electrocatalytic water splitting. *Applied Catalysis B: Environmental*, 292:120202, 2021.

[155] W-F Chen, C-H Wang, Kotaro Sasaki, Nebojsa Marinkovic, Wenqian Xu, James T Muckerman, Yimei Zhu, and RR Adzic. Highly active and durable nanostructured molybdenum carbide electrocatalysts for hydrogen production. *Energy & Environmental Science*, 6(3):943–951, 2013.

[156] Soumyabrata Roy, Debabrata Bagchi, Vamseedhara Vemuri, Saurav Ch Sarma, Vinita Ahuja, Vincent Rajaji, Chandrabhas Narayana, and Sebastian C Peter. Deconvolution of phase–size–strain effects in metal carbide nanocrystals for enhanced hydrogen evolution. *Nanoscale*, 12(28):15414–15425, 2020.

[157] Younes Abghoui and Egill Skulason. Hydrogen evolution reaction catalyzed by transition-metal nitrides. *The Journal of Physical Chemistry C*, 121(43):24036–

24045, 2017.

[158] Lin Chen, Ling-Ran Zhang, Ling-Yan Yao, Ya-Hui Fang, Lin He, Guang-Feng Wei, and Zhi-Pan Liu. Metal boride better than pt: Hcp pd 2 b as a superactive hydrogen evolution reaction catalyst. *Energy & Environmental Science*, 12(10):3099–3105, 2019.

[159] Sangmin Jeong, Hien Duy Mai, Tri Khoa Nguyen, Jong-Sang Youn, Ki-Hun Nam, Cheol-Min Park, and Ki-Joon Jeon. Atomic interactions of two-dimensional pts2 quantum dots/tic heterostructures for hydrogen evolution reaction. *Applied Catalysis B: Environmental*, 293:120227, 2021.

[160] Panyong Kuang, Min He, Haiyuan Zou, Jiaguo Yu, and Ke Fan. 0d/3d mos2-nis2/n-doped graphene foam composite for efficient overall water splitting. *Applied Catalysis B: Environmental*, 254:15–25, 2019.

[161] Debabrata Bagchi, Nithi Phukan, Shreya Sarkar, Risov Das, Bitan Ray, Pavithra Bellare, Narayanan Ravishankar, and Sebastian C Peter. Ultralow non-noble metal loaded mof derived bi-functional electrocatalysts for the oxygen evolution and reduction reactions. *Journal of Materials Chemistry A*, 9(14):9319–9326, 2021.

[162] Abdul Majeed, Xin Li, Peng-Xiang Hou, Hassina Tabassum, Lili Zhang, Chang Liu, and Hui-Ming Cheng. Monolayer carbon-encapsulated mo-doped ni nanoparticles anchored on single-wall carbon nanotube film for total water splitting. *Applied Catalysis B: Environmental*, 269:118823, 2020.

[163] Yi Shen, Ling Li, Jingyu Xi, and Xinping Qiu. A facile approach to fabricate free-standing hydrogen evolution electrodes: riveting tungsten carbide nanocrystals to graphite felt fabrics by carbon nanosheets. *Journal of Materials Chemistry A*, 4(16):5817–5822, 2016.

[164] Yagya N Regmi, Gregory R Waetzig, Kyle D Duffee, Samantha M Schmuecker, James M Thode, and Brian M Leonard. Carbides of group iva, va and via transition metals as alternative her and orr catalysts and support materials. *Journal of Materials Chemistry A*, 3(18):10085–10091, 2015.

[165] Qiufang Gong, Yu Wang, Qi Hu, Jigang Zhou, Renfei Feng, Paul N Duchesne, Peng Zhang, Fengjiao Chen, Na Han, Yafei Li, et al. Ultrasmall and phase-pure w 2 c nanoparticles for efficient electrocatalytic and photoelectrochemical hydrogen evolution. *Nature communications*, 7(1):1–8, 2016.

[166] Yanna Guo, Jing Tang, Joel Henzie, Bo Jiang, Wei Xia, Tao Chen, Yoshio Bando, Yong-Mook Kang, Md Shahriar A Hossain, Yoshiyuki Sugahara, et al. Mesoporous iron-doped mos2/como2s4 heterostructures through organic–metal cooperative interactions on spherical micelles for electrochemical water splitting. *ACS nano*, 14(4):4141–4152, 2020.

[167] Qi Wang, Zhi Liang Zhao, Sha Dong, Dongsheng He, Matthew J Lawrence, Shaobo Han, Chao Cai, Shuhuai Xiang, Paramaconi Rodriguez, Bin Xiang, et al. Design of active nickel single-atom decorated mos2 as a ph-universal catalyst for hydrogen evolution reaction. *Nano Energy*, 53:458–467, 2018.

[168] Sean T Hunt, Tathiana Midori Kokumai, Daniela Zanchet, and Yuriy Roman-Leshkov. Alloying tungsten carbide nanoparticles with tantalum: Impact on electrochemical oxidation resistance and hydrogen evolution activity. *The Journal of Physical Chemistry C*, 119(24):13691–13699, 2015.

[169] Ming Gong and Hongjie Dai. A mini review of nife-based materials as highly active oxygen evolution reaction electrocatalysts. *Nano Research*, 8(1):23–39, 2015.

[170] Kostya S Novoselov, Andre K Geim, Sergei V Morozov, De-eng Jiang, Yanshui Zhang, Sergey V Dubonos, Irina V Grigorieva, and Alexandr A Firsov. Electric

field effect in atomically thin carbon films. *science*, 306(5696):666–669, 2004.

[171] Changgu Lee, Xiaoding Wei, Jeffrey W Kysar, and James Hone. Measurement of the elastic properties and intrinsic strength of monolayer graphene. *science*, 321(5887):385–388, 2008.

[172] Jian-Hao Chen, Chaun Jang, Shudong Xiao, Masa Ishigami, and Michael S Fuhrer. Intrinsic and extrinsic performance limits of graphene devices on sio 2. *Nature nanotechnology*, 3(4):206–209, 2008.

[173]

[174] Rahul Raveendran Nair, Peter Blake, Alexander N Grigorenko, Konstantin S Novoselov, Tim J Booth, Tobias Stauber, Nuno MR Peres, and Andre K Geim. Fine structure constant defines visual transparency of graphene. *Science*, 320(5881):1308–1308, 2008.

[175] Meryl D Stoller, Sungjin Park, Yanwu Zhu, Jinho An, and Rodney S Ruoff. Graphene-based ultracapacitors. *Nano letters*, 8(10):3498–3502, 2008.

[176] Kostya S Novoselov, Andre K Geim, Sergei Vladimirovich Morozov, Dingde Jiang, Michail I Katsnelson, IVa Grigorieva, SVb Dubonos, Firsov, and AA. Two-dimensional gas of massless dirac fermions in graphene. *nature*, 438(7065):197–200, 2005.

[177] YP Venkata Subbaiah, KJ Saji, and A Tiwari. Atomically thin mos2: A versatile nongraphene 2d material. *Advanced Functional Materials*, 26(13):2046–2069, 2016.

[178] Kin Fai Mak, Changgu Lee, James Hone, Jie Shan, and Tony F Heinz. Atomically thin mos 2: a new direct-gap semiconductor. *Physical review letters*, 105(13):136805, 2010.

[179] Andre K Geim and Irina V Grigorieva. Van der waals heterostructures. *Nature*, 499(7459):419–425, 2013.

[180] KS Novoselov, o A Mishchenko, o A Carvalho, and AH Castro Neto. 2d materials and van der waals heterostructures. *Science*, 353(6298), 2016.

[181] Ravi K Biroju, Deya Das, Rahul Sharma, Shubhadeep Pal, Larionette PL Mawlong, Kapil Bhorkar, PK Giri, Abhishek K Singh, and Tharangattu N Narayanan. Hydrogen evolution reaction activity of graphene–mos2 van der waals heterostructures. *ACS Energy Letters*, 2(6):1355–1361, 2017.

[182] Linfeng Wang, Xiang Zhou, Tianbao Ma, Dameng Liu, Lei Gao, Xin Li, Jun Zhang, Yuanzhong Hu, Hui Wang, Yadong Dai, et al. Superlubricity of a graphene/mos 2 heterostructure: a combined experimental and dft study. *Nanoscale*, 9(30):10846–10853, 2017.

[183] Sushant Kumar Behera, Pritam Deb, and Arghya Ghosh. Mechanistic study on electrocatalytic hydrogen evolution by high efficiency graphene/mos2 heterostructure. *ChemistrySelect*, 2(13):3657–3667, 2017.

[184] Horacio Coy Diaz, Jose Avila, Chaoyu Chen, Rafik Addou, Maria C Asensio, and Matthias Batzill. Direct observation of interlayer hybridization and dirac relativistic carriers in graphene/mos2 van der waals heterostructures. *Nano letters*, 15(2):1135–1140, 2015.

[185] Kun Chang and Weixiang Chen. In situ synthesis of mos 2/graphene nanosheet composites with extraordinarily high electrochemical performance for lithium ion batteries. *Chemical Communications*, 47(14):4252–4254, 2011.

[186] Honglin Li, Ke Yu, Chao Li, Zheng Tang, Bangjun Guo, Xiang Lei, Hao Fu, and Ziqiang Zhu. Charge-transfer induced high efficient hydrogen evolution of mos 2/graphene cocatalyst. *Scientific reports*, 5(1):1–11, 2015.

[187] Shaobin Tang, Weihua Wu, Shiyong Zhang, Dongnai Ye, Ping Zhong, Xiaokang Li, Liangxian Liu, and Ya-Fei Li. Tuning the activity of the inert mos 2 surface via graphene oxide support doping towards chemical functionalization and hydrogen evolution: a density functional study. *Physical Chemistry Chemical Physics*, 20(3):1861–1871, 2018.

[188] LS Panchakarla, KS Subrahmanyam, SK Saha, Achutharao Govindaraj, HR Krishnamurthy, UV Waghmare, and CNR Rao. Synthesis, structure, and properties of boron-and nitrogen-doped graphene. *Advanced Materials*, 21(46):4726–4730, 2009.

[189] Congcong Ma, Xiaohong Shao, and Dapeng Cao. Nitrogen-doped graphene nanosheets as anode materials for lithium ion batteries: a first-principles study. *Journal of Materials Chemistry*, 22(18):8911–8915, 2012.

[190] Yandong Ma, Ying Dai, Meng Guo, Chengwang Niu, and Baibiao Huang. Graphene adhesion on mos 2 monolayer: an ab initio study. *Nanoscale*, 3(9):3883–3887, 2011.

[191] Xingen Liu and Zhongyao Li. Electric field and strain effect on graphene-mos2 hybrid structure: ab initio calculations. *The Journal of Physical Chemistry Letters*, 6(16):3269–3275, 2015.

[192] Ravi K Biroju, Shubhadeep Pal, Rahul Sharma, PK Giri, and Tharangattu N Narayanan. Stacking sequence dependent photo-electrocatalytic performance of cvd grown mos2/graphene van der waals solids. *Nanotechnology*, 28(8):085101, 2017.

[193] Klaas Derk Bronsema, JL De Boer, and F Jellinek. On the structure of molybdenum diselenide and disulfide. *Zeitschrift für anorganische und allgemeine Chemie*, 540(9-10):15–17, 1986.

[194] Sobhit Singh, Camilo Espejo, and Aldo H Romero. First-principles investigation of graphene/mos2 bilayer heterostructures using tkatchenko-scheffler van der waals method. *arXiv preprint arXiv:1802.03919*, 2018.

[195] Arjun Cherevotan, Jithu Raj, Lakshay Dheer, Soumyabrata Roy, Shreya Sarkar, Risov Das, Chathakudath P Vinod, Shaojun Xu, Peter Wells, Umesh V Waghmare, et al. Operando generated ordered heterogeneous catalyst for the selective conversion of co2 to methanol. *ACS Energy Letters*, 6(2):509–516, 2021.

[196] Brian M Tackett, Elaine Gomez, and Jingguang G Chen. Net reduction of co 2 via its thermocatalytic and electrocatalytic transformation reactions in standard and hybrid processes. *Nature Catalysis*, 2(5):381–386, 2019.

[197] Geoffrey A Ozin. You can't have an energy revolution without transforming advances in materials, chemistry and catalysis into policy change and action. *Energy & Environmental Science*, 8(6):1682–1684, 2015.

[198] Alain Goeppert, Miklos Czaun, John-Paul Jones, GK Surya Prakash, and George A Olah. Recycling of carbon dioxide to methanol and derived products–closing the loop. *Chemical Society Reviews*, 43(23):7995–8048, 2014.

[199] Jens Artz, Thomas E Muller, Katharina Thenert, Johanna Kleinekorte, Raoul Meys, Andre Sternberg, André Bardow, and Walter Leitner. Sustainable conversion of carbon dioxide: an integrated review of catalysis and life cycle assessment. *Chemical reviews*, 118(2):434–504, 2018.

[200] Andrés González-Garay, Matthias S Frei, Amjad Al-Qahtani, Cecilia Mondelli, Gonzalo Guillén-Gosálbez, and Javier Pérez-Ramírez. Plant-to-planet analysis of co 2-based methanol processes. *Energy & Environmental Science*, 12(12):3425–3436, 2019.

[201] Evgenii V Kondratenko, Guido Mul, Jonas Baltrusaitis, Gastón O Larrazábal, and Javier Pérez-Ramírez. Status and perspectives of co 2 conversion into fuels and chemicals by catalytic, photocatalytic and electrocatalytic processes. *Energy & environmental science*, 6(11):3112–3135, 2013.

[202] Gabriele Centi, Elsje Alessandra Quadrelli, and Siglinda Perathoner. Catalysis for co 2 conversion: a key technology for rapid introduction of renewable energy in the value chain of chemical industries. *Energy & Environmental Science*, 6(6):1711–1731, 2013.

[203] K Fujimoto and Y Yu. Spillover effect on the stabilization of cu-zn catalyst for co2 hydrogenation to methanol. In *Studies in Surface Science and Catalysis*, volume 77, pages 393–396. Elsevier, 1993.

[204] Thomas Lunkenbein, Frank Girgsdies, Timur Kandemir, Nygil Thomas, Malte Behrens, Robert Schlögl, and Elias Frei. Bridging the time gap: a copper/zinc oxide/aluminum oxide catalyst for methanol synthesis studied under industrially relevant conditions and time scales. *Angewandte Chemie International Edition*, 55(41):12708–12712, 2016.

[205] Malte Behrens, Felix Studt, Igor Kasatkin, Stefanie Kühl, Michael Hävecker, Frank Abild-Pedersen, Stefan Zander, Frank Girgsdies, Patrick Kurr, Benjamin-Louis Kniep, et al. The active site of methanol synthesis over cu/zno/al2o3 industrial catalysts. *Science*, 336(6083):893–897, 2012.

[206] Sebastian Kuld, Christian Conradsen, Poul Georg Moses, Ib Chorkendorff, and Jens Sehested. Quantification of zinc atoms in a surface alloy on copper in an industrial-type methanol synthesis catalyst. *Angewandte Chemie*, 126(23):6051–6055, 2014.

[207] Roy Van Den Berg, Gonzalo Prieto, Gerda Korpershoek, Lars I Van Der Wal, Arnoldus J Van Bunningen, Susanne Lægsgaard-Jørgensen, Petra E De Jongh, and Krijn P De Jong. Structure sensitivity of cu and cuzn catalysts relevant to industrial methanol synthesis. *Nature communications*, 7(1):1–7, 2016.

[208] Bing An, Zhe Li, Yang Song, Jingzheng Zhang, Lingzhen Zeng, Cheng Wang, and Wenbin Lin. Cooperative copper centres in a metal–organic framework for selective

conversion of co 2 to ethanol. *Nature Catalysis*, 2(8):709–717, 2019.

[209] Xiaoben Zhang, Shaobo Han, Beien Zhu, Guanghui Zhang, Xiaoyan Li, Yi Gao, Zhaoxuan Wu, Bing Yang, Yuefeng Liu, Walid Baaziz, et al. Reversible loss of core–shell structure for ni–au bimetallic nanoparticles during co 2 hydrogenation. *Nature Catalysis*, 3(4):411–417, 2020.

[210] Shyam Kattel, Ping Liu, and Jingguang G Chen. Tuning selectivity of co2 hydrogenation reactions at the metal/oxide interface. *Journal of the American Chemical Society*, 139(29):9739–9754, 2017.

[211] Shuxing Bai, Qi Shao, Pengtang Wang, Qiguang Dai, Xingyi Wang, and Xiaoqing Huang. Highly active and selective hydrogenation of co2 to ethanol by ordered pd–cu nanoparticles. *Journal of the American Chemical Society*, 139(20):6827–6830, 2017.

[212] Molly Meng-Jung Li, Ziyan Zeng, Fenglin Liao, Xinlin Hong, and Shik Chi Edman Tsang. Enhanced co2 hydrogenation to methanol over cuzn nanoalloy in ga modified cu/zno catalysts. *Journal of Catalysis*, 343:157–167, 2016.

[213] Gonzalo Prieto, Jovana Zečević, Heiner Friedrich, Krijn P De Jong, and Petra E De Jongh. Towards stable catalysts by controlling collective properties of supported metal nanoparticles. *Nature materials*, 12(1):34–39, 2013.

[214] Shyam Kattel, Pedro J Ramírez, Jingguang G Chen, José A Rodriguez, and Ping Liu. Active sites for co2 hydrogenation to methanol on cu/zno catalysts. *Science*, 355(6331):1296–1299, 2017.

[215] Andres García-Trenco, Edward R White, Anna Regoutz, David J Payne, Milo SP Shaffer, and Charlotte K Williams. Pd2ga-based colloids as highly active catalysts for the hydrogenation of co2 to methanol. *ACS Catalysis*, 7(2):1186–1196, 2017.

[216] Andrés García-Trenco, Anna Regoutz, Edward R White, David J Payne, Milo SP Shaffer, and Charlotte K Williams. Pdin intermetallic nanoparticles for the hydrogenation of co2 to methanol. *Applied Catalysis B: Environmental*, 220:9–18, 2018.

[217] Zhisheng Shi, Qingqing Tan, Chao Tian, Yu Pan, Xuewei Sun, Jinxin Zhang, and Dongfang Wu. Co2 hydrogenation to methanol over cu-in intermetallic catalysts: Effect of reduction temperature. *Journal of Catalysis*, 379:78–89, 2019.

[218] Athimotlu Raju Rajamani, PC Ashly, Lakshay Dheer, Saurav Ch Sarma, Sumanta Sarkar, Debabrata Bagchi, Umesh V Waghmare, and Sebastian C Peter. Synergetic effect of ni-substituted pd2ge ordered intermetallic nanocomposites for efficient electrooxidation of ethanol in alkaline media. *ACS Applied Energy Materials*, 2(10):7132–7141, 2019.

[219] Qiurong Shi, Chengzhou Zhu, Cuixia Bi, Haibing Xia, Mark H Engelhard, Dan Du, and Yuehe Lin. Intermetallic pd 3 pb nanowire networks boost ethanol oxidation and oxygen reduction reactions with significantly improved methanol tolerance. *Journal of Materials Chemistry A*, 5(45):23952–23959, 2017.

[220] Shuiyun Shen, Yangge Guo, Liuxuan Luo, Fan Li, Lin Li, Guanghua Wei, Jiewei Yin, Changchun Ke, and Junliang Zhang. Comprehensive analysis on the highly active and stable pdau/c electrocatalyst for ethanol oxidation reaction in alkaline media. *The Journal of Physical Chemistry C*, 122(3):1604–1611, 2018.

[221] Tong Wu, Jinchen Fan, Qiaoxia Li, Penghui Shi, Qunjie Xu, and Yulin Min. Palladium nanoparticles anchored on anatase titanium dioxide-black phosphorus hybrids with heterointerfaces: highly electroactive and durable catalysts for ethanol electrooxidation. *Advanced Energy Materials*, 8(1):1701799, 2018.

[222] Kenneth W Lux and Karien J Rodriguez. Template synthesis of arrays of nano fuel cells. *Nano letters*, 6(2):288–295, 2006.

[223] JD Lović, Nevenka R Elezović, BM Jović, Piotr Zabinski, Lj Gajić-Krstajić, and Vladimir D Jović. Electrodeposited agpd alloy coatings as efficient catalysts for the ethanol oxidation reaction. *International Journal of Hydrogen Energy*, 43(39):18498–18508, 2018.

[224] Sheng Dai, Tzu-Hsi Huang, Xingxu Yan, Chao-Yu Yang, Tsan-Yao Chen, Jeng-Han Wang, Xiaoqing Pan, and Kuan-Wen Wang. Promotion of ternary pt–sn–ag catalysts toward ethanol oxidation reaction: Revealing electronic and structural effects of additive metals. *ACS Energy Letters*, 3(10):2550–2557, 2018.

[225] Wenxin Du, Guangxing Yang, Emily Wong, N Aaron Deskins, Anatoly I Frenkel, Dong Su, and Xiaowei Teng. Platinum-tin oxide core–shell catalysts for efficient electro-oxidation of ethanol. *Journal of the American Chemical Society*, 136(31):10862–10865, 2014.

[226] ZX Liang, TS Zhao, JB Xu, and LD Zhu. Mechanism study of the ethanol oxidation reaction on palladium in alkaline media. *Electrochimica Acta*, 54(8):2203–2208, 2009.

[227] D González-Quijano, WJ Pech-Rodríguez, JA González-Quijano, JI Escalante-García, C Morais, TW Napporn, and FJ Rodríguez-Varela. Performance and in-situ ftir evaluation of pt- sn/c electrocatalysts with several pt: Sn atomic ratios for the ethanol oxidation reaction in acidic media. *ChemElectroChem*, 5(22):3540–3547, 2018.

[228] Liang Ma, Deryn Chu, and Rongrong Chen. Comparison of ethanol electro-oxidation on pt/c and pd/c catalysts in alkaline media. *International Journal of Hydrogen Energy*, 37(15):11185–11194, 2012.

[229] Kezhu Jiang, Pengtang Wang, Shaojun Guo, Xu Zhang, Xuan Shen, Gang Lu, Dong Su, and Xiaoqing Huang. Ordered pdcu-based nanoparticles as bifunctional

oxygen-reduction and ethanol-oxidation electrocatalysts. *Angewandte Chemie*, 128(31):9176–9181, 2016.

[230] Yizhong Lu, Yuanyuan Jiang, Xiaohui Gao, Xiaodan Wang, and Wei Chen. Strongly coupled pd nanotetrahedron/tungsten oxide nanosheet hybrids with enhanced catalytic activity and stability as oxygen reduction electrocatalysts. *Journal of the American chemical Society*, 136(33):11687–11697, 2014.

[231] Aicheng Chen and Cassandra Ostrom. Palladium-based nanomaterials: synthesis and electrochemical applications. *Chemical reviews*, 115(21):11999–12044, 2015.

[232] Sumanta Sarkar, Rajkumar Jana, Umesh V Waghmare, Balamurugan Kuppan, S Sampath, and Sebastian C Peter. Ordered pd2ge intermetallic nanoparticles as highly efficient and robust catalyst for ethanol oxidation. *Chemistry of Materials*, 27(21):7459–7467, 2015.

[233] W Wopersnow and K Schubert. Nickel-palladium-germanium alloys. *Journal of the Less Common Metals*, 52(1):1–12, 1977.

[234] Gun-hee Moon, Wooyul Kim, Alok D Bokare, Nark-eon Sung, and Wonyong Choi. Solar production of h2o2 on reduced graphene oxide–tio2 hybrid photocatalysts consisting of earth-abundant elements only. *Energy & Environmental Science*, 7(12):4023–4028, 2014.

[235] Claudlus Kormann, Detlef W Bahnemann, and Michael R Hoffmann. Photocatalytic production of h2o2 and organic peroxides in aqueous suspensions of tio2, zno, and desert sand. *Environmental science & technology*, 22(7):798–806, 1988.

[236] Daijiro Tsukamoto, Akimitsu Shiro, Yasuhiro Shiraishi, Yoshitsune Sugano, Satoshi Ichikawa, Shunsuke Tanaka, and Takayuki Hirai. Photocatalytic h2o2 production from ethanol/o2 system using tio2 loaded with au–ag bimetallic alloy nanoparticles. *Acs catalysis*, 2(4):599–603, 2012.

[237] Yasuhiro Shiraishi, Shunsuke Kanazawa, Yoshitsune Sugano, Daijiro Tsukamoto, Hirokatsu Sakamoto, Satoshi Ichikawa, and Takayuki Hirai. Highly selective production of hydrogen peroxide on graphitic carbon nitride (g-c3n4) photocatalyst activated by visible light. *Acs Catalysis*, 4(3):774–780, 2014.

[238] J Bandara, CPK Udawatta, and CSK Rajapakse. Highly stable cuo incorporated tio 2 catalyst for photocatalytic hydrogen production from h2o. *Photochemical & Photobiological Sciences*, 4(11):857–861, 2005.

[239] Valter Maurino, Claudio Minero, Giuseppe Mariella, and Ezio Pelizzetti. Sustained production of h 2 o 2 on irradiated tio 2–fluoride systems. *Chemical Communications*, (20):2627–2629, 2005.

[240] Yusuke Isaka, Kohei Oyama, Yusuke Yamada, Tomoyoshi Suenobu, and Shunichi Fukuzumi. Photocatalytic production of hydrogen peroxide from water and dioxygen using cyano-bridged polynuclear transition metal complexes as water oxidation catalysts. *Catalysis Science & Technology*, 6(3):681–684, 2016.

[241] Kentaro Mase, Masaki Yoneda, Yusuke Yamada, and Shunichi Fukuzumi. Efficient photocatalytic production of hydrogen peroxide from water and dioxygen with bismuth vanadate and a cobalt (ii) chlorin complex. *ACS Energy Letters*, 1(5):913–919, 2016.

[242] Satoshi Kato, Jieun Jung, Tomoyoshi Suenobu, and Shunichi Fukuzumi. Production of hydrogen peroxide as a sustainable solar fuel from water and dioxygen. *Energy & Environmental Science*, 6(12):3756–3764, 2013.

[243] Yusuke Isaka, Satoshi Kato, Dachao Hong, Tomoyoshi Suenobu, Yusuke Yamada, and Shunichi Fukuzumi. Bottom-up and top-down methods to improve catalytic reactivity for photocatalytic production of hydrogen peroxide using a ru-complex

and water oxidation catalysts. *Journal of Materials Chemistry A*, 3(23):12404–12412, 2015.

[244] Kentaro Mase, Kei Ohkubo, and Shunichi Fukuzumi. Much enhanced catalytic reactivity of cobalt chlorin derivatives on two-electron reduction of dioxygen to produce hydrogen peroxide. *Inorganic chemistry*, 54(4):1808–1815, 2015.

[245] Suman Thakur, Tolendra Kshetri, Nam Hoon Kim, and Joong Hee Lee. Sunlight-driven sustainable production of hydrogen peroxide using a cds–graphene hybrid photocatalyst. *Journal of Catalysis*, 345:78–86, 2017.

[246] Yasuhiro Shiraishi, Shunsuke Kanazawa, Yusuke Kofuji, Hirokatsu Sakamoto, Satoshi Ichikawa, Shunsuke Tanaka, and Takayuki Hirai. Sunlight-driven hydrogen peroxide production from water and molecular oxygen by metal-free photocatalysts. *Angewandte Chemie International Edition*, 53(49):13454–13459, 2014.

[247] Shen Zhao, Xu Zhao, Hui Zhang, Jiang Li, and Yongfa Zhu. Covalent combination of polyoxometalate and graphitic carbon nitride for light-driven hydrogen peroxide production. *Nano Energy*, 35:405–414, 2017.

[248] Liping Yang, Guohui Dong, Daniel L Jacobs, Yuanhao Wang, Ling Zang, and Chuanyi Wang. Two-channel photocatalytic production of h2o2 over g-c3n4 nanosheets modified with perylene imides. *Journal of catalysis*, 352:274–281, 2017.

[249] Zedong Zhu, Honghui Pan, Muthu Murugananthan, Jianyu Gong, and Yanrong Zhang. Visible light-driven photocatalytically active g-c3n4 material for enhanced generation of h2o2. *Applied Catalysis B: Environmental*, 232:19–25, 2018.

[250] Wen-Che Hou and Yi-Sheng Wang. Photocatalytic generation of h2o2 by graphene oxide in organic electron donor-free condition under sunlight. *ACS Sustainable Chemistry & Engineering*, 5(4):2994–3001, 2017.

[251] Yasuhiro Shiraishi, Shunsuke Kanazawa, Yoshitsune Sugano, Daijiro Tsukamoto, Hirokatsu Sakamoto, Satoshi Ichikawa, and Takayuki Hirai. Highly selective production of hydrogen peroxide on graphitic carbon nitride (g-c3n4) photocatalyst activated by visible light. *Acs Catalysis*, 4(3):774–780, 2014.

[252] Shaozheng Hu, Xiaoyu Qu, Ping Li, Fei Wang, Qiang Li, Lijuan Song, Yanfeng Zhao, and Xiaoxue Kang. Photocatalytic oxygen reduction to hydrogen peroxide over copper doped graphitic carbon nitride hollow microsphere: the effect of cu (i)-n active sites. *Chemical Engineering Journal*, 334:410–418, 2018.

[253] Avdhoot Datar, Maya Bar-Sadan, and Ashwin Ramasubramaniam. Interactions between transition-metal surfaces and mos2 monolayers: Implications for hydrogen evolution and co2 reduction reactions. *The Journal of Physical Chemistry C*, 124(37):20116–20124, 2020.

[254] Ibrahim Saana Amiinu, Zonghua Pu, Xiaobo Liu, Kwadwo Asare Owusu, Hellen Gabriela Rivera Monestel, Felix Ofori Boakye, Haining Zhang, and Shichun Mu. Multifunctional mo–n/c@ mos2 electrocatalysts for her, oer, orr, and zn–air batteries. *Advanced Functional Materials*, 27(44):1702300, 2017.

[255] Zhongxu Wang, Jingxiang Zhao, Qinghai Cai, and Fengyu Li. Computational screening for high-activity mos 2 monolayer-based catalysts for the oxygen reduction reaction via substitutional doping with transition metal. *Journal of Materials Chemistry A*, 5(20):9842–9851, 2017.

[256] Peter E Blöchl. Projector augmented-wave method. *Physical review B*, 50(24):17953, 1994.

[257] Ronen Bar-Ziv, Priyadarshi Ranjan, Anna Lavie, Akash Jain, Somenath Garai, Avraham Bar Hen, Ronit Popovitz-Biro, Reshef Tenne, Raul Arenal, Ashwin Ra-

masubramaniam, et al. Au-mos2 hybrids as hydrogen evolution electrocatalysts. *ACS Applied Energy Materials*, 2(8):6043–6050, 2019.

[258] Joyce A Ober. Mineral commodity summaries 2016. Technical report, US Geological Survey, 2016.

[259] Wanghui Zhao, Lifu Zhang, Qiquan Luo, Zhenpeng Hu, Wenhua Zhang, Sean Smith, and Jinlong Yang. Single mo1 (cr1) atom on nitrogen-doped graphene enables highly selective electroreduction of nitrogen into ammonia. *ACS Catalysis*, 9(4):3419–3425, 2019.

[260] Egill Skulason, Thomas Bligaard, Sigrídur Gudmundsdóttir, Felix Studt, Jan Rossmeisl, Frank Abild-Pedersen, Tejs Vegge, Hannes Jónsson, and Jens K Nørskov. A theoretical evaluation of possible transition metal electro-catalysts for n 2 reduction. *Physical Chemistry Chemical Physics*, 14(3):1235–1245, 2012.

[261] Zhong-Hua Xue, Shi-Nan Zhang, Yun-Xiao Lin, Hui Su, Guang-Yao Zhai, Jing-Tan Han, Qiu-Ying Yu, Xin-Hao Li, Markus Antonietti, and Jie-Sheng Chen. Electrochemical reduction of n2 into nh3 by donor–acceptor couples of ni and au nanoparticles with a 67.8% faradaic efficiency. *Journal of the American Chemical Society*, 141(38):14976–14980, 2019.

[262] Lianqiao Tan, Na Yang, Xun Huang, Lishan Peng, Cheng Tong, Mingming Deng, Xianyi Tang, Li Li, Qiang Liao, and Zidong Wei. Synthesis of ammonia via electrochemical nitrogen reduction on high-index faceted au nanoparticles with a high faradaic efficiency. *Chemical Communications*, 55(96):14482–14485, 2019.

[263] Chan Chen, Cong Liang, Jun Xu, Jiankun Wei, Xiangrong Li, Ying Zheng, Junrui Li, Haolin Tang, and Junsheng Li. Size-dependent electrochemical nitrogen reduction catalyzed by monodisperse au nanoparticles. *Electrochimica Acta*, 335:135708, 2020.

[264] Wenyi Li, Ke Li, Yixing Ye, Shengbo Zhang, Yanyan Liu, Guozhong Wang, Changhao Liang, Haimin Zhang, and Huijun Zhao. Efficient electrocatalytic nitrogen reduction to ammonia with aqueous silver nanodots. *Communications Chemistry*, 4(1):1–11, 2021.

[265] Miao-Miao Shi, Di Bao, Ba-Ri Wulan, Yong-He Li, Yue-Fei Zhang, Jun-Min Yan, and Qing Jiang. Au sub-nanoclusters on tio2 toward highly efficient and selective electrocatalyst for n2 conversion to nh3 at ambient conditions. *Advanced Materials*, 29(17):1606550, 2017.

[266] Uttam Kumar Ghorai, Sourav Paul, Biswajit Ghorai, Ashadul Adalder, Samadhan Kapse, Ranjit Thapa, Abharana Nagendra, and Amal Gain. Scalable production of cobalt phthalocyanine nanotubes: Efficient and robust hollow electrocatalyst for ammonia synthesis at room temperature. *ACS nano*, 15(3):5230–5239, 2021.

[267] Jingxiang Zhao and Zhongfang Chen. Single mo atom supported on defective boron nitride monolayer as an efficient electrocatalyst for nitrogen fixation: a computational study. *Journal of the American Chemical Society*, 139(36):12480–12487, 2017.

[268] Xingwu Zhai, Lei Li, Xiaoyue Liu, Yafei Li, Jueming Yang, Dezheng Yang, Jinli Zhang, Hongxia Yan, and Guixian Ge. A dft screening of single transition atoms supported on mos 2 as highly efficient electrocatalysts for the nitrogen reduction reaction. *Nanoscale*, 12(18):10035–10043, 2020.

[269] Ritesh Kumar and Abhishek K Singh. Electronic structure based intuitive design principle of single-atom catalysts for efficient electrolytic nitrogen reduction. *ChemCatChem*, 12(21):5456–5464, 2020.

[270] Hao-Ran Zhu, Yan-Ling Hu, Shi-Hao Wei, and Da-Yin Hua. Single-metal atom anchored on boron monolayer (β12) as an electrocatalyst for nitrogen reduction into

ammonia at ambient conditions: A first-principles study. *The Journal of Physical Chemistry C*, 123(7):4274–4281, 2019.

[271] Changhyeok Choi, Seoin Back, Na-Young Kim, Juhyung Lim, Yong-Hyun Kim, and Yousung Jung. Suppression of hydrogen evolution reaction in electrochemical n2 reduction using single-atom catalysts: a computational guideline. *Acs Catalysis*, 8(8):7517–7525, 2018.

[272] Chongyi Ling, Xianghong Niu, Qiang Li, Aijun Du, and Jinlan Wang. Metal-free single atom catalyst for n2 fixation driven by visible light. *Journal of the American Chemical Society*, 140(43):14161–14168, 2018.

[273] Xin Liu, Yan Jiao, Yao Zheng, Mietek Jaroniec, and Shi-Zhang Qiao. Building up a picture of the electrocatalytic nitrogen reduction activity of transition metal single-atom catalysts. *Journal of the American Chemical Society*, 141(24):9664–9672, 2019.

[274] Yanming Liu, Yan Su, Xie Quan, Xinfei Fan, Shuo Chen, Hongtao Yu, Huimin Zhao, Yaobin Zhang, and Jijun Zhao. Facile ammonia synthesis from electrocatalytic n2 reduction under ambient conditions on n-doped porous carbon. *ACS Catalysis*, 8(2):1186–1191, 2018.

[275] Marc-André Légaré, Guillaume Bélanger-Chabot, Rian D Dewhurst, Eileen Welz, Ivo Krummenacher, Bernd Engels, and Holger Braunschweig. Nitrogen fixation and reduction at boron. *Science*, 359(6378):896–900, 2018.

[276] Xiaomin Yu, Peng Han, Zengxi Wei, Linsong Huang, Zhengxiang Gu, Sijia Peng, Jianmin Ma, and Gengfeng Zheng. Boron-doped graphene for electrocatalytic n2 reduction. *Joule*, 2(8):1610–1622, 2018.

[277] Chuangwei Liu, Qinye Li, Chengzhang Wu, Jie Zhang, Yonggang Jin, Douglas R MacFarlane, and Chenghua Sun. Single-boron catalysts for nitrogen reduction re-

action. *Journal of the American Chemical Society*, 141(7):2884–2888, 2019.

[278] Hui Tang and Sohrab Ismail-Beigi. Novel precursors for boron nanotubes: the competition of two-center and three-center bonding in boron sheets. *Physical review letters*, 99(11):115501, 2007.

[279] Xiaojun Wu, Jun Dai, Yu Zhao, Zhiwen Zhuo, Jinlong Yang, and Xiao Cheng Zeng. Two-dimensional boron monolayer sheets. *ACS nano*, 6(8):7443–7453, 2012.

[280] Evgeni S Penev, Somnath Bhowmick, Arta Sadrzadeh, and Boris I Yakobson. Polymorphism of two-dimensional boron. *Nano letters*, 12(5):2441–2445, 2012.

[281] Zhi-Qiang Wang, Tie-Yu Lü, Hui-Qiong Wang, Yuan Ping Feng, and Jin-Cheng Zheng. Review of borophene and its potential applications. *Frontiers of Physics*, 14(3):1–20, 2019.

[282] Andrew J Mannix, Xiang-Feng Zhou, Brian Kiraly, Joshua D Wood, Diego Alducin, Benjamin D Myers, Xiaolong Liu, Brandon L Fisher, Ulises Santiago, Jeffrey R Guest, et al. Synthesis of borophenes: Anisotropic, two-dimensional boron polymorphs. *Science*, 350(6267):1513–1516, 2015.

[283] Baojie Feng, Jin Zhang, Qing Zhong, Wenbin Li, Shuai Li, Hui Li, Peng Cheng, Sheng Meng, Lan Chen, and Kehui Wu. Experimental realization of two-dimensional boron sheets. *Nature chemistry*, 8(6):563–568, 2016.

[284] Vivekanand Shukla, John Warna, Naresh K Jena, Anton Grigoriev, and Rajeev Ahuja. Toward the realization of 2d borophene based gas sensor. *The Journal of Physical Chemistry C*, 121(48):26869–26876, 2017.

[285] Tingting Liu, Yuhong Chen, Meiling Zhang, Lihua Yuan, Cairong Zhang, Jing Wang, and Jiajia Fan. A first-principles study of gas molecule adsorption on borophene. *Aip Advances*, 7(12):125007, 2017.

[286] Chieh-Szu Huang, Altynbek Murat, Vasudeo Babar, Enrique Montes, and Udo Schwingenschlogl. Adsorption of the gas molecules nh3, no, no2, and co on borophene. *The Journal of Physical Chemistry C*, 122(26):14665–14670, 2018.

[287] Muhammad Isa Khan, Abdul Majid, Naveed Ashraf, and Irslan Ullah. A dft study on a borophene/boron nitride interface for its application as an electrode. *Physical Chemistry Chemical Physics*, 22(6):3304–3313, 2020.

[288] Xiaoming Zhang, Junping Hu, Yingchun Cheng, Hui Ying Yang, Yugui Yao, and Shengyuan A Yang. Borophene as an extremely high capacity electrode material for li-ion and na-ion batteries. *Nanoscale*, 8(33):15340–15347, 2016.

[289] Showkat H Mir, Sudip Chakraborty, Prakash C Jha, John Wärnå, Himadri Soni, Prafulla K Jha, and Rajeev Ahuja. Two-dimensional boron: lightest catalyst for hydrogen and oxygen evolution reaction. *Applied Physics Letters*, 109(5):053903, 2016.

[290] Li Shi, Chongyi Ling, Yixin Ouyang, and Jinlan Wang. High intrinsic catalytic activity of two-dimensional boron monolayers for the hydrogen evolution reaction. *Nanoscale*, 9(2):533–537, 2017.

[291] Xin Tan, Hassan A Tahini, and Sean C Smith. Borophene as a promising material for charge-modulated switchable co2 capture. *ACS applied materials & interfaces*, 9(23):19825–19830, 2017.

[292] Haoming Shen, Yawei Li, and Qiang Sun. Cu atomic chains supported on β-borophene sheets for effective co 2 electroreduction. *Nanoscale*, 10(23):11064–11071, 2018.

[293] Yashpal Singh, Seoin Back, and Yousung Jung. Computational exploration of borophane-supported single transition metal atoms as potential oxygen reduction

and evolution electrocatalysts. *Physical Chemistry Chemical Physics*, 20(32):21095–21104, 2018.

[294] Chuangwei Liu, Qinye Li, Jie Zhang, Yonggang Jin, Douglas R MacFarlane, and Chenghua Sun. Conversion of dinitrogen to ammonia on ru atoms supported on boron sheets: a dft study. *Journal of Materials Chemistry A*, 7(9):4771–4776, 2019.

[295] Chi-Cheng Lee, Baojie Feng, Marie D'angelo, Ryu Yukawa, Ro-Ya Liu, Takahiro Kondo, Hiroshi Kumigashira, Iwao Matsuda, and Taisuke Ozaki. Peculiar bonding associated with atomic doping and hidden honeycombs in borophene. *Physical Review B*, 97(7):075430, 2018.

[296] Hui Tang and Sohrab Ismail-Beigi. Self-doping in boron sheets from first principles: A route to structural design of metal boride nanostructures. *Physical Review B*, 80(13):134113, 2009.

[297] Yao Yao, Haijiang Wang, Xiao-zi Yuan, Hui Li, and Minhua Shao. Electrochemical nitrogen reduction reaction on ruthenium. *ACS Energy Letters*, 4(6):1336–1341, 2019.

[298] Shisheng Zheng, Shunning Li, Zongwei Mei, Zongxiang Hu, Mihai Chu, Jiahua Liu, Xin Chen, and Feng Pan. Electrochemical nitrogen reduction reaction performance of single-boron catalysts tuned by mxene substrates. *The journal of physical chemistry letters*, 10(22):6984–6989, 2019.

[299] Min Yu and Dallas R Trinkle. Accurate and efficient algorithm for bader charge integration. *The Journal of chemical physics*, 134(6):064111, 2011.